Dissertation

Assessment of functionality and safety of organic electrolytic photocapacitors for wireless brain stimulation

submitted by

Dr. med. vet.

Marta NOWAKOWSKA

for the Academic Degree of

Doctor of Philosophy

(PhD)

at the

Medical University of Graz

Department of Neurosurgery

under the Supervision of

Assoz. Prof. Priv.-Doz. Dipl.-Ing. Dr.techn. Rainer Schindl

2024

STATUTORY DECLARATION

I hereby declare that this thesis is my own original work and that I have fully acknowledged by name all of those individuals and organisations that have contributed to the research for this thesis. Due acknowledgement has been made in the text to all other material used. Throughout this thesis and in all related publications I followed the “Guidelines of the Medical University of Graz on Good Scientific Practice“.

Graz, 7.08.2024

DISCLOSURES

Parts of this thesis have been published in:

Nowakowska M.[a,g], Jakešová M.[b], Schmidt T.[c,g], Opančar A.[b,d], Polz M.[e], Reimer R.[c], Fuchs J.[c,e], Patz S.[a], Ziesel D.[c,e], Scheruebel S.[c], Kornmueller K.[c], Rienmüller T.[e,g], Đerek V.[d], Głowacki E.D.[b], Schindl R.[c,g], Üçal M.[a,f,g] (2024). Light-Controlled Electric Stimulation with Organic Electrolytic Photocapacitors Achieves Complex Neuronal Network Activation: Semi-chronic Study in Cortical Cell Culture and Rat Model. *Advanced Healthcare Materials* (accepted)
doi: 10.1002/adhm.202401303

[a] Department of Neurosurgery, Medical University of Graz, Auenbruggerplatz 29, 8036 Graz, Austria

[b] Bioelectronics Materials and Devices Laboratory, CEITEC, Brno University of Technology, Purkyňova 123, 612 00 Brno, Czech Republic

[c] Gottfried Schatz Research Center for Cell Signaling, Metabolism and Aging, Division of Medical Physics and Biophysics, Medical University of Graz, Neue Stiftingtalstraße 6, 8010 Graz, Austria

[d] Department of Physics, Faculty of Science, University of Zagreb, Bijenička c. 32, 10000 Zagreb, Croatia

[e] Institute of Health Care Engineering with European Testing Center of Medical Devices, Graz University of Technology, Stremayrgasse 16/II, 8010 Graz, Austria

[f] Department of Neurology, Medical University of Graz, Auenbruggerplatz 22, 8036 Graz, Austria

[g] BioTechMed-Graz, Mozartgasse 12/II, 8010 Graz, Austria

All co-authors were asked for permission and agreed to use their data in this thesis. Their consent has been provided to the research management unit of the Medical University of Graz.

Another part of this thesis contains unpublished data.

During my PhD, I contributed to the following publications:

1. Haindl M.T., Üçal M., Tafrali C., Wonisch W., Erdogan C., **Nowakowska M.**, Adzemovic M.Z., Khalil M., Enzinger C., Hochmeister S. (2024) Sex Differences under Vitamin D Supplementation in an Animal Model of Progressive Multiple Sclerosis. *Nutrients*, 16, 554. doi:10.3390/nu16040554
2. Haindl M.T., Üçal M., Wonisch W., Lang M., **Nowakowska M.**, Adzemovic M.Z., Khalil M., Enzinger C., Hochmeister S. (2023) Vitamin D—An Effective Antioxidant in an Animal Model of Progressive Multiple Sclerosis. *Nutrients* 15, 3309. doi:10.3390/nu15153309
3. Ziesel D., **Nowakowska M.**, Scheruebel S., Kornmueller K., Schaefer U., Schindl R., Baumgartner C., Üçal M., Rienmüller T. (2023) Electrical stimulation methods and protocols for the treatment of traumatic brain injury: a critical review of preclinical research. *Journal of NeuroEngineering and Rehabilitation*, 20, 51. doi:10.1186/s12984-023-01159-y
4. **Nowakowska M.**, Üçal M., Charalambous M., Bhatti S.F.M., Denison T., Meller S., Worrell G.A., Potschka H., Volk H.A. (2022). Neurostimulation as a Method of Treatment and a Preventive Measure in Canine Drug-Resistant Epilepsy: Current State and Future Prospects. *Frontiers in Veterinary Science*, 9:889561. doi:10.3389/fvets.2022.889561
5. Schmidt T., Jakešová M., Đerek V., Kornmueller K., Tiapko O., Bischof H., Burgstaller S., Waldherr L., **Nowakowska M.**, Baumgartner C., Üçal M., Leitinger G., Scheruebel S., Patz S., Malli R., Głowacki E.D., Rienmüller T., Schindl R. (2022). Light stimulation of neurons on organic photocapacitors induces action potentials with millisecond precision. *Advanced Materials Technologies*, 2101159. doi:10.1002/admt.202101159
6. Waldherr L., Seitanidou M., Jakešová M., Handl V., Honeder S., **Nowakowska M.**, Tomin T., Karami Rad M., Schmidt T., Distl J., Birner-Gruenberger R., von Campe G., Schäfer U., Berggren M., Rinner B., Asslaber M., Ghaffari-Tabrizi-Wizsy N., Patz S., Simon D.T., Schindl R. (2021). Targeted chemotherapy of glioblastoma spheroids with an iontronic pump. *Advanced Materials Technologies*, 6, 5, 2001302. doi:10.1002/admt.202001302

„We are not making science for science.

We are making science for the benefit of humanity“

Françoise Barré-Sinous

ACKNOWLEDGMENTS

Humans are social animals and as such they heavily depend on others. This holds especially true for modern research, where scientists build a network for a better flow of data, ideas, and support. Therefore, I would like to express my thanks to the people who supported me throughout my PhD journey.

Rainer Schindl has not only been an excellent PhD supervisor, but also a great advisor full of ideas. I could always learn something useful or thought-provoking from every discussion we had, which is extremely valuable in the everyday life of a scientist. Rainer is also a great conference companion and a fantastic skier, which I could appreciate during many events in Austria.

Muammer Üçal, as a thesis co-supervisor and the lead of Logos-TBI project, is the person who taught me almost everything I know in the lab and gave me the most guidance during my experiments. I could really appreciate both his theoretical and practical knowledge, as well as his continued support for my scientific career.

I would like to thank Ute Schäfer for the opportunity of working in her group and her insights during our regular meetings. I am also very grateful towards Silke Patz, who shared with me her in-depth know-how in cell and tissue culture, and supported with her knowledge and experience – especially when not everything went smooth in the lab. A huge thank you goes to all of the current and previous members of the AG Schäfer: Gerda Grünbacher, Vanessa Etschmeier, Amila Zolota-Mehmedović, James Smith, and Dominik Dominković. It is not an understatement to say that without their support my experimental work would be impossible.

AG Schindl has been my safe haven to find the support in the harder times of my studies. I would like to thank everyone involved, especially Tony Schmidt, Verena Handl, and Linda Waldherr. You all are great colleagues and friends, and you made the sometimes bumpy PhD road more bearable. I would also like to thank Sonja Hochmeister, a great advisor, cooperation partner, and my role model in terms of accommodating clinical work with research.

I would like to appreciate Karin Kornmüller, Robert Reimer, Julia Fuchs, Theresa Rienmüller, Mathias Polz, Daniel Ziesel, and all people involved in Logos-TBI project. Great thanks to our international collaborators, Eric Głowacki, Marie Jakešová, Vedran Đerek, and Aleksandar

Opančar, who made the entire project possible through the conception and manufacture of OEPC.

A word of appreciation is directed to all my colleagues from the PhD school of molecular medicine, in particular to Denis Krivić and Begüm Okutan as well as my Polish ZMF-floor-companions: Ilona Mertelseder and Marta Szmyra-Połomka.

I would like to express my particular gratitude towards my thesis reviewers. I really appreciate you took your time to read and comment the whole thesis, especially since I know I have a tendency to tell fairy tales to describe the smallest thing.

Agata Szymańska, Zosia Ratajewicz, Marta and Konstantin Tikhomirov, and Aneta Gerlak are my dear friends, whom I unfortunately cannot see regularly, as they all do not live in Austria. Despite that, they managed to continuously support me during all those years, providing their advice, help, or sometimes just a good meme or two to cheer me up.

Ich möchte mich bei den Schiedsrichtern des Steirischen Fußballverbandes bedanken. Unsere Treffen und Spieleinsätze haben mich regelmäßig gezwungen, ab und zu den Kopf frei zu bekommen und einen Ausgleich nach der Arbeit zu finden.

Al miaj grazaj kaj ekstergrazaj esperantaj geamikoj: kiel ja skribis unu poeto – mi volas diri dankon, al miaj plej bonaj amikoj en la mondo!

Dziękuję również moim Rodzicom, Aleksandrze i Grzegorzowi, za ich nieustanne wsparcie nie tylko w trakcie doktoratu, ale również przez całą moja edukację i karierę zawodową. Bez Was nie byłoby to możliwe i cieszę się, że jesteście ze mną.

Et enfin et surtout, merci à mon fiancé Matthieu. Je ne peux même pas imaginer, comme c'était difficile d'écouter mes plaintes tous les jours. Je suis tellement contente de t'avoir, tu roxxes du poney !

During my PhD studies, I was a part of the PhD program Molecular Medicine (MolMed) of the Medical University of Graz. I received funding from the Austrian Science Fund (FWF; project number ZK17).

TABLE OF CONTENTS

LIST OF ABBREVIATIONS

AMPA.....α-amino-3-hydroxy-5-methyl-4-isoxazolepropionic acid
Ara-C ..... Cytosine-β-D-arabinoside

BBB.....Blood-brain barrier
bFGF..... Basic fibroblast growth factor
BME ..... Basal Medium Eagle

CA.....Cornu Ammonis
CaMK.....Ca^{2+}/calmodulin-dependent protein kinase
CB..... Cacodylate buffer
CD..... Cluster of differentiation
CMOSComplementary metal-oxide-semiconductor
CNS .....Central nervous system
CR..... Calretinin
CRE .....CREB response element
CREB cAMP response element-binding protein
CSF..... Cerebrospinal fluid

DAB ..... 3,3'-diaminobenzidine
DALYs.....Disability-adjusted life years
DAPI ..... 4′,6-diamidino-2-phenylindole
DBS .....Deep brain stimulation
DG .....Dentate gyrus
diH_2O .....Deionised water
DIV.....Day *in vitro*
DMEM...Dulbecco's Minimal Essential Medium

EC..... Entorhinal cortex
ECM.....Extracellular matrix
ECoG .....Electrocorticography
ELK1 .....ETS Like-1 protein
ER .....Endoplasmic reticulum

FA..... Formaldehyde
FBR..... Foreign body reaction
FBS .....Fetal bovine serum
FDA..... US Food and Drug Administration
FdUrd ..... 5-fluoro-2'-deoxyuridine
FMD .....Fentanyl-midazolam-medetomidine

GABA ..... γ-aminobutyric acid
GAP..... Growth-associated protein
GFAP ..... Glial fibrillary acidic protein

H_2Pc .....Phthalocyanine
HC..... Hippocampus
HDMS..... Hexamethyldisilazane
HIER..... Heat-induced epitope retrieval

Iba1Ionised calcium-binding adapter molecule 1
ICC..... Immunocytochemistry
IEG..... Immediate-early gene
IF .....Immunofluorescence
IHC..... Immunohistochemistry
ITO .....Indium-tin oxide

K_V .....Voltage-gated potassium channels

LDH..... Lactate dehydrogenase
LEC ..... Lateral entorhinal cortex
LED .....Light-emitting diode

MAPK..... Mitogen-activated protein kinase
MEC .....Medial entorhinal cortex
MRI..... Magnetic resonance imaging

Na_v ..... Voltage-gated sodium channels
NGS ..... Normal goat serum
NMDA ..... N-methyl-D-aspartate

OEPC..... Organic electrolytic photocapacitor(s)
OTC ..... Organotypic tissue culture

PBS..... Phosphate-buffered saline
PBST ..... PBS with 0.3% Triton X-100
PD ..... Parkinson's disease
PDL ..... Poly-D-lysine
PEDOT:PSS ..... Poly(3,4-ethylenedioxythiophene):polystyrene sulfonate
PEI ..... Polyethylenimine
PET ..... Polyethylene terephthalate
PHC ..... Parahippocampal cortex
PNS ..... Peripheral nervous system
PTCDI *N,N′*-dimethyl perylene-3,4,9,10-tetracarboxylic diimide
PV ..... Parvalbumin

RNS ..... Responsive neurostimulation
ROI ..... Region of interest
ROS ..... Reactive oxygen species
rTMS Repetitive transcranial magnetic stimulation

SCI ..... Spinal cord injury
SCS ..... Spinal cord stimulation
SEM ..... Scanning electron microscopy
SOM ..... Somatosensory cortex
SRE ..... Serum response element
SRF ..... Serum response factor
SST ..... Somatostatin

tACS Transcranial alternating current stimulation
TBI ..... Traumatic brain injury
tDCS..... Transcranial direct current stimulation
TMS..... Transcranial magnetic stimulation
TRPV1 Transient receptor potential cation channel subfamily V member 1

VIP ..... Vasoactive intestinal peptide
VNS ..... Vagus nerve stimulation

LIST OF FIGURES

ABSTRACT

Neurostimulation, the targeted modulation of nervous tissue activity, stands as a pivotal technique in both neuroscientific inquiry and clinical applications. Successful applications of electrical brain stimulation range from restoring motor control in Parkinson's disease to reducing seizures in drug-resistant epilepsy, and enhancing rehabilitation post-stroke or injury. The development of wireless neurostimulation methods represents a significant goal in this field, with researchers aiming to minimise invasiveness and enhance patients' comfort by eliminating the need for cumbersome cables and control units.

Among potential solutions, photoactive organic semiconductors emerge as particularly promising. Their distinct properties enable the conversion of light signals into electric fields, which is achievable within thin layers, thereby significantly reducing the bulk of stimulatory devices. However, before a new technique can be considered for clinical application, its safety and efficacy must be rigorously established through preclinical studies. Hence, the primary objective of this study was to investigate the feasibility, biocompatibility, and efficacy of wireless light-controlled organic electrolytic photocapacitors (OEPC) in neurostimulation.

In this study, OEPC were applied across various models encompassing *in vitro*, *ex vivo*, and *in vivo* rat brain applications. The *in vivo* model was based on primary cortical cell culture. Over a two-week cultivation period, no discernible differences in cytotoxicity were observed between cells grown atop OEPC versus those cultured on standard glass cover slips. Light stimulation of cells on OEPC led to elevated c-Fos expression compared to cells maintained in darkness, indicating effective stimulation. This effect was achieved primarily through the device's photoactive layer, with signal propagation noted within the neuronal network.

OEPC stimulation of organotypic hippocampal slice cultures similarly yielded increased c-Fos expression throughout the entire section. Following daily stimulation sessions over seven days, elevated expression levels of GAP-43 and NeuN were observed, suggesting potential protective effects of the treatment.

In an intricate *in vivo* setup, flexible OEPC were implanted on top of the somatosensory cortex in adult rats. Initial analysis of c-Fos expression within post-implantation periods less than 48 hours was confounded by early post-surgical inflammatory processes, making it challenging to discern the neurostimulatory effect. However, after three weeks post-implantation, OEPC stimulation resulted in increased c-Fos$^+$ cells not only in the somatosensory cortex, but also in the entorhinal cortex and hippocampus, across both

ipsilateral and contralateral hemispheres, indicative of signal propagation across the extensive neuronal network.

Implanted devices evoked no foreign body reaction and remained functional following the three-week implantation period. Mild adverse immune reactions near the surgical site were observed in both implanted and non-implanted animals, suggesting an effect primarily attributable to the surgical procedure rather than the implant itself. Scanning electron microscopy revealed a smoother surface of the implanted device, hinting at protein adhesion. Nevertheless, it did not negatively influence OEPC's charging and discharging behaviour, indicating its sustained functionality.

This study is the first investigation into the innovative neurostimulation approach employing organic semiconductors over semi-chronic periods. The successful application of OEPC could bring significant benefits to the field of neurostimulation, offering a wireless, lightweight alternative to conventional methods. The devices demonstrated both safety and functionality for neurostimulation applications over semi-chronic periods, underscoring their potential as therapeutic implants or platforms for further neuroscientific studies. However, to fully ascertain their safety and efficacy, prolonged investigations beyond three weeks post-implantation periods are necessary. Additionally, further exploration into OEPC interactions with nervous tissue is essential for a deeper understanding of stimulation controllability in target brain regions.

ZUSAMMENFASSUNG

Die Neurostimulation, als gezielte Modulation der neuronalen Aktivität, ist ein zentrales Verfahren sowohl in der neurowissenschaftlichen Forschung als auch in der klinischen Praxis. Erfolgreiche Anwendungen elektrischer Hirnstimulation reichen von der Wiederherstellung der motorischen Kontrolle bei der Parkinson-Krankheit über die Verringerung von Krampfanfällen bei arzneimittelresistenter Epilepsie bis hin zur Verbesserung der Rehabilitation nach Schlaganfall oder Trauma. Die Entwicklung drahtloser Neurostimulationsmethoden ist ein wichtiges Ziel, um die Invasivität zu minimieren und den Patientenkomfort durch Vermeidung von Verkabelung und Steuergeräten zu erhöhen.

Für potenziellen Lösungen zeigen photoaktive organische Halbleiter besonderes Potential. Durch sie können Lichtsignale in elektrische Felder umgewandelt werden.Diese Technologie ermöglicht die Anwendung in Form einer extrem dünnen Schicht, die auf eine Matrix aufgebracht werden kann, wodurch sich die Kompaktheit und Komplexität des Stimualtionskörpers erheblich reduziert. Bevor jedoch diese neue Technik klinisch eingesetzt werden kann, müssen ihre Sicherheit und Wirksamkeit in präklinischen Studien umfassend überprüft werden. Das Hauptziel dieser Studie war daher die Untersuchung der Realisierbarkeit, Biokompatibilität und Wirksamkeit von drahtlosen, lichtgesteuerten organischen elektrolytischen Photokondensatoren (OEPC) für die Neurostimulation.

In dieser Studie wurden OEPC in verschiedenen Modellen von *in vitro*-, *ex vivo*- und *in vivo*-Anwendungen im Rattengehirn eingesetzt. Das *in vitro*-Modell wurde mit Hilfe der primären kortikalen Zellkultur umgesetzt. Über einen Zeitraum von zwei Wochen zeigten sich keine erkennbaren Unterschiede in der Zytotoxizität zwischen Zellen auf OEPC und solchen auf Deckgläser. Die Lichtstimulation von Zellen auf OEPC führte zu einer erhöhten c-Fos-Expression im Vergleich zu den Zellen, die im Dunkeln kultiviert wurden, was auf eine effektive Stimulation hindeutet. Dieser Effekt wurde durch die photoaktive Schicht des OEPC erzielt, wobei eine Signalausbreitung innerhalb des neuronalen Netzwerks beobachtet wurde.

Die *ex vivo* OEPC-Stimulation von organotypischen Hippocampus-Schnittkulturen führte ebenfalls zu einer erhöhten c-Fos-Expression in der gesamten Kultur. Nach täglicher Stimulation über sieben Tage wurden erhöhte Expressionen von GAP-43 und NeuN festgestellt, was auf mögliche protektive Effekte der Behandlung hindeutet.

In einem komplexen *in vivo*-Modell wurden flexible OEPC auf den somatosensorischen Kortex erwachsener Ratten implantiert. Die ursprüngliche Analyse der c-Fos-Expression 48 Stunden

nach der Implantation wurde durch frühe postoperative Entzündungsprozesse beeinträchtigt. Nach drei Wochen führte die OEPC-Stimulation jedoch zu einer erhöhten Anzahl von c-Fos$^+$ Zellen, nicht nur im somatosensorischen Kortex, sondern auch im entorhinalen Kortex und im Hippocampus, sowohl in der ipsilateralen als auch in der kontralateralen Hemisphäre, was auf eine umfangreiche Signalübertragung im neuronalen Netzwerk hinweist.

Die implantierten OEPC lösten keine Immunreaktion aus und blieben auch drei Wochen nach Implantation funktionsfähig. Geringfügige, unerwünschte Immunreaktionen in der Nähe der Operationsstelle wurden sowohl bei Tieren mit und ohne Implantat beobachtet, was in erster Linie auf das chirurgische Verfahren und nicht auf das Implantat selbst zurückzuführen ist. Rasterelektronenmikroskopisch zeigte sich eine glatte Oberfläche des implantierten OEPC, was auf eine Proteinadhäsion hindeutet. Das hatte jedoch keinen negativen Einfluss auf das Lade- und Entladeverhalten der OEPC, was auf ihre anhaltende Funktionalität hinweist.

Diese Studie ist die erste Untersuchung eines innovativen Neurostimulationsansatzes, bei dem organische Halbleiter über einen subchronischen Zeitraum eingesetzt werden. Die erfolgreiche Anwendung von OEPC könnte erhebliche Vorteile für die Neurostimulation bieten, da sie eine drahtlose und geringgewichtige Alternative zu herkömmlichen Methoden darstellen. OEPC eignen sich sowohl in Sicherheit als auch in Funktionalität für Neurostimulation über einen subchronischen Zeitraum, was ihr Potenzial als therapeutische Implantate oder Plattformen für weitere neurowissenschaftliche Studien unterstreicht. Um Sicherheit und Funktionalität vollständig zu gewährleisten sind jedoch längere Untersuchungen als drei Wochen nach der Implantation erforderlich. Darüber hinaus ist die weitere Erforschung der Wechselwirkungen zwischen OEPC und Nervengewebe für ein besseres Verständnis der Steuerbarkeit der Stimulation in den Zielhirnregionen von entscheidender Bedeutung.

1 MOTIVATION

Neurological disorders represent one of the most significant burdens on global health. The loss of nervous system function adversely affects multiple organs, deteriorating physical and psychological well-being of millions worldwide. At a global level, these disorders are a leading cause of disability-adjusted life years (DALYs) and mortality (1, 2). The Global Burden of Disease study highlighted a substantial increase in DALYs, deaths, and prevalence of non-communicable brain diseases from 1990 to 2019, including stroke, migraine, Parkinson's disease (PD), idiopathic epilepsy, and head injuries (1, 2). In Europe, neurological disorders rank as the third most common cause of disability and premature death (3), with their prevalence and burden expected to rise due to the aging population.

For many patients with severe symptoms or drug-resistant diseases, neurostimulation has emerged as a highly effective therapy. Deep brain stimulation (DBS) is established as a state-of-the-art intervention for refractory tremor, with over 90% of prescriptions in the US for PD and essential tremor (4, 5). Vagus nerve stimulation (VNS) has been employed in a significant portion of refractory epilepsy cases, with over 100,000 implanted devices worldwide (6). With the increasing prevalence of those diseases, and the inclusion of veterinary patients increasingly undergoing similar treatments as humans (7), the importance of research and development in the neurostimulation field will continue to grow.

Current neurostimulatory interventions, considered the "gold standard," involve the introduction of metal electrodes with external connections to controllers and batteries. Despite their effectiveness, the extensive wiring, dependence on external power sources, and presence of rigid and electrically active foreign bodies in nervous tissue can increase patients' burden, including the risk of implant-associated infections (8) and general discomfort (9, 10) often associated with lifelong therapy. Therefore, in the recent years, a significant focus have been put on research into wireless, lightweight, and soft electronics. A promising approach involves wireless energy delivery using light. Photoactive materials efficiently convert light into electrical power, offering potential for minimally invasive neurostimulation methods (11, 12). Lasers and light-emitting diodes (LED) enable precise manipulation of light intensity, focus, pulse length, and shape, facilitating the use of complex stimulation protocols.

The effectiveness of photoactive materials has been demonstrated in depolarising both excitable and non-excitable cells (13, 14, 15), as well as in animal models (16, 17, 18). However, a better understanding of evoked electrical activity propagation and the interactions

between materials and biological systems is essential for the development of novel neurostimulation devices. Approaching this challenge from the cellular level to the whole organism allows for a deeper comprehension of stimulated neuronal activity complexity and biological reactions to foreign materials during long-term contact. This understanding is crucial for improving the design and development of the most effective and safe implants.

Insights gained from *in vitro*, *ex vivo*, and *in vivo* studies are bringing the use of wireless, light-controlled, and lightweight devices closer to reality for both human and non-human neurological patients. Ideally, photostimulation would alleviate symptoms, reduce disease burden, and enhance overall quality of life. This shared goal unites engineers, materials scientists, chemists, physicists, biologists, medical professionals, and veterinarians collaborating on projects like the one underlying this dissertation.

2 NEUROSTIMULATION AS A TREATMENT

Neuromodulation has become increasingly important in the treatment of various neurological and psychiatric conditions. The benefits of many neuromodulation modalities, particularly electrical neurostimulation, are being harnessed in therapies for epilepsy, movement disorders, neuropathic pain, depressive disorders, and functional deficits following stroke and traumatic brain injury (TBI) (19, 20, 21, 22, 23, 24). For the sake of comprehension, it is important to precisely define the term and distinguish its respective techniques.

2.1 DEFINITION OF NEUROMODULATION AND NEUROSTIMULATION

The International Neuromodulation Society – comprising clinicians, engineers, and scientists – defines neuromodulation as the "alteration—or modulation—of nerve activity by delivering electrical or pharmaceutical agents directly to a target area" (25). In essence, it encompasses any localised, targeted intervention aimed at controlling neuronal excitability, excluding naturally occurring electrical activity in the body.

Neuromodulation can be categorised based on:

1. Goal:
    a. Increasing neuronal activity and strengthening of neuronal connections (e.g. to improve rehabilitation following stroke or TBI)
    b. Inhibiting excessive neuronal signalling (e.g. in refractory epilepsy)
    c. Other alterations of neuronal activity (e.g. selective stimulation of specific nervous fibres in therapy of neuropathic pain or bladder dysfunction; synchronisation or de-synchronisation of neuronal firing)
2. Type:
    a. Electric: using electrodes (e.g., DBS) or externally applied forces (e.g., transcranial magnetic stimulation – TMS)
    b. Pharmaceutical: employing chemical agents delivered directly onto the site of action (e.g., intrathecal or intraspinal drug delivery for pain management) or designer drugs
    c. Gene-based: utilising experimental genetic techniques (e.g., optogenetics, chemogenetics, viral transfection)
3. Localisation:
    a. Central nervous system (CNS; e.g., DBS, spinal cord stimulation – SCS)

b. Peripheral nervous system (PNS; stimulation of single nerves, e.g., VNS)

4. Invasiveness:
    a. Invasive: requiring surgical implantation (e.g., DBS)
    b. Non-invasive: applied externally (e.g., transcranial direct current stimulation – tDCS)

Irrespective of the modality, neuromodulation is always non-destructive, reversible, and adjustable (26). Therefore, surgical interventions (except for electrode implantation) and intraoperative stimulations or cell transplants are not considered neuromodulation, even if they can potentially influence neuronal excitability.

Neurostimulation is a mode of neuromodulation which applies electrical currents to activate or inhibit specific neuronal groups, pathways or networks (26). Since the research underlying this monograph aimed precisely at activating neuronal cells in cell culture, tissue culture, and living animals, this term will be further applied and analysed in-depth.

2.2 HISTORICAL OVERVIEW OF NEUROSTIMULATION

Exploring the history of medicine is not only captivating, but it also offers valuable lessons and insights, built upon centuries – or even millennia – of observation and experimentation. In the realm of neurostimulation, this historical journey is particularly significant, stretching back to ancient civilisations, where the electrical properties of certain fish species were reputedly employed for pain relief in Egypt, Babylon, and Greece (27). The earliest documented recognition of electric current's analgesic potential dates to the 1st century C.E., when a Roman physician Scribonius Largus described the use of torpedo fish for treating gout (28). However, detailed exploration of electricity's connection with living organisms did not become feasible until the 18th century.

Luigi Galvani's seminal work in 1780 marked the first recording of electrical activity in tissues, proposing the existence of "animal electricity" as the source of nerve and muscle function – in contrast to Alessandro Volta's assertion that muscle contractions caused by electricity were mere artifacts (29). The resolution to this dispute came in the 19th century, when German physicist Emil du Bois-Reymond developed a neutral means of coupling electric instruments to tissues, enabling precise control and recording of electric currents, leading to the first description of an action potential (29, 30).

Despite quite a vast knowledge regarding excitability of muscle and peripheral nervous tissue, brain was considered an inactive mass for a long time in human history. Only in the second

half of the 18th century the work of two German physicians challenged that belief. Gustav Theodor Fritsch and Julius Eduard Hitzig, based on works of other neuroscientists, such as Paul Broca and John Jackson, as well as on their own experience (Fritsch noticed that mechanical stimulation of cortex during dressing open wounds of soldiers during the Prusso-Danish war of 1864 led to muscle contractions), started paying attention to motor activity of the brain cortex. They performed a series of experiments of threshold stimulation using bipolar currents and direct current intensity in the cortex in conscious dogs. Upon stimulation, the animals started moving contralateral muscles, which proved cortex excitability and its role in movement initiation (31, 32). Similarly, damage to the cortex on one side led to significant difficulties of movement on the opposite side. As a follow-up to the seminal achievements of Fritsch and Hitzig, in 1874 Robert Bartholow performed a series of faradaic stimulations of exposed cortex in a conscious human patient, which led to spasms of contralateral muscles, carrying out the first documented electrical stimulation of living human brain (26). The experiment was controversial already at that moment, since there had been doubts on the patient's ability to consent due to her advanced brain disease (31). Ultimately, the experiment had to be abandoned due to worsening health of the patient and her precocious death, which was supposedly hastened by subduing repeated brain stimulation.

Advancements in understanding of electrical properties of the nervous tissue were paralleled by progress in surgical techniques. In 1908, Horsley and Clarke introduced a stereotactic frame for animals and in that, facilitating detailed exploration of brain anatomy and electric stimulation of the cerebellar cortex (33). The first stereotactic surgery in humans was carried out by Spiegel and Wycis in 1947, utilising electrical stimulation for precise electrode placement (34). Due to lack of effective imaging techniques, this method continued to be used during brain surgeries for the next decennia and is still employed nowadays in certain cases (26).

Neurostimulation emerged not only as a tool for understanding nervous system anatomy and physiology, but also as a therapeutic modality. Initially, it was used in a form of non-invasive electrodes placed on the skin above target muscles or nerves. In 1967, Norman Shealy and colleagues implanted the first SCS device with external radiofrequency control for pain management, gaining US Food and Drug Administration (FDA) approval a year later (35). Subsequent decades saw a surge in the development of sensory neuroprostheses, such as cochlear implants (1961) and visual and auditory prostheses for cortical surface stimulation (1968 & 1973) (27). The groundwork for DBS using implanted

electrodes was laid in the 1960s, eventually receiving FDA approval for specific movement disorders in 1997 and more generalised forms in 2002 (36). In 2018, DBS garnered approval for refractory epilepsy treatment, marking another significant milestone in neurostimulation's therapeutic evolution.

2.3 STATE-OF-THE-ART METHODS IN THE STIMULATION OF CENTRAL NERVOUS SYSTEM

Stimulation of the CNS encompasses a vast range of methods with diverse applications (Figure 1). Among neuromodulatory devices, the FDA approves the use of DBS in movement disorders (PD, essential tremor, dystonia (37)) and in obsessive-compulsive disorder (37). Responsive neurostimulation (RNS) and VNS are approved for therapy in drug-resistant epilepsy (38), TMS – in the treatment of major depressive disorder (39), and various SCS devices for the management of chronic back pain (40, 41). However, the application of neurostimulation extends beyond the FDA approval and includes more of established treatment techniques.

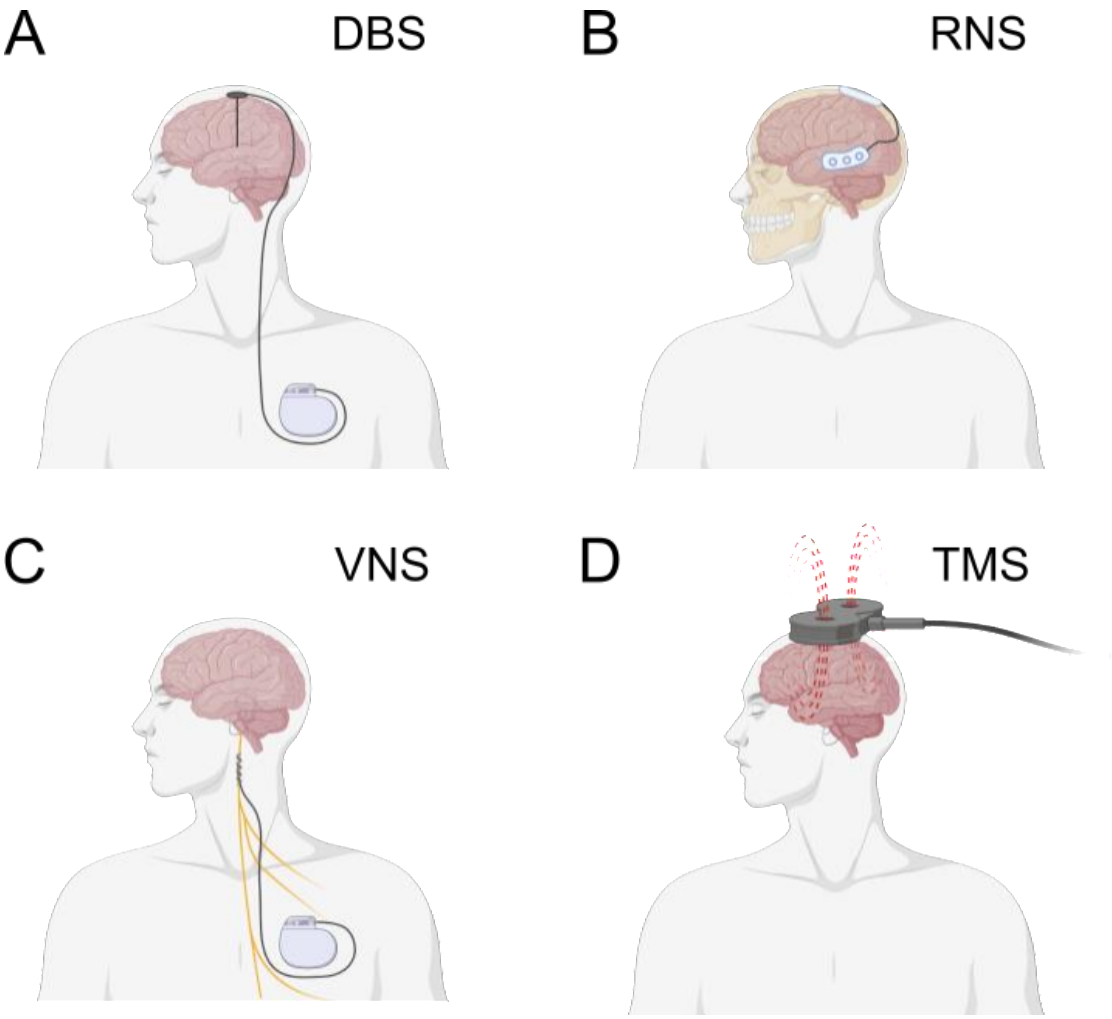

Figure 1. Schematic representations of state-of-the-art neurostimulation methods, FDA-approved. *(A) DBS electrode placement with the pulse generator located on the chest. (B) RNS, showing the electrode positioned superficially above the epileptic focus and the pulse generator at the craniectomy site. (C) VNS, illustrating the electrode placement around the vagus nerve and the pulse generator located on the chest. (D) TMS, indicating the placement of the coil on the head surface and the location of the generated magnetic field. Created with BioRender.com*

In the most commonly used DBS system, a stimulating electrode is stereotactically implanted in the target region (Figure 1A), typically located in deeper brain structures, although experimental employment of DBS in cortex also yields promising results (42). Usually, electrodes are placed bilaterally, although unilateral stimulation may be necessary in some cases (43). The electrodes are connected to a pulse generator placed on the upper chest near the collarbone via a subcutaneous wire. Stimulation protocols can be adjusted wirelessly, in order to maximise symptom relief and minimise side effects (43). Typically, stimulation protocols employ either high-frequency (>100 Hz, mostly 130 or 150 Hz) or low-

frequency (<100 Hz, mostly 60 or 80 Hz) current, resulting in various therapeutic effects on motor function (44).

RNS is a relatively new neurostimulation approach, combining stimulation electrodes implanted either subdurally or in the seizure focus with constant electrocorticography (ECoG; Figure 1B) (45). Upon detection of abnormal neuronal activity associated with seizures, a stimulation protocol is activated. The system allows for the use of preprogrammed activity patterns (45) or application of machine learning to tailor the detection to each patient (46). Unlike DBS, the pulse generator in RNS is located inside a device-shaped craniectomy in the skull (47).

Although VNS technically does not directly influence the CNS as it targets a cranial nerve, its effects on the brain, particularly on the locus coeruleus and raphe nuclei, are significant (48). A VNS unit consists of electrodes in form of helical cuffs, implanted on the left cervical vagus nerve, connected via a wire to a control unit, similar to DBS, placed on the upper chest (Figure 1C). Most protocols employ intermittent 20-30 Hz stimulation, with a cycle of 30 seconds on and 5 minutes off (48).

Unlike DBS, RNS, or VNS, TMS is a non-invasive neurostimulation approach, which may be advantageous in some cases. A TMS unit consists of a wire coil, usually round or figure-of-eight-shaped, connected to a source of electrical current (Figure 1D). The coil is placed on the surface of the head, and the current flow creates a magnetic field, which is appropriately pulsed to induce an electric field in the brain, causing action potentials in the targeted cortical region (49). Among stimulation protocols, repetitive TMS (rTMS) is the most widely used one. It consists of a train of stimuli spaced by an identical inter-stimulus interval (50). Effects depend on stimulation frequency: at low frequency (< 1 Hz), rTMS depresses excitability in the cortex, whereas at high frequency (> 5 Hz), the excitability is increased (50).

Transcranial electrical stimulation is a non-invasive technique employing direct (tDCS) or alternating (tACS) currents. In both techniques, electrodes are placed on top of the scalp, with an electrolyte used as a buffer between the electrode and the skin (51). In tDCS, one electrode is designated as an anode and another as a cathode, whereas in tACS anodes and cathodes change during the cycle of an AC oscillation, leading to a fluctuation between depolarising and hyperpolarising effects (52).

A more detailed insight in the application of these methods in various neurological disorders shall shed more light onto the current state of the art in the neurostimulation field.

2.3.1 Parkinson's disease

One of the most remarkable success stories in the field of neurostimulation is undoubtedly treatment of PD and other movement disorders, like essential tremor, dystonic tremor, and cerebellar tremor. DBS has become the gold standard therapy for refractory motor symptoms, although its mechanism of action is still not fully understood. Several hypotheses attempt to elucidate the physiological effects of DBS, with the most prevalent suggesting local neuronal inhibition and the disruption of abnormal signalling (53).

PD is a neurodegenerative disorder characterised by loss of dopaminergic neurons in substantia nigra pars compacta, resulting in decreased dopamine release in the basal ganglia and subsequent alterations in movement control circuits (54). This leads to decreased signal transmission and pathological network activity, including abnormal neuronal synchronisation and oscillations in the beta frequency band, manifesting as motor disabilities such as bradykinesia, tremor, or rigidity (55). High-frequency DBS disrupts the pathological activity and restores the "pro-kinetic" gamma band (55).

DBS is indicated in patients with clear diagnosis of idiopathic PD with refractory motor fluctuations or tremor despite an optimal medication (56). Patients should be ambulatory on levodopa, a standard drug prescribed for PD, and have retained cognitive abilities (56). Exclusion criteria include advanced age (over 75 years), major comorbidity contraindicating surgery (e.g., cardiovascular diseases, severe diabetes), chronic immunosuppression, poor response to levodopa, limited cognitive function, severe psychiatric disorders, and distinct brain atrophy (56, 57).

The main targets for DBS in PD and other movement diseases include ventral intermediate nucleus of the thalamus as well as basal ganglia: subthalamic nucleus and globus pallidus pars interna (57). However, new brain regions are emerging as putative stimulation targets and there is no consensus regarding selections of the target or whether to perform uni-or bilateral stimulation (58, 59). There were also trials with multitargeted therapy, leading to promising results, especially in cases of neuropsychiatric symptoms and severe refractory impairments (58).

Typical stimulation parameters in PD management are monopolar stimulation, voltage 2.5–3.5 V, impulse duration 60–90 μs and frequency 130–180 Hz (56). Stimulation protocol is adjusted according to the patient, so that an equilibrium between maximum symptom relief and minimum adverse effects can be achieved. The stimulation amplitude should be increased successively, with a concomitant decrease of levodopa dosage. Currently, there

is a significant focus on development of algorithms with an aim to optimise selection of the stimulation parameters based on data (60, 61, 62).

DBS treatment in patients with movement disorders results in a significant improvement of motor function, with tremor reduction ranging from 30 to 80%, depending on the target and stimulation protocol (63). In PD, DBS improves multiple important outcome parameters, including limb dyskinesia, speech, postural stability, and gait, and this effect increases with time (64). Additionally, DBS exerts a positive effect on non-motor function, such as cognition, neuropsychiatric symptoms, sleep, and autonomic functions (64). The therapy leads to a decrease in drug dosage, significantly diminishing medication-induced side effects (57). Overall, DBS is highly effective, improving not only specific medical parameters, but also the overall quality of life, especially in the long term (57, 64).

Complications and adverse effects include mostly perioperative intracranial/intracerebral haemorrhages, infections (local and general, e.g., pneumonia), mental changes (including cases of suicide), and incidents related to the device (lead twisting, lead breakage, migration of the pulse generator) (57, 64). The incidence of perioperative death is low, and its causes are usually unrelated to the surgery (64).

2.3.2 Epilepsy

Epilepsy is a neurological disorder characterised by recurrent seizures accompanied by enduring alterations in the brain that increase the likelihood of future events (65). The seizures can be caused by underlying disease of the CNS (structural epilepsy) or be of genetic or unknown cause (idiopathic epilepsy). Depending on the regions of the brain involved in generation of abnormal activity, seizures can be further subdivided into focal (stemming from a single focus), generalised (stemming from an abnormal activity of the entire brain), or focal with subsequent generalisation. An epileptic focus can be located in various brain regions – in case of mesial temporal lobe epilepsy, seizures are generated in hippocampus (HC), which undergoes severe pathological changes: neuronal loss in Cornu Ammonis (CA) region (mostly inhibitory interneurons), loss of γ-aminobutyric acid (GABA) receptors in CA, mossy fibre sprouting in the hilus of the dentate gyrus (DG), reactive astrogliosis etc. (66, 67). CA3 principal cells serve as a generator of seizure activity, leading to hypersynchronous signalling that further propagates throughout the HC (68).

Approximately 20-40% of patients with epilepsy fail to respond satisfactorily to standard anti-seizure medication and do not reach appropriate seizure control or suffer intolerable side effects despite appropriate therapy – a condition defined as refractory or drug-resistant

epilepsy (69). In these cases, one of listed methods can be applied: surgical interventions, dietary therapy, and neurostimulation (70). Among stimulation techniques, VNS, DBS and RNS yielded the most promising results so far.

VNS targets vagal afferents reaching several brain regions, some of which can be an epileptic focus: cerebellum, HC, amygdala, thalamus, brain stem, insular cortex. The target regions can be innervated monosynaptically or via locus coeruleus and raphe nuclei – their stimulation modulates the seizure threshold through serotonin and noradrenaline signalling (71). As a stimulation target, usually left vagus nerve is selected, due to differences in efferent innervation of the heart between the two sides. Right vagus nerve is rarely used, as it innervates sinoatrial node, stimulation of which can lead to a severe bradycardia (72).

Patients eligible for VNS must be diagnosed with refractory epilepsy, regardless of the aetiology. One of advantages of VNS is its application in children – FDA approves VNS therapy in patients as young as 4 years of age (73). Even though VNS is widely well-tolerated, it cannot be used in patients with impairments of vagus function, progressive neurologic or systemic disease, pregnancy, cardiac arrhythmia, asthma, chronic obturative pulmonary disease, peptic ulcer and insulin-dependent diabetes (71).

Stimulation parameters are usually initially set at output current 0.25 mA, signal frequency 20-30 Hz, pulse width 250-500 μs, stimulation “on” time 30 seconds, and stimulation “off” time 180-300 seconds (74, 75). If needed, the output current can be increased, and the intensity up to 2-3 mA is generally well-tolerated (74). However, due to battery lifetime, the maximum dose shall not exceed 1.5 mA (75).

VNS exerts predominantly positive effect on seizure frequency: median seizure reduction varies between 25-55%, with the responder rate (≥50% reduction in seizure frequency) of 45-65% (6, 76, 77, 78). There is a positive influence of treatment duration, with a more pronounced seizure frequency reduction and higher percentage of patients reaching seizure freedom at 24-48 months of stimulation compared to the first 0-4 months (77). Aside from seizure-related parameters, an improved cognitive function, such as memory and learning skills, and overall better quality of life were observed (71, 79, 80).

Common adverse effects of VNS include hoarseness, cough and paraesthesia (6). Perioperative complications include infections, vocal cord injury and facial paresis (71). Similarly to DBS, lead twisting, lead breakage, and pulse generator migration have to be considered. However, they can be avoided by application by non-invasive VNS, which is a rapidly evolving alternative technique (6).

VNS is not the only neurostimulation method used in patients with refractory epilepsy. Other successful techniques include DBS, with excellent results of long-term stimulation of the anterior nucleus of the thalamus (81). The median seizure reduction from at 1 year was 41% and 69% at 5 years, which follows the pattern of increased improvement with time. Similarly, the responder rate at 1 year was 43%, and 68% at 5 years. A significant 16% of patients achieved seizure-freedom for at least six months (81). Another fairly commonly used neurostimulation technique is RNS, a closed-loop system continuously analysing ECoG data for patterns indicative of seizures and activating stimulation protocol accordingly. Closed-loop systems can be also implemented in VNS (82) and DBS (83).

2.3.3 Traumatic brain injury, spinal cord injury, and stroke

Unlike PD or epilepsy, electrical stimulation in therapy of TBI, spinal cord injury (SCI) or ischemic stroke sequellae does not aim to directly modulate abnormal neuron spiking activity, but rather targets long-term improvements in neuroplasticity, leading to restoration of a lost function. In addition, neurostimulation following those incidents is not applied as a sole treatment, but it needs to accompany rehabilitative training – a gold standard therapy following the traumatic or ischemic injuries (24, 84). Neurostimulation enhances activity-dependent plasticity caused by the exercise, leading to better functional outcome, especially regarding motor function (84, 85), but also enhancing histological signs of recovery: dendrite and dendritic spine density, growth-associated protein (GAP)-43 expression, growth factors synthesis, etc. (24, 84, 85, 86, 87, 88)

TBI and ischemic stroke belong to the by far most common neurological events worldwide. Global incidence of TBI is estimated for over 27 million per year (89). In Austria, yearly TBI incidence is typical for a European country, reaching 75,000 cases per year (303/100,000/year) (90). Stroke incidence in the European Union reaches over 1 million cases per year, and the incidence is estimated to increase in the coming years (91). SCI is less common, with 900,000 new cases per year worldwide and around 1,000/year reported in Austria (92). Following stroke and moderate-to-severe TBI, about 80% of patients suffer from motor impairments (93, 94). Among other dysfunctions, commonly present are cognitive deficiencies (memory-, language- or mood-related) as well as post-injury epilepsy or tremor (24, 84, 85). Therefore, there is a room for electrical stimulation as an assistive therapy in those disorders.

Usually, the nervous system reaches a level of spontaneous restoration for several months following the injury, until the improvement stagnates (84, 85). To differentiate the effect of spontaneous recovery from the effects of the therapy, studies mostly aim to initiate

the treatment after the stagnation period is reached and patients acquired moderate to good recovery (84, 95). Since there is no FDA approval for neurostimulation following injury, and the population undergoing the treatment is highly heterogenous, the methods and parameters applied are diverse and depend on multiple factors: patient characteristics, lesion type and extent, time elapsed since the injury, and the progression of recovery (84).

Methods employed in the brain include cortical stimulation (tDCS, TMS, minimally invasive epidural electric stimulation) or DBS (24, 84, 85). Similarly, in case of SCI, electrodes can be placed intraspinally, epidurally, or transcutaneously (84). Transcutaneous methods have the advantage of being non-invasive, however, patients must be stationary during the treatment, which significantly limits the possibility of rehabilitation-accompanying stimulation. tDCS is in addition limited by the high resistance of the skin, leading to low selectivity in the stimulation targets (96). The effect of repetitive transcutaneous stimulation also proved to be transient and diminishing after finished therapy (85). In DBS, the localisation of the electrodes varies and often depends on the presence of secondary symptoms, such as epileptic seizure or tremors. However, in a recently published clinical trial in a cohort with a history of moderate-to-severe TBI, the electrode was placed in the thalamus with the main goal of improvement of motor deficits, reaching satisfactory results (95).

In summary, neurostimulation leads to a faster and better functional recovery following CNS injuries. Nevertheless, standardised preclinical trials as well as well-reported, controlled clinical trials should be encouraged to establish the best-suited methods and optimal parameters for the treatment.

2.3.4 Migraine

Electrical stimulation for pain management has been vastly applied and described in the peripheral nerve system (97, 98, 99). In the CNS, application of electric stimulation is predominantly focused on pain relief in primary headaches, among which migraine is the main type.

Due to somewhat elusive diagnostic criteria, it is challenging to indicate specific epidemiologic data regarding migraine. Current estimation indicates a yearly prevalence of approximately 14-15% of the global population (100), whereas Austrian sources count 10.2% prevalence with possibly 8.5% more uncertain diagnoses (101). In Austria, in total 30.7% of the population suffers from different causes of primary headaches (101). Migraines afflict mostly young people, and women are five times more likely to develop the disease, with symptoms reaching their peak at the age of 40 (100, 102). Nearly 5% of patients with migraine

suffer from daily headaches and 1-2% fail to respond to the standard medication (102). To those people, neurostimulation offers an attractive alternative for pain control.

Among stimulation methods applied in cases of migraine, only VNS has been approved by FDA. Other approaches include non-invasive cortical stimulation with rTMS and tDCS, invasive DBS of hypothalamus, or minimally invasive nerve treatment, targeting occipital or supraorbital nerves (102, 103). Nerve stimulation, unlike non-invasive cortical stimulation, is independent of hospital visits and can be applied on demand by the patient. Contraindications include recent facial or brain trauma, and skin abrasions in the region of interest. Among adverse effects, tingling sensation during stimulation, skin irritation, sleepiness or headaches, as well as lead twisting, breakage or perioperative infections should be taken into account (102, 103).

The common goal of all the methods is regulation of pathological sensory activity in the trigeminal nerve, which plays a significant role in the aetiopathology of migraine (103). In case of acute migraine, neurostimulation possibly blocks the processes generating the pain attack. In long-term stimulation, changes in neuronal connections reduce the central sensitisation leading to chronic headaches. (102, 103). Long-term occipital nerve stimulation results in a chronic pain relief in up to 75% cases, rendering it a very effective solution for pain control (102).

3 CELLULAR EFFECTS OF NEUROSTIMULATION

The neuronal excitability is based on characteristic structure of the cell membrane. Organisation and function of ion channels enables action potential generation, which propagates along the neuronal axon and gets further transmitted to neighbouring cells via neurotransmitters. Changes in ionic concentrations within the cell occurring during the action potential trigger several molecular mechanisms, some of which can serve as markers of the recent neuronal activity.

3.1 FUNDAMENTALS OF THE NERVOUS TISSUE ACTIVITY

Cell membrane consists predominantly of a phospholipid bilayer, interspersed with proteins. Only hydrophobic substances can independently diffuse through the cell membrane, whereas charged particles cannot pass it without assistance. For that reason, ions remain on one of the sides of the cell membrane and are able to transverse it only through the hydrophilic centres of designated proteins: ion channels (passive transport) and ion pumps (active transport).

Ion concentrations on the intra- and extracellular side of the cell membrane vary: Na^+, Ca^{2+} and Cl^- reach higher concentrations in the extracellular space than inside the cell, whereas concentration of K^+ is higher intracellularly. Difference in charge distribution across the membrane in an inactive (non-signalling) cell is called a resting potential. In differentiated neurons, resting potential is usually measured as -70 mV (Figure 2).

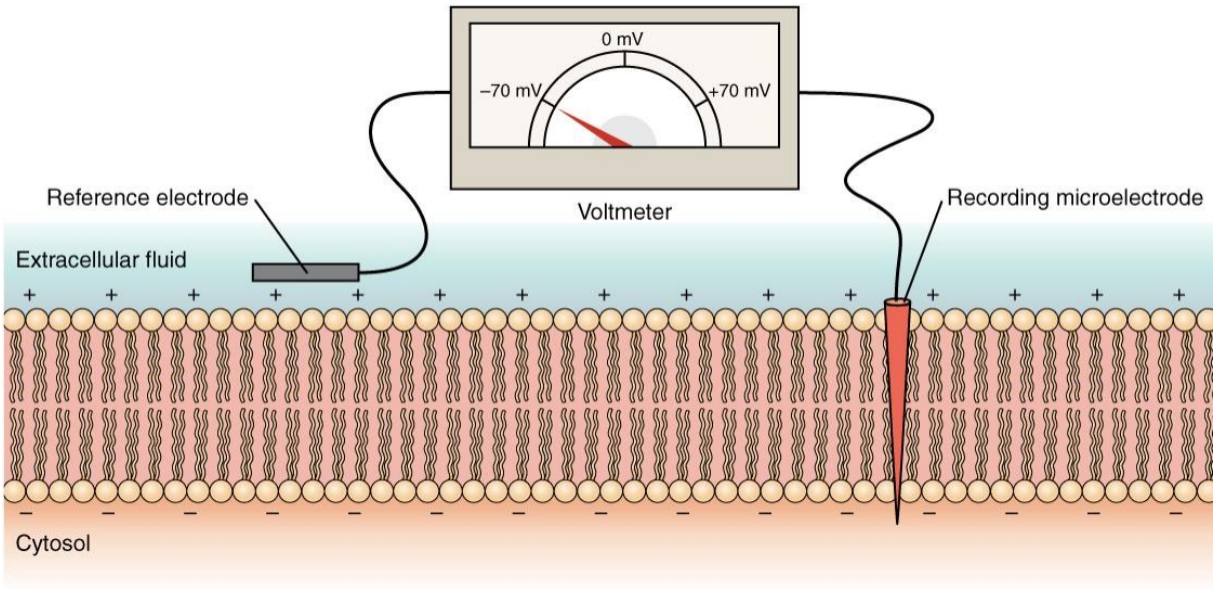

Figure 2. Resting membrane potential of a neuron. *Potential is measured through a recording microelectrode inserted into the cell with a reference electrode placed outside the cell. Image from Anatomy and Physiology 2e, Chapter 12.4: The Action Potential, published on Apr 20, 2022 by OpenStax, access for free at https://openstax.org/books/anatomy-and-physiology-2e/pages/1-introduction and distributed under a CC-BY 4.0 license.*

Basis of neuronal functionality is capacity of generation of action potentials. An action potential is initially determined by the flow of Na^+ inward the cell. The main motor of Na^+ movement is its electrochemical gradient – the cations are trying to reach their Nernst potential (equilibrium potential across the membrane) at + 55 mV and to equilibrate their concentrations on both sides of the membrane. Na^+ flow across the membrane is possible only through sodium-selective ion channels – such as ligand-gated (opening upon binding to a neurotransmitter; Figure 3A) or voltage-gated (responsive to transmembrane potential changes; Figure 3B) sodium channels. Ion channels act in an all-or-none manner, meaning they can be either open or closed with no states in-between.

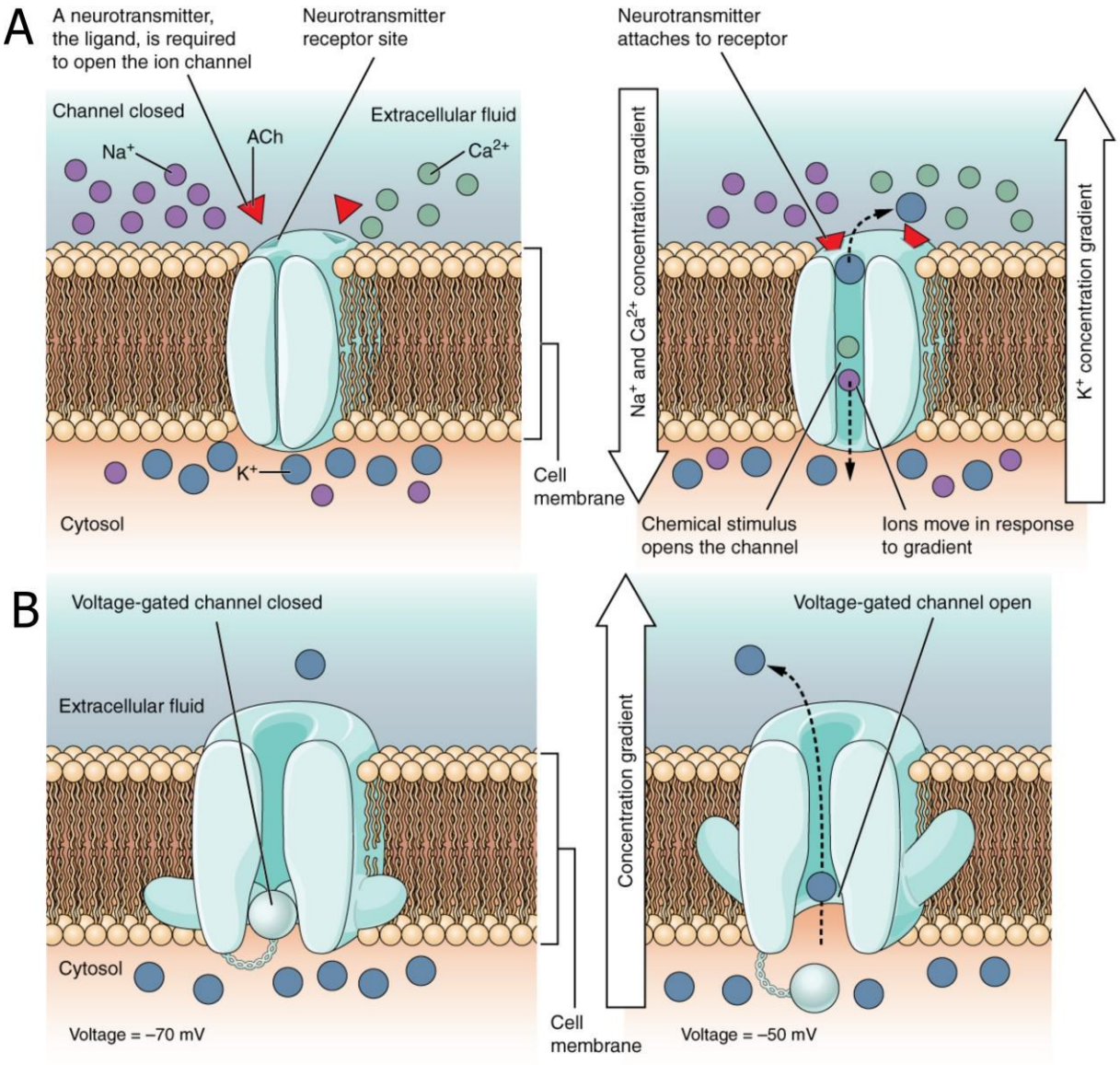

Figure 3. Selected types of ion channels in neuronal membrane. *(A) Ligand-gated ion channels open upon binding of a ligand (in this case acetylcholine) to the receptor portion of the channel. Selected ions cross through the hydrophobic pore according to the electrochemical gradient (Nernst potential and chemical concentration). (B) Voltage-gated channels open upon potential changes in their vicinity. Sensitive to charge amino acids undergo modifications, enabling pore opening and subsequent flow of the selected ions. Images from Anatomy and Physiology 2e, Chapter 12.4: The Action Potential, published on Apr 20, 2022 by OpenStax, access for free a thttps://openstax.org/books/anatomy-and-physiology-2e/pages/1-introduction and distributed under a CC-BY 4.0 license.*

Voltage-gated sodium channels (Na_v) exist in three configurations: open (conductive), closed, or inactive. The percentage of the channel population in a given state depends on the cell membrane potential (104). In general, increasing potential increases probability of Na_v opening. The threshold for action potential firing lays at around -55 mV (Figure 4). Then, multiple Na_v

open, which drives the cell membrane potential change into positive (+20 mV or more; depolarisation). Increasing potential triggers voltage-gated potassium channels (K_v) opening. While Na_v close quickly, K_v remain open until the recovery of the resting membrane potential through the outward K^+ flow (repolarisation). Na_v remain in the inactive state for the duration of the refractory period, during which sodium-potassium pumps re-establish the initial ionic balance and resting membrane potential.

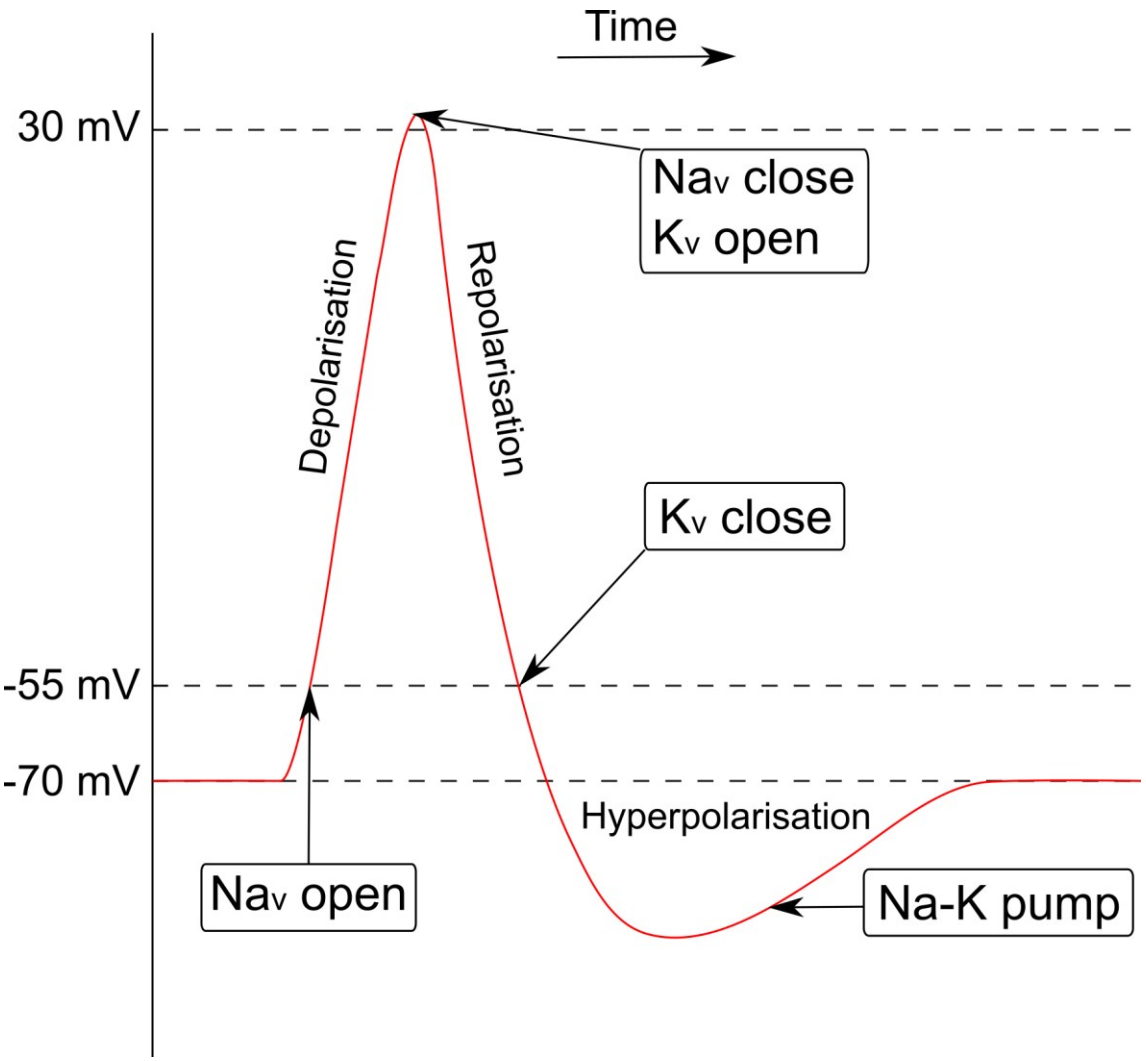

Figure 4. Membrane potential change during an action potential. *After reaching a threshold potential at around -55 mV, rapid opening of Na_v and inward Na^+ flux drive the depolarisation phase. Repolarisation is caused by an outward flow of K^+, leading to a temporary hyperpolarisation of the cell membrane. Resting potential is recovered by action of sodium-potassium pumps.*

Depending on the myelination status of the axon, action potential can propagate either continuously (non-myelinated axons), or in a saltatory manner (myelinated axons). Change in the membrane potential initiates transient depolarisation in the adjacent parts of the cell

membrane (in a neighbouring node of Ranvier in case of myelinated axons), leading to local activation of the voltage-gated ion channels and signal propagation. At the end of the axon, action potential triggers opening voltage-dependent calcium channels in the vicinity of vesicles filled with neurotransmitter (105). This leads to a neurotransmitter release into the synaptic cleft and the signal spreads to the neighbouring neurons.

Axon diameter also plays a crucial role in the action potential propagation – large axons spread the signal faster than small ones. Similarly, during the electrical stimulation, a higher stimulus amplitude is needed to activate small axons (106). This discrepancy stems from Ohm's law $R = \frac{L}{\sigma A}$, where L – length, σ – conductivity, A – area of the cylinder cross-section. In two axons with the same length and conductivity, the bigger the diameter of its cross-section, the smaller its resistance.

Action potentials can be also generated at the termination of a long period of hyperpolarisation ("anode break excitation"). As the membrane becomes hyperpolarised, the number of Na_v in closed/able-to-activate state increases, lowering the threshold necessary for the action potential firing (104). After the hyperpolarising stimulus is removed, the membrane potential returns towards the resting potential and automatically reaches the threshold, generating the action potential.

3.2 c-Fos as a marker of recent neuronal activity

3.2.1 Transduction of the neuronal activity into c-Fos signalling

Electrical signalling of neurons is based on changes in ionic concentrations in the intracellular and extracellular space. Calcium plays a crucial role within neurons, standing in the focal point of several signalling pathways (107). Increase of the neuronal calcium concentrations occurs through two main routes: extracellular and intracellular. Ca^{2+} enters from the extracellular space either through receptors of glutamate – an excitatory neurotransmitter – or through voltage-gated calcium channels opened by action potentials (108). Among glutamate receptors, N-methyl-D-aspartate (NMDA) receptor is the main motor of the Ca^{2+} influx, whereas its movement across α-amino-3-hydroxy-5-methyl-4-isoxazolepropionic acid (AMPA) receptors and metabotropic glutamate receptors is limited (108). Within the cell, calcium is stored in the endoplasmic reticulum (ER) and can be released by signalling of the secondary messenger, such as inositol 1,4,5-trisphosphate (107). However, little is known about the contribution of the intracellular Ca^{2+} flux to the c-Fos expression (108).

Local Ca^{2+} concentration increase is one of several extracellular stimuli that can initiate fast transcription of so-called immediate early genes (IEG): *c-fos*, *Egr1/Zif268*, *Arc/Arg3.1* or *Homer1a* (108). Calcium activates IEG expression through multiple kinase cascades, including mitogen-activated protein kinase (MAPK), Ca^{2+}/calmodulin-dependent protein kinase (CaMK) II or CaMKIV (108). However, *c-fos* expression is predominantly controlled by MAPK, activated through a Ras/Raf/MEK/MAPK pathway (Figure 5). Ras is a protein that requires high Ca^{2+} concentration increase to bind to GTP, necessary for its activation (109). Hence, only strong stimuli can initiate *c-fos* transcription, rendering it an advantageous marker of neuronal activity. MAPK further phosphorylates cAMP response element-binding protein (CREB), a transcription factor bound to the CREB response element (CRE) in the *c-fos* promotor. Concurrently, it phosphorylates ETS Like-1 protein (ELK1) connected to serum response factor (SRF), bound to the serum response element (SRE) sequence in the *c-fos* promoter (108). Following transcription in the nucleus and translation in the ER, c-Fos protein migrates back to the nucleus, where it acts as a transcription factor in many downstream pathways through its interaction with the activator protein 1 (AP-1).

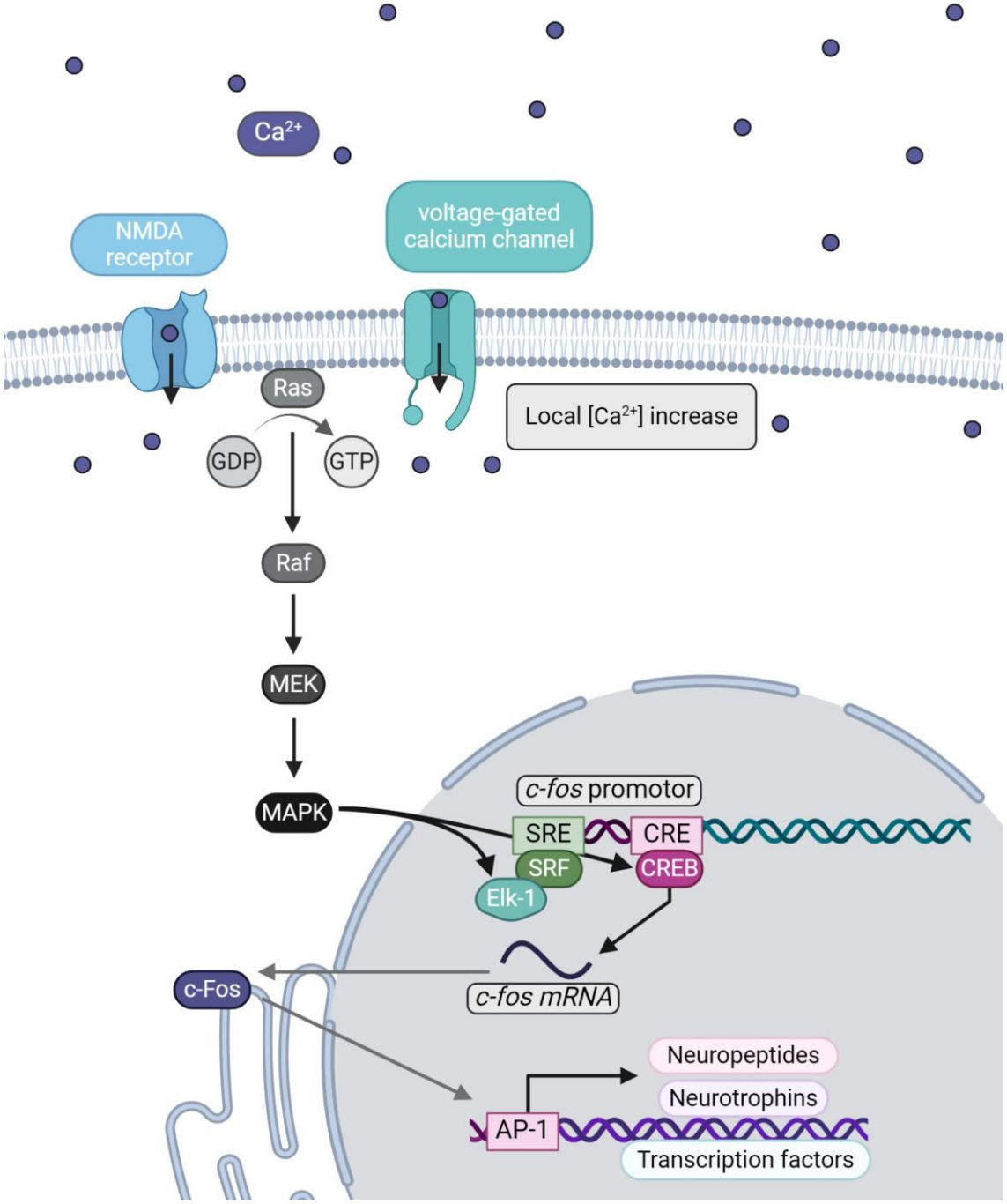

Figure 5. Transduction of neuronal activity into c-Fos signalling. *Ca^{2+} influx from the extracellular space and local increase inside the cell leads to activation of Ras/Raf/MEK/MAPK pathway. MAPK further phosphorylates proteins bound to the c-fos promotor, initiating transcription of c-fos mRNA. c-Fos protein is then synthesised on ER and transferred back into the nucleus to act as a transcription factor for various pathways. Created with BioRender.com*

3.2.2 Use of c-Fos in neuroscience

Among all IEG products, *c-fos* mRNA and c-Fos protein have been studied to the greatest detail. In neurons, they show low basal expression levels and have distinct expression curves: *c-fos* mRNA reaches its maximum expression level 30 min after stimulus returning to baseline values after 3 h, whereas c-Fos reaches its peak 1-2 h following the stimulus, with baseline values recovered after 6 h (110). Rapid decrease in c-Fos levels after the induction of its biosynthesis stems from its autoregulatory repressive action (111). This renders it an even more advantageous marker of neuronal activity, especially in combination with prior sensory deprivation and/or movement restriction of the animals in *in vivo* studies (108). Expectedly, c-Fos found its use in many fields of neuroscience, such as studies of learning and memory formation (112, 113, 114, 115) or pain sensing (116, 117), and has become a standard go-to protein to mark neuronal response to the different modes of neurostimulation (118, 119, 120, 121). Multiple molecular biology techniques can serve as *c-fos* mRNA or c-Fos protein detection approaches, strengthening its position as a versatile marker of recent neuronal activity.

4 ELECTRODE-TISSUE INTERACTIONS IN THE BRAIN

Bioelectronics is a multidisciplinary field, spreading across materials science, electrochemistry, neuroscience and immunology. The electrode-tissue interface and interactions between the device and cells are crucial to both engineers and biologists working on diagnostic and therapeutic tools. In neurostimulation, this includes considerations regarding electrode design, anatomical placement, protocol selection, foreign body reaction, and device functionality following the implantation.

4.1 ELECTRODE DESIGN AND PLACEMENT

The electrode serves as a direct interface between the stimulation unit and nervous tissue. In a standard galvanic cell, the electrode, where oxidative reactions occur (electrode with a positive charge) is called an anode, whereas its counterpart, where reduction takes place (electrode with a negative charge) – a cathode. Conventionally, current is described as movement of the positive charge from the anode towards the cathode, whereas the electrons move in the opposite direction.

In a stimulation unit, the electrode in the closest vicinity to the target tissue is called a stimulation electrode. The stimulation electrode aims at modulation of the cell membrane potentials of neurons in order to trigger action potentials. The electrode located away from the tissue is called a back electrode or a return electrode.

Charge injection capacity of an electrode is characterised by its size. It determines the charge applied to the tissue and the current density (charge flow per unit area). In principle, current density injected into the tissue decreases with the increasing electrode size (122). The charge necessary for neuronal stimulation decreases also with the increasing distance from the electrode. A crucial role in the electrode design plays also the size of the target axon, as the smaller cross-section area of the axon necessitates a higher stimulus (vide Chapter 3.1 Fundamentals of the nervous tissue activity). Electrodes aimed at the nuclei (collection of neuronal cell bodies) tend to be bigger, however, they need to be smaller than the target nucleus (96).

Placement of the electrode is critical in the CNS due to its high complexity and specialised functionality of each of its parts. It also heavily depends on the innate electrical properties of the tissue. Grey matter is in general more conductive than the white matter, however, its conductivity can be modified by neurological conditions, e.g., epileptogenic grey matter is more conductive than the healthy one (123). Electrical properties of the tissue depend also

on its homogeneity. Inhomogeneous tissue will not have uniform conductivity, resulting in a non-uniform current density. White matter is highly anisotropic, with transverse fibres being more conductive than longitudinal ones (106). Defining brain tissue properties *in vivo* is challenging, however, magnetic resonance imaging (MRI) techniques to determine the conductivity of given brain regions have been developed (124).

Another crucial factor for the selection of the electrode placement is its proximity to target neurons. To achieve optimal results, the electrode should be located as close as possible to the tissue of interest. For unique stimulation of single cortical neurons, electrodes need to be placed less than 50 μm from the target cell (96). However, if stimulation resolution is not that crucial, and it is more important to lower the invasiveness of the implant, electrodes can be placed further away, e.g., on the surface of the skin. Minimally invasive electrodes (e.g., placed on the cortical surface) offer a good stimulation resolution-tissue damage balance, as they bypass high skin resistivity without a necessity for deep implantation.

4.2 STIMULUS CHARACTERISTICS

Electric current is measured in amperes and is defined as a rate of charge flow per unit time. Voltage is defined as an electric potential difference between two points. Both current and voltage are needed to characterise a stimulus applied during neurostimulation.

Usually, stimuli are delivered in pulses, characterised by their:

- Width (duration of a single pulse)
- Amplitude (in the case of electric stimulation: voltage or current; photostimulation: light intensity)
- Shape (rectangular, sinusoidal, triangular – rising or falling)
- Phase (monophasic, biphasic balanced or biphasic imbalanced)

In general, shorter pulses require higher amplitudes for action potential generation (104). The relationship between threshold current and pulse duration can be pictured as a hyperbole (Figure 6), approaching a minimal current amplitude value still capable of generating the action potential – a rheobase. Rheobase is a theoretical value described in terms of infinitely long pulses – in practice, maximal duration of a pulse is several hundreds of milliseconds (104). Chronaxie is a characteristic describing the shortest duration of an electrical stimulus with the amplitude equal to twice the rheobase. It is a measure of the excitability of a given tissue type under given conditions.

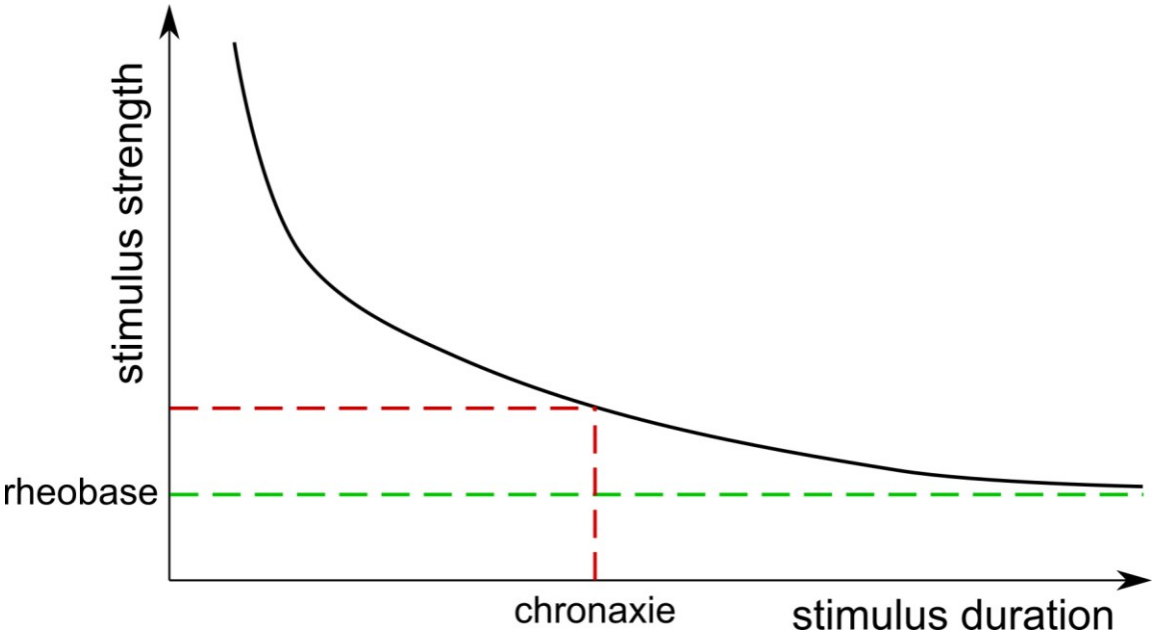

Figure 6. Relationship between the stimulus strength (current amplitude) and duration (pulse width) capable of action potential generation. *Rheobase is a minimal current amplitude of indefinite duration resulting in action potential generation. Chronaxie is duration of a stimulus of the amplitude equal to twice the rheobase, characteristic for a tissue type and conditions.*

A good practice in protocol establishment is to select the shortest pulse that the stimulator can support and/or aim for close to or less than the chronaxie (104). To protect the electrode from repetitive redox reactions, monophasic pulses are avoided. During a monophasic pulse, oxygen and water molecules get reduced at the cathode, generating reactive oxygen species (ROS), which can be noxious to the tissue. In addition, oxygen depletion hampers aerobic metabolism of the nearby cells. Although useful in some applications (e.g., tumour treatments), these reactions are undesirable during neurostimulation. In biphasic stimulation, a cathodic current pulse is followed by an anodic current pulse (balanced – delivering exactly the same positive charge as the negative charge delivered during the cathodic phase, or imbalanced – delivering different charge values). When the current flows in the opposite direction in the anodic phase, the redox reactions are reversed, preventing excessive oxygen and water reduction. Optimally, charge in the cathodic and the anodic phases should be balanced.

4.3 FOREIGN BODY REACTION

Glial tissue serves as an active support of neurons in the CNS and is responsible for, among other things, neurotransmitter metabolism, maintaining ionic balance, and immunological response. In the CNS, the main glial cell types include astrocytes, oligodendrocytes,

and microglia. These cells are responsible for cytokine and chemokine signalling in the foreign body reaction (FBR) in response to the mechanical injury caused by the implantation and the foreign material of the electrode.

The extent of the FBR depends on pressure and strain caused by the device as well as on the surface chemistry of the electrode. To be considered safe, pressure should be kept below 20-60 mmHg, and tissue strain below 8-15% (96). Higher stiffness of the electrode exerts higher pressure and strain on the tissue, and mismatches with the stiffness of the brain tissue, causing a stronger FBR (96). Also, thicker materials are known to induce more serious FBR than thinner materials (125).

4.3.1 Acute response

The acute phase of the FBR starts immediately after the implant insertion. Tissue damage and blood-brain barrier (BBB) disruption cause pro-inflammatory signalling and immune cells migration into or towards the implant. Additionally, rapid and spontaneous protein adsorption to the electrode initiates the contact between the inflammatory cells and the surface material through adhesion receptors. With time, smaller proteins (such as albumin or fibrinogen) are replaced by larger ones, changing the protein composition of the adsorbed layer and its interaction with the immune cells (126).

Neutrophils are the first population of the immune cells recruited during the acute phase of the FBR. They adhere to the layer of proteins adsorbed to the implant surface and start releasing factors promoting migration of the microglia and, in a lesser extent, monocytes as well as their conversion into macrophages. The initial neutrophilic wave is almost completely replaced by monocytes and macrophages during the first two days after the implantation (126). Microglia and macrophages also release pro-inflammatory cytokines and chemokines, further exacerbating the FBR. In an attempt to destroy the foreign body, they release ROS and may phagocytise parts of the electrode surface (126).

Nervous tissue damage also leads to a significant release of adenosine triphosphate from damaged cells, interacting with purinergic receptors on the surface of astrocytes, activating them (127). Astrocyte activation can also be initiated by pro-inflammatory factors released by microglia and macrophages. Within the first days following the implantation, astrocytes rapidly proliferate and extend their processes towards the lesion (127). Sustained astrocytic proliferation can ultimately lead to glial scar formation.

4.3.2 Chronic response

The chronic phase of the FBR is characterised by a gradual shift from the inflammatory into fibrotic processes. During this stage, macrophages change their pro-inflammatory phenotype into the anti-inflammatory one, facilitating recruitment of fibroblasts and stimulating production and release of the extracellular matrix (ECM) components, such as fibronectin and collagen type I, and forming the fibrotic scar (126).

At the same time, reactive astrocytes decrease their proliferation rate and stop orienting their processes towards the implant, but rather parallel to it (127). Thick layer of astrocytes is known as a glial scar, which, together with the fibrotic tissue, encapsulates the implanted electrode and isolates it from the rest of the tissue. Collagenous tissue increases electrical resistance, significantly dampening the electrical stimuli reaching the neurons.

In the thick cell layer adhering to the implant surface macrophages can fuse together, forming characteristic multinucleated foreign body giant cells (Figure 7) (128). These cells are capable of phagocytising larger particles and are a hallmark of the chronic phase of the FBR (126). They can also be responsible for damage to the surface of the material, further reducing the neurostimulation efficacy.

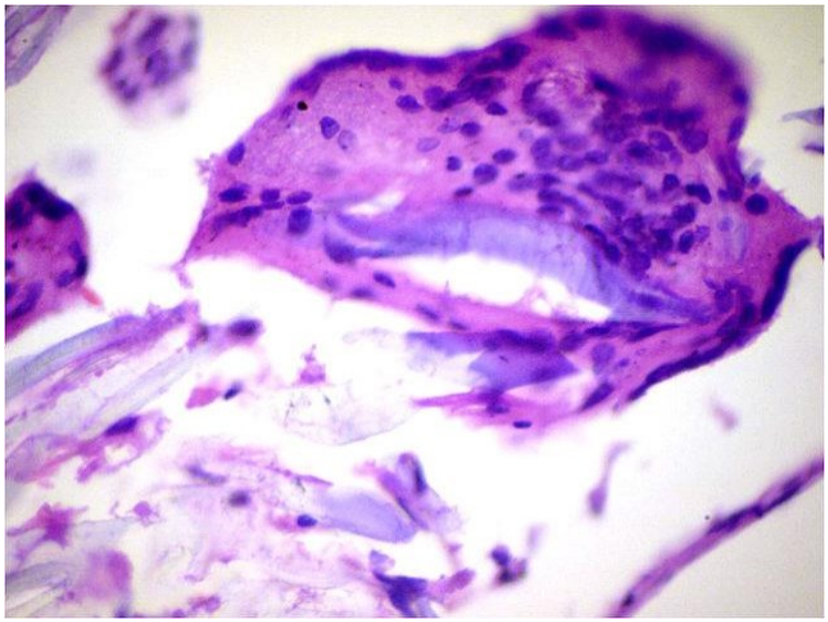

Figure 7. Haematoxylin-eosin staining of a foreign body giant cell. *The cell is capable of phagocyting larger foreign particles (violet object) and forms during the chronic phase of FBR. Photo by Department of Pathology, Calicut Medical College, obtained from the Wikimedia Commons, published on Oct 31, 2014, distributed under a CC-BY 4.0 license.*

4.4 DEVICE DURABILITY

In optimal conditions, electrodes should be able to remain functional for at least 20 years of implantation (96). Selection of the appropriate material and manufacturing method is therefore crucial, but very often highly challenging, and necessitates compromises, which can be a source of device failure:

- Abiotic sources:
    - Electrochemical reactions (reduction and oxidation) and corrosion leading to a material dissolution.
    - Delamination of the electrode contact.
    - Detachment of insulating coating or fluid allowance can result in current leakage.
    - In wired devices, lead twisting and breakage.
- Biotic sources:
    - Protein and cell adsorption to the surface in the early post-implantation phase.
    - Glial and fibrotic scar formation.
    - ROS release and phagocytosis of single particles from the surface by adherent immune cells.

Acute device failure is usually caused by the surgery and the insertion, and it is recognisable during the first hours following the implantation. Inflammation impact takes up to two weeks post-implantation, chronic effects can accumulate over several months or years.

5 LIGHT-CONTROLLED NEUROSTIMULATION

One of the common issues with standard invasive neurostimulation methods is the necessity of wiring. The connection between the electrode and the pulse generator is absolutely crucial for a successful application of the electric stimulation. However, events leading to disconnection, such as lead twisting, lead breakage, and pulse generator migration, have been reported in all invasive methods described above (6, 57, 64, 102, 103). Additionally, the necessity of regular battery changes further increase patients' burden and overloads the healthcare system with frequent visits during what is usually lifelong therapy. Therefore, unsurprisingly, significant research focus has been placed on the development of wireless, minimally invasive neurostimulation systems.

Even though multiple wireless stimulation methods, such as magnetic stimulus delivery or wireless power transfer, have been successfully implemented (129, 130, 131), light-controlled stimulation offers incomparable advantages in many aspects. Light pulses can be modified to different lengths, intensities, and shapes, imitating electric pulses used in standard electrodes and allowing for the testing of various stimulation parameters. Laser light can be highly focused, enabling precise stimulation, whereas more disperse light sources (such as LEDs) allow stimulation of larger surfaces. The use of LEDs also makes it possible to create cheap and extensive arrays that can be employed in high-throughput experiments. Finally, red spectrum light reaches high skin penetration depths (Figure 8) and, to some extent, penetrates bone and brain tissue (132, 133), allowing for transcutaneous, non-invasive stimulation. All in all, light serves as a well-suited stimulus delivery mode that has been harnessed in optogenetics, photopharmacology, and light-controlled electric stimulation.

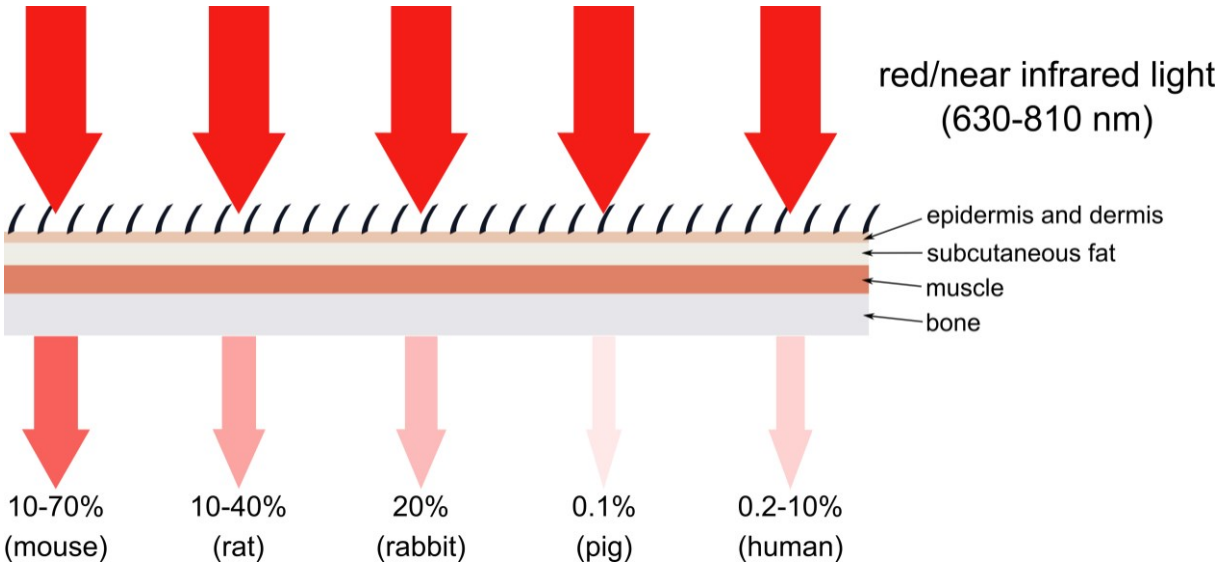

Figure 8. Scalp and skull tissue penetrability of red/near infrared light spectrum (630-810 nm) in various species. *Percentages for the mouse and rabbit describe skull-only penetrability, whereas percentages for the rat, pig, and human include both the scalp and skull. Based on works reviewed by Salehpour et al. (133)*

5.1 OPTOGENETICS

Optogenetics is a technique involving the introduction of genes encoding photosensitive ion channels – usually of microbial origin, such as channelrhodopsins or halorhodopsins – into cells of interest. In non-photosensitive cells, such as neurons, optogenetics enables easy and precise control of cellular activity. Upon illumination, light-sensitive channels open and ion currents lead either to depolarisation of the neuronal membrane (leading to firing of action potentials) or, in case of chloride ions, to membrane hyperpolarisation and neuronal spiking inhibition (134). Unlike electric stimulation, optogenetics allows for selective activation of specific types of cells. Therefore, this method of neuronal activity modulation has found its use in basic neuroscience, resulting in a significant progress in the research of memory formation, behavioural studies, and disease pathologies. However, the application of optogenetics in preclinical studies of therapeutic approaches has been relatively limited so far.

Most therapeutic applications of optogenetics involve vision restoration. In blinding diseases, such as retinitis pigmentosa, photoreceptors degenerate over time. The aim is therefore focused on surviving retinal cells, where the introduction of genes expressing light-sensitive ion channels renders them photosensitive, and helps recover visual function (135, 136). To date, the most data comes from *in vitro, ex vivo* and *in vivo* preclinical applications (135,

136, 137), however, several clinical studies in humans are currently underway, with the first successful trials of partial visual restoration reported recently (138).

In the CNS, optogenetics as a means of treatment has been employed in several preclinical rodent studies. Optogenetic stimulation of the secondary motor cortex and activation of cortical somatostatin interneurons improved motor functions in mouse models of PD (139, 140). In a similar mouse model of Parkinsonism, optogenetic inhibition of the subthalamic nucleus alleviated motor symptoms (141). In a mouse model of temporal lobe epilepsy, optogenetic stimulation was used to inhibit spontaneous seizures in a closed-loop system, mimicking current state-of-the-art stimulation methods described in detail in Chapter 2.3.2 – Epilepsy (142). Interestingly, in line with the above-mentioned tissue permeability of light in the red spectrum, optogenetic neuronal activation was achievable in deep regions of the mouse brain with light penetrating through the intact skull (143).

Despite these advancements, the translatability of optogenetics into human subjects is fairly limited and highly dependent on the development of efficient genetic modifications. Progress in the application of viral vectors and the employment of techniques such as CRISPR-Cas9 may facilitate the transfection of cells, however, ethical considerations of genetically modifying humans, especially in an irreversible manner, still linger. It is therefore crucial to fully inform the participants and to include clear and specific safety endpoints for human clinical trials (144). Compared to the rodent model organisms, light penetrates the human scalp and skull tissue to a lesser extent (133). Additional light absorption by brain parenchyma may further attenuate the signal reaching deeper regions, rendering deep optogenetic stimulation even more challenging. Additionally, the majority of photosensitive ion channels currently available only respond to light in the blue/green spectrum (145). Since the depth of penetration is highly dependent on the wavelength, the shorter wavelengths might not be able to reach the light-sensitive proteins without the invasive introduction of the light source into the brain (146).

5.2 PHOTOPHARMACOLOGY

Using light to directly influence pharmacokinetic or pharmacodynamic properties of synthetic molecules and thereby modify their biological activity is known as photopharmacology (147). Photochemical modifications of the light-sensitive molecules can be irreversible (photoinactivation, photoactivation through cleavage of “cages” – the most commonly used method) or reversible (photoswitches: photoactive ligands, adopting different isomeric forms depending on the light wavelength, or light-sensitive cross-linking portions of a molecule,

changing their conformation upon illumination) (147). As in the case of standard, non-photosensitive medication, photoactive molecules can act as receptor agonists, antagonists, partial agonists, etc.

A well-described and researched target for photopharmacological modulation are ion channels. Targeted and timed activation or deactivation of glutamate ionotropic receptors enables control of neuronal activity, which may serve both basic neuroscientific exploration and the development of novel therapeutic approaches. Photoswitchable agonists of the AMPA receptor have been proven effective in reversible generation of action potentials in the rodent cortical cultures (148), brain slices (149), and blind retinae (150). On the other hand, an AMPA receptor antagonist managed to silence neuronal activity in a culture despite high glutamate concentrations (151). Similar experiments with other compounds have allowed for selective control of NMDA receptors (152, 153, 154), kainate receptors (155, 156), and even voltage-gated ion channels (157).

Apart from ionotropic receptors, photopharmacology can be used to modify neurotransmitter transporters, controlling neuronal activity through modulated uptake of GABA (158) or glutamate (159). Light-controlled interaction of ligands with G-protein coupled receptors, such as acetylcholine receptors (160, 161), opioid receptors (162, 163), cannabinoid receptors (164) or metabotropic glutamate receptors (165), allows for further modulation and fine-tuning of neuronal activity. Enzymes, although a frequent target in oncological, haematological or immunological studies, are not common targets for photoswitches in the neuroscientific environment. One exception seems to be acetylcholinesterase, which was successfully blocked by a photoswitchable ligand in both *in vivo* and *ex vivo* settings (166).

Despite the numerous advantages of photopharmacology, such as precise temporal and spatial control and typically no need for genetic modification, its brain-specific use in preclinical animal models is still infrequent. Some groups have successfully employed photopharmacological tools in the modification of rodent behaviour (167, 168, 169), whereas *in vivo* therapeutic applications have been mostly tested in pain control (170) and vision restoration (171). Some of the limitations of photopharmacology include the stability and toxicity of the chemical compounds, commonly based on azobenzene (147). To render the particles less toxic, they might need further modifications or encapsulation, which might negatively influence their efficacy. However, in the CNS, the presence of the brain-blood barrier significantly limits the range of applicable molecules and possible modifications. Furthermore, as mentioned in Chapter 5.1 – Optogenetics, this approach might

require the implantation of the light source, further limiting its translatability into preclinical and clinical studies.

5.3 LIGHT-CONTROLLED STIMULATION WITH PHOTOACTIVE MATERIALS

Since neuronal activity is based on electric signalling, use of electric stimulation remains the most direct way to modulate it. To avoid issues associated with leads and pulse generators, such as migration, twisting and/or breaking, wireless applications have been brought into focus in the field of neurostimulation. The idea of wireless stimulation is by no means novel – inductive systems using radiofrequency were described as early as the 1960s (172, 173). However, it was not until the beginning of the 21st century that miniaturised, chip-based devices for recording and stimulation were developed (174, 175, 176). At approximately the same time, first light-sensitive appliances, usually complementary metal-oxide-semiconductor (CMOS)-based, were used as retinal prostheses (177, 178, 179, 180). Even then, the devices mostly required the presence of a sensor or receiver with appropriate circuitry to be able to trigger and control the stimulation, rendering them quite bulky and expensive.

Use of biocompatible, photoactive materials allows for fully harnessing advantages that come from using light as a stimulus delivery method, without relying on genetic modifications or generation of non-toxic, stable photoswitches capable of crossing the blood-brain barrier. Organic semiconductors have gained a lot of attention in recent years, with the first concepts and animal studies emerging in the 2000s (181, 182) and their development gaining momentum a decade later, mostly focusing on the development of retinal prostheses (183, 184, 185). Many organic semiconductors act as very efficient light absorbers even in ultrathin layers, rendering them an attractive candidate for production of minimally invasive, lightweight and wireless electrodes (186). This approach combines advantages of light-controlled stimulation, with high spatial and temporal resolution, with the benefits of traditional electric stimulation, offering a direct interface with the tissue and well-known mechanisms of neuronal excitation.

In principle, whether light will be absorbed by a material depends on the band gap between the valence and conduction bands of the semiconductor. If a photon has enough energy, upon its absorption, the electron can jump from the valence to the conduction band, leaving a positive hole behind. This charge separation is only temporary, resulting in the recombination of the positive and negative charges. However, if two semiconductors with different band gaps are placed next to or on top of each other, forming a so-called p-n

heterojunction, one of the materials will tend to accept the negative charge (electrons; n-layer), whereas the other one – the positive charge (holes; p-layer). To make the separation even more effective, the p-n heterojunction may be placed on top of a conductor (such as metal or highly-doped semiconductors), which further accepts the positively charged holes. Due to this physical separation, the electron-hole pairs avoid immediate recombination, effectively charging the device.

Photoactive devices made of semiconductors placed on top of the conductor form efficient transducers of light into electricity. However, the exact nature of stimulation by photoactive organic semiconductors heavily depends on material properties and architecture as well as on the light protocol (11, 186). Organic semiconductors used as a standalone stimulation device or deposited on an insulator will predominantly exhibit thermal or electrochemical effects, whereas the use of a conductor involves additional faradaic and capacitive mechanisms (Figure 9) (186). Each of these mechanisms has its own specific applications and can serve different modalities of neurostimulation, depending on the goal of the treatment.

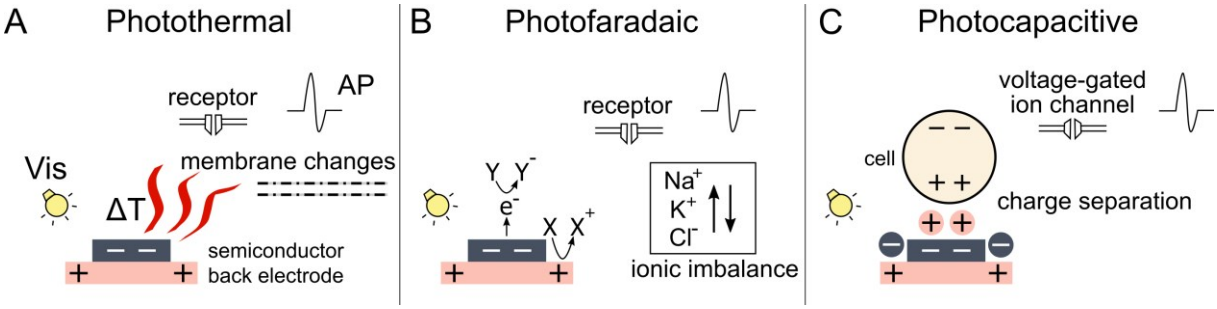

Figure 9. Types of cell stimulation using photoactive semiconductors. *(A) Photothermal stimulation. Upon illumination, the semiconductor heats up, leading to activation of heat-sensitive receptors (e.g., TRPV1) or to membrane changes, resulting in membrane depolarisation and generation of the action potential (AP). (B) Photofaradaic stimulation. Charges separated in the photoactive device are transferred into the electrolyte, leading to electrochemical reduction-oxidation reactions. Activation of receptors (e.g., TRPV1 activation after H_2O_2-sensitisation) or changes in ionic concentrations lead to depolarisation and AP generation. (C) Photocapacitive stimulation. Charges separated in the device attract charged molecules in the electrolyte and within the nearby cells. Ionic imbalance close to the membrane of electrically active cells (neurons, muscle cells) can activate voltage-gated ion channels and result in AP firing.*

5.3.1 Photothermal stimulation

Even though not electrical, thermal stimulation plays an important role in neuronal activation, especially since pulsed illumination leads to temperature increases (13). Local heating

of the material is a by-product of recombination of the electron-hole pairs, and some materials are particularly effective at heat generation. Remarkable results have been described for carbon nanotubes, gold nanoparticles, as well as semiconductor nanoparticles (11). For the stimulation, the temperature change dynamics are more crucial than the absolute temperature value (11).

The exact mechanism of photothermal neurostimulation has not been fully elucidated so far; however, there are three main processes contributing to this effect (Figure 9A). The first one is the activation of heat-gated ion channels, such as transient receptor potential cation channel subfamily V member 1 (TRPV1) expressed in sensory neurons (187, 188), but also in various brain regions, including HC, amygdala, hypothalamus, and cortex (189). Photothermal stimulation using nanometre-sized transducers allowed for minimally invasive TRPV1-mediated activation of neurons in HC, motor cortex, and ventral tegmental area in freely moving mice (190). Besides receptor activation, local heating of the cell membrane can lead to changes in its electrical capacitance, effectively depolarising the cell and generating action potentials (191). Increased temperature also influences the dynamics of ion channel activation, leading to their faster opening and effectively increasing the neuronal excitability (11). Nevertheless, temperature modifications in the nervous system should be applied with caution, as they may trigger several negative-feedback mechanisms or directly damage the tissue (192).

5.3.2 Photofaradaic and photoelectrochemical stimulation

Charge transfer in the form of reduction or oxidation of chemical species in the electrolyte surrounding the device is known as a faradaic current. The faradaic current generated between the illuminated photoactive material and the electrolyte is the basis of the photofaradaic stimulation (Figure 9B). In organic semiconductors, reduction reactions involve predominantly oxygen (186, 193), leading to the generation of ROS, such as superoxide or hydrogen peroxide (H_2O_2). These, in turn can interact with some ion channels (e.g., TRPV1 (194), TRPM2 (195)), leading to the generation of action potentials. Reduction-oxidation reactions of ions present in the electrolyte can create local ionic imbalances, effectively leading to depolarisation or hyperpolarisation of the nearby neuronal membranes, further modulating the activity of these cells (11).

Photoelectrochemical stimulation is not restricted to the closest vicinity of the device, as the generated chemical compounds diffuse within the electrolyte, creating a gradient, which allows them to interact with cells located further away (196). However, repeated reduction-

oxidation reactions at the device-electrolyte interface lead to wear of the material, which may result in irreversible damage to the device (197). In standard neurostimulation electrodes, noxious effects on the electrode are prevented through biphasic pulsing of the electric current (197). In the case of light-responsive semiconductors, the polarity changes between the illumination and the dark phase – however, it is not certain, whether it exerts the same protective effects on the material as the classical biphasic electric stimulation. In addition, uncontrolled ROS generation can result in direct tissue damage or deplete anti-oxidative defence, which may lead to or exacerbate certain CNS diseases (198).

5.3.3 Photocapacitive stimulation

In photocapacitive stimulation, the charges separated within the light-responsive semiconductors during the illumination do not transfer to the electrolyte, but create a potential difference, which in turn causes the movement of the surrounding charged particles towards the device surface. This results in a build-up of an electrolytic double-layer (Figure 9C). The redistribution of ions takes place also within the cells located in the vicinity of the charged device, leading to the local changes in polarisation of the cell membrane (14). The membrane portion close to the negatively charged surface (cathode) becomes positively charged. If the membrane potential reaches the depolarisation threshold, a neuron can effectively generate the action potential (Figure 10A). Anodic stimulation hyperpolarises the cell membrane close to the electrode, as the negative charge inside the cell approaches the positively charged electrode surface. However, in the neighbouring cell parts, a lack of the positive charge can result in enough membrane depolarisation, so the action potential generation is still possible (Figure 10B). Nevertheless, to reach anodic stimulation, current pulses must be substantially higher than in the cathodic stimulation (104).

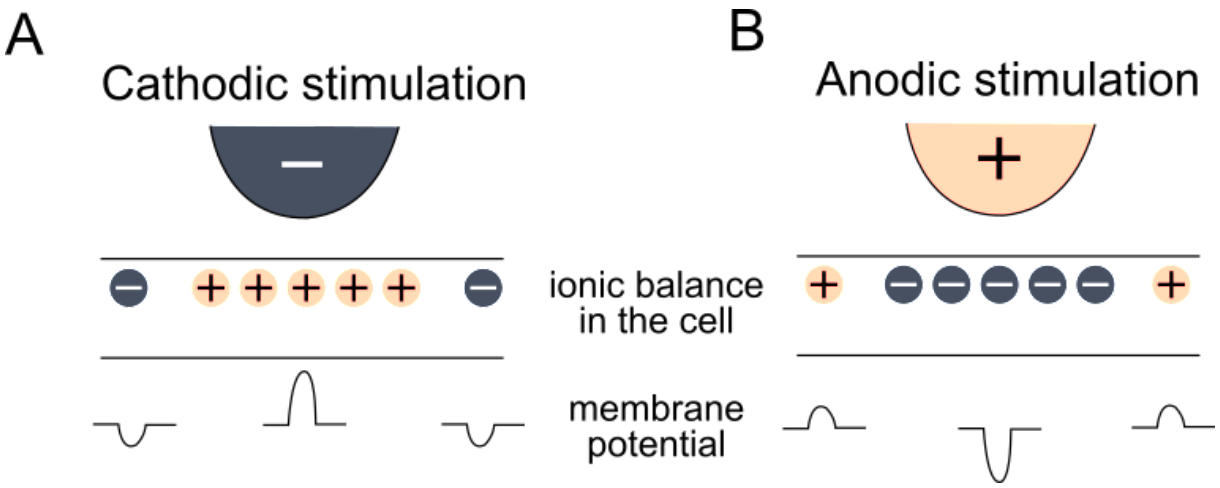

Figure 10. Charge movement and membrane potential during the cathodic and anodic stimulation. *(A) During the cathodic stimulation, positive charge accumulates close to the electrode, and membrane potential increases, leading to depolarisation. When the threshold potential is reached, an action potential can be fired. (B) During the anodic stimulation, negative charge accumulates close to the electrode, and membrane potential decreases, resulting in hyperpolarisation. Neighbouring portions of the cell membrane depolarise and can generate an action potential, if stimulated with a strong anodic current.*

Capacitive stimulation is considered to be safer for the nervous tissue, avoiding possibly detrimental chemical reactions (e.g., ROS generation) or heat dissipation (11, 186, 197). Although useful in certain applications, photothermal and photoelectrochemical mechanisms do not allow for high temporal resolution of the stimulation, due to the kinetics of temperature changes and chemical reactions (13). Therefore, photocapacitive stimulation poses the most promising mode of light-controlled electrical neurostimulation. Nevertheless, organic semiconductors often present mixed, faradaic-capacitive behaviour, and the dominance of one or the other depends on the material's time constant and architecture on one hand, and on the light pulse duration on the other hand (186).

5.4 Organic electrolytic photocapacitors (OEPC)

A need for wireless, light-controlled and capacitive neurostimulation through soft and lightweight devices was a starting point for the development of organic electrolytic photocapacitors (OEPC; Figure 11) (13). OEPC consist of two nanometre-thin organic semiconductors, vastly used in the industry as paints, dyes, printing inks or cosmetics: *N,N'*-dimethyl perylene-3,4,9,10-tetracarboxylic diimide (PTCDI), of reddish colour, and metal-free phthalocyanine (H_2Pc), a blue dye (13). PTCDI is known for high photochemical stability, strong electron acceptance, outstanding stability in aqueous solutions and high temperatures

(199). In the p-n heterojunction of OEPC, PTCDI serves as an n-layer, accepting the negative charge. H_2Pc is also known for its high stability in water, at high temperatures, and during long illuminations (200). Due to its broad wavelength absorption and proven biocompatibility, it has already been established for use in optical imaging and phototherapy (201, 202, 203). In the OEPC, H_2Pc serves as a positive-charge-accepting p-layer. Additionally, the p-layer is deposited on top of a conductor serving as a back electrode further accepting the positive charge.

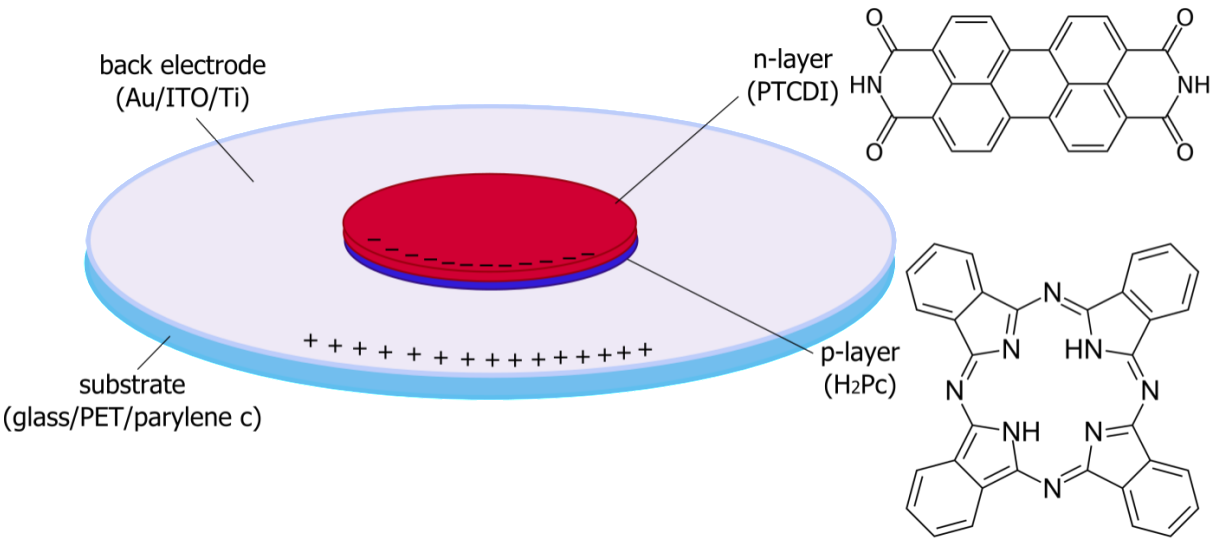

Figure 11. Schematic representation of an OEPC. *Light-sensitive organic semiconductors, PTCDI and H_2Pc, form a p-n heterojunction, in which electron-hole pairs are generated during red-spectrum irradiation. Negative charge accumulates on top of the n-layer, whereas positive charge is transferred to the conductive back electrode. Depending on the application (in vitro study, long-term in vivo implantation), OEPC can be deposited on top of various substrates.*

The basis of the OEPC mode of action is charge separation within the p-n heterojunction during red-spectrum light irradiation. The charging of the device is predominantly capacitive in nature, at least when light pulses last from 100 µs to 5 ms and the device is planar (186). However, hours-long irradiation of similar, PTCDI-based nanodevices led to significant increase of H_2O_2 (204). Moreover, choice of the back electrode material (e.g., gold, titanium, indium-tin oxide [ITO]) can further influence the balance between the photocapacitive and photofaradaic mechanisms – OEPC with a gold back electrode can produce ROS, whereas ITO-based OEPC have been described not to (14). Therefore, the photofaradaic component of the OEPC-based stimulation cannot be fully excluded and must be considered during the study design.

Semiconductor-conductor triple layer can be deposited onto various carrier substrates: glass, PET foil, parylene foil, etc. Substrate selection depends mostly on the application of OEPC – in cases of *in vitro* cell culture rigid glass coverslip facilitates handling, whereas soft, lightweight and biocompatible parylene foil enables the implantation of the device into the body. OEPC designed in various shapes and sizes can not only facilitate the manufacturing of specialised implants (e.g., nerve cuffs (18) or cortical implants (16)), but also influence the charge delivered to the tissue. Additionally, the devices can be coated with other materials, such as poly(3,4-ethylenedioxythiophene):polystyrene sulfonate (PEDOT:PSS), further increasing their capacitance (14).

Since their conception, OEPC have been applied as neurostimulation devices in several *in vitro* and *in vivo* studies. In the seminal work, OEPC were successfully employed in the light-insensitive embryonal chick retina, serving as a proof of concept for the device functionality (13). Patch-clamp recordings of *Xenopus laevis* oocytes shed more light on the details of cell membrane response, revealing its effective depolarisation in the vicinity of the OEPC, whereas the membrane portion located on the opposite side of the cell underwent a slight hyperpolarisation (14). Building on this experience, an electrophysiological study of primary mouse hippocampal cells proved an effective modulation of neuronal activity through light-controlled OEPC stimulation (15).

Based on the knowledge gathered from the *in vitro* experiments, OEPC devised as implants were introduced in both the central and peripheral nervous systems. In the CNS, acute stimulation of the mouse motor cortex responsible for whisker movement resulted in visible whisker deflections and electrophysiological responses of the somatosensory cortex (16). Application of OEPC on rat ischiadicus not only proved the device effective in peripheral nerve stimulation, but also underlined its biocompatibility, sustaining its functionality for over 100 days without histological marks of tissue damage or excessive inflammation (18).

In summary, OEPC pose an already tried and tested platform for basic neuroscientific research and an attractive wireless neurostimulation device with prospective clinical applications. However, to ensure their application in clinics, extensive preclinical studies aimed at their efficacy in neurostimulation and their biocompatibility are still necessary.

6 SOMATOSENSORY CIRCUITS IN THE BRAIN

The somatosensory system is pivotal in an animal's interaction with its environment. It facilitates the connection between the individual and its surroundings by sensing, transmitting, and interpreting both innocuous and noxious stimuli from the body surface (exteroception). Moreover, it monitors the body's position relative to the external world through signals from muscles, joints, and tendons (proprioception). While the organisation of the somatosensory system is complex, involving multiple organs and intricate nervous connections, its primary analytical component lies within the somatosensory cortex (SOM).

6.1 SOMATOSENSORY CORTEX

6.1.1 Anatomy

SOM is a part of the neocortex, which is evolutionarily the most recent component of the cerebral cortex found in mammals and is responsible for higher cognitive functions. It is a part of parietal cortex, which in rodents is located dorsolaterally beneath the parietal bone of the skull. In humans, SOM reaches thickness of 2-4 mm (205). In rats, it is approx. 1.1-1.8 mm thick (206, 207).

Structurally, as a neocortex, SOM consists of six distinct layers, numbered from I to VI, with layer I being the most superficial and VI the deepest, organised in vertical columns of cell bodies and processes (Figure 12).

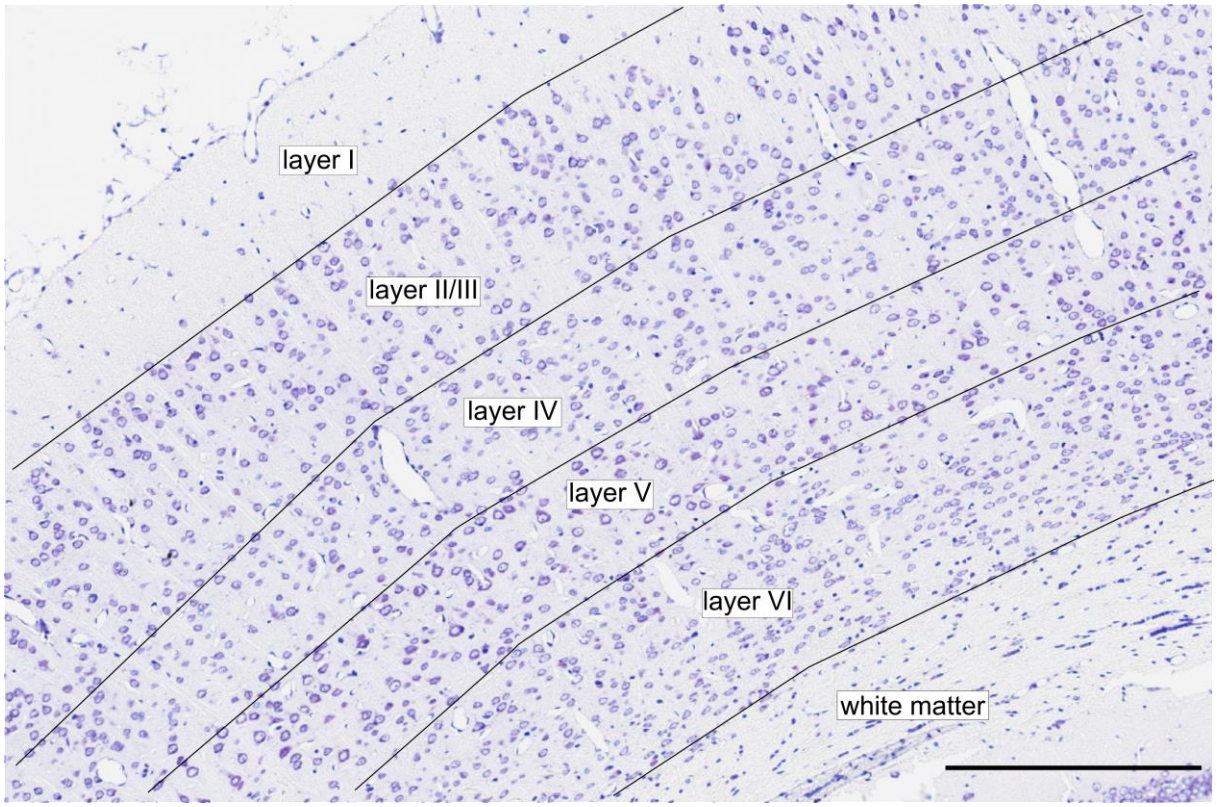

Figure 12. Photomicrograph of thionin staining of rat SOM with demarcated layers. *Scale bar: 300 µm.*

Starting from the brain surface, one can distinguish:

- **Layer I**: molecular layer, characterised by scarce neuronal somas – if present, predominantly interneurons, such as 5HT3aR$^+$ neurogliaform and single 5HT3aR$^+$ bouquet cells – and primarily composed of transverse axons and glial cells.
- **Layer II**: external granular layer and **layer III**: external pyramidal layer. Since the boundary between the layers in SOM is poorly defined, it is common to refer to those layers as one, **layer II/III**. Pyramidal cells project to other cortical regions and are accompanied by interneurons, including mostly somatostatin (SST)$^+$ Martinotti cells, vasoactive intestinal peptide (VIP)$^+$ bipolar cells, single parvalbumin (PV)$^+$ chandelier cells (innervating processes), and PV$^+$ basket cells (innervating soma).
- **Layer IV**: internal granular layer, containing granule cells and interneurons, notably PV$^+$ basket cells and SST$^+$ non-Martinotti interneurons. In SOM, granule cells are particularly prominent, except in parts called dysgranular zones.
- **Layer V**: internal pyramidal layer, predominantly comprising pyramidal cells projecting to the basal ganglia, brain stem, and spinal cord. It can be further subdivided into layer

Va (with fewer cells) and Vb (with abundant cells). It contains interneurons, such as SST^+ Martinotti cells and PV^+ basket cells.

- **Layer VI**: multiform layer, housing cells projecting to the thalamus, along with PV^+ chandelier cells and PV^+ basket cells.
- White matter below layer VI, consisting of fibre tracts, which are collections of axons within the CNS. In the brain, the tracts are mostly non-linear.

SOM can be divided into primary and secondary portions, each containing neuronal representations of the body surface, including limbs, trunk, face, and whiskers. In rodents, the primary SOM represents predominantly face and whiskers, with relatively smaller portions dedicated to sensation in the limbs and trunk (208). In primates, it encompasses Brodmann areas 3 (subdivided into 3a and 3b), 1, and 2, where areas 3b and 1 receive predominantly external information, while areas 3a and 2 are responsible for proprioception (209). Known for its high plasticity, SOM undergoes reorganisation after deafferentation, such as limb loss or nerve trauma, where deafferented regions represent other intact peripheral parts (209).

In regions responsible for whisker sensation, layer IV granule cells organise into "barrels" – cubic, regions of densely packed cells with a hollow inner part. Each barrel corresponds to a single whisker. Granule cells form numerous connections within the barrel, with only few between the barrels.

6.1.2 Connections

Sensory stimuli are transduced from mechanical forces into electrical signals through receptors located in the skin, muscles, and connective tissue. In the limbs and trunk, receptor information is transmitted by primary afferent neurons through the dorsal root ganglia into the spinal cord. From there, the signal is relayed further via ascending spinal pathways to medullary nuclei (gracile, cuneate, external cuneate) in the brainstem. In the head, the stimuli are conveyed by the trigeminal nerve through the trigeminal ganglion into trigeminal nuclei in the brainstem. Subsequently, sensory information from the medullary nuclei reaches the ventrobasal part of the thalamus, with its ventroposterolateral nucleus processing signals from the trunk and limbs, and the ventroposteromedial nucleus relaying sensations from the head.

The thalamus serves as the main source of the sensory input reaching SOM, with its afferents connecting predominantly to the cortical layer IV. Additional afferents include those from the raphe nuclei and locus coeruleus. Efferents from SOM to subcortical regions originate from layers V and VI, encompassing reciprocal connections with the thalamus, brainstem,

and trigeminal nuclei, as well as connections with the striatum, red nucleus, pontine nuclei, and spinal cord (208).

Within the cortex, SOM forms robust mutual connections with the primary motor cortex and the agranular cortex. Moreover, both primary and secondary SOM interconnect with their contralateral counterparts via the corpus callosum. Callosal connections primarily originate from layers II/III and V, terminating in corresponding layers in the contralateral hemisphere (208).

6.2 HIPPOCAMPAL FORMATION

HC and the parahippocampal cortex (PHC) are integral components of the hippocampal formation, a complex structure nestled within the temporal cortex and constituting a part of the limbic system. Among its multiple functions, the hippocampal formation is pivotal for memory formation and retrieval, processing novel information, and facilitating spatial navigation. The hippocampal and parahippocampal network consists of extensive internal and external connections and demonstrates a unique feature – a mostly unidirectional signal processing. Dysregulation within this network can precipitate various disorders, including neuropsychiatric conditions and epilepsy.

6.2.1 Anatomy

6.2.1.1 Hippocampus

HC derives its name from its structural resemblance to a seahorse. However, this holds true only for the primate brain. In rodents, HC is prominent, but C-shaped, extending from the septal nuclei to the amygdaloid complex. Its long axis, known as the septotemporal axis, runs obliquely relative to the brain's long axis, with the septal pole positioned dorsally, medially, and rostrally, while the temporal pole lies ventrally, laterally, and caudally.

HC can be segmented into three main regions: DG, CA – also referred to as the proper hippocampus – and the subiculum. Each of these regions exhibits characteristic cytoarchitecture, clearly identifiable in the histological staining (Figure 13).

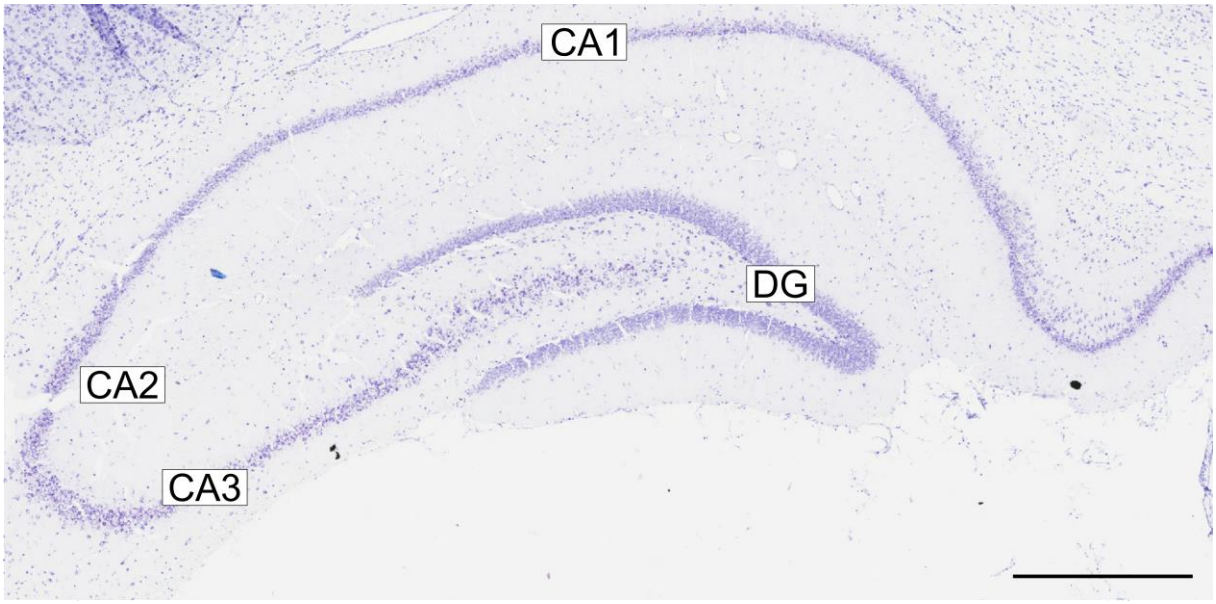

Figure 13. Photomicrograph of thionin staining of rat HC with its subregions. *CA – cornu Ammonis, DG – dentate gyrus. Scale bar: 600 µm.*

Dentate gyrus

In a coronal section, DG forms a V- or U-shaped structure, located medially (Figure 13). The portion situated superficially, closer to CA1, is referred to as the upper or suprapyramidal blade, whereas the deeper part is termed the lower or infrapyramidal blade. DG consists of three distinct layers (Figure 14):

- Granule cell layer (**stratum granulosum**): the principal cell layer of DG, densely populated with cells. Depending on age, rat strain, and sex, it may contain up to 2 million cells (210). The principal neuron type is the granule cell, characterised by a small cell body and extensive dendritic arborisation. The primary interneuron type is the basket cell, which forms close connections with the soma of granule cells.
- Molecular layer (**stratum moleculare**): located superficially to the stratum granulosum. It contains sparse cells, predominantly interneurons, such as basket cells and chandelier cells. It mainly consists of granule cell dendrites.
- **Hilus**: portion enclosed between the upper and lower blades. The main neuron of the hilus is known as a mossy cell, characterised by complex and dense dendritic spines. They serve as terminals for mossy fibres – unmyelinated axons projecting from granule cells. The primary interneuron type is the axo-axonic chandelier cell.

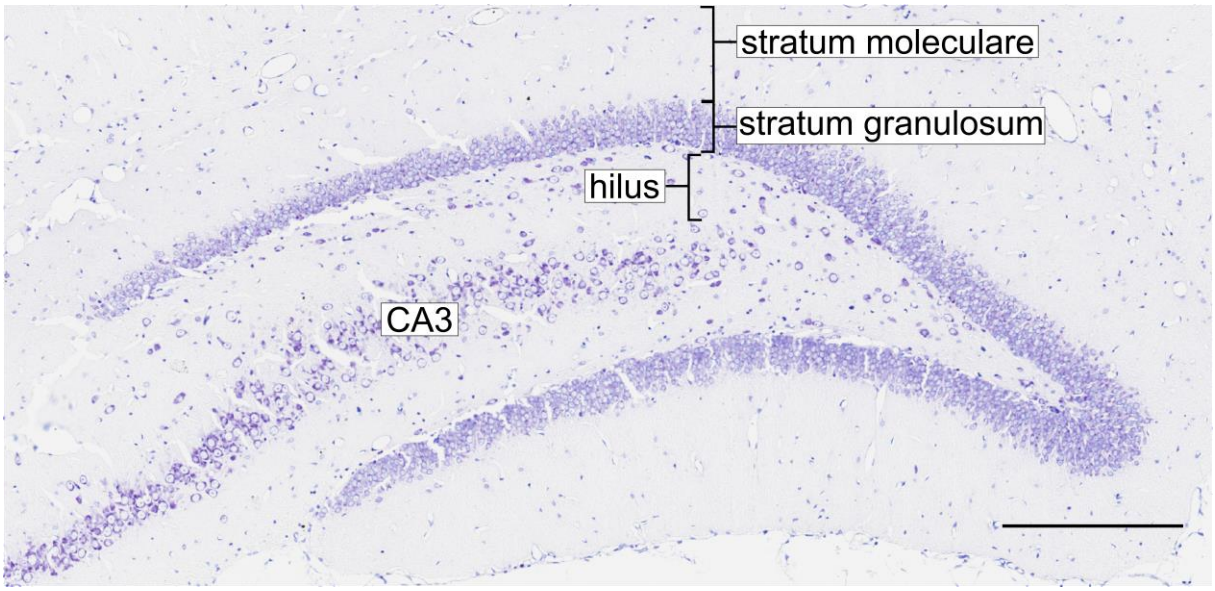

Figure 14. Photomicrograph of thionin staining of rat DG with demarcated layers. *CA – cornu Ammonis. Scale bar: 300 µm.*

The subgranular zone of DG is one of the two main regions – alongside the subventricular zone – housing residual neural stem cells, which actively proliferate and differentiate into neurons throughout life (adult neurogenesis).

Cornu Ammonis

A coronal section of HC reveals the structure of CA resembling an elongated "C", beginning in the hilus of DG, extending latero-dorsally, and terminating near the subiculum. It contains three subregions, ordered from the part nearest to the hilus (Figure 13):

- CA3: comprising large cells with dense dendritic spines similar to mossy cells.
- CA2: comprising large cells lacking dense dendritic spines.
- CA1: comprising smaller, densely packed cells.

The boundaries between CA3/CA2 and CA2/CA1 are often unclear by cytoarchitectonic criteria, typically necessitating molecular biology techniques for precise distinction (210). Border regions exhibit mixed cellular populations.

Cytoarchitectonically, the CA regions can be further subdividied into (Figure 15):

- Pyramidal cell layer (**stratum pyramidale**): the principal layer of CA, inhabited by pyramidal cells, with basket cells as the primary interneuron type.

- **Stratum oriens**: situated superficially to the stratum pyramidale, primarily containing pyramidal cell dendrites and a sparse population of interneurons. CA harbors at least 21 types of hippocampus-specific interneurons (210).
- **Stratum lucidum**: present exclusively in CA3, located deeper than the stratum pyramidale, consisting mostly of mossy fibres.
- **Stratum radiatum**: located deeper than the stratum pyramidal or stratum lucidum, containing mostly dendrites and axons of pyramidal cells.
- **Stratum lacunosum-moleculare**: the deepest layer of CA, serving as a terminus for the perforant pathway projecting from the entorhinal cortex (EC).

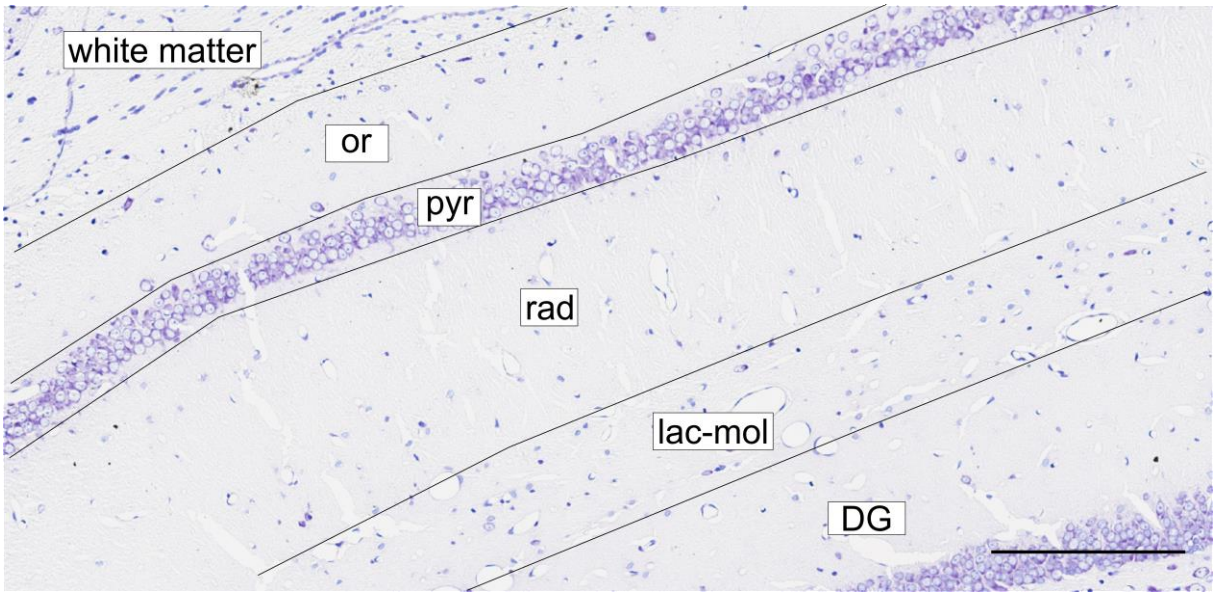

Figure 15. Photomicrograph of thionin staining of rat CA1 with demarcated layers. *or – stratum oriens, pyr – stratum pyramidale, rad – stratum radiatum, lac-mol – stratum lacunosum-moleculare, DG – dentate gyrus. Scale bar: 200 µm.*

Subiculum

Subiculum is a portion of HC linking CA1 with PHC. Structurally, it comprises two distinct layers: the stratum moleculare, which extends continuously from the stratum radiatum of CA1, and the stratum pyramidale, which similarly continues from the corresponding layer in CA1. While a boundary between the stratum moleculare of the subiculum and the stratum radiatum of CA1 is not apparently distinguishable, the border between the two strata pyramidalia is clearly visible.

6.2.1.2 Parahippocampal cortex

PHC is situated in the ventrocaudal region of the rat brain and encompasses several distinct areas, including the presubiculum, parasubiculum, entorhinal cortex (EC), perirhinal cortex, and postrhinal cortex. For the sake of brevity, this overview will focus primarily on EC, given it constitutes a substantial part of PHC, and forms an extensive network of both efferent and afferent connections with HC.

EC borders the parasubiculum, perirhinal and postrhinal cortices, piriform cortex, and amygdaloid complex. Cytoarchitectonically, it represents a periallocortex – a structure intermediate between the neocortex and the paleocortex. The neocortex is evolutionarily relatively recent and consists of six distinct layers (as detailed in Chapter 6.1 Somatosensory cortex). In the mammalian brain, the paleocortex is the most conserved, but also relatively small part of the cerebrum. It consists of three layers and is primarily found in the olfactory system, forming the piriform cortex. The periallocortex represents a transitional form between the two, with several layers present, but not always clearly distinguishable.

Conventionally, EC is divided into six layers (I-VI; Figure 16). Layers II, III, V, and VI are termed cellular layers, characterised by a high density of cell bodies, while layers I and IV are acellular. Similar to the neocortex, layer I primarily contains processes and single inhibitory cells. Layers II and V of the EC are predominantly populated by pyramidal cells. In contrast to the neocortex, layer IV lacks granule cells and is alternatively referred to as lamina dissecans. Layers III and VI also exhibit differences to the neocortex, displaying a higher heterogeneity and comprising pyramidal, multipolar, bipolar, and horizontal cells (210). The interneuronal composition mirrors that of the neocortex, with basket cells typically situated in close proximity to the soma of excitatory cells, while chandelier cells and bipolar cells are located in the vicinity of the processes.

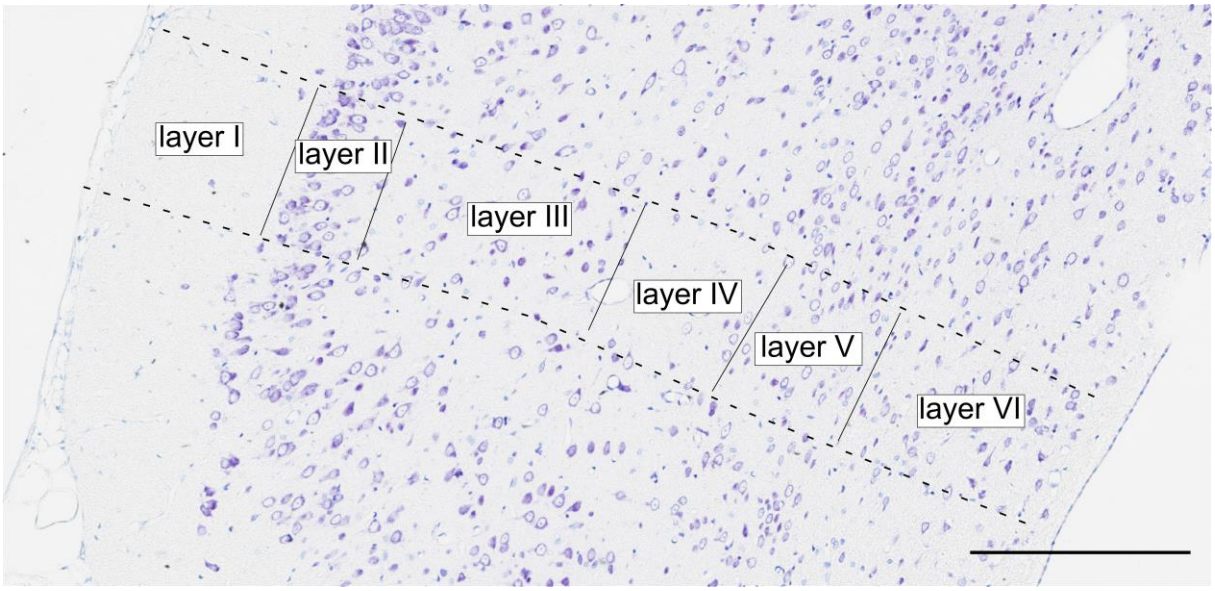

Figure 16. Photomicrograph of thionin staining of rat EC with demarcated layers. *At this bregma level (around -4.00), EC is a narrow portion of the cortex (marked in-between the dashed lines). Increasing in its size in the caudoventral direction. Scale bar: 300 µm.*

EC is composed of lateral (LEC) and medial (MEC) portions, each distinguished by its location, histology, and function. LEC is positioned rostrolaterally, near the rhinal fissure, and borders the perirhinal and piriform cortices. In contrast, MEC is situated caudomedially, between the piriform cortex and parasubiculum. The two portions diverge in their cellular composition: layer II of the MEC contains numerous stellate cells, serving as the primary source of axons for the perforant pathway (210). Additionally, they differ in cellular organisation, with MEC exhibiting a more columnar structure and LEC displaying a less distinct layer IV (210).

6.2.2 Connections

Unidirectional signal processing is a hallmark of the hippocampal formation, enabling its specialised functionality. In short, signal propagates from EC to DG, then to CA3, and subsequently to CA1, thereby constituting a trisynaptic circuit (Figure 17). Returning from CA1, information completes the loop by re-entering the EC. However, the hippocampal networks in reality extend beyond this linear pathway, encompassing serial, parallel, intrinsic, and reciprocal connections that integrate information from various brain regions.

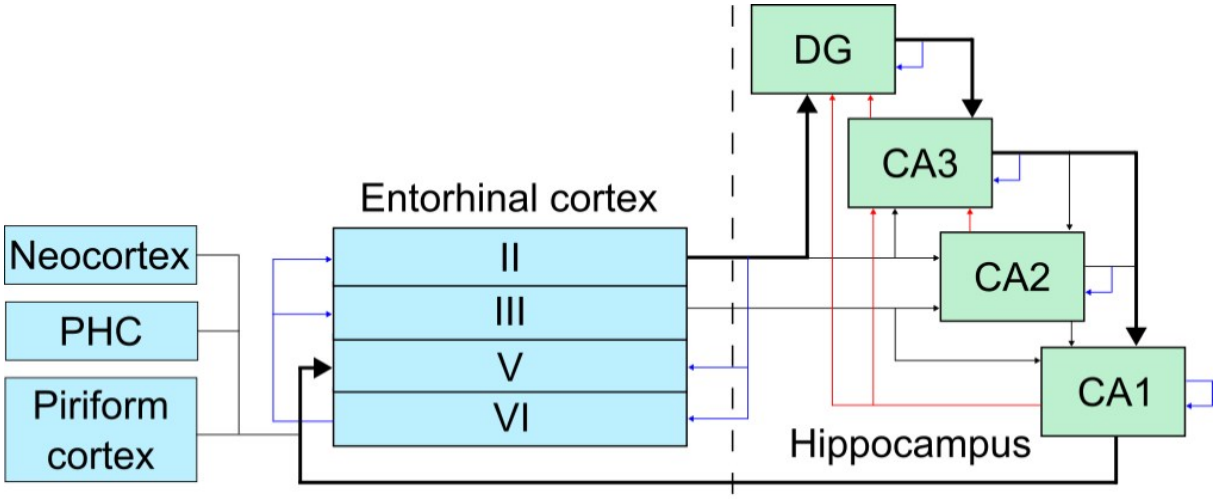

Figure 17. Connections between the cortex and the hippocampus. *Thick arrows indicate the connections involved in the unidirectional trisynaptic circuit. Blue arrows show intrinsic connections within a given brain region. Red arrows mark inhibitory backward connections. Detailed description can be found in the text.*

The EC acts as a hub, receiving and projecting connections to and from numerous cortical regions. Notably, it forms robust contact with adjacent regions, such as the perirhinal, postrhinal, and piriform cortices, while forming moderate to weak connectivity with the neocortex, including the frontal, insular, cingulate, temporal, and somatosensory cortices. EC receives efferents from layers II, V and VI of SOM, and projects to the primary SOM from LEC (210).

EC relays signals to all hippocampal subregions via the perforant pathway, which originates primarily in layers II and III. Distribution of these connections shows high level of organisation. Within the ipsilateral HC, axons stemming from the stellate cells of layer II predominantly terminate in DG and CA3, while those originating in the pyramidal cells of layer III end mostly in CA1. CA2 receives efferents from both layers. Additionally, some EC projections extend to the contralateral HC. They originate exclusively from layer III and terminate primarily in DG.

DG constitutes the next component of the classical trisynaptic circuit. Axons from the perforant pathway establish connections with the dendrites of granule cells within the stratum moleculare. Subsequently, the signal is transmitted through mossy fibers, leading to activation in the hilus, CA3, and CA2 regions. Within the hilus, mossy fibers form connections with mossy cells, which predominantly activate GABAergic interneurons leading to inhibition of granule cells, thus establishing a negative feedback loop. Conversely, connections with the CA regions are excitatory, primarily targeting pyramidal cells.

CA3 sends inhibitory projections back to DG, both through the stratum moleculare and the hilus. Excitatory signal reaches CA1 through Schaffer collaterals, terminating in the strata radiatum and oriens. The connections between CA3 and CA1 exhibit spatial organisation: proximal (relative to hilus) CA3 neurons predominantly project to distal CA1 cells (located near the subiculum), while distal CA3 neurons terminate at proximal CA1 cells (close to the CA2). However, the boundaries between these organisational units are flexible, creating a "gradient of connections".

From CA1, inhibitory signals are relayed back to CA3 and DG, while excitatory stimuli are directed toward the subiculum (which further connects to EC), or directly to EC as well as the perirhinal and postrhinal cortices. In the cortex, axons from CA1 terminate in layer V. Similarly to other regions within the hippocampal formation, projections from CA1 to EC are spatially organised: septal portion of CA1 links with LEC, while the temporal part connects with MEC (210).

Detailed knowledge concerning CA2 connections remains limited. It is known to project primarily to the hilus of the DG, with sparse connections extending to CA3 and CA1.

Similarly to EC, principal neurons of DG and CA project commisural connections to their corresponding regions of the contralateral HC. They terminate primarily in the stratum moleculare or stratum oriens of the homologous regions (210).

The hippocampal formation – both HC and PHC – forms additional connections with other brain regions, including the septal nuclei, hypothalamus, thalamus, amygdaloid complex, brain stem, and more. However, delving into these networks falls beyond the scope of this overview.

6.3 ELECTRICAL STIMULATION OF THE SOMATOSENSORY CORTEX

Until present, electrical stimulation of SOM has been a primary focus in development of neuroprostheses and brain-machine interfaces. Human studies indicate that SOM stimulation induces evoked sensations, often described as tingling, itching, or pressure, in the dermatome corresponding to the stimulated area, both in chronically paralysed patients (211, 212), and in non-paralysed subjects (213, 214). Stimulation not only could evoke new sensations, but also modify a feeling of warmth and cold (214), and has shown potential in suppressing deafferentation pain (215). Human trials investigating plasticity have demonstrated improvements in sensorimotor tasks following SOM stimulation, suggesting its potential to enhance the neurorehabilitation process after brain injuries (216).

However, there is limited knowledge concerning the further propagation of neuronal signals evoked during SOM stimulation. Studies on rats subjected to sensory stimulation of paws and whiskers have shown increased electrical activity in both SOM and HC (217), and simultaneous activation of SOM and striatum (218). Nevertheless, effects of direct electrical stimulation of SOM on other brain regions are not sufficiently understood.

Electric and optogenetic stimulation of motor cortex has been reported to activate neurons and trigger regenerative responses in the contralateral hemisphere (219, 220). This kind of indirect stimulation from the healthy cortex to the injured counterpart could offer advantages in cases of stroke or TBI by avoiding interaction with the injured area and potentially diminishing the risk of symptom exacerbation. However, it remains uncertain whether stimulation of SOM could produce similar outcomes.

7 STUDY AIMS AND SCOPE OF THE DISSERTATION

Neurostimulation through light-controlled, wireless, soft bioelectronics represents a groundbreaking approach with broad applicability, necessitating comprehensive interdisciplinary studies spanning materials science, electrophysiology, neuroscience, immunology, and imaging. Despite significant progress in organic electrolytic photocapacitive devices, uncertainties regarding their functionality and interactions with biological systems prevail, which motivated this work. The primary aim is to assess the potential of light-controlled stimulation using OEPC to induce molecular changes in cells and tissue and to describe the biocompatibility of the device. In our hypothesis, OEPC can effectively stimulate extensive neuronal networks of the brain, demonstrate long-term durability and biocompatibility, and its repeated use can lead to regenerative responses, potentially aiding in the treatment and rehabilitation of various brain injuries.

To accomplish this, several objectives were established:

1. Develop and validate models:
    a. Establish ***in vitro***, ***ex vivo***, and ***in vivo*** models of cortical stimulation.
    b. Validate the effectiveness of these models.
2. Investigation of neuronal activation after OEPC stimulation:
    a. Employ single neurostimulation treatments to induce **c-Fos** expression within neurons.
    b. Investigate the extent of stimulation, focusing on signal propagation within **neuronal networks**.
3. Assessment of tissue-device interaction:
    a. Assess short and long-term effect on **tissue**, emphasising cytotoxicity and foreign body response.
    b. Investigate long-term **device durability**.
4. Evaluate regenerative responses:
    a. Use repetitive stimulation protocols to trigger molecular changes associated with **regeneration** (GAP-43).

Insights gained from this research contribute significantly to advancing neurostimulation techniques, benefiting both technology development and medical progress. The biocompatibility and durability of organic pigment-based soft bioelectronics could facilitate the manufacture of novel devices for various applications. Furthermore, the potential to activate extensive neuronal networks, especially in contralateral regions, offers promising

treatment approaches for patients with brain injuries without affecting the injured site. Finally, achieving regeneration through repetitive stimulation holds promise for enhancing rehabilitation outcomes and accelerating recovery, ultimately reducing patient burden and improving quality of life with minimally invasive, wireless, light-controlled, soft bioelectronics.

8 MATERIALS AND METHODS

Full list of used materials and devices used in this study is available in the Appendix.

8.1 OEPC USED IN THE STUDY

The exact fabrication procedure stretches beyond the scope of this monograph, and it has been described in detail in publications of our cooperation partners (13, 14), as well as in the publication of this study (221).

Depending on the model used in a given experiment (*in vitro*, *ex vivo* or in *vivo* model), three different OEPC have been developed (Figure 18):

1. **Glass OEPC**: used in cell culture, fabricated by physical vapour deposition of organic pigments, H_2PC and PTCDI, on gold or ITO-covered round glass substrates, rigid (Figure 18A). Substrate ⌀: 30 mm, thickness: 0.4 mm. p-n layer ⌀: 11 mm, thickness: 60 nm (p-layer: 30 nm, n-layer: 30 nm).
2. **Polyethylene terephthalate (PET) OEPC:** used in organotypic slice culture, fabricated by physical vapour deposition of pigments on ITO thin films, deposited on PET foil, rigid (Figure 18B). Substrate size: cut to approx. 12 x 9 mm, thickness: 0.2 mm. p-n layer size: 5 × 2 mm, thickness: 60 nm (p-layer: 30 nm, n-layer: 30 nm).
3. **Parylene OEPC:** used in rat brain implantations, fabricated by the means of photolithography and deposition of pigments on parylene-C, soft and flexible (Figure 18C, Figure 19). Metal back electrode consisted of gold layer covered with titanium. Substrate ⌀: 5 mm, thickness: 2.5 µm. p-n layer ⌀: 3 mm, thickness: 60 nm (p-layer: 30 nm, n-layer: 30 nm).

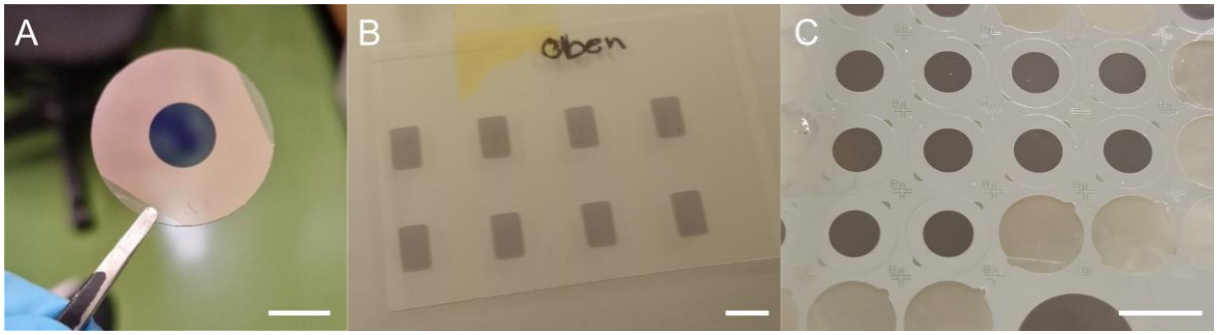

Figure 18. OEPC used in the study. *(A) Glass OEPC with a gold back electrode used in in vitro cell cultures. Scale bar: 10 mm (B) PET OEPC employed in ex vivo organotypic slice cultures. Originally, p-n layer was deposited onto an ITO-covered PET foil, which then was cut to fit into the culture tube. Scale bar: 5 mm. (C) Parylene OEPC used in in vivo study as short-term or long-term implants. Devices were prepared as a wafer, ready to remove. Scale bar: 5 mm.*

Additionally, parylene OEPC were either plain (without pores), or containing interspersed pores (⌀: 100 µm) in the substrate layer (Figure 19). Introduction of pores in the parylene-C layer aimed at enabling the flow of the cerebrospinal fluid (CSF), which would be impaired by the implant positioned on top of the brain surface. Plain OEPC were used in the acute, intraoperative stimulation, whereas OEPC with pores were employed in short- and long-term implantations.

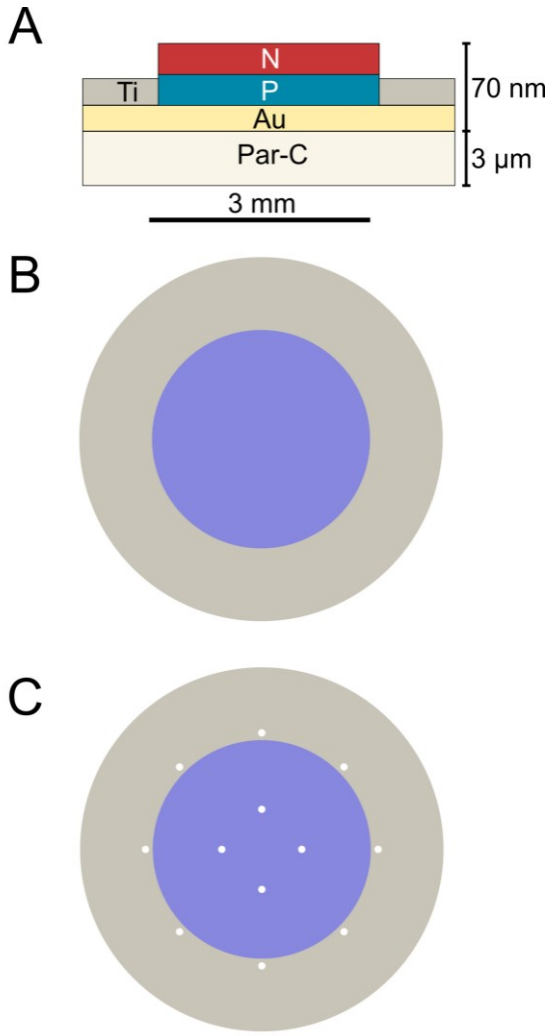

Figure 19. Schematic representation of parylene OEPC used in the in vivo study. *(A) Cross-section of the device. A protective layer of titanium covered the gold back electrode to avoid electrochemical reactions and improve the device's durability. (B) Top view of a plain OEPC, without pores in the parylene-C layer. This type of device was used in the acute stimulation. (C) Top view of an OEPC with pores, enabling CSF flow. These devices were implanted for a short and long term. Adapted and reproduced with permission from John Wiley and Sons: Advanced Healthcare Materials (221), under the terms of the Creative Commons CC BY license.*

8.2 STIMULATION *IN VITRO*

8.2.1 Primary cortical cell culture

Rat pups for primary cell cultures and organotypic tissue culture (OTC) were obtained from in-house breeding of Sprague Dawley rats housed under the conditions described in detail

in Chapter 8.3.1 Animal housing and husbandry. The day on which the animal caretakers first observed the pups in the nest was designated as their day of birth (P0).

Postnatal (P0-P1) Sprague Dawley rats were placed on ice for 2-3 minutes, until anaesthesia was reached, then euthanised by decapitation. 70% ethanol was applied onto the head skin, and the head was transferred to the laminar flow, where the dissection and tissue preparation were carried out. The skull was opened through one longitudinal cut in the midline and two transverse cuts below the ears. Both cerebral hemispheres were then carefully extracted and placed in approx. 1 mL of bench-cold sterile phosphate-buffered saline (PBS, pH 7.4). Any non-cortical brain part, such as the hippocampus or remnants of the midbrain or olfactory bulb, were removed. The remaining cortical tissue was then placed on a Teflon plate and finely dissected by a tissue chopper in 100 µm steps in two perpendicular axes. The chopped tissue was then enzymatically digested with Accutase at 37 °C for 20 minutes.

First, to select the coating material, cells were seeded on glass/ITO OEPC coated with Geltrex (0.12 to 0.18 mg/mL), poly-D-lysine (PDL; 0.1 mg/mL), polyethylenimine (PEI; 0.1%), or without any coating material. Due to the optimal outcome in cultures with PDL, from then on cells were seeded on PDL-coated surfaces. Seeding density reached 500 000 cells/sample.

Four experimental stimulations of the primary cell culture were carried out: in Experiment 1, glass/ITO OEPC were used; in Experiment 2, a light control experiment, cells were put onto glass cover slips (⌀: 30 mm); in Experiments 3 and 4, cells were seeded on top of glass/Au OEPC.

To promote cellular attachment, the seeding Dulbecco's Minimal Essential Medium (DMEM) was enriched with 10% fetal bovine serum (FBS). Additionally, non-essential amino acids (100 µM) were added to increase cell survival, and penicillin-streptomycin (100 U/mL) was added to diminish the risk of contamination. To ensure the cells would attach only to the desired parts of the OEPC, metal rings (⌀: 10 mm) were placed on top of the p-n layer in Experiments 1, 2, and 3. In Experiment 4, two glass rings (⌀: 6 mm) were situated – one in the centre of the p-n layer, and one on the back electrode, close to the border, physically separating the cell clusters from each other. Cells were seeded only inside the rings.

Three hours following the cell seeding, the rings were removed, and the cell medium was changed to the initial cortical medium (Neurobasal A, B-27 supplement 2%, GlutaMAX 0.5 mM, basic fibroblast growth factor [bFGF] 5 ng/mL, epidermal growth factor [EGF] 20 ng/mL, Normocin 100 µg/mL), sustaining the culture for further 4 days. No media change

was performed during this period. Subsequently, cells were provided with the continuation cortical medium (Neurobasal A, B-27 supplement 2%, GlutaMAX 0.5 mM, bFGF 10 ng/mL, Normocin 100 µg/mL).

To inhibit excessive glial cell proliferation, a mitosis inhibitor (final concentrations: 5-fluoro-2'-deoxyuridine [FdUrd] 100 nM, uridine 100 nM, cytosine-β-D-arabinoside [Ara-C] 10 nM) was added at day *in vitro* (DIV) 5 for 24 hours to the continuation medium. Cell medium was then completely replaced, followed by additional changes of 50% of the media three times per week. The culture was sustained for additional 10-11 days (14-15 days in total), until the full maturation of neuronal networks was reached.

8.2.2 Light stimulation

For light stimulation, 6-well plates with mature cell cultures were placed in a custom-made chamber made of polylactic acid. The chamber was 3D printed using fused deposition modelling. As a light source, the chamber was equipped with six high-power, deep-red matrix LED with a power of 10 W. LED were located approximately in the middle of each well of the well plate. The LED were mounted 8 mm below the well plate to ensure full and homogeneous illumination of the OEPC photoactive layer. The light output on the irradiated surface reached 8.21 mW/mm². To minimise temperature fluctuations in the cell culture during the stimulation, an aluminium heat sink was used as a cooling body (Figure 20).

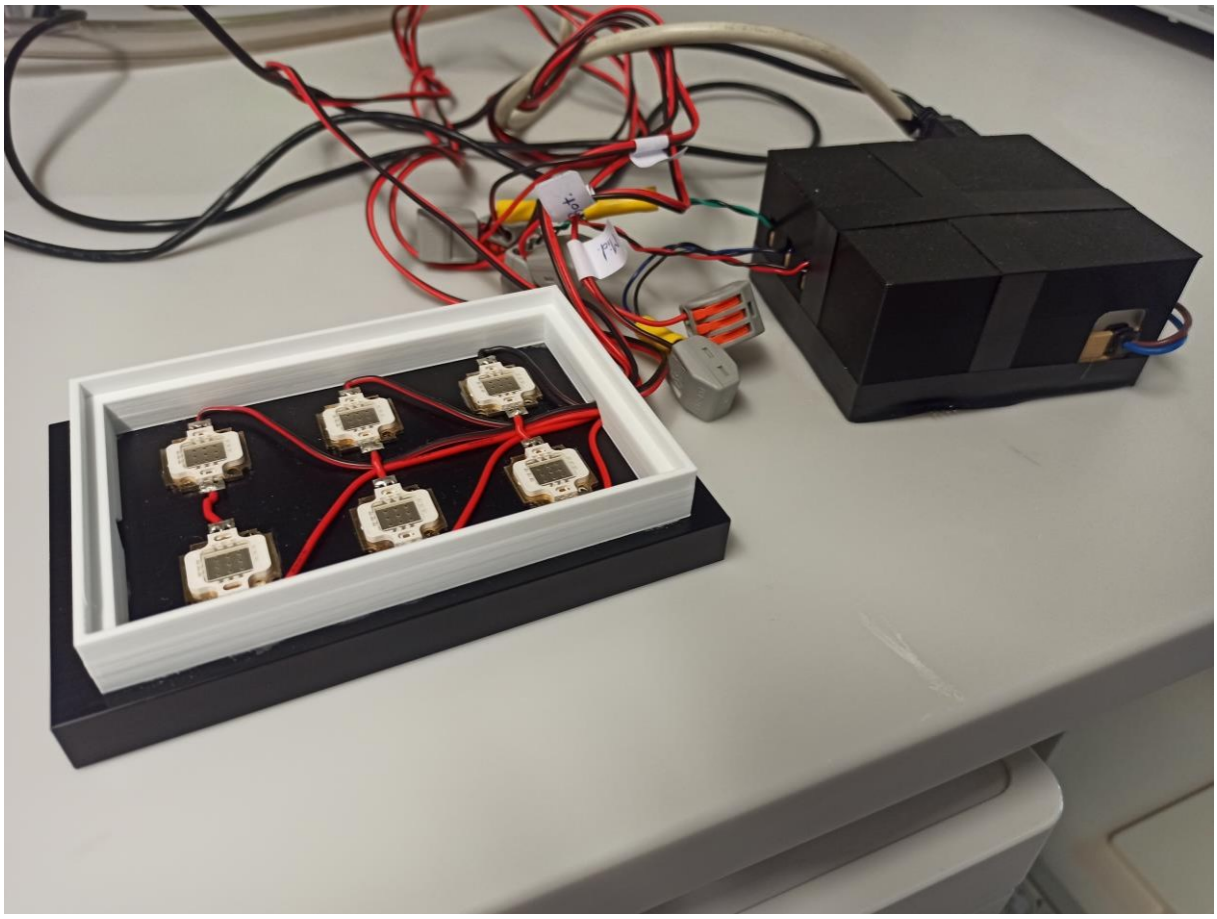

Figure 20. Stimulation setup for cell culture. *Chamber with 10 W LED (left-hand side) connected to the control unit (right-hand side).*

Control of the high power LED was achieved using pulse-width modulation of a constant current source. It ensured a flexibility of pulse width ranging from µs to ms pulses. The minimum pulse width was however limited to 10 µs, due to the internal capacity and afterglow of the LED. A second-order low-pass filter was employed to transform the high-frequency signal into an analogue signal. In order to make the stimulation protocols flexibly adaptable, an Arduino Uno board was used to directly control the constant current source.

Primary cortical cells on glass/ITO OEPC (Experiment 1) underwent a 30-minute stimulation using two distinct protocols:

1. **Low frequency** (2 Hz), with a light pulse of 5 ms, interpulse time of 495 ms, repeated for 10 cycles, followed by a 5 s darkness period.
2. **High frequency** (20 Hz), with a light pulse of 2 ms, interpulse time of 48 ms, repeated for 100 cycles, followed by a 5 s darkness period.

Following the treatment, the 6-well plates containing cells were removed from the chamber and left in the incubator for an additional period of 60 minutes before proceeding with further processing.

Primary cortical cells on glass cover slips (Experiment 2) or on glass/Au OEPC (Experiment 3 & 4) were subjected to a 30-minute stimulation using the high-frequency (20 Hz) protocol described above. Subsequently, the cells were left in the incubator for additional 60 minutes before further processing.

In all experiments, cells used as controls were also cultured on top of the OEPC to ascertain identical conditions during imaging. The plates with controls were placed in the chamber as described above, but the LED remained switched off for the whole duration of the experiment. In the experiments involving glass/ITO OEPC and glass cover slips, the addition of 20 µM L-glutamic acid ("Glutamate") to the cell culture media served as a positive control for neuronal activation. No additional procedures were conducted for the negative control. Following 30 minutes, the well-plates were removed from the chambers and left for additional 60 minutes in the incubator before further processing.

8.2.3 Cytotoxicity assay

Cytotoxic effects of the composite materials of glass/Au OEPC were evaluated using a colorimetric lactate dehydrogenase (LDH) assay. This assay provides an estimate of cytotoxicity by detecting extracellular LDH, which indicates damage to cellular membranes. The accuracy of this method in determining cell damage in primary cortical cultures has been previously demonstrated (222). Moreover, its reliance on cell culture media rather than the cells themselves enables longitudinal assessments in the same culture.

A sample of media was collected from cells cultured on the entire surface of glass/Au-OEPC (n = 6) and on PDL-coated round glass cover slips (n = 6; ⌀: 30 mm) at DIV5, DIV10 and DIV14. The collected samples were transferred in triplicates to a transparent 96-well plate. Similarly, on the day of stimulation (DIV14), samples were collected from cell culture before and after the stimulation (n = 5) or sham treatment (n = 5) as well as from the glass-cultivated cells.

The LDH assay was conducted using a commercial kit according to the manufacturer's instructions. For each measurement (DIV5, DIV10, DIV14 before stimulation and DIV14 after stimulation), one additional glass-cultivated sample was lysed by addition of a manufactuter-provided detergent to establish maximum LDH activity for LDH level normalisation. A sample of deionised water (diH_2O) was used as a blank. Absorbance was determined with

a microplate reader (SPECTROstar Omega). Relative cytotoxicity was calculated, using the formula:

$$\%Cytotoxicity = \frac{(A490-A680)treated-(A490-A680)water}{(A490-A680)maximum-(A490-A680)water},$$

where A490 indicates absorbance measured at 490 nm, and A680 – a measurement at 680 nm.

8.2.4 Immunocytochemistry

For immunocytochemistry (ICC), cells underwent a brief wash in in PBS (pH 7.4) and were subsequently fixed in 4% (v/v) formaldehyde (FA) solution in diH_2O for 15 minutes. Samples were then washed in PBS with 0.3% Triton X-100 (PBST; 3×5 min). Blocking unspecific binding sites from the primary antibody was achieved through application of a 5% (v/v) normal goat serum (NGS) in PBST for 60 minutes at room temperature. The samples were then incubated overnight at 4 °C with polyclonal rabbit c-Fos primary antibody (diluted 1:1000 in blocking solution). Negative control was prepared with omission of the primary antibody (only 5% NGS was applied). The following day, the samples were washed in PBST (3×5 min). From that moment on, all the steps were carried out in darkness, to avoid fluorophore bleaching. The secondary goat anti-rabbit antibody coupled with AlexaFluor488 diluted 1:500 in blocking solution was added for 60 minutes at room temperature. Following the final wash in PBST (3×5 min), samples were covered using aqueous anti-fading mounting media with 4′,6-diamidino-2-phenylindolev (DAPI) and 18 x 18 mm square glass cover slips, sealed with transparent nail polish.

8.2.5 Image acquisition and analysis

Confocal microscopy was used to capture images of ICC c-Fos staining. Samples were visualised with 200× magnification and 12-bit 1024×1024 size images were captured with a pixel dwell time of 0.5 µs, and an optical resolution of 470 µm. For the final image, pixel values from four scans were averaged. In Experiment 1, five separate images were acquired for each sample at the level of the p-n layer of the OEPC, with one in the middle and four at each arm of an imaginary compass rose (Figure 21A). The same pattern was used in the samples on glass cover slips in Experiment 2. In Experiment 3, three images were captured for each of the device regions: inner part of the p-n layer, outer part of the p-n layer, and back electrode (Figure 21B). In Experiment 4, three images of the culture on the p-n layer and three images of the culture on the back electrode were acquired (Figure 21C). Within each experiment, the laser intensity, gain, and offset settings were kept constant for each channel to enable quantitative analysis of c-Fos$^+$ cells.

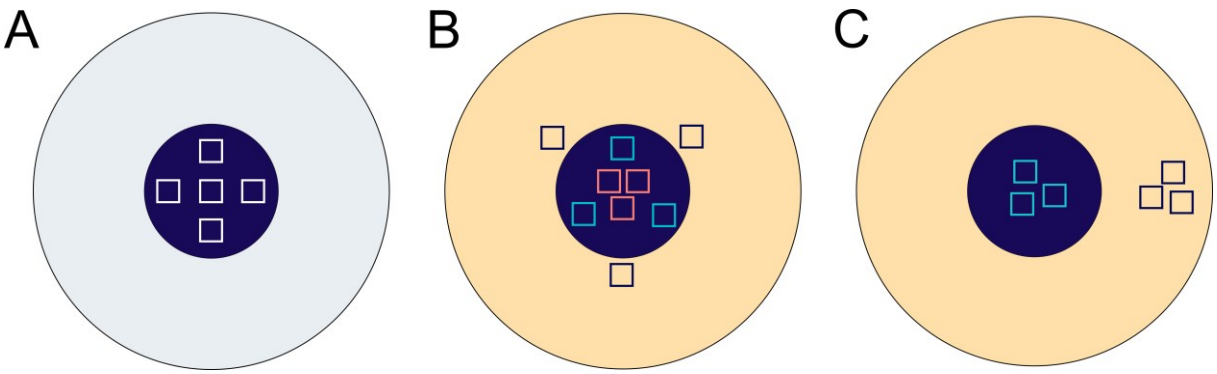

Figure 21. Sampling location for image acquisition in c-Fos staining of primary cell cultures. *(A) Experiments 1 and 2. Dark-blue circle represents the p-n layer, whereas light-silver circle depicts ITO back electrode (Experiment 1). On glass cover slips (Experiment 2), the same sampling pattern was used. (B) Experiment 3. Dark-blue circle represents the p-n layer, whereas yellow circle depicts gold back electrode. Square colour indicates location of the image acquisition: pastel red – inner part of the p-n layer; turquoise – outer part of the p-n layer; dark blue – back electrode. (C) Experiment 4. Two cell clusters were cultured on top of the p-n layer and back electrode, physically separated to avoid network signal propagation between the two groups. Square colour indicates location of the image acquisition: turquoise – p-n layer; dark blue – back electrode. Adapted and reproduced with permission from John Wiley and Sons: Advanced Healthcare Materials (221), under the terms of the Creative Commons CC BY license.*

Image analysis was performed using Fiji software (223). Images in the native microscope format (ND2) were opened with the Fiji Bio-Formats plugin (224). In Experiments 1, 3, and 4, a percentage of c-Fos positive cells was calculated. For this purpose, the blue channel image with DAPI staining was used to set the original threshold. Automatic, Fiji-innate Moments threshold successfully encompassed all cell nuclei and was therefore used in the analysis. Applying the threshold generated a black-and-white image of nuclei, and the number of nuclei was determined using the Measure Particles tool with specific parameters (particle size: 25 – 200 µm; circularity: 0.2-1.0). The nuclei were calculated and automatically added to the region of interest (ROI) manager. Saved ROI were then used during the green channel (c-Fos) image processing. In this manner, precisely the same regions as in the DAPI image were quantified. The final percentage of c-Fos$^+$ cells was calculated as the proportion of nuclei calculated in the green channel relative to those in the blue channel. Values from all images in a given area were averaged to serve as a single data point in the statistical analysis.

In Experiment 2, mean grey value of the whole green channel image was calculated. The grey value threshold was set using the automatic Fiji-innate method (Moments; threshold mean:

198.84; threshold standard deviation: 75.95). The mean grey values from all images in a given region were averaged to a single data point for the statistical analysis.

8.3 STIMULATION *EX VIVO*

8.3.1 Organotypic slice culture

OTC of hippocampal slices were prepared according to the rolling tube method (225). Hippocampi were acquired from postnatal (P3-P5) Sprague Dawley rat pups. Cryo-anaesthesia and subsequent euthanasia were carried out as described in Chapter 8.2.1 Primary cortical cell culture. Following the skull opening and brain extraction, both hemispheres were put into approx. 1 mL ice-cold preparation medium, containing 2% (m/v) glucose in Basal Medium Eagle (BME). Hippocampus was then carefully prepared and put on a Teflon plate. The tissue was then sliced by the tissue chopper at 350 µm steps and subsequently transferred to 15 mm Petri dishes containing 2 mL of ice-cold preparation medium. Hippocampal slices were dissociated by gently shaking the dish.

To fix the tissue slices in place, a plasma-thrombin clot was prepared. A 10 µL drop of chicken plasma was placed either on top of the p-n layer of PET OEPC. A 10 µL drop of bovine thrombin was put in the close vicinity to the plasma. One hippocampal slice was transferred with a spatula into the plasma drop with a subsequent careful mixing of plasma with thrombin. The slices were then left on the bench for 10-15 minutes, protected from desiccation.

The OEPC and cover slips were then positioned on the bottom of culture tubes with addition of OTC medium (BME, Hank's Balanced Salt Solution 25% (v/v), horse serum 25% (v/v), GlutaMAX 1 mM, glucose 0.2%) and placed in the rolling tube incubator (Figure 22).

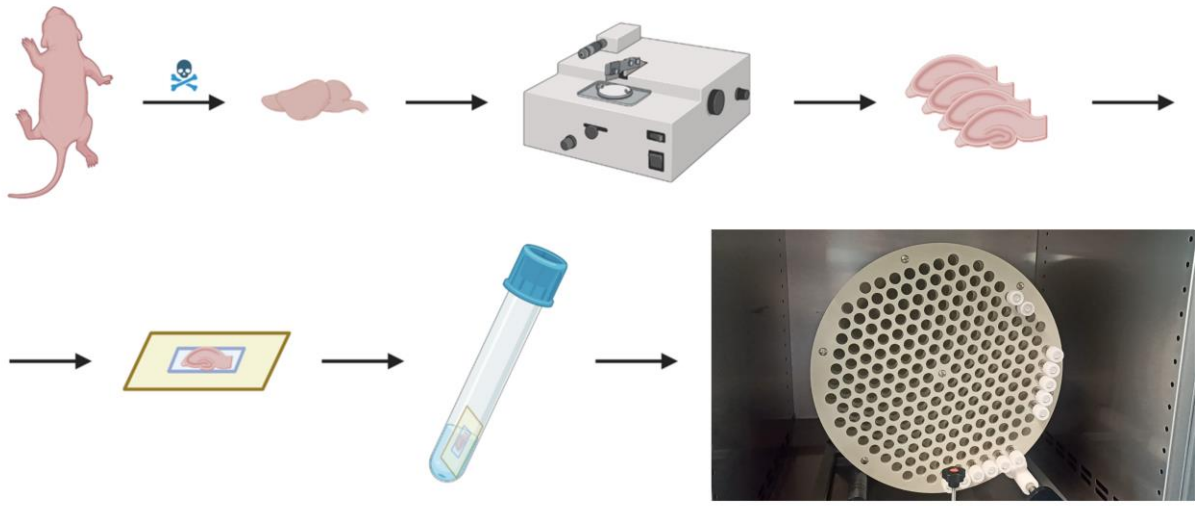

Figure 22. Schematic representation of hippocampal OTC preparation. *Rat pups were sacrificed, their brain was removed, sliced with tissue chopper, dissociated and put onto OEPC or glass cover slip. After fixation with plasma-thrombin, samples were transferred to culture tubes and placed in the rolling tube incubator. Created with BioRender.com*

Culture was sustained in 37 °C at 12 rotations/h with the roller set at 5° inclination. These settings allow for even distribution between medium and air exposure, both necessary for a successful OTC. At DIV2, 10 µL of mitosis inhibitor (as described in Chapter 8.2.1 Primary cortical cell culture) was added for 24 hours. Media were fully changed twice a week.

8.3.2 Light stimulation

For light stimulation, culture tubes with samples were placed in custom-made 3D printed holders made of black polylactic acid (Figure 23). Chambers containing 3 W LED located centrally were situated approx. 15 mm underneath the bottom of the tube. The light output on the irradiated part of the tube was approx. 3.2 mW/mm^2. Tubes were separated with thin PLA walls to avoid cross-contamination with light.

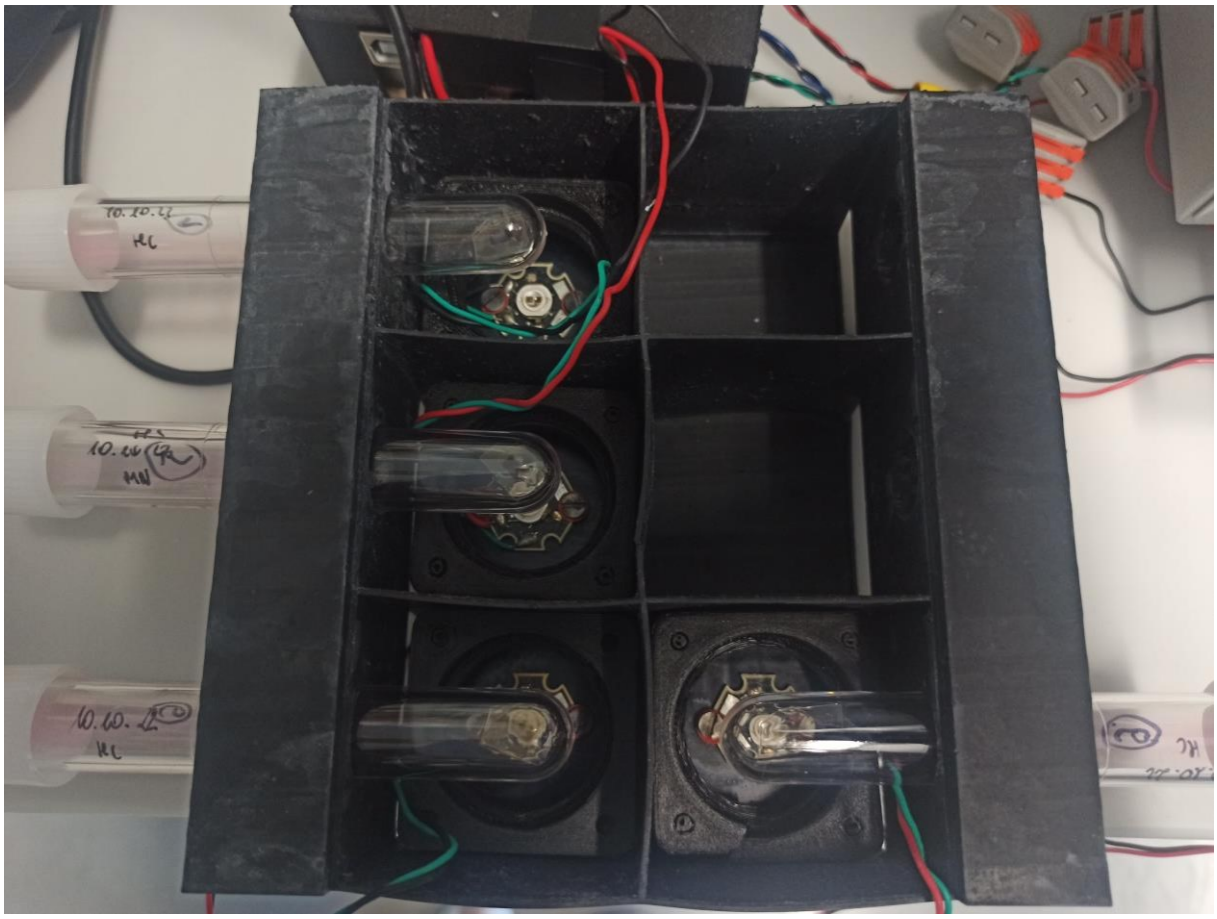

Figure 23. Placement of culture tubes with OTC hippocampal slices in preparation for light stimulation.

For a single stimulation, DIV7 samples were illuminated with light pulses of 5 ms at 2 Hz, with interpulse time of 495 ms, repeated for 10 cycles, and followed by a 5 s darkness period. Those light pulse trains interspersed with dark periods were repeated for 30 minutes. Control slices were kept in darkness for 30 minutes. Slices were subsequently handed back to the rolling incubator and kept for 30 minutes before further processing.

For repetitive stimulation, DIV6 samples were illuminated once daily for 60 minutes with the protocol described above. Control slices were kept in darkness for 60 minutes. The treatment was repeated during seven consecutive days. Following the last stimulation session, samples were put back to the incubator for 30 minutes before further processing.

8.3.3 Tissue processing, immunohistochemistry, and image acquisition

For tissue fixation, OTC hippocampal slices were placed in 4% FA for 60 minutes at room temperature. Samples were automatically dehydrated with a tissue processor, and embedded

in paraffin. Slices on OEPC were then cut into serial 7 µm sections using a rotary microtome and mounted on object slides. After desiccation on a warm plate, samples were stored in room temperature until further processing.

Sections were deparaffinised in xylene (4×5 min) and rehydrated a graded series of ethanol (100% 1×5 min, 96% 1×5 min, 70% 1×5 min, 50% 1×5 min). The slices were then washed in distilled water (3×5 min). For heat-induced epitope retrieval (HIER), slices were placed in 0.1 M sodium citrate buffer (pH 6.0) for 20 minutes at 93 °C in a microwave. The samples were again washed with PBS blocked with a commercial blocking solution for 10 minutes.

Primary and secondary antibodies used in OTC immunohistochemistry (IHC) are listed in Table 1.

Table 1. List of antigens, applications and dilutions of antibodies used in *ex vivo* experiments.

Antibody	Host	Dilution	Company	Catalog #	# RRID
c-Fos	rabbit	1:1000	Abcam	ab190289	AB_2737414
NeuN [A60]	mouse	1:500	Millipore	MAB377	AB_2298772
GAP-43	rabbit	1:1000	Atlas Antibodies	HPA013392	AB_1849468
Alexa Fluor™ 546 conjugated anti-rabbit IgG	goat	1:200	Thermo Fisher Scientific	A-11010	AB_2534077
Alexa Fluor™ 633 conjugated anti-mouse IgG	goat	1:200	Thermo Fisher Scientific	A-21050	AB_2535718

Primary antibodies were diluted in a commercial antibody diluent and incubated on the sections for 30 minutes at room temperature.

For negative controls, rabbit (15 mg/mL) and mouse (0.1 mg/mL) immunoglobulin fractions were diluted to match the antibody concentration.

The samples were then washed with PBS and incubated with the appropriate secondary antibodies for 30 minutes at room temperature (Table 1). 1:2000 DAPI solution was used as a counterstaining. Finally, the slices were covered using anti-fading mounting media.

To acquire images, a fluorescent slide scanner was used. Images were obtained under 200× magnification under constant settings for each channel.

8.4 STIMULATION *IN VIVO*

8.4.1 Animal housing and husbandry

Adult male Sprague Dawley rats (10-14 weeks old; n = 43) were purchased from Charles River Laboratories in Sulzfeld, Germany, and allowed a minimum acclimatisation period of one week. The animals were housed in the animal facility of the Biomedical Research Institute at the Medical University of Graz, maintaining a constant room temperature of 21±1 °C, relative humidity at 50±5%, and a 12-hour light/dark cycle. Standard polycarbonate cages type III, accommodating two rats per cage, were enriched with red polycarbonate rat fun tunnels and chew wooden blocks. Rats had access to a standard rodent diet and tap water *ad libitum*.

To ensure animal well-being, qualified personnel monitored the health status of the rats at least once a day. If an animal reached any of the humane endpoints (severe neurological impairments, seizures, or wound infection not responsive to the standard medication or surgical therapy), the caretaker was obligated to promptly report it to the person in charge of the experiment. All animal experiments were conducted with the approval of the local authorities (Bundesministerium für Wissenschaft und Forschung; licence number: 2021-0.724.203). Special attention was given to minimising potential animal suffering throughout the study.

In the experimental design, rats were randomly designated to one of the three groups (Table 2): animals implanted with parylene OEPC and subjected to light stimulation (“Stimulation”; n = 18), animals implanted with parylene OEPC without light stimulation (“Sham”, n = 15) and animals undergoing the surgery and light stimulation, without parylene OEPC implantation (“Light control”; n = 8). Acute light or sham treatment was applied to n = 5 immediately after the surgery. A delayed treatment 24 hours post-implantation was implemented in n = 11 rats, with n = 6 animals having the dura mater removed and n = 5 with the dura left intact. N = 7 animals were treated 48 hours and n = 18

three weeks following the implantation. Regrettably, two control animals died due to an idiopathic cardiovascular arrest during anaesthesia.

Table 2. Experimental design and animal numbers for *in vivo* OEPC implantation and stimulation. Adapted and reproduced with permission from John Wiley and Sons: Advanced Healthcare Materials (221), under the terms of the Creative Commons CC BY license.

Experiment -No.	Animal age (weeks)	Dura removal	Latency to stimulation	Stimulation (n)	Sham (n)	Light control (n)	Sum
1	12	+	none	3	2	0	5
2	12	-	24 h	3	2	0	5
3	14	+	24 h	3	3	0	6
4	11	+	48 h	3	3	1	7
5	10	+	3 weeks	6	5	7	18
			Sum	18	15	8	41
Durectomy control = 2						**Total**	43

Additionally, two adult male rats, previously used in breeding, underwent sham craniectomy without parylene OEPC implantation – one with dura mater removal (n = 1) and the other without durectomy (n = 1). Thus, the total number of animals involved in the experiment amounted to n = 43.

One control animal subdued a trauma during the surgery, which resulted in extensive tissue loss following the next three weeks and had to be excluded from the experiment.

8.4.2 Surgical procedure

Anaesthesia was induced with 4% isoflurane using rat-size anaesthesia box. When animals were fully anaesthetised, a mixture (FMD) of fentanyl (0.04 mg/kg), midazolam (0.8 mg/kg), and medetomidine (0.4 mg/kg) was administered intraperitoneally. Depth of anaesthesia was monitored by evaluation of deep pain perception through pinching the periosteum of a toe. This procedure was consistent for evaluating anaesthesia during light or sham treatment (Chapter 8.4.4 Light stimulation), as well as before the euthanasia and transcardial perfusion (Chapter 8.4.5 Euthanasia and tissue processing).

Animals were securely positioned on a stereotactic frame using ear bars and bite plate. Temperature stability was assured using a heat blanket equipped with a rectal thermometer. Additionally, a cling film covering the entire rat body, except for the head, was applied in order

to minimise body heat loss and prevent contamination from fur and skin. Scalp hair was removed with an electric trimmer, and the skin was disinfected using alcohol pads and povidone-iodine solution. To avoid cornea desiccation, eye drops were applied. Furthermore, eyes were protected from light and contamination with aluminium foil.

A longitudinal incision (1.5-2 cm) into the skin in the midline and the subsequent periosteum removal revealed the skull bone. A craniectomy (⌀: 5 mm) was drilled on the right convexity, with the lateral edge adjacent to the right lateral ridge and the anterior edge located approximately 2 mm caudally to the bregma (Figure 24A). The bone flap was removed, followed by careful dura removal performed in 3-5 steps. To avoid possible brain trauma, it was critical not to touch the exposed surface of the brain. In one experiment (n = 5 animals), dura was left intact.

Two additional holes (⌀: 0.5 mm) were drilled – one over the left parietal cortex (approx. -3.50 relative to the bregma) and another rostrally over the right parietal cortex (approx. 1.50 relative to the bregma) – to place metal anchor screws. The screws were tightened by 2-2.5 turns.

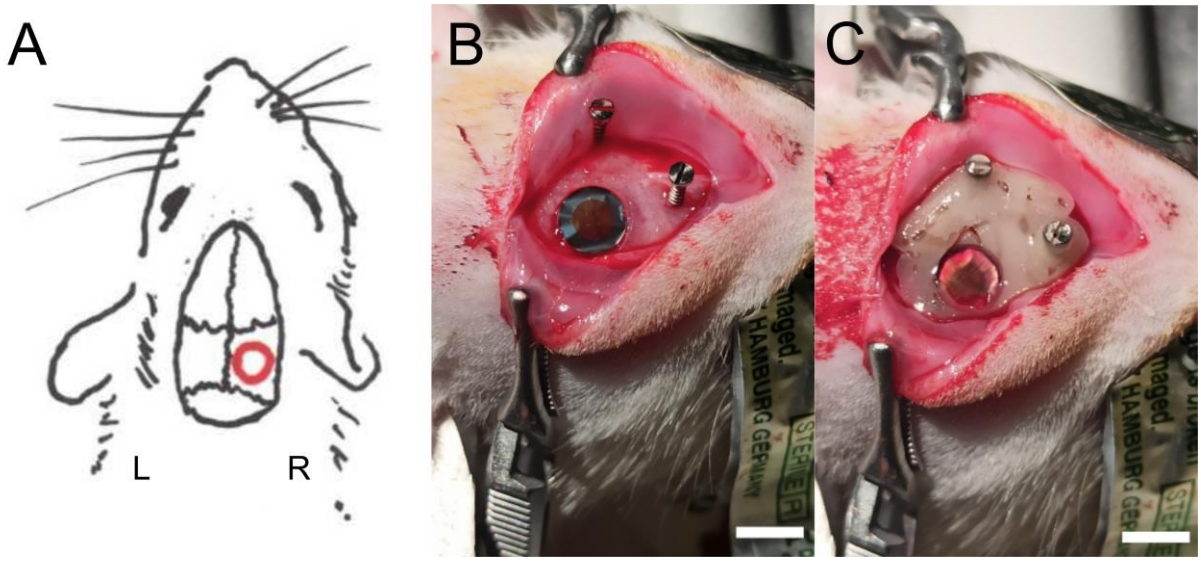

Figure 24. Surgical procedure of OEPC implantation. *(A) Schematic of craniectomy on the right parietal bone. (B) Intraoperative view of OEPC placed on top of exposed right somatosensory cortex. Two anchor screws are placed to fix the dental cement. (C) Intraoperative view of OEPC closed with a cranial window made of transparent resin and embedded in dental cement. Scale bar: 5 mm. Adapted and reproduced with permission from John Wiley and Sons: Advanced Healthcare Materials (221), under the terms of the Creative Commons CC BY license.*

For parylene OEPC implantation, a drop of diH_2O was placed on top of a single device, and it was carefully removed from the wafer with a fine brush. Water facilitated the removal thanks

to the hydrophilicity of the device's back side. The exposed cortex was pre-washed with physiological saline solution, and the device was placed on top of it, with the photoactive layer facing downward (Figure 24B). The remaining saline was carefully removed with a sterile cotton swab. In the light control group, the implantation step was omitted. The craniectomy was sealed with a custom 3D-printed round implant made of medical-grade transparent resin (⌀: 5 mm; thickness: 1 mm). Dental cement was used to fix the implant with the anchor screws. The transparent window above the photoactive layer was left uncovered for future light stimulation (Figure 24C).

The skin was sutured with absorbable material using 4-5 horizontal mattress sutures or simple interrupted sutures. The animals received subcutaneous injections of enrofloxacin (7.5 mg/kg) to prevent post-surgical infection and carprofen (2 mg/kg; diluted 2% v/v in physiological saline solution) for pain control. Finally, anaesthesia was reversed with subcutaneous administration of a mixture of flumazenil (0.105 mg/kg) and atipamezole (0.63 mg/kg). The whole procedure took 45-60 minutes in one animal. No more than 8 animals underwent surgery on one day. The post-surgical recovery was uneventful in all cases.

8.4.3 Post-surgical animal welfare

As a means of post-operative medication, the animals received subcutaneous injections of enrofloxacin and carprofen as described in Chapter 8.4.2 Surgical procedure. The injections were administered once daily for two days in animals stimulated 48 hours after surgery and for four days in the group receiving light treatment three weeks later.

To assess the animals' well-being post-surgery, two parameters were analysed: body mass and nest building behaviour. Rodents display a natural drive to build a shelter, which can be affected by stress and pain (226), resulting in lower nest quality. Similarly, post-surgical discomfort can lead to lowered appetite, which can be reflected in decrease in animal weight.

To monitor the body mass, animals were weighed on the day of surgery, 3 days post-surgery, and on the day of stimulation and sacrifice. Nest scores were evaluated on day 4, 10 and 17 post-surgery through the analysis of images taken from the top and side of each cage (Figure 25). For the nest building control, two cages with two naive age-matched male rats each were evaluated. Animal identifiers were then concealed and nest building quality was quantified on a scale from 0 to 4, following the methodology described in Schwabe et al. (226):

- 0: the nest material left almost untouched.
- 1: the nest material touched and distributed over more than half of the cage area; no visible nesting area

- 2: clearly visible nesting area, smaller than half of the cage area, flat, edges may not be smooth
- 3: clearly delineated nest with visible indentation, smaller than ¼ of the cage height
- 4: clearly delineated nest with prominent indentation, taller than ¼ of the cage height

Figure 24 shows nests graded with 2, 3, and 4. No nests with 0 or 1 grade were observed during this study.

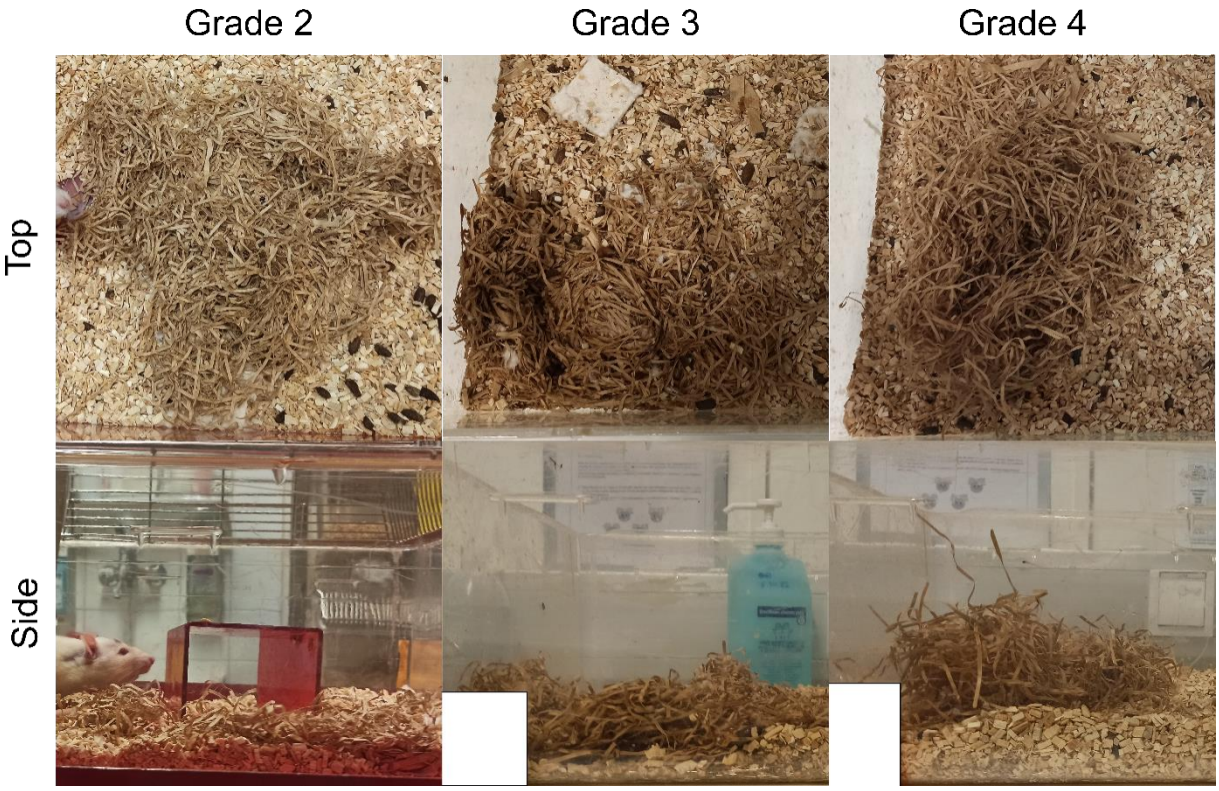

Figure 25. Nest building assessment.*Exemplary photographs of nests graded as 2, 3, and 4. Nest assessment is performed based on a view from the top (upper row) and from the side (lower row).*

8.4.4 Light stimulation

Depending on the experimental group, the animals underwent:

- acute stimulation: immediately after the OEPC implantation, before wound suturing,
- 24 hours after implantation,
- 48 hours after implantation, or
- three weeks after implantation.

Acute stimulation did not require additional anaesthesia steps. For all other trials, anaesthesia was induced with 4% isoflurane and maintained with an FMD mixture as described in Chapter 8.4.2 Surgical procedure. Once full anaesthesia was reached,

the animals were placed in the stereotactic frame, the wound was re-opened, and a 700mW 638nm diode laser was positioned approx. 10 mm above the implant. The laser light was focused so that it completely covered the visible p-n layer of the OEPC, or above the centre of the transparent resin window in the light control group. Light stimulation (20 Hz: 2 ms light pulse, 48 ms interpulse length) was continuously repeated for 30 minutes. The sham animals were left in darkness for the same duration. The experimenter assessed the animal well-being 2-3 times during the treatment. Following the light or sham treatment, the wound was re-sutured, and the anaesthesia was reversed as described in Chapter 8.4.2 Surgical procedure. The animals left undisturbed in the home cage for 60 minutes.

8.4.5 Euthanasia and tissue processing

The animals were anaesthetised with 4% isoflurane, and received an intraperitoneal injection of thiopental (200 mg/kg). Following the respiratory arrest, the thorax was opened, and the animal subjected to transcardial perfusion with 4% FA in PBS (pH 7.4) for 15-20 minutes. Once the tissue was satisfactorily fixated (assessed based on muscle rigidity and liver colour), the head was cut off, and the skull was opened. The brain was carefully removed and immersed in 4% FA for 24 hours at 4 °C for further fixation.

Brain samples immersed in 4% FA underwent different processing methods based on the time of stimulation: cryomicrotome processing for samples obtained after acute stimulation and 24 hours post-surgery, or dehydration in an alcohol gradient using a tissue processor for samples from animals stimulated 48 hours or three weeks post-surgery.

Cryosectioning

Following 24 h immersion in 4% FA, brain samples were transferred to 30% (w/v) sucrose solution for cryoprotection. Samples were considered saturated with sucrose, when the brain – initially swimming on top of the solution – was fully sunk to the bottom of the recipient.

Then, the samples were removed from the sucrose, quick-frozen with a cryo-spray, embedded in an OCT medium and left at -20 °C until fully frozen. Brain were sectioned at 20 µm in five series, spanning from bregma approx. 0.00 to approx. -5.50, encompassing regions rostral to the implant and those lying underneath the OEPC. After overnight drying step at room temperature, sections were stored at -20 °C until further processing.

Paraffin embedding and sectioning

An automated dehydration step (formalin 6% 2×1 h, ethanol 70% 1×1 h, 80% 1×1 h, 96% 2×1 h, 100% 2×1 h, tissue clear 2×1 h, paraffin 2×1 h and 2×2 h) was followed

by paraffin embedding with a paraffin dispenser. From each brain, fifteen series of 2 μm sections were acquired from five regions regions: a) bregma +1.92 to 0.48, b) bregma 0.00 to -1.28, c) bregma -2.56 to -3.36, d) bregma -4.08 to -4.72 and e) bregma -4.92 to -5.68, corresponding to: a) and b) brain parts rostral to the implant, not exposed to the stimulation, encompassing mostly the motor cortex; c)-e) brain parts under various parts of the implant, exposed to the stimulation, encompassing mostly SOM. Object slides holding 2-3 brain paraffin-embedded sections were left on a heating plate for 60 min to ensure tissue adherence to the glass, and then stored at room temperature until further processing.

8.4.6 Histological staining

One series of paraffin-embedded brain sections from all animals was dedicated for Nissl staining, to allow the orientation in the brain regions during quantification of c-Fos IHC. For this purpose, 0.005M thionin solution was prepared and kept at 60 °C. Sections were first deparaffinised and rehydrated through treatment with xylene (2×3 min) and decreasing ethanol gradient (100% 1×3 min, 90% 1×3 min, 70% 1×3 min, and 50% 1×3 min). They were subsequently washed with distilled water (1×3 min), and immersed in thionin solution at room temperature for 20 seconds. The increasing gradient of ethanol (50% 1×3 min, 70% 1×3 min, 90% 1×3 min and 100% 1×3 min) with subsequent immersion in xylene (2×3 min) served tissue rehydration. Object slides were cover slipped using xylene-based mounting media.

8.4.7 Immunohistochemistry

Full list of antibodies and their dilutions used in brain slice IHC can be found in Table 3. In all cases, negative control was prepared by addition of 5% NGS in PBST without primary antibody.

Table 3. List of antigens, applications and dilutions of antibodies used in *in vivo* experiments. Adapted and reproduced with permission from John Wiley and Sons: Advanced Healthcare Materials (221), under the terms of the Creative Commons CC BY license.

Antibody	Host	Application	Dilution	Company	Catalog #	# RRID
c-Fos [EPR24046-20]	rabbit	DAB IHC IF IHC	1:100	Abcam	ab289723	-
GFAP [GA5]	mouse	DAB IHC IF IHC	1:500	Thermo Fisher Scientific	14-9892-82	AB_10598206

Iba1	rabbit	DAB IHC	1:2000	FUJIFILM Wako Shibayagi	019-19741	AB_839504
CD45	mouse	DAB IHC	1:50	BD Biosciences	554875	AB_395568
CD68 [ED1]	mouse	DAB IHC	1:50	Origene	BM4000S	AB_1613055
NeuN [A60]	mouse	IF IHC	1:500	Millipore	MAB377	AB_2298772
Calretinin [6A9]	mouse	IF IHC	1:1000	Abcam	ab277631	-
Parvalbumin	chicken	IF IHC	1:1000	Thermo Fisher Scientific	PA5-143579	AB_2942808
Somatostatin [SOM018]	mouse	IF IHC	1:100	GeneTex	GTX71935	AB_383280
Biotinylated anti-rabbit IgG	goat	DAB IHC	1:200-1:400	Vector	BA-1000	AB_2313606
Biotinylated anti-mouse IgG	horse	DAB IHC	1:50-1:200	Vector	BA-2001	AB_2336180
Alexa Fluor™ 488 conjugated anti-rabbit IgG	goat	IF IHC IF ICC	1:500	Thermo Fisher Scientific	A-11008	AB_143165
Alexa Fluor™ 568 conjugated anti-mouse IgG	goat	IF IHC	1:500	Thermo Fisher Scientific	A-11004	AB_2534072
Alexa Fluor™ 647 conjugated anti-chicken IgY	goat	IF IHC	1:500	Thermo Fisher Scientific	A-21449	AB_2535866

Cryosections

In cryosections, immunofluorescent (IF) staining of c-Fos was conducted. In the initial step, an ice-cold methanol was applied for 10 minutes, serving further fixation of the samples. Brain sections were then subjected to a wash in diH2O (3×3 min). Next, 10 mM sodium citrate

buffer (pH 6.0) was boiled in the microwave and the samples were soaked for 3 minutes on the bench for antigen retrieval. After another wash in diH2O (3×3 min), samples were encircled with a hydrophobic PAP pen and placed in a humidity chamber filled with tissue paper soaked in distilled water. 5% NGS in PBST blocking solution was applied for 30 minutes at room temperature, then exchanged to c-Fos primary antibody and left in the humidity chambers overnight at 4 °C.

The following day, the samples were washed in PBST (3×5 min). From this point onward, all steps were performed in darkness to prevent fluorophore bleaching. Secondary antibody was applied for 60 minutes at room temperature, followed by wash with PBST (3×5 min). Object slides were cover slipped using aqueous anti-fading mounting medium with DAPI. Glass cover slips were additionally sealed with nail polish.

Paraffin-embedded sections

In samples collected following three-week-implantation and stimulation, IHC served quantitative analysis of c-Fos expression and qualitative investigation of glial and immune cell markers. One entire section from all animals was stained for c-Fos. Four series were used to mark astrocytes (Glial fibrillary acidic protein, GFAP), microglia (ionised calcium-binding adapter molecule 1, Iba1), leukocytes (cluster of differentiation 45, CD45), and monocytes and macrophages (cluster of differentiation 68, CD68) in the assessment of FBR. For this purpose, IHC was conducted on sections in the vicinity of the implant, involving n = 6 animals after the OEPC implantation and n = 3 animals subjected to surgery without the implant.

Sections underwent deparaffinisation and rehydration steps, involving xylene (2×10 min), a 1:1 mixture of xylene and 100% ethanol (1×10 min), and ethanol gradient (100% 1×5 min, 90% 1×5 min, 70% 1×5 min and 50% 1×5 min). After the 100% ethanol step, the tissue was immersed in a 0.67% H_2O_2 solution in methanol for 30 min to quench endogenous peroxidase activity. The alcohol gradient was continued from 90% ethanol downwards. Samples were then washed in distilled water (2×5 min), and placed in a decloaking chamber, soaked in sodium citrate buffer (10 mM, pH 6.0). HIER was performed at 95 °C for 20 minutes under constant pressure.

The sections were then washed in PBST (2×5 min), encircled with a hydrophobic PAP pen (Merck), and placed in a humidity chamber filled with tissue paper soaked in distilled water. Depending on the secondary antibody host, blocking solution containing 5% NGS or 5% horse serum in PBST was added for 60 minutes at room temperature. It was then removed and replaced with a primary antibody diluted in the blocking solution. After an overnight

incubation at 4 °C, samples were again washed in PBST (3×5 min), and a secondary antibody in blocking solution was applied for 1 hour at room temperature. After a PBST wash (3×5 min), avidin-biotin complex (ABC) kit was added to amplify the signal, and incubated for 30 minutes at room temperature. Following a wash in PBST (3×5 min), a chromogen (3,3'-diaminobenzidine, DAB) solution was applied onto each slide for 1-3 min for colour development. The sections were then washed in distilled water (2×5 min), and briefly (1-2 s) immersed in haematoxylin solution acting as a counterstaining for nuclei. For the next 5 minutes they were washed with running tap water, to change soluble red haematoxylin into its insoluble blue dye. The sections were then dehydrated in an increasing gradient of ethanol (50% 1×5 min, 70% 1×5 min, 90% 1×5 min, 100% 1×5 min), a 1:1 mixture of xylene and 100% ethanol (1×5 min), and xylene (2×5 min). Finally, they were cover-slipped with xylene-based mounting media.

To characterise cells expressing c-Fos, double and triple IF were performed. c-Fos was coupled with markers of astrocytes (GFAP), differentiated neurons (NeuN), and three interneuron marker: calretinin (CR), PV, and SST. Staining protocols did not differ from the ones described for c-Fos, except for application of two primary and secondary antibodies mixed in one vial. From the preparation of the secondary antibodies on, all steps were performed in darkness. Following the incubation with the secondary antibodies, the sections were washed in PBST (3×5 min). Object slides were then cover-slipped using aqueous anti-fading mounting media with DAPI, and sealed with nail polish.

8.4.8 Image acquisition and analysis

DAB-stained sections were imaged using a bright-field slide scanner. Scans were acquired with 200× (c-Fos) and 400× (glial and immune cell markers) magnifications. One haematoxylin-eosin staining of human spleen was used to set the camera contrast and gain settings as well as white balance for all experiments.

c-Fos expression was quantified with QuPath software (v0.4.3). For this purpose, SOM, EC, and HC (both dorsal and, if available, ventral parts) were marked in each brain section, in both ipsilateral (relative to the surgery), and contralateral hemispheres. Positive cells were counted automatically, with the threshold value of mean optical density within the nucleus of 0.2 in the DAB channel (Figure 26). The total cell number was quantified in the haematoxylin channel, with the optical density threshold value of 0.05. Percentage of positive cells was calculated for each region of interest. Values from all sections on one object slide were averaged and served as one data point. Due to high spontaneous activity in slices rostral to the implant, these slides were not included in the analysis.

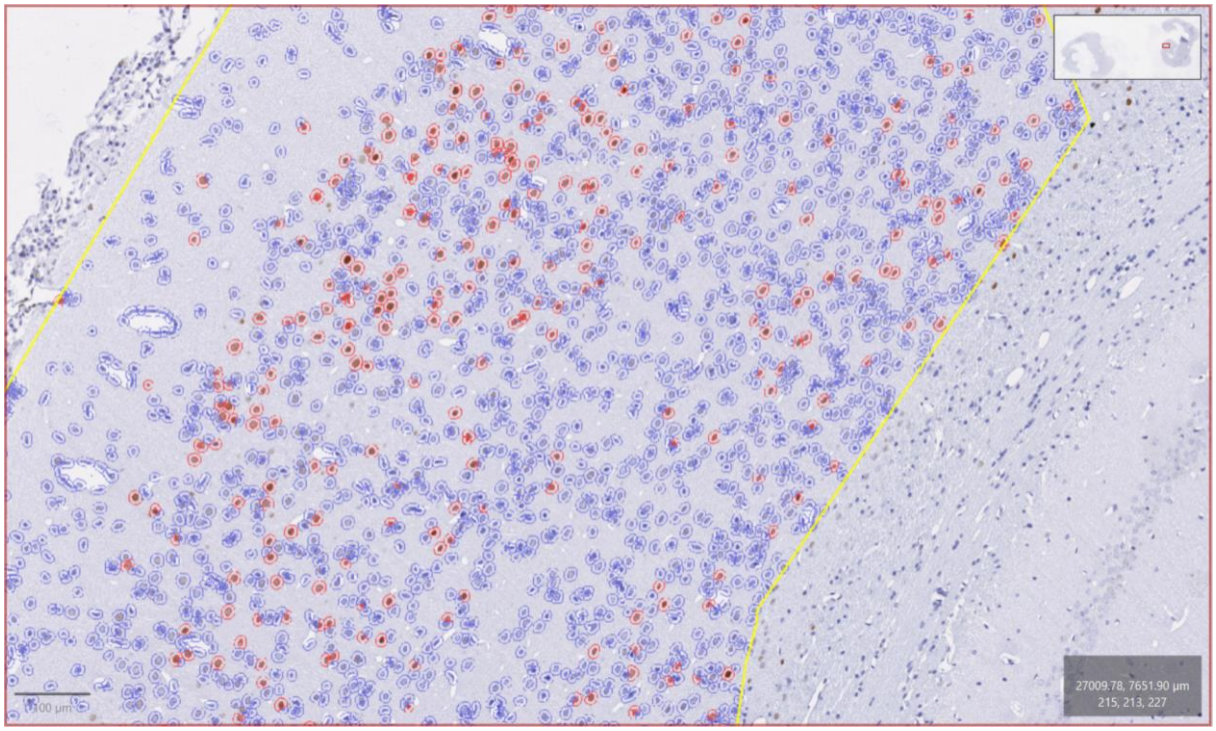

Figure 26. An example of c-Fos quantification in SOM of a stimulated animal. *Cells marked with red are considered positive, while blue lines encircle all cells with automatically recognised nuclei. Analysis is possible only within the region marked with the yellow lines. Scale bar: 100 µm*

Double and triple IF of c-Fos with various cellular markers were inspected in three randomly selected animals from each group, resulting in a total sample size of n = 9 (paraffin-embedded slices) or in all available samples (cryo-embedded slices). Sections located beneath the implanted device or the craniectomy site were specifically chosen for the analysis. For each, one image of the ipsilateral and contralateral SOM and HC was captured using a confocal microscope (parameters: as described in Chapter 8.2.4 Image acquisition and analysis). These images were subsequently visually evaluated for the co-expression of the respective markers. Laser intensity, gain, and offset settings were kept constant for each channel.

8.5 Structural and functional analysis of explanted OEPC

After a three-week period of implantation, the animals underwent light stimulation and were subsequently sacrificed according to the procedure described in Chapter 8.4.4 Light stimulation. Upon skull opening, all parylene OEPC were carefully removed (Figure 27). Following explantation, a total of n = 11 samples remained intact and available for further characterisation.

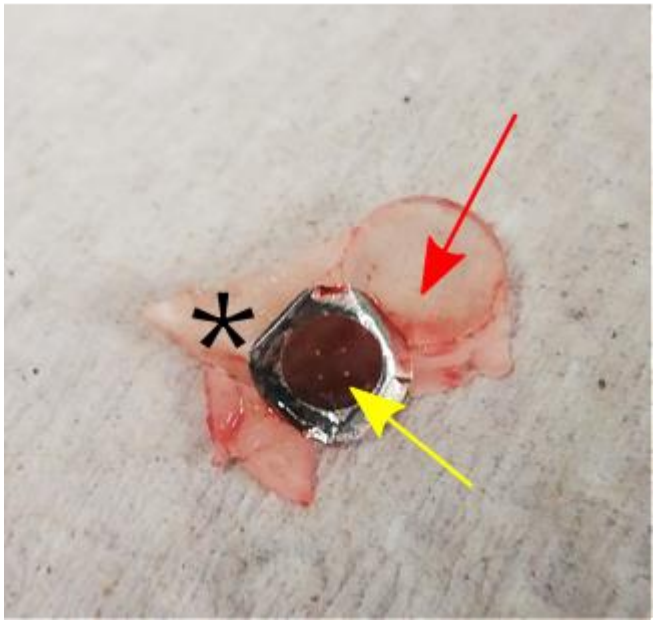

Figure 27. Parylene OEPC after three weeks of implantation. *Yellow arrow indicates an intact OEPC, used later in a functional analysis. Red arrow shows an intact transparent resin window. Asterisk marks remnants of dental cement. Adapted and reproduced with permission from John Wiley and Sons: Advanced Healthcare Materials (221), under the terms of the Creative Commons CC BY license.*

8.5.1 Scanning electron microscopy

Two explanted samples were designated for scanning electron microscopy (SEM) imaging. Additionally, two more devices, freshly removed from the wafer served as non-implanted controls.

For the fixation step, a mixture of 2 % paraformaldehyde and 2.5 % glutaraldehyde in 0.1 M cacodylate buffer (CB; pH 7.4) was applied for 60 minutes. The samples were then transferred to cacodylate buffer for 30 minutes (CB; 0.1 M, pH 7.4). N = 2 explanted devices and n = 1 control devices were designated for osmium staining. For this purpose, CB was removed, and OsO_4 solution (2 % OsO_4 in 0.1 M CB) was applied for 30-minute in darkness. OsO_4 solution was subsequently exchanged for CB. The control sample not designated for osmium staining remained in CB.

The samples were subjected to dehydration in an increasing ethanol gradient (30% 1×15 min, 50% 1×15 min, 70% overnight, 80% 1×15 min, 90% 1×15 min, 96% 1×15 min, and 100% 2×7 min). They were then dried in a 1:1 mixture of 100% ethanol and hexamethyldisilazane (HDMS; 1×5 min), followed by the exchange for pure HDMS (1×5 min). After drying, samples were placed in a desiccator overnight, followed by sputter-coating with carbon to render them conductive. Electron microscope images were acquired under a 30 000× magnification, using ImageSP software.

8.5.2 Transient voltage measurement

Transient voltage evoked by pulsed LED illumination of explanted parylene OEPC served the validation of their functionality. The measurement was performed with devices soaked in PBS (pH 7.4), with one Ag/AgCl electrode put close to the centre of the p-n layer, and the other electrode placed directly in the solution (Figure 28). The voltage was measured between the two electrodes by an oscilloscope.

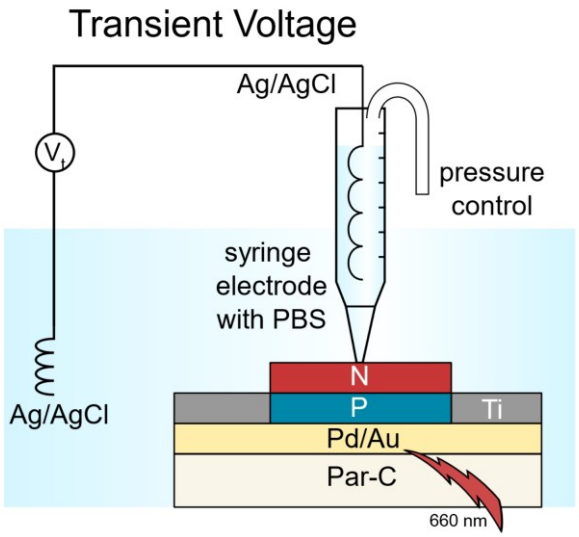

Figure 28. Transient voltage measurement. *Explanted parylene OEPC were illuminated with LED, while photogenerated voltage was measured above the centre of the p-n layer.*

8.6 STATISTICS

Statistical analysis of all numerical data was performed using R Statistical Software (v4.2.0, 2022-04-22 (227)) and its relevant packages:

- dplyr (v1.1.4, 2023-11-17 (228))
- tidyverse (v2.0.0, 2023-02-22 (229))
- car (v3.0-13, 2022-05-02 (230))
- ggplot2 (v 3.4.4, 2023-10-12 (231))
- ggrepel (v0.9.4, 2023-10-13 (232))
- ggpubr (v0.6.0, 2023-02-10 (233))

Shapiro-Wilk test was used to assess normality of data distribution. Homogeneity of variances was tested using the F-test for two groups and Levene's test for three or more groups.

Statistical tests used in the analysis of *in vitro* and *in vivo* experiments are listed in Table 4. Significance for all tests was considered at $p < 0.05$.

Table 4. List of statistical tests and post hoc tests used in the analyses of experiments in this study.

Experiment	Test	Post hoc
LDH – comparisons between groups and time points	Two-way repeated measures ANOVA	Tukey's HSD
LDH – comparison between before and after stimulation	Student's t-test	-
Body mass	Two-way repeated measures ANOVA	-
Nest score	Two-way repeated measures ANOVA	-
c-Fos$^+$ cell percentage – Experiment 1 with glass/ITO OEPC	Kruskal$^-$ Wallis test	Dunn's test
c-Fos$^+$ cell percentage – back electrode – Experiment 3 with glass/Au OEPC	Mann$^-$ Whitney U test	-
c-Fos$^+$ cell percentage – p-n layer (inner and outer parts) – Experiment 3 with glass/Au OEPC	Two-way ANOVA	-
c-Fos$^+$ cell percentage – back electrode – Experiment 4 with glass/Au OEPC	Student's t-test	-
c-Fos$^+$ cell percentage – p-n layer – Experiment 4 with glass/Au OEPC	Mann-Whitney U test	
c-Fos$^+$ cell percentage in brain slices	Two-way ANOVA	Tukey's HSD

9 RESULTS

The results obtained from the primary cell culture and animal experiments have been published in Advanced Healthcare Materials (221) and are adapted and reproduced with permission from John Wiley and Sons under the terms of the Creative Commons CC BY license.

9.1 PRIMARY CELL CULTURE ON GLASS OEPC

9.1.1 Cell survival and device cytotoxicity

To establish optimal culture conditions, primary cortical cells from neonatal rats were cultivated on glass/ITO OEPC, coated with various standard coating materials (Figure 29). The selection of the optimal coating was based on visual inspection of the cells throughout the culture.

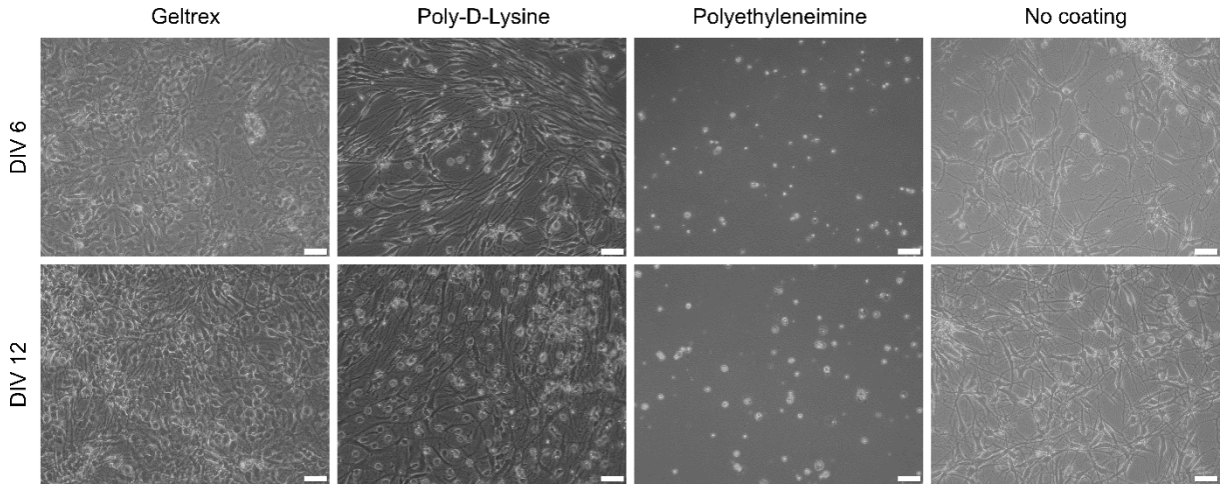

Figure 29. Different coating strategies for glass OEPC. *Representative photomicrographs of rat primary cortical cell culture on glass/ITO OEPC at DIV6 and DIV12. Geltrex coating yielded the highest cell density, followed by poly-D-lysine coating. Cells failed to survive on top of the polyethyleneimine coating. It was possible to culture cells on an uncoated OEPC surface, although at lower density compared to Geltrex and poly-D-lysine. Scale bar: 50 µm. Adapted and reproduced with permission from John Wiley and Sons: Advanced Healthcare Materials (221), under the terms of the Creative Commons CC BY license.*

During both the first and the second week of the culture, the highest cell density was observed on the Geltrex-coated samples (Figure 29A, 29E). Cells cultured on PDL-coated OEPC also reached satisfactory density and intricate neuronal networks throughout the experiment (Figure 29B, 29F). Only a few cells attached to the OEPC coated with PEI, but they did not

survive on the surface (Figure 29C, 29G). At the same time, cells managed to adhere to the uncoated devices (Figure 29D, 29H), although the neuronal network appeared to be less dense than on the OEPC coated with Geltrex or PDL. In all following cell culture experiments, all surfaces (OEPC, glass cover slips) were coated with PDL.

Biocompatibility of OEPC in the cell culture was assessed by microscopic inspection (Figure 30) accompanied by repeated LDH cytotoxicity tests (Figure 31). Primary cortical cells were cultivated on PDL-coated glass/Au OEPC and glass cover slips for two weeks (Figure 30A). During the first week, cell attachment and network development was observed at DIV5. The network matured further throughout the second culture week, on DIV10 to DIV14. It appeared that cell density diminished over time on both surfaces, leading to the aggregation of cell debris on DIV14. Cells seeded on top of the p-n layer did not visibly differ from the ones cultured on top of the back electrode, showing comparable cell density and complexity of neuronal networks (Figure 30B).

To assess cytotoxic effects of surface materials of glass/Au OEPC, LDH tests were conducted on DIV5, DIV10, and DIV14 (Figure 31A). Due to challenges in reaching the limit of detection when cells were cultured only on the p-n layer, for the purpose of this study, cells were seeded over the whole device. Therefore, the results reflect the cytotoxicity of the entire OEPC, and the exact effects of the organic materials of the p-n layer and the gold of the back electrode cannot be discerned.

LDH activity in the cell culture media did not vary between OEPC and glass at any of selected time points (Figure 31A 2J; $F(1, 8) = 0.00042$, $p = 0.98$). However, LDH release was significantly influenced by time ($F(1.16, 9.31) = 86.82$, $p = 3.47e\text{-}06$), increasing and reaching its peak at DIV10 (mean difference to DIV5: 11.9), and decreasing at DIV14 (mean difference to DIV10: -7.95). However, the value at DIV14 remained significantly higher than at DIV5 (mean difference to DIV5: 3.95). This effect should be interpreted in terms of glial cell death after the application of mitosis inhibition at DIV5, and culture ageing, as cells grown both on OEPC and glass followed the same pattern.

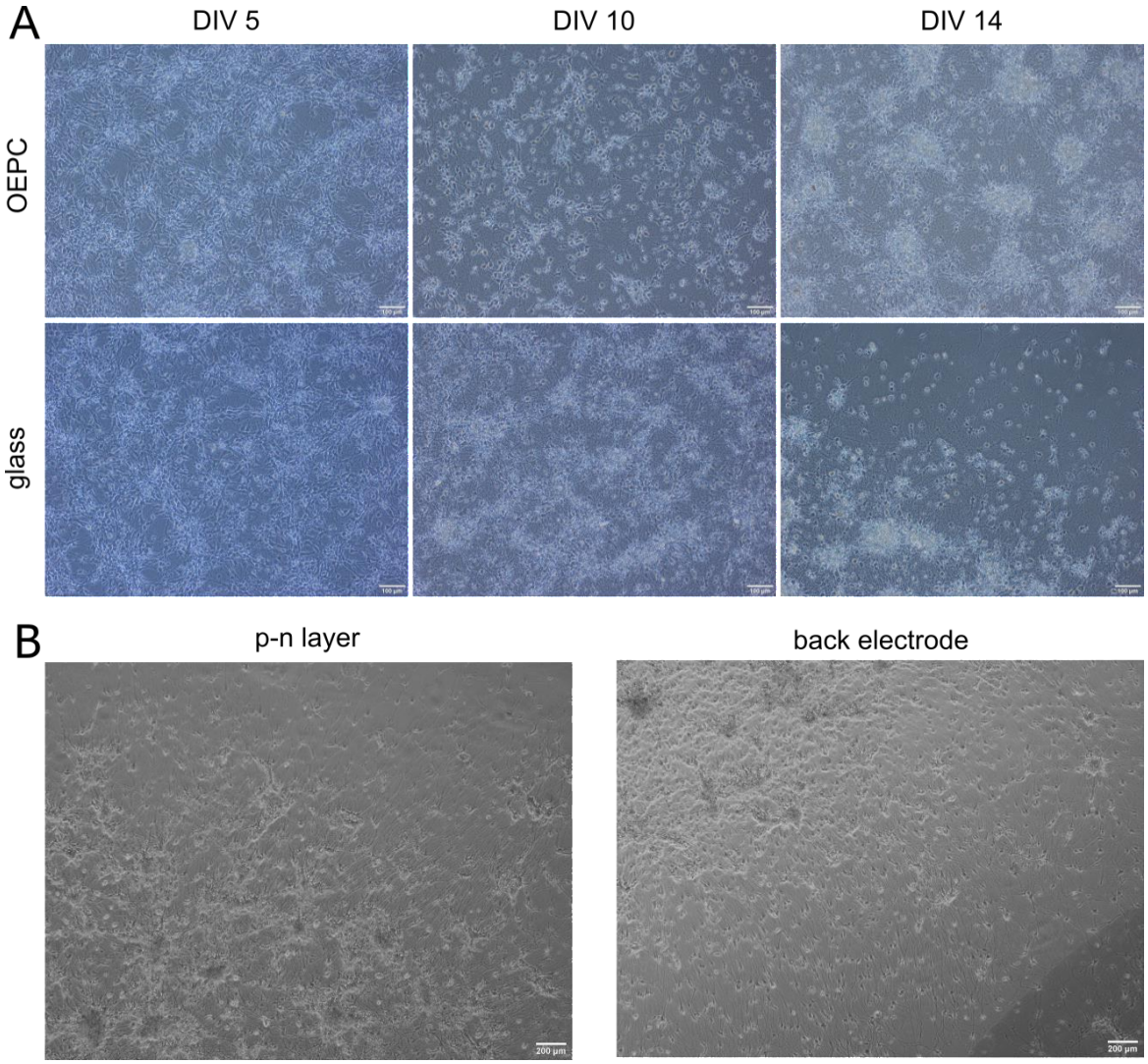

Figure 30. Cell culture survival on top of OEPC. *(A) Representative photomicrographs of rat primary cortical cell culture on the p-n layer of glass/Au OEPC and on glass cover slips at DIV5, DIV10, and DIV14. No discernible differences were observed in regard to cellular interactions with the two surfaces. Scale bar: 100 µm (B) Comparison between the cells grown on top of the p-n layer and back electrode at DIV14. No visible differences in cell culture density or network complexity were observed between the two surfaces. Scale bar: 200 µm. Adapted and reproduced with permission from John Wiley and Sons: Advanced Healthcare Materials (221), under the terms of the Creative Commons CC BY license.*

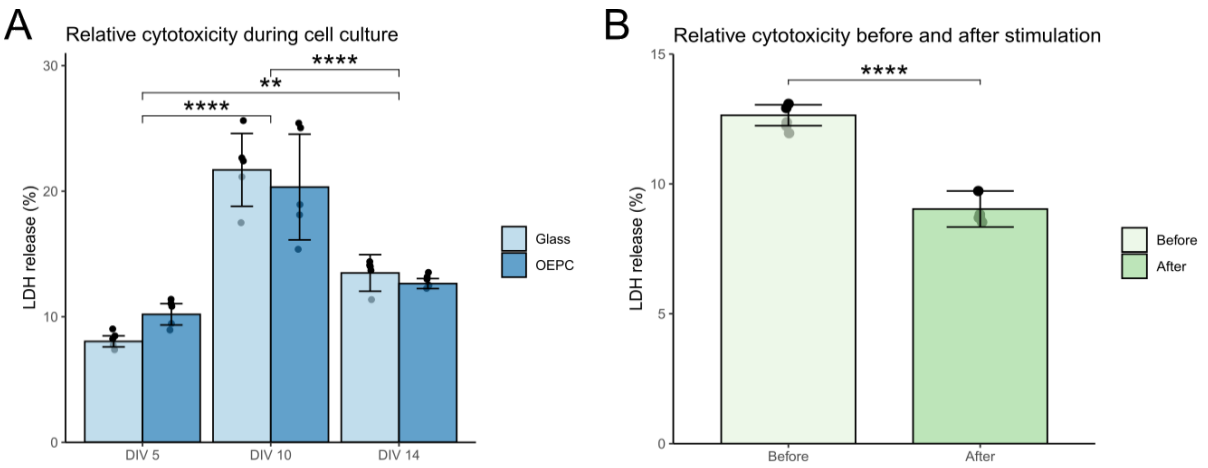

Figure 31. Relative cytotoxicity measured in terms of LDH absorbance in cell culture media. *(A) Cytotoxicity of the OEPC material at DIV5, DIV 10 and DIV14. (D) Cytotoxicity before and after OEPC stimulation. ** p < 0.01; **** p < 0.0001. Adapted and reproduced with permission from John Wiley and Sons: Advanced Healthcare Materials (221), under the terms of the Creative Commons CC BY license.*

To explore, whether light-controlled OEPC stimulation causes cytotoxic effects, LDH levels were compared before and after light treatment (Figure 31B). LDH activity in cell culture medium decreased significantly following the stimulation ($t(6.4038) = 10.083$, $p = 3.65e\text{-}05$).

In summary, rat primary cortical cells not only survived on the surface of OEPC, but also formed expansive and intricate neuronal networks, which further enabled the investigation of the effects of light-controlled stimulation on the culture. Cultivation on the surface of the OEPC did not result in an increased LDH leakage compared to the glass controls, indicating the absence of any cytotoxic effect of the device or the stimulation on neurons.

9.1.2 c-Fos expression after OEPC stimulation

c-Fos, a marker of recent neuronal activity, was used to differentiate, whether light-controlled electric stimulation with OEPC induces molecular changes in primary cortical cells. In the first experiment (Experiment 1), cells cultured on top of the p-n layer of glass/ITO OEPC were stimulated with low-frequency (2 Hz) and high-frequency (20 Hz) light pulses. Cell culture with addition of 20 µM glutamic acid (glutamate) in the medium served as a positive control for glutamatergic signalling. Cells left in darkness were considered a negative control.

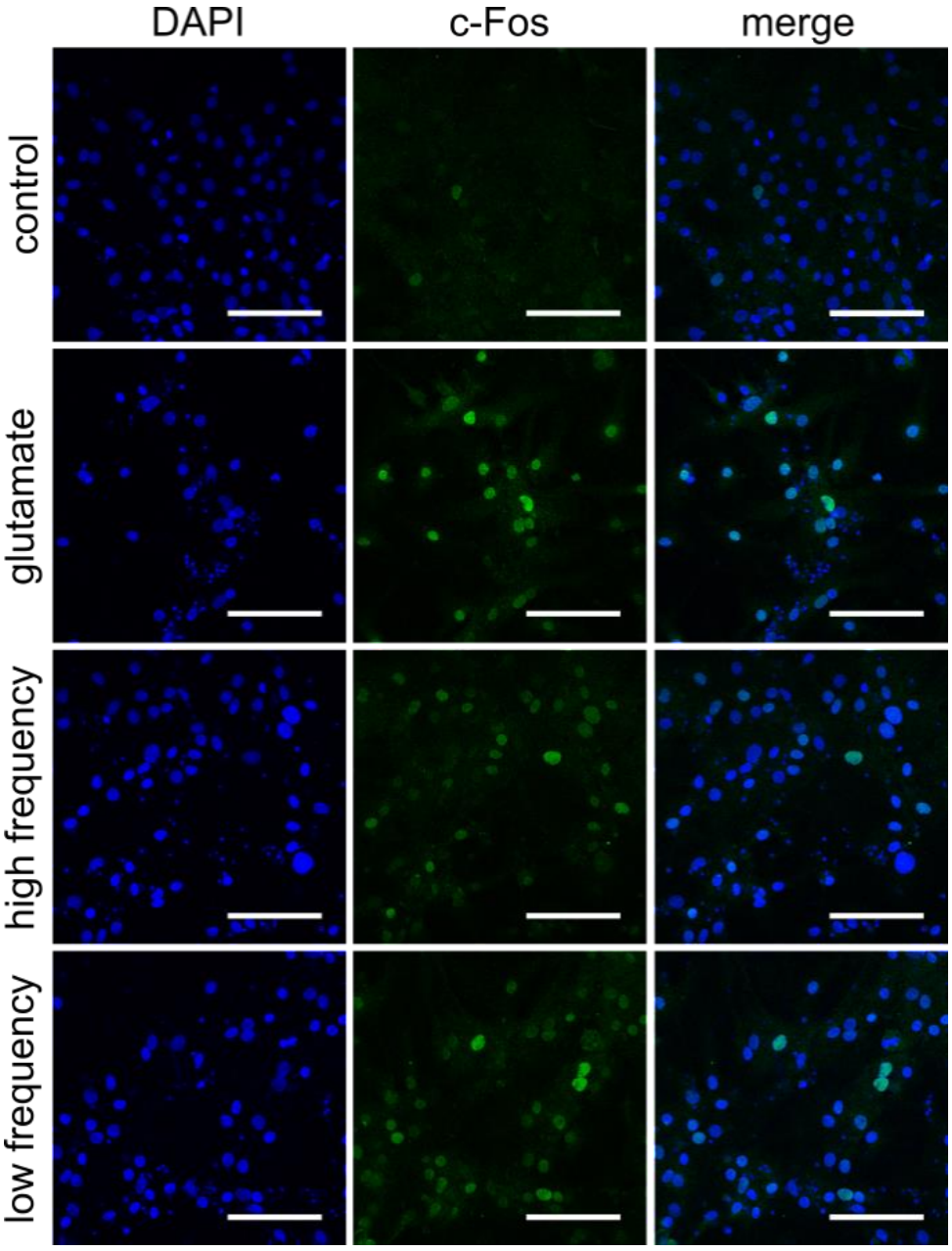

Figure 32. c-Fos expression in OEPC-stimulated primary cortical culture in Experiment 1.*Representative photomicrographs of c-Fos IF staining (green) with DAPI counterstaining of nuclei (blue) following 30 min stimulation. "Control" – cells left in darkness; "glutamate" – cells left in darkness with addition of 20 μM L-glutamic acid; "high frequency" – cells stimulated with red light pulsed at 20 Hz (2 ms pulse); "low frequency" – cells stimulated with red light pulsed at 2 Hz (5 ms pulse). Scale bar: 100 μm. Adapted and reproduced with permission from John Wiley and Sons: Advanced Healthcare Materials (221), under the terms of the Creative Commons CC BY license.*

ICC staining revealed upregulation of c-Fos expression following light or glutamate treatment in comparison to the negative control. The percentage of c-Fos$^+$ cells significantly differed among the four groups (Figure 33; control: M = 12.51, SD = 3.86; glutamate: M = 25.69,

SD = 8.3; high frequency: M = 26.43, SD = 10.29; low frequency: M = 27.4, SD = 5.73; $\chi 2$ (3) = 9.01, p = 0.03). Although the increase in c-Fos$^+$ cell percentage was visible in the glutamate, low-frequency and high-frequency groups, post hoc comparisons indicated a significant difference only in the cells stimulated with low-frequency light pulses (p = 0.03).

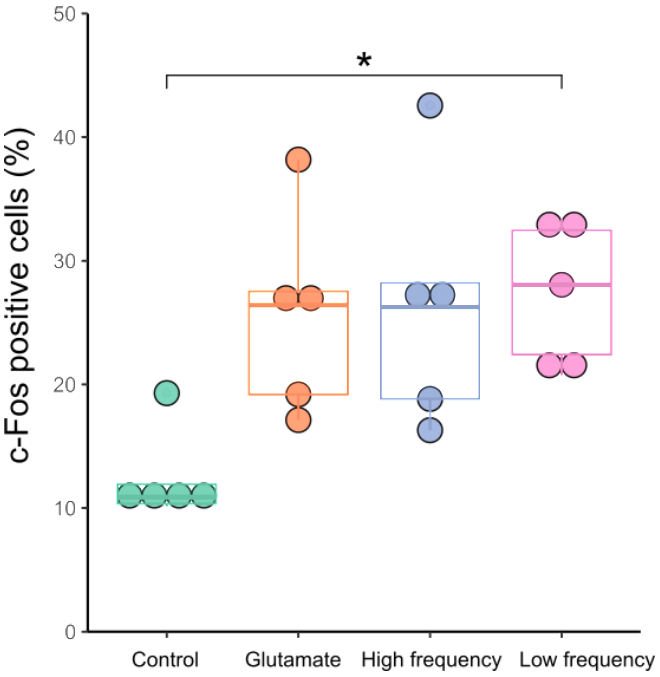

Figure 33. Statistical analysis of the percentage of c-Fos+ cells after OEPC stimulation in Experiment 1. *Positive cell percentage was calculated relatively to the total number of nuclei 60 min following stimulation or control conditions. * p < 0.05. Adapted and reproduced with permission from John Wiley and Sons: Advanced Healthcare Materials (221), under the terms of the Creative Commons CC BY license.*

To exclude a potential effect of the light treatment itself, primary cortical cells grown on glass cover slips were treated with light pulsed at 20 Hz frequency (Experiment 2). The addition of 20 µM glutamate served as a positive control, whereas cells left in darkness were used as a negative control. Due to a very low c-Fos$^+$ cell number in the control and in the treated groups, the mean grey value of the whole image was analysed. The mean grey values of the control and light treated cells did not differ between these groups, while staining of glutamate-treated cells demonstrated visibly more intense staining (Figure 34).

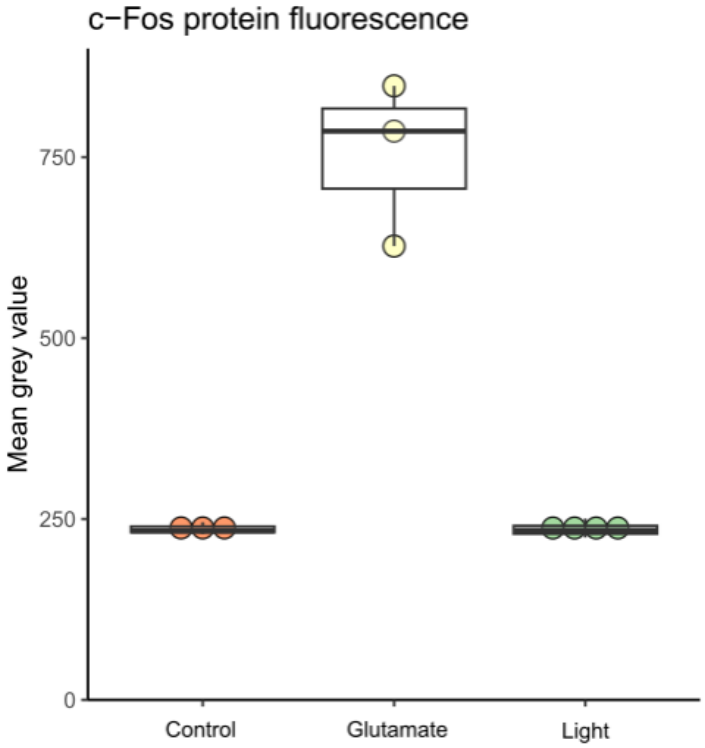

Figure 34. Mean grey value of c-Fos ICC staining after OEPC stimulation in Experiment 2. *To exclude a potential effect of the light treatment itself, cells grown on glass cover slips were subjected to either control conditions ("Control" – cells left in darkness; "Glutamate" – cells with addition of 20 µM L-glutamic acid) or light treatment ("Light" – cells treated with red light at 20 Hz). The mean grey value of c-Fos in control and light-treated groups did not differ, while glutamate-treated cells demonstrated visibly more intense staining. Adapted and reproduced with permission from John Wiley and Sons: Advanced Healthcare Materials (221), under the terms of the Creative Commons CC BY license.*

In Experiments 3 and 4, glass/Au OEPC were employed. In Experiment 3, primary cortical cells were seeded predominantly on the p-n layer, with only a margin of cells reaching the metal back electrode, in order to explore whether cell localisation on the photoactive layer influences neuronal activity. For this purpose, pictures of c-Fos$^+$ cells were acquired in the central part and on the periphery of the p-n layer, as well as at the level of the back electrode (refer to Figure 21B). Visual inspection of the ICC staining revealed more positive cells in the stimulated cultures both in the inner (Figure 35A) and the outer part of the p-n layer (Figure 35B). Similarly, more c-Fos$^+$ cells were observed in the stimulated group on the back electrode (Figure 35C).

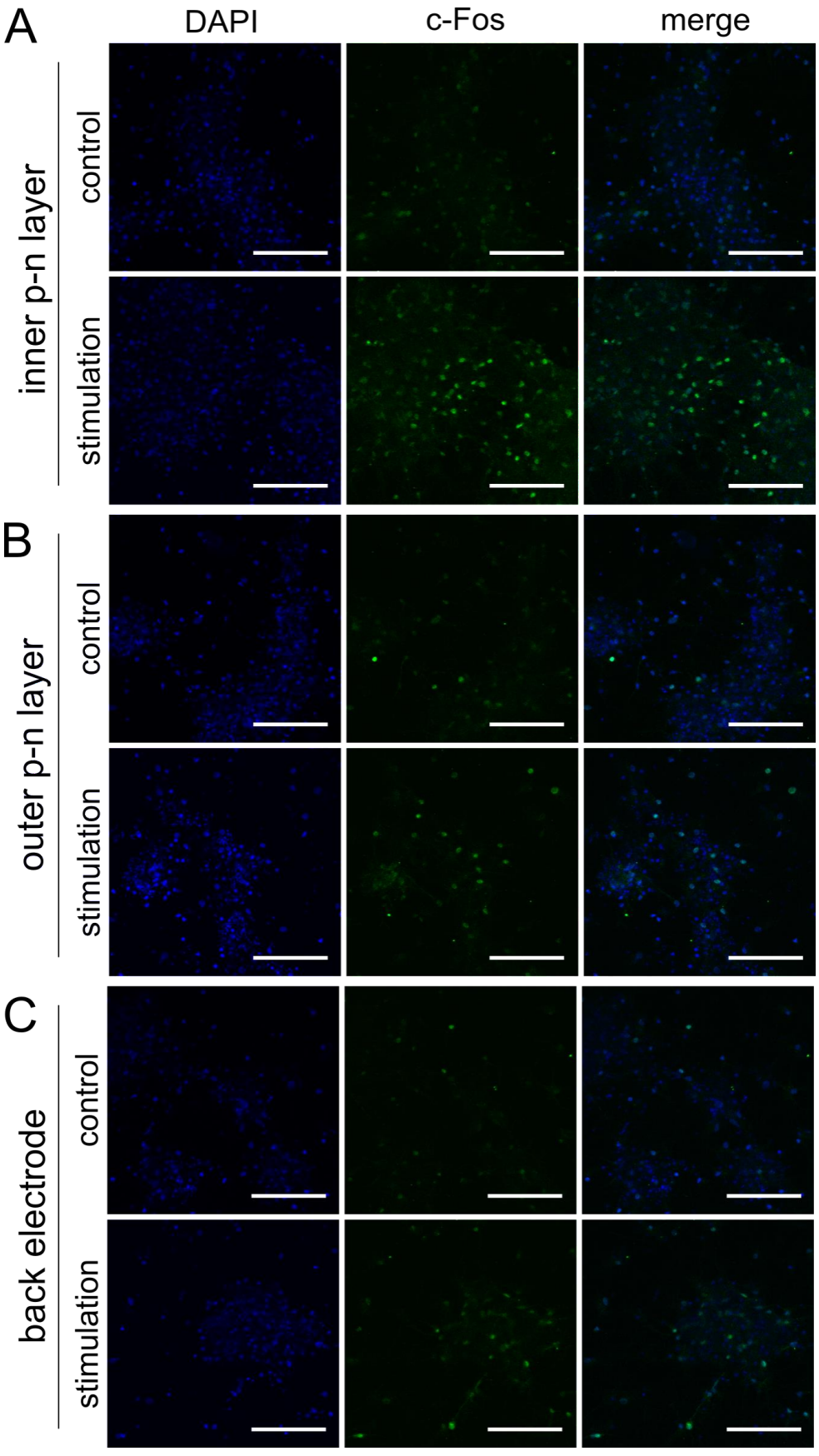
A
DAPI
c-Fos
merge
inner p-n layer
control
stimulation
B
outer p-n layer
control
stimulation
C
back electrode
control
stimulation

Figure 35. c-Fos expression in OEPC-stimulated primary cortical culture in Experiment 3. *Representative photomicrographs of c-Fos IF staining (green) with DAPI counterstaining of nuclei (blue) following 30 min stimulation protocol. "Control" – cells left in darkness; "stimulation" – cells stimulated with red light pulsed at 20 Hz (2 ms pulse). (A) Cells growing in the centre of the p-n layer. (B) Cells growing at the periphery of the p-n layer. (C) Cells growing on the back electrode. Scale bar: 100 µm. Adapted and reproduced with permission from John Wiley and Sons: Advanced Healthcare Materials (221), under the terms of the Creative Commons CC BY license.*

Statistical analysis confirmed the observed increase of c-Fos⁺ cells in OEPC-stimulated cultures (Figure 36A; $F(1, 18) = 12.74$, $p = 0.002$), while no significant effect of localisation on the photoactive layer was observed ($F(1, 18) = 1.48$, $p = 0.24$). Comparison of the percentage of c-Fos⁺ cells on the back electrode also revealed a statistically significant increase in the stimulated group as compared to the control (Figure 36B; control: $M = 3.91$, $SD = 1.61$; stimulation: $M = 30.51$, $SD = 23.11$; $W = 2$, $p = 0.017$).

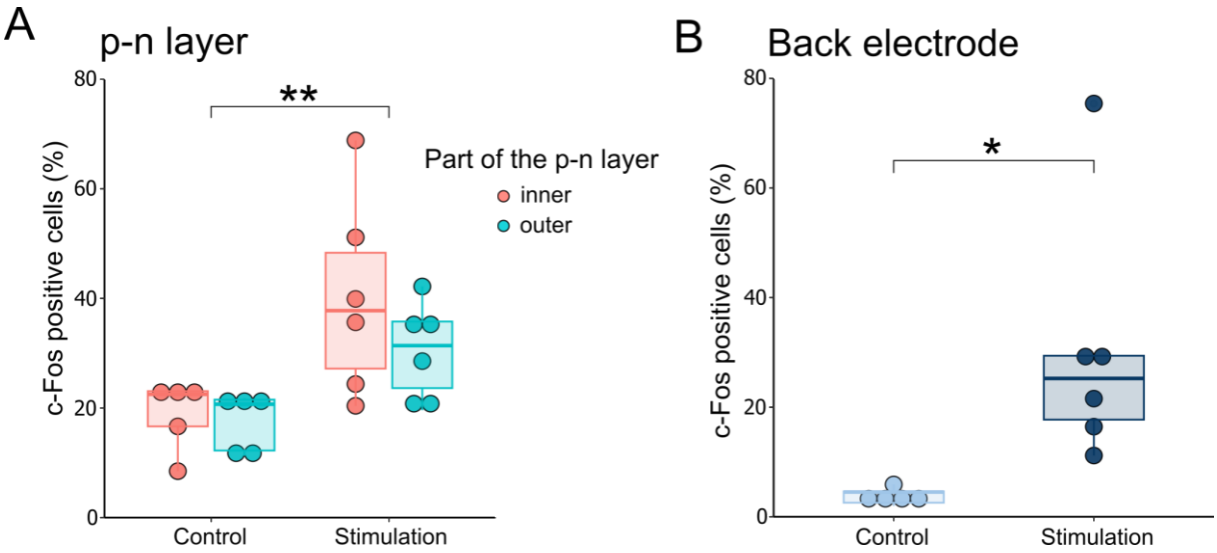

Figure 36. Statistical analysis of the percentage of c-Fos+ cells after OEPC stimulation in Experiment 4. *Positive cell percentage was calculated relatively to the total number of nuclei 60 min following stimulation or control conditions. (A) Comparison between the inner and outer parts of the photoactive p-n layer in the stimulated and control cultures. (B) Comparison between the stimulated and control cultures grown on the back electrode. * $p < 0.05$. Adapted and reproduced with permission from John Wiley and Sons: Advanced Healthcare Materials (221), under the terms of the Creative Commons CC BY license.*

To elucidate whether the upregulation of c-Fos expression on the back electrode is evoked through direct stimulation or through signal propagation within the neuronal network from the cells activated on the p-n layer, Experiment 4 was devised. Two separate primary cortical cell clusters were seeded onto one glass/Au OEPC (refer to Figure 21C). Special care

was taken to ensure minimal physical connection between the two cell clusters. The ICC staining following the stimulation revealed extensive c-Fos expression in the cell cluster cultured on top of the photoactive p-n layer (Figure 37A). Visibly fewer cells were noticeable in the cluster grown on the gold back electrode (Figure 37B).

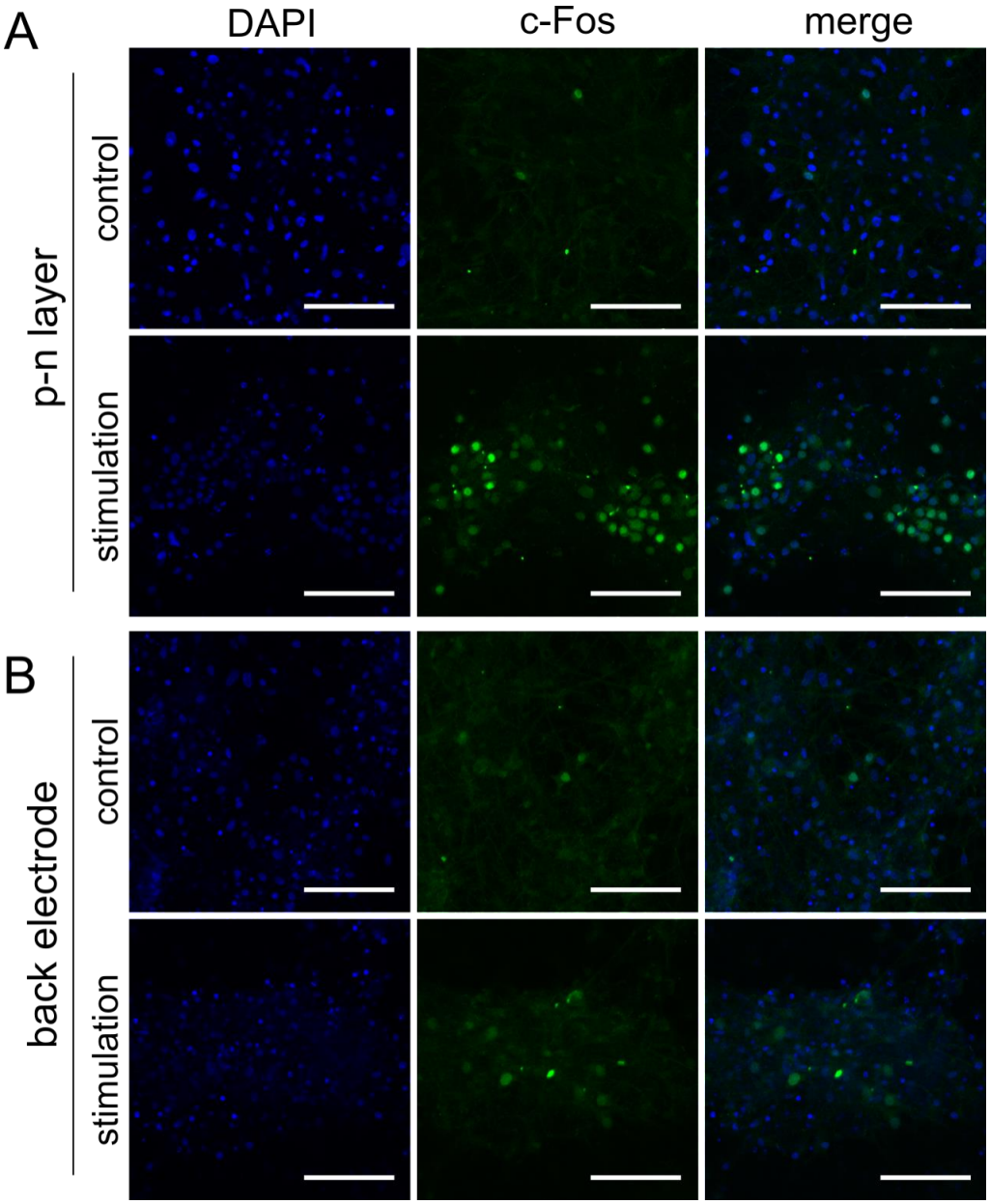

Figure 37. c-Fos expression in OEPC-stimulated primary cortical culture in Experiment 4. *Representative photomicrographs of c-Fos IF staining (green) with DAPI counterstaining of nuclei (blue) following 30 min stimulation protocol. "Control" – cells left in darkness; "stimulation" – cells stimulated with red light pulsed at 20 Hz (2 ms pulse). (A) Cells growing on the p-n layer. (B) Cells growing on the back electrode. Both clusters were physically separated. Scale bar: 100 µm. Adapted and*

reproduced with permission from John Wiley and Sons: Advanced Healthcare Materials (221), under the terms of the Creative Commons CC BY license.

Statistical analysis of the imaging data revealed a statistically significant increase in c-Fos expression in stimulated cells grown on the p-n layer (Figure 38A; M = 52.7, SD = 18.06) as compared to the same culture without light stimulation (M = 14.11, SD = 7.34; W = 0, p = 0.014). No differences in the c-Fos positive cell percentage between the cells stimulated on the back electrode were observed (Figure 38B; M = 26.05, SD = 12.6) as compared to the non-stimulated controls (M = 20.1, SD = 13.25; t(7) = -0.69, p = 0.51). These data supported the hypothesis that the increase of c-Fos in Experiment 3 stemmed from the network propagation of the action potentials rather than from the (predominantly anodic) stimulation of the gold electrode.

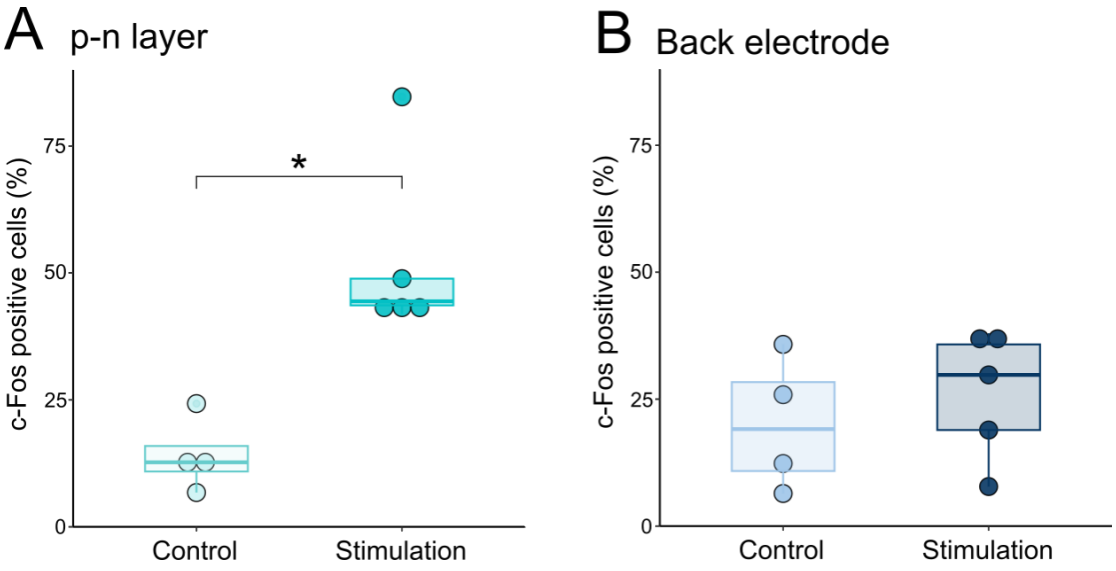

Figure 38. Statistical analysis of the percentage of c-Fos+ cells after OEPC stimulation in Experiment 4. *Positive cell percentage was calculated relatively to the total number of nuclei 60 min following stimulation or control conditions. Both cell clusters were physically separated to avoid network signal propagation. (A) Comparison between the stimulated and control cultures grown on the p-n layer. (B) Comparison between the stimulated and control cultures grown on the back electrode. * p < 0.05. Adapted and reproduced with permission from John Wiley and Sons: Advanced Healthcare Materials (221), under the terms of the Creative Commons CC BY license.*

9.2 Hippocampal OTC on PET OEPC

9.2.1 c-Fos expression after single OEPC stimulation

OTC of hippocampal slices were subjected to 30 minutes of 2 Hz light stimulation with 5 ms pulses at DIV7. IF double staining of c-Fos and NeuN revealed more c-Fos$^+$ in the treated

slices as compared to controls left in darkness (Figure 39). Almost all c-Fos$^+$ cells also expressed NeuN, a marker of differentiated neurons. c-Fos$^+$/NeuN$^+$ cells were present in the whole slice, not only in the cellular layer located in the vicinity of the OEPC, indicative of neuronal activation throughout the culture. Single c-Fos$^+$/NeuN$^-$ were observed in the upper part of the culture, attributable to the dividing layer of glial scar tissue, both in the stimulated and control slices.

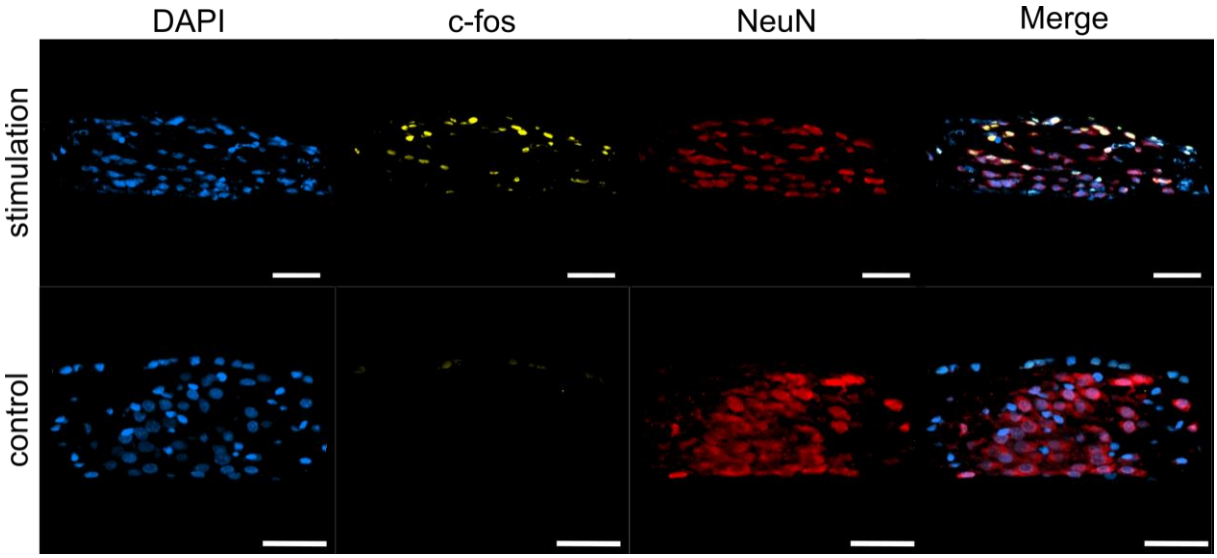

Figure 39. c-Fos expression after single OEPC stimulation in OTC hippocampal slices.*Representative photomicrographs of IF staining in cross-sections of hippocampal OTC subjected to the stimulation (upper row) or left in darkness (lower row). Majority of c-Fos$^+$ cells are also NeuN$^+$. Scale bar: 50 µm*

9.2.2 GAP-43 expression after repeated stimulation

Repeated OEPC stimulation started at DIV6 and continued for seven consecutive days. All prepared slices survived until the end of the experiment. Slices became flattened and transparent with time, indicative of good culture conditions (Figure 40). At DIV8, characteristic hippocampal anatomy was still well visible (Figure 40B), but becaume less clear, though discernible, at DIV12 (Figure 40C).

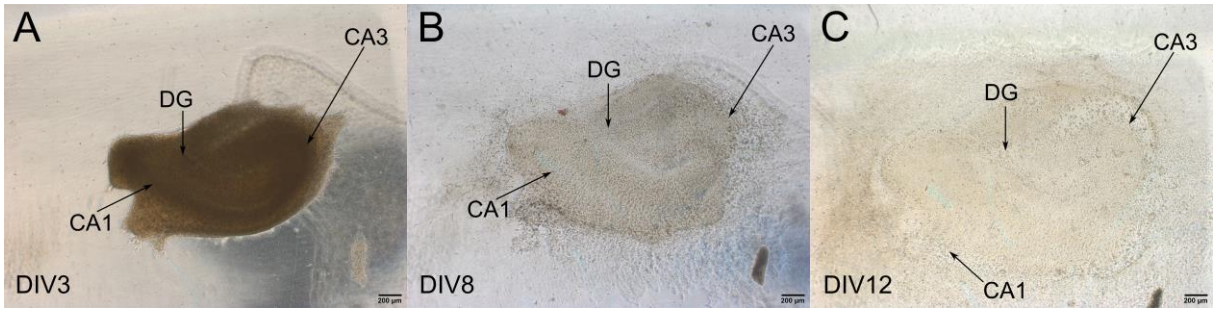

Figure 40. OTC hippocampal slices during the culture. *Representative microphotographs of the hippocampal slices at (A) DIV3, (B) DIV8, and (C) DIV12 of the OTC. Flattening and increasing transparency of the slices indicates good culturing conditions. Visible distinctive features of the hippocampal anatomy. DG – dentate gyrus, CA – cornu Ammonis. Scale bar: 200 µm*

Double GAP-43/NeuN staining revealed a more pronounced signal of both markers in the repeatedly stimulated groups (Figure 41). Single NeuN$^+$ cells co-expressed GAP-43 (Figure 41, arrow).

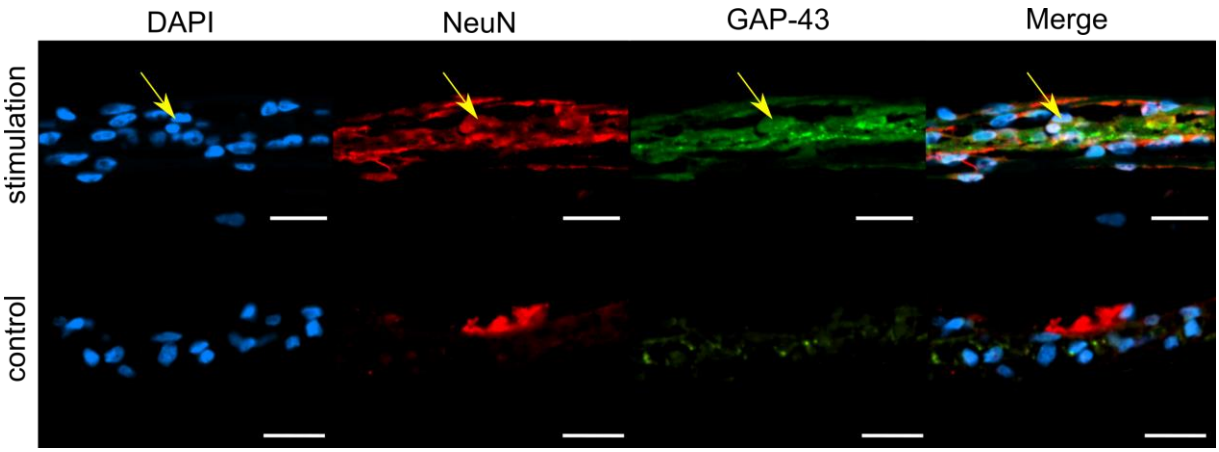

Figure 41. GAP-43 expression after repetitive OEPC stimulation in OTC hippocampal slices. *Representative photomicrographs of IF staining in cross-sections of HC OTC subjected to the stimulation (upper row) or left in darkness (lower row) for seven consecutive days. Arrow indicates an exemplary NeuN$^+$/GAP-43$^+$ cell. Scale bar: 20 µm*

9.3 PARYLENE OEPC IMPLANTATION IN RATS

9.3.1 Animal welfare post-surgery

To estimate the burden of the surgery and parylene OEPC implantation on experimental animals, two quantifiable parameters were assessed: body mass and nest score (Figure 42). Over the course of three weeks following the surgery, there was a consistent increase in body weight across all animals, with the exception of one individual, whose body mass remained

stable (Figure 42A). No differences between the groups were observed ($F(2,15) = 0.734$; $p = 0.5$). The evaluation of the nest score was based on images acquired during the same three-week period and involved a comparative analysis among cages with animals subjected to various treatments (Figure 42B):

- "**Implanted**" (with two animals after OEPC implantation; n = 4 cages)
- "**Control**" (with two animals after surgery without implantation; n = 3 cages)
- "**Mixed**" (with one animal after OEPC implantation and one animal after surgery without implantation; n = 5 cages)
- "**Naive**" (with two male rats, age-matched with the experimental animals, not subjected to any experiments and reserved for future breeding; n = 2 cages).

In all cases, the nest score consistently surpassed a threshold of 2.5, indicative of well-constructed nests. Statistical analysis did not reveal any significant changes in the nest score, both between the treatment groups ($F(3, 10) = 1.138$; $p = 0.38$) and across different time points ($F(2, 20) = 1.004$; $p = 0.384$).

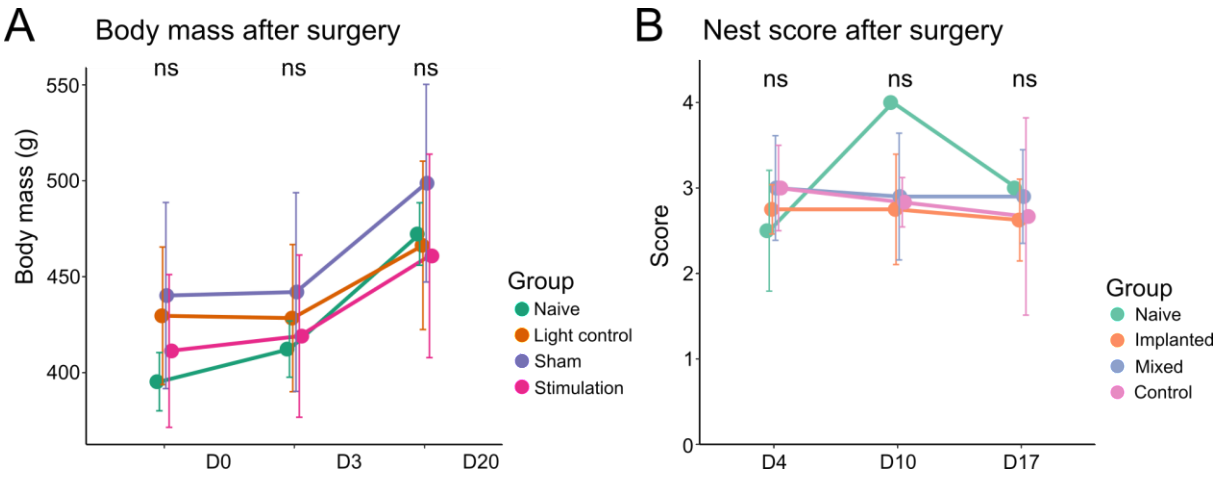

Figure 42. Post-surgery animal welfare parameters. *(A) Body mass change in animals during a three week post-surgery period. Visible consistent increase of body mass over time, with no differences between the groups. "Light control" – light treatment without OEPC (n = 5); "Sham" – no light treatment with OEPC (n = 5 animals); "Stimulation" – light treatment with OEPC (n = 6), "Naive" – age-matched males (n = 4). (B) Comparison of nest scores in the three weeks following the surgery. Nest quality was scored in each cage housing two animals: "Implanted" (n = 4 cages), "Control" (surgery without OEPC implantation; n = 3), "Mixed" (one implanted + one surgery control; n = 5), "Naive" (age-matched males; n = 2). Statistical analysis revealed no significant differences between the time points or groups. ns – not statistically significant. Adapted and reproduced with permission from John Wiley and Sons: Advanced Healthcare Materials (221), under the terms of the Creative Commons CC BY license.*

9.3.2 c-Fos expression after single OEPC stimulation

Acute stimulation

Acute OEPC stimulation was performed during the surgery, immediately after the implantation of the device. Since the animals were sacrificed shortly after the stimulation, and the disruption in CSF flow was not crucial for the experiment, plain OEPC without pores were used.

Upon visually inspecting IF-stained cryosections, vast c-Fos expression in the cortex of the entire ipsilateral hemisphere was observed, spanning through all cortical layers (Figure 43). This pattern was present in all animals, regardless of the OEPC stimulation or lack thereof. This occurrence masked any putative stimulation-induced c-Fos expression and rendered it impossible to compare stimulated and sham-treated brains (Figure 44).

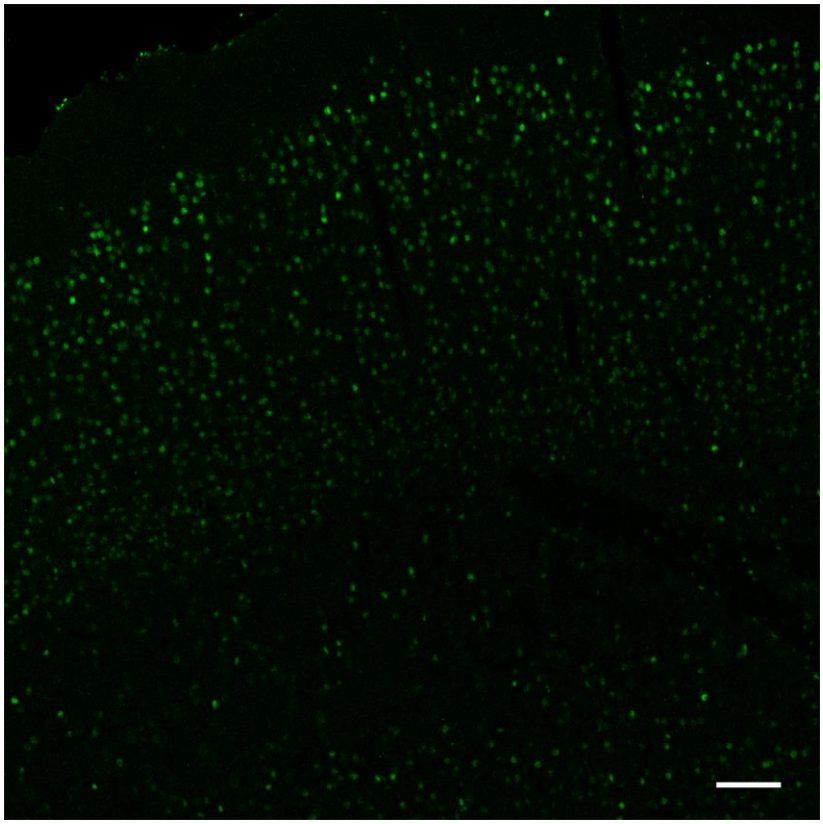

Figure 43. IF c-Fos staining in SOM of an animal sacrificed 60 minutes after OEPC implantation. *Representative photomicrograph showing ipsilateral cortex close to the implantation site. Visible vast c-Fos expression throughout all cortical layers. Scale bar: 100 µm*

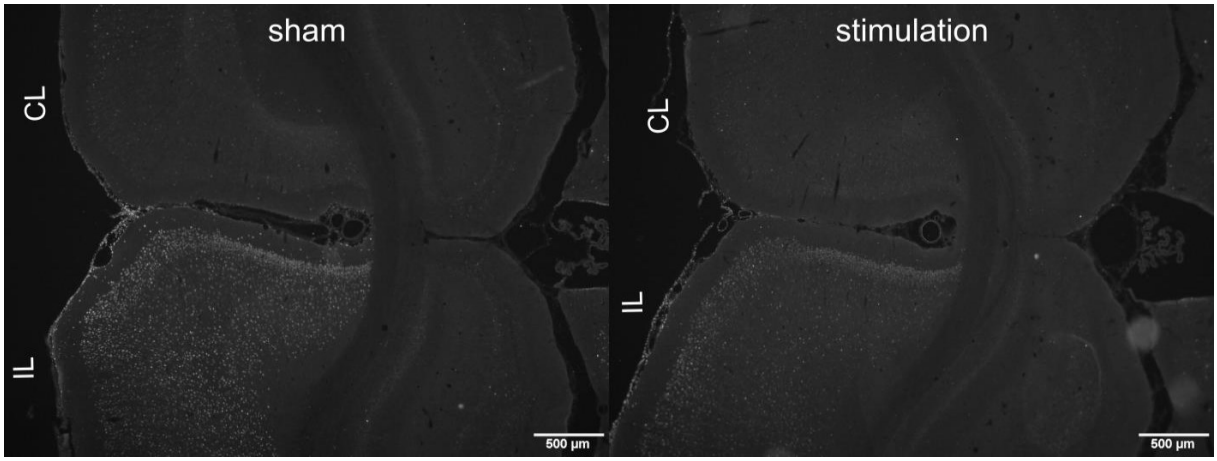

Figure 44. Representative microphotographs of IF c-Fos staining in sham and stimulated animals. *Discernible vast c-Fos expression throughout the ipsilateral cortex in both groups with sparse c-Fos⁺ cells visible in the contralateral hemisphere. CL – contralateral, IL – ipsilateral. Scale bar: 500 µm. Adapted and reproduced with permission from John Wiley and Sons: Advanced Healthcare Materials (221), under the terms of the Creative Commons CC BY license.*

Effect of durectomy

The presence of extensive c-Fos expression in both control and treated groups indicated a common confounding factor, probably linked to the surgery. Dura mater removal was the step with the highest risk of injuring the brain, which could heavily influence the outcome of the experiment. To exclude this potential influence of durectomy, a control experiment was devised, in which one animal was subjected to craniectomy with dura mater removal and another was left with intact dura. Neither parylene OEPC implantation nor light stimulation was carried out. Effectively, a similar vast c-Fos expression pattern emerged exclusively in the rat subjected to craniectomy and dura mater removal, mirroring the observations in the previous cohort of animals (Figure 45).

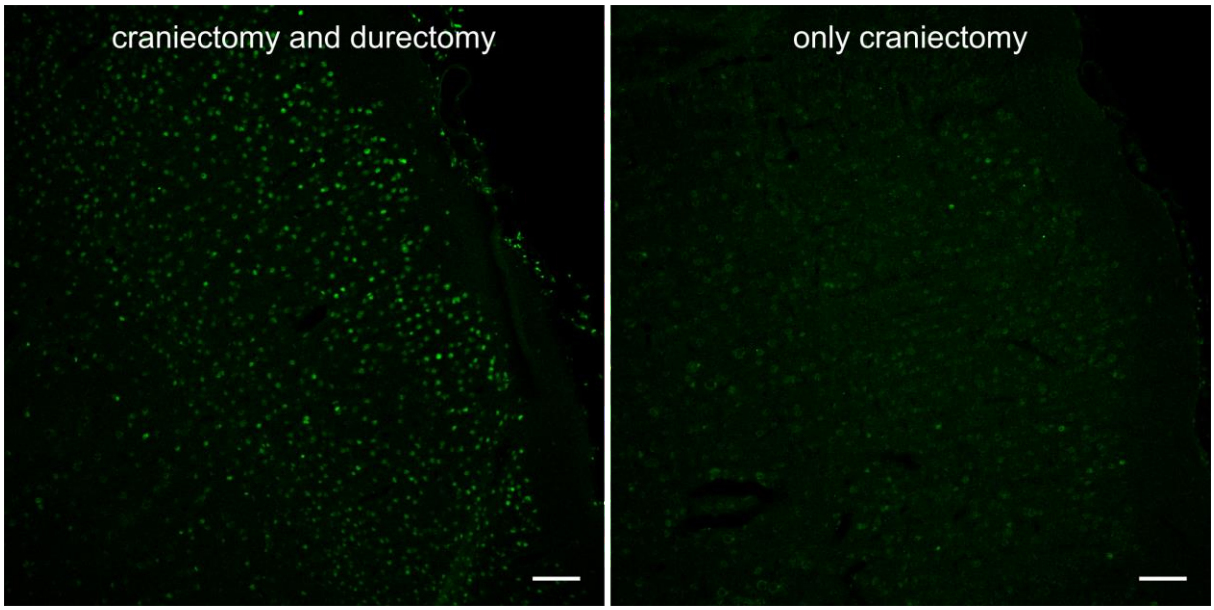

Figure 45. IF c-Fos staining in SOM of animals sacrificed 60 minutes after control surgery. *Representative photomicrograph showing ipsilateral cortex close to the surgical site. Extensive c-Fos expression was observed in the cortex following craniectomy with subsequent durectomy, whereas the animal subjected to craniectomy with intact dura mater displayed only individual c-Fos⁺ cells. Scale bar: 100 µm. Adapted and reproduced with permission from John Wiley and Sons: Advanced Healthcare Materials (221), under the terms of the Creative Commons CC BY license.*

Stimulation 24 h post-surgery

To eliminate the immediate effect of the surgery on c-Fos expression, the latency between the surgery and light stimulation was increased to 24 hours. Additionally, effects of epidural (Figure 46A-D) and subdural (Figure 46E-H) stimulation protocols were compared. Both modes of stimulation resulted in a noticeable increase in the number of c-Fos⁺ cells in the ipsilateral SOM (Figure 46A-B, E-F). On the contralateral side, however, c-Fos expression did not follow the same pattern, and differences between sham and stimulated animals were not easily discernible (Figure 46C-D, G-H). Moreover, in four animals, a vast c-Fos expression spanning the entire ipsilateral cortex was still present, posing a substantial challenge for quantitative analysis.

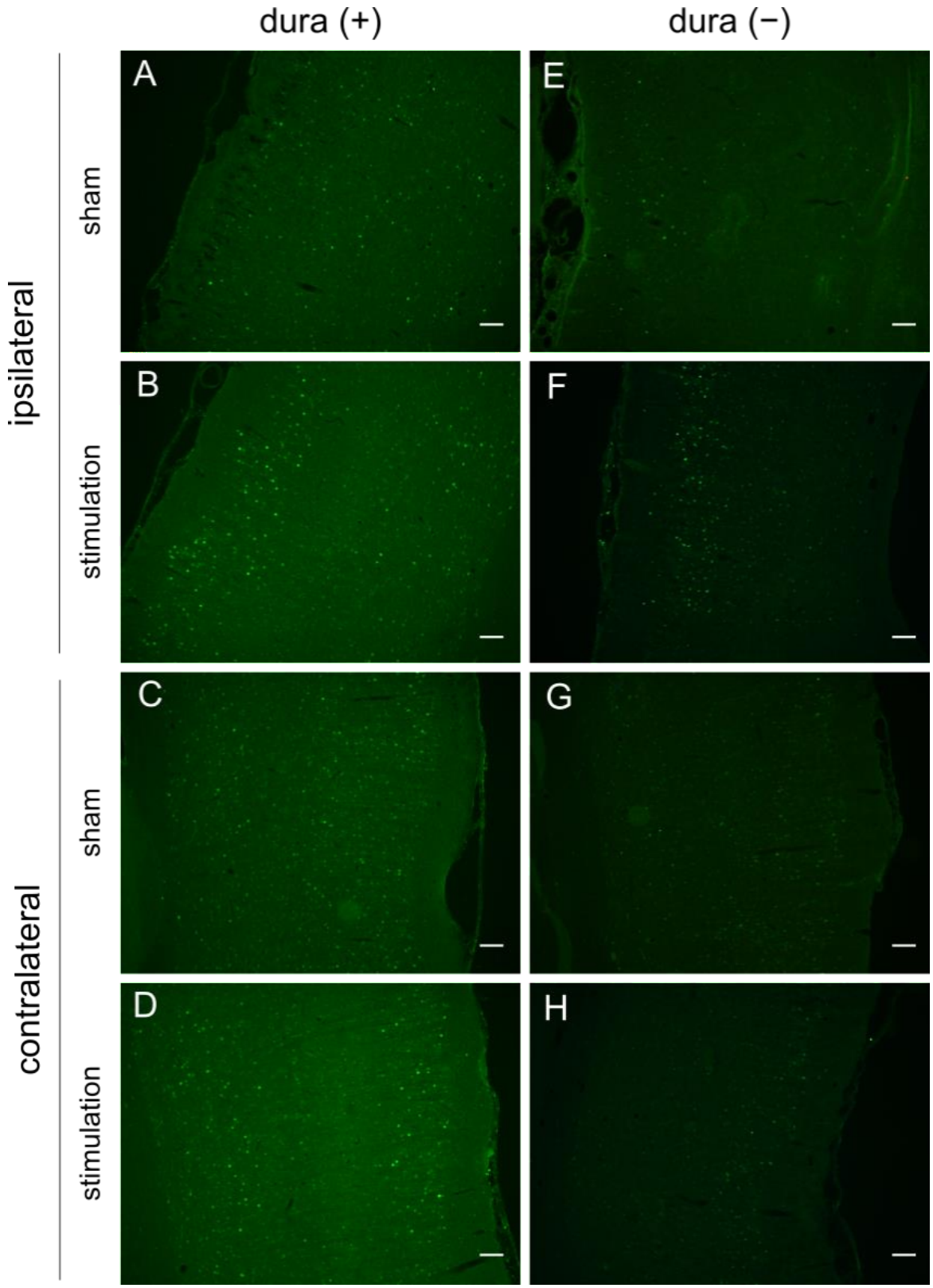

Figure 46. Representative photomicrographs of IF c-Fos staining in SOM of animals stimulated and sacrificed 24 hours after OEPC implantation. *(A-D) c-Fos immunoreactivity in brain section from animals with OEPC positioned epidurally. (E-F) c-Fos immunoreactivity in brain section from animals*

with OEPC positioned subdurally. Ipsilaterally, more c-Fos⁺ cells were observed in SOM after the stimulation compared to the sham treatment in both animals with intact dura (A, B), and after durectomy (E, F). The signal was mostly discernible in the cortical layers II/III. No visible differences in c-Fos expression were observed between the sham and stimulated brains on the contralateral side, regardless of the status of the dura mater (C, D, G, H). Scale bar: 100 µm. Adapted and reproduced with permission from John Wiley and Sons: Advanced Healthcare Materials (221), under the terms of the Creative Commons CC BY license.

Due to a slightly more intense c-Fos⁺ signal in animals subjected to subdural stimulation compared to the epidural protocol, as well as more pronounced differences between the ipsi- and contralateral hemispheres, in the subsequent experiments dura mater was always removed.

Stimulation 48 h post-surgery

The period between the implantation and stimulation was further prolonged to 48 hours to avoid possible confounding factors present during the first hours after the surgery. However, DAB immunostaining once again revealed c-Fos expression spreading throughout the entire cortex, further hindering the comprehension of the stimulation effect (Figure 47).

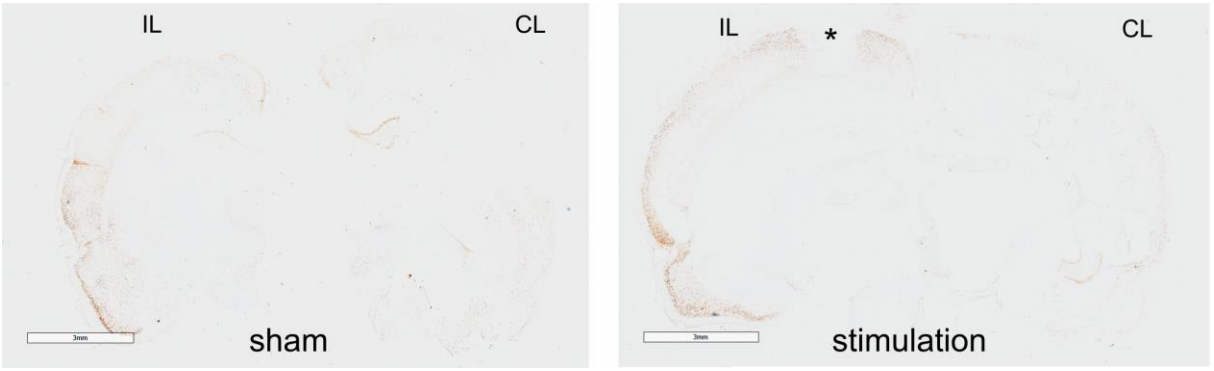

Figure 47. Representative photomicrographs of DAB c-Fos staining in sections of animals stimulated and sacrificed 48 hours after OEPC implantation. *Visible widespread c-Fos expression throughout the cortex in the ipsilateral hemisphere in both sham and stimulated animals. Asterisk indicates a site of cell loss due to surgical trauma. CL – contralateral, IL – ipsilateral. Scale bar: 3 mm. Adapted and reproduced with permission from John Wiley and Sons: Advanced Healthcare Materials (221), under the terms of the Creative Commons CC BY license.*

Stimulation three weeks post-surgery

Due to challenges in analysing c-Fos expression shortly after OEPC implantation, the latency between surgery and stimulation was further extended to three weeks. By the prolonged timeframe, we aimed to mitigate any potential confounding factors associated with the surgery

itself, such as pain signalling, wound healing, and inflammation. Notably, the previously observed pattern of vast pancortical c-Fos expression was not observed in any of the animals, allowing for the quantification of c-Fos expressing cells.

Three regions of interest, SOM, EC, and HC, both on the ipsilateral and contralateral sides, were analysed quantitatively in regard to c-Fos$^+$ cell percentage. In SOM (Figure 48), IHC staining revealed increased immunoreactivity in the light-stimulated, OEPC-implanted animals ("stimulation") compared to the two control groups: sham-treated, OEPC-implanted rats ("sham") and light-treated, rats without OEPC implantation ("light control"). Most positive cells localised in layers II/III and IV of SOM, with fewer cells visible in deeper cortical layers. In the control groups, only single c-Fos$^+$ cells were present, predominantly in layers II/III, indicative of circumscribed spontaneous activity. No discernible differences were noticed between the ipsilateral and contralateral hemispheres in all of the groups.

In the study, only LEC was taken into analysis, as MEC spans brain regions located caudally to the regions of interest of this study. Visual inspection of c-Fos IHC staining in this region revealed more pronounced immunoreactivity in the stimulation group compared to the two control groups (Figure 49). c-Fos$^+$ cells spanned across all cortical layers, with the highest density in deep layers V and VI. Slightly stronger signal was detected in the contralateral hemisphere of the stimulated animals compared to the ipsilateral cortex.

Within HC, c-Fos expression was most prominent in DG, particularly in its upper blade (Figure 50). The vast majority of c-Fos$^+$ was present in the granular cell layer, with only single cells discernible in the hilus (Figure 50, black arrow). CA3 and CA1 contained fewer positive cells than DG, with the majority of them present in the stratum pyramidale, with single cells in other strata (e.g., stratum oriens, red arrow).

Visual comparison of c-Fos immunostaining in HC revealed more pronounced expression in stimulated animals compared to both control groups (Figure 51). In the stimulation group, slightly more c-Fos$^+$ cells were discernible in the ipsilateral HC compared to the contralateral hemisphere.

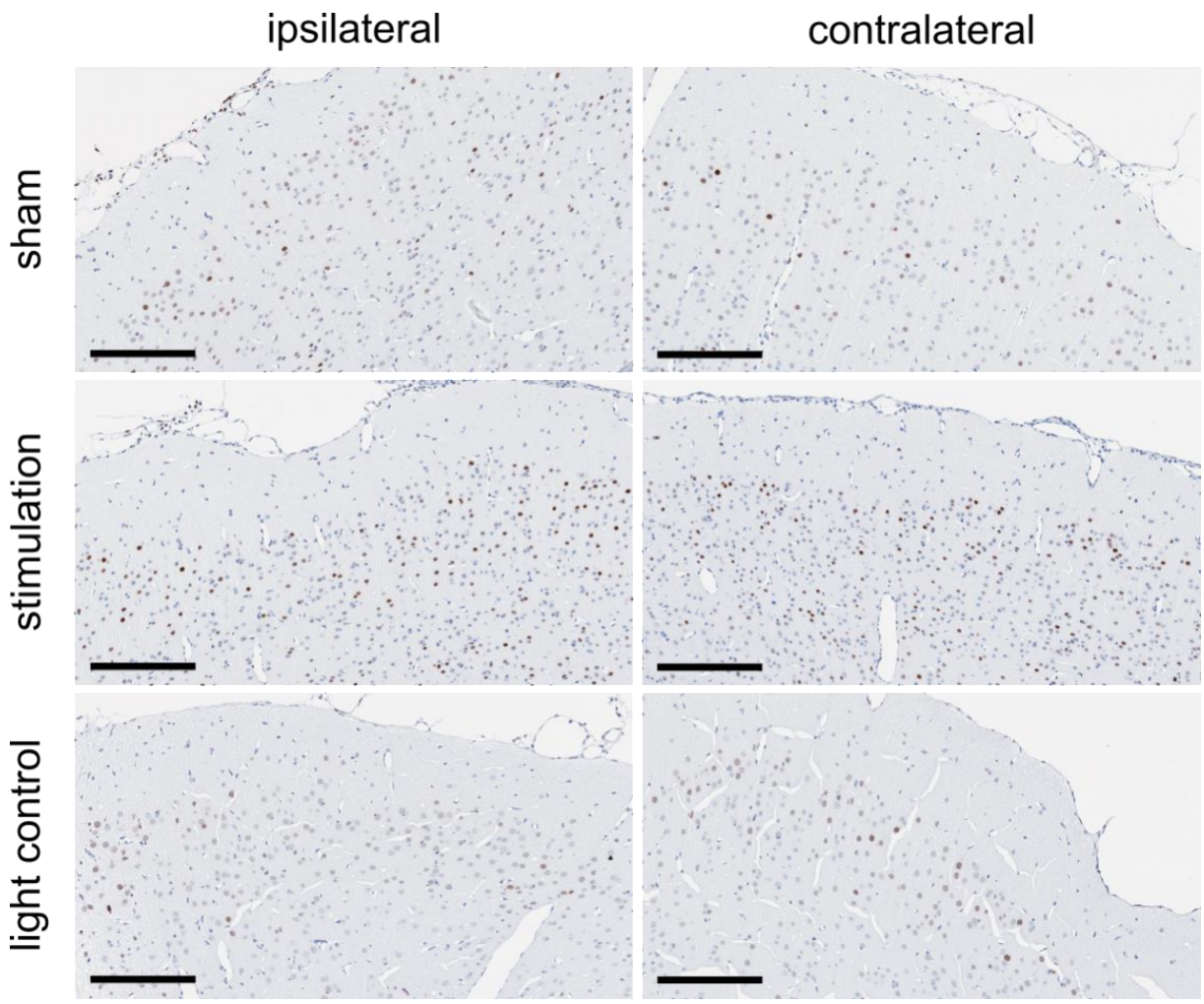

Figure 48. Representative photomicrographs of DAB c-Fos staining in SOM of animals stimulated and sacrificed three weeks after OEPC implantation. *Stronger c-Fos expression was discernible after OEPC stimulation, mostly in the layers II-IV. No visible differences can be distinguished between the ipsilateral and contralateral cortices. Scale bar: 200 μm. Adapted and reproduced with permission from John Wiley and Sons: Advanced Healthcare Materials (221), under the terms of the Creative Commons CC BY license.*

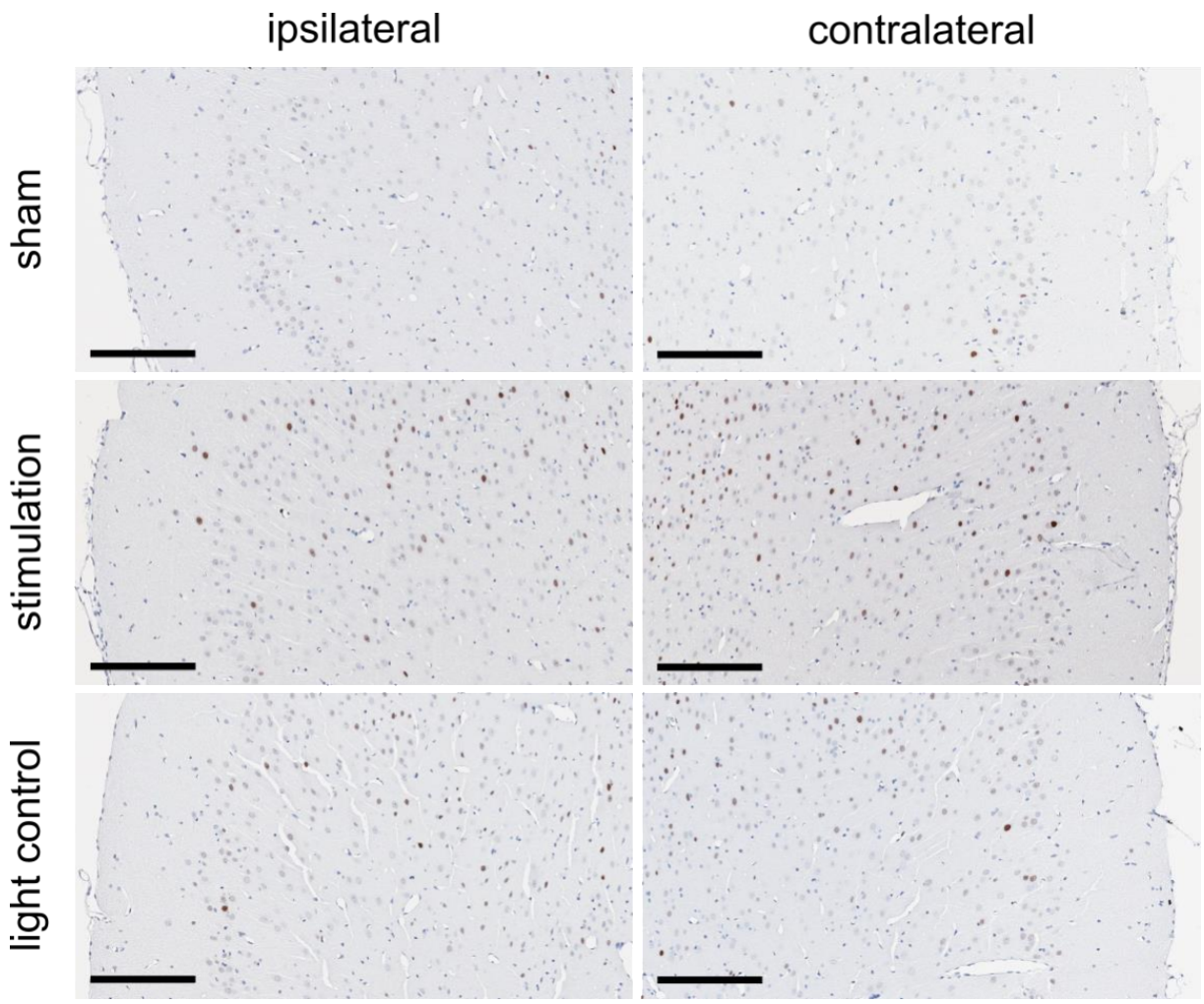

Figure 49. Representative photomicrographs of DAB c-Fos staining in EC of animals stimulated and sacrificed three weeks after OEPC implantation. *Stronger c-Fos expression was discernible after OEPC stimulation, spanning the entire cortex, but mostly pronounced in the deep layers V and VI. Slightly more c-Fos⁺ cells were noticed in the contralateral cortex of the stimulated animals. Scale bar: 200 µm. Adapted and reproduced with permission from John Wiley and Sons: Advanced Healthcare Materials (221), under the terms of the Creative Commons CC BY license.*

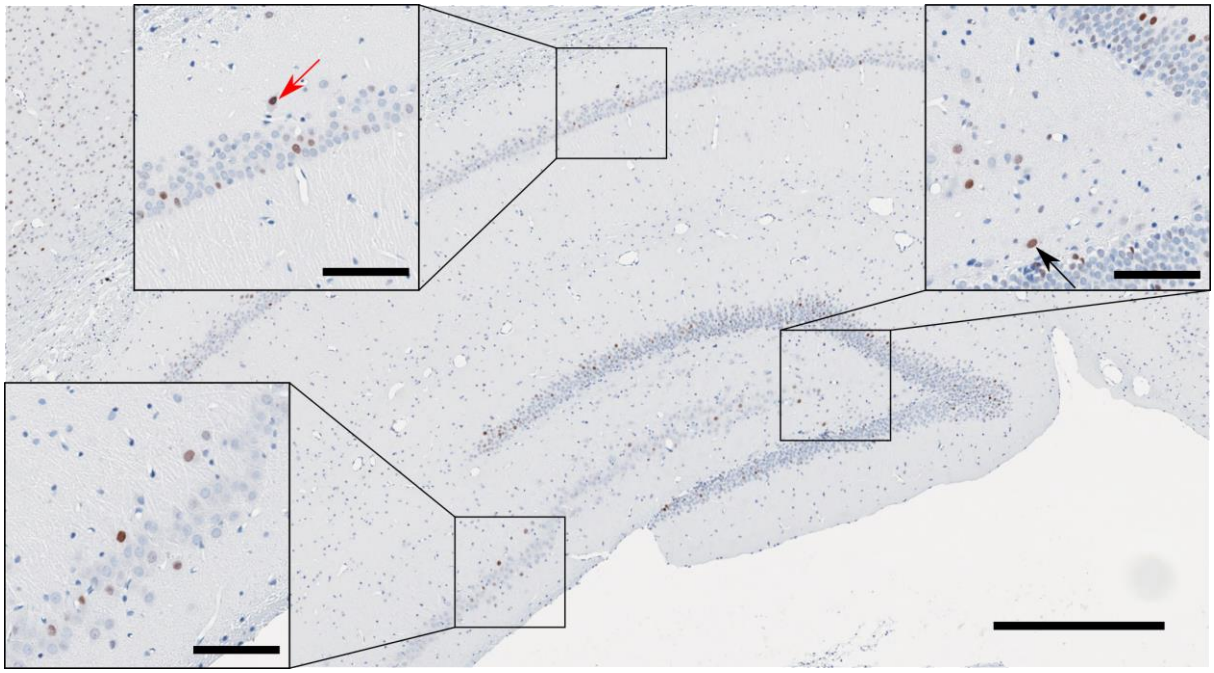

Figure 50. Representative photomicrograph of DAB c-Fos staining in HC and its subregions of a stimulated animal following three-week OEPC implantation.*c-Fos⁺ cells were predominantly present in DG, particularly in the granular cell layer, with single positive cells in the hilus (black arrow). In CA regions, fewer c-Fos⁺ cells were discernible, mostly in the stratum pyramidale, with single cells present in other strata (e.g., stratum oriens of CA1; red arrow). Image scale bar: 500 µm; insert scale bar: 100 µm.*

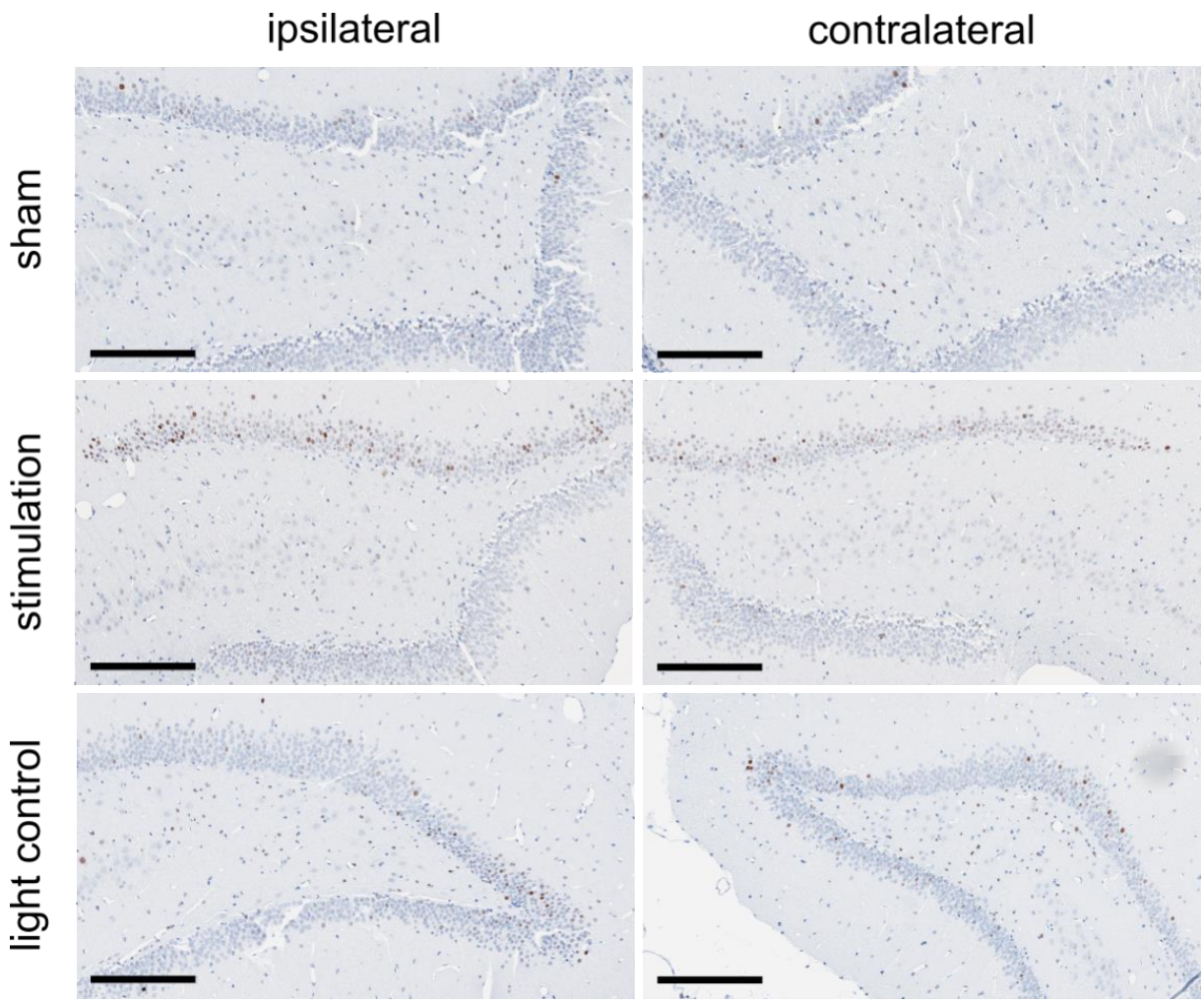

Figure 51. Representative photomicrographs of DAB c-Fos staining in HC of animals stimulated and sacrificed three weeks after OEPC implantation. *Stronger c-Fos expression was discernible after OEPC stimulation, visible in the whole HC, but mostly pronounced in the upper blade of DG. Slightly more c-Fos⁺ cells were noticed in the ipsilateral HC of the stimulated animals. Scale bar: 200 µm. Adapted and reproduced with permission from John Wiley and Sons: Advanced Healthcare Materials (221), under the terms of the Creative Commons CC BY license.*

Statistical analysis of c-Fos$^+$ cell percentage in SOM revealed a significant effect of treatment on c-Fos expression (Figure 52A; $F(2, 26) = 6.099$, $p = 0.0067$). The percentage was significantly higher in the stimulated animals ($M = 7.86$, $SD = 1.74$) compared to the sham rats ($M = 4.6$, $SD = 2.5$; $p = 0.018$), and to the light control ($M = 4.5$, $SD = 3.18$; $p = 0.015$). No significant differences were observed between the ipsi- and contralateral sides ($F(1, 26) = 0.184$, $p = 0.67$).

In EC, a significant difference was observed between the groups (Figure 52B; $F(2, 26) = 6.2$; $p = 0.0063$). Post-hoc analysis revealed statistically significant increase of c-Fos$^+$ cells in the stimulated group ($M = 3.46$, $SD = 1.87$) compared to the sham ($M = 1.43$, $SD = 0.94$; $p = 0.0072$) and to the light control animals ($M = 1.9$, $SD = 1.19$; $p = 0.043$). Similarly to SOM, no significant differences were observed between the ipsi- and contralateral sides ($F(1, 26) = 2.77$, $p = 0.11$). Only a subtle trend towards an increase of c-Fos$^+$ cell percentage on the contralateral side was noticed in all groups. A similar trend was observed during the visual inspection of the staining.

In HC, significant differences in c-Fos$^+$ cell percentage were observed between the groups (Figure 52C; $F(2, 26) = 3.474$, $p = 0.046$), specifically between the stimulation ($M = 2.86$, $SD = 1.03$) and the light control ($M = 1.3$, $SD = 0.87$; $p = 0.04$) groups. An increased cell percentage was noted between the stimulation and sham groups, however the difference was not statistically significant ($M = 1.83$, $SD = 2.06$; $p = 0.22$). This could be explained by a presence of an outlier, which was not excluded. No significant difference was observed between the two sides of the brain ($F(1, 26) = 0.477$, $p = 0.5$). Only a trend towards a higher c-Fos$^+$ cell percentage on the ipsilateral side in the stimulated group was discernible, mirroring the results of the visual inspection.

In summary, light-controlled OEPC stimulation led to an increase in c-Fos$^+$ cell percentage compared to sham treatment and light treatment without implanted OEPC. This held true for all explored regions, on both ipsi- and contralateral sides.

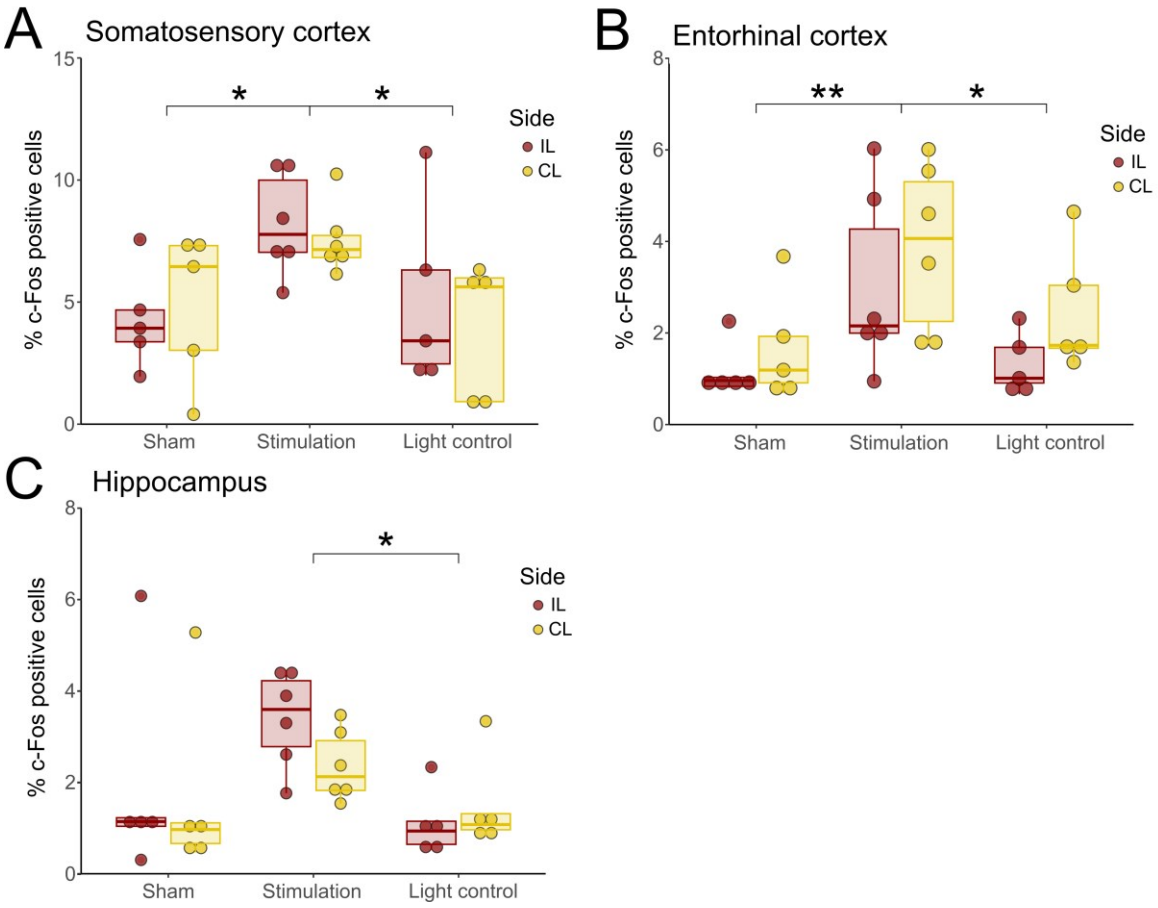

Figure 52. Statistical analysis of the percentage of c-Fos+ cells in various brain regions after OEPC stimulation following a three-week implantation. *Positive cell percentage was calculated relatively to the total number of nuclei 60 min following stimulation or control conditions. (A) Comparison between the stimulated and control groups in SOM. (B) Comparison between the stimulated and control groups in EC. (C) Comparison between the stimulated and control groups in HC. * p < 0.05, ** p < 0.01. Adapted and reproduced with permission from John Wiley and Sons: Advanced Healthcare Materials (221), under the terms of the Creative Commons CC BY license.*

9.3.3 Characterisation of c-Fos expressing cells

To describe in detail which brain cell types express c-Fos following OEPC stimulation, several double and triple IF staining of the protein with common neuronal and glial markers were performed. In all inspected sections from all selected animals, c-Fos showed co-expression with NeuN, a marker of differentiated neurons (Figure 53). This co-expression was present in all explored brain regions, in both the ipsi- and contralateral hemispheres.

c-Fos expression in interneurons was assessed through multiple IF staining with CR, PV, and SST. Triple IF staining of c-Fos with CR and PV did not reveal co-expression in any

configuration (c-Fos/CR, c-Fos/PV, CR/PV) in the investigated brain regions (Figure 54). In the double IF staining of c-Fos and SST, a few c-Fos$^+$/SST$^+$ cells were observed in SOM (Figure 55) and the hilus of DG (data not shown) of stimulated animals. However, the visible majority of SST$^+$ did not show c-Fos co-expression.

To explore whether c-Fos is also expressed by glia, double IF staining of c-Fos with GFAP, a marker of astrocytes, was conducted. In n = 8 animals, no c-Fos signal was detected in GFAP$^+$ cells in any of the investigated regions (Figure 56). Notably, in one animal, two c-Fos$^+$/GFAP$^+$ cells were observed in one field of view in the ipsilateral cortex, specifically in cortical layer I, near the site of contact with the OEPC implant (Figure 57).

In summary, c-Fos was expressed almost exclusively in differentiated neuronal cells. Given the shape and localisation of the c-Fos$^+$ cells in the brain tissue, the main cell type stimulated by OEPC at the given parameters seems to be the major excitatory projection neuron, particularly a layer II/III pyramidal cell. Only single SST$^+$ interneurons were responsive to the stimulation.

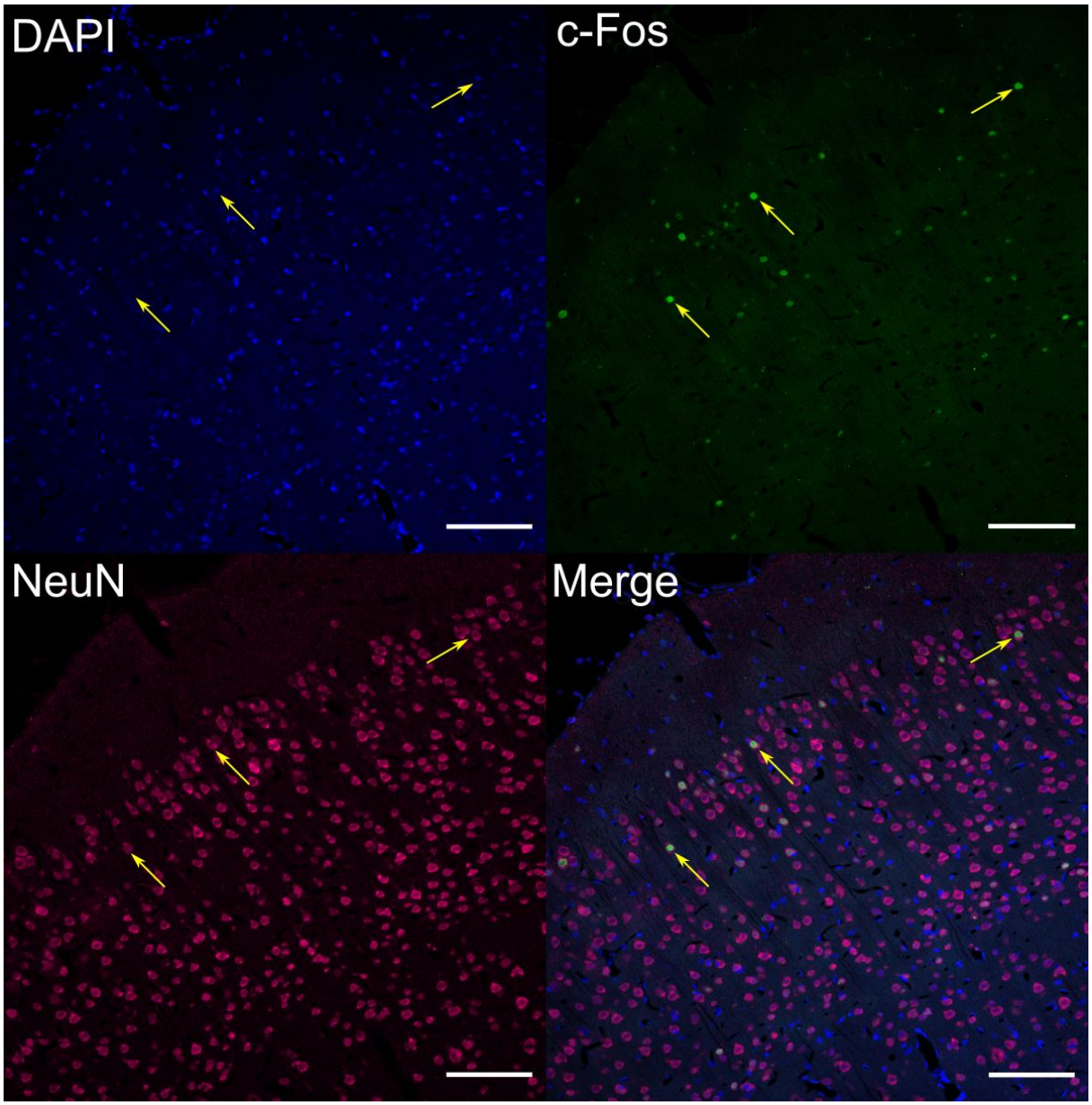

Figure 53. Representative image of double IF staining of c-Fos and NeuN in stimulated animals.*c-Fos (green) is co-expressed with NeuN, a marker of differentiated neurons (magenta), indicative of neuronal expression of c-Fos. DAPI counterstaining of nuclei (blue) was used to facilitate orientation in the section. Arrows indicate examples of c-Fos⁺/NeuN⁺ cells. Scale bar: 100 µm. Adapted and reproduced with permission from John Wiley and Sons: Advanced Healthcare Materials (221), under the terms of the Creative Commons CC BY license.*

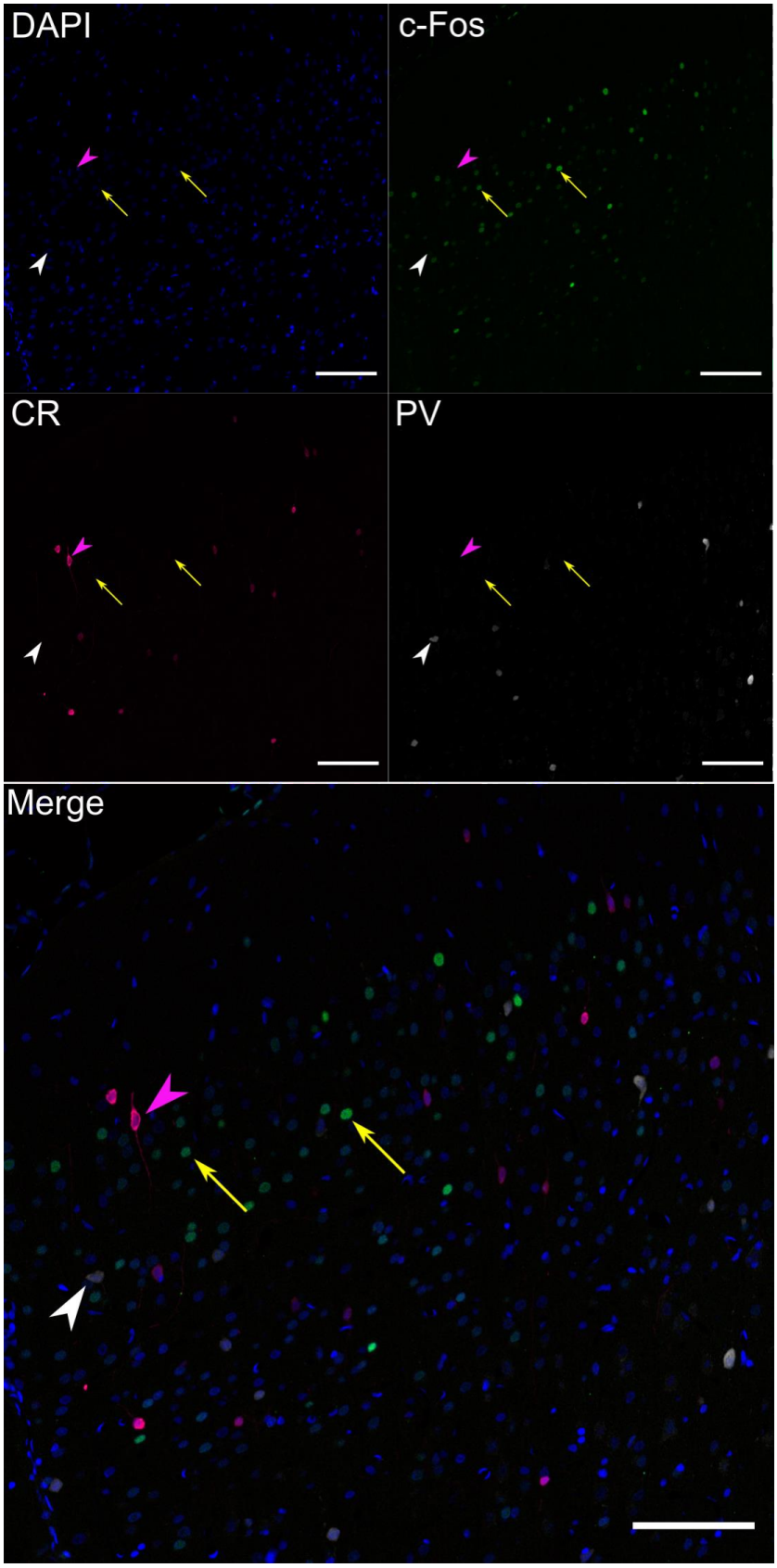
DAPI
c-Fos
CR
PV
Merge

Figure 54. Representative image of triple IF staining of c-Fos with CR and PV in stimulated animals.*c-Fos (green) is not expressed in cells marked with calretinin (magenta) nor parvalbumin (white), two common markers of interneurons. DAPI counterstaining of nuclei (blue) was used to facilitate orientation in the section. Arrows indicate examples of c-Fos⁺ cells, magenta arrowheads point examples of CR⁺ cells, and white arrowheads – PV⁺ cells. Scale bar: 100 µm. Adapted and reproduced with permission from John Wiley and Sons: Advanced Healthcare Materials (221), under the terms of the Creative Commons CC BY license.*

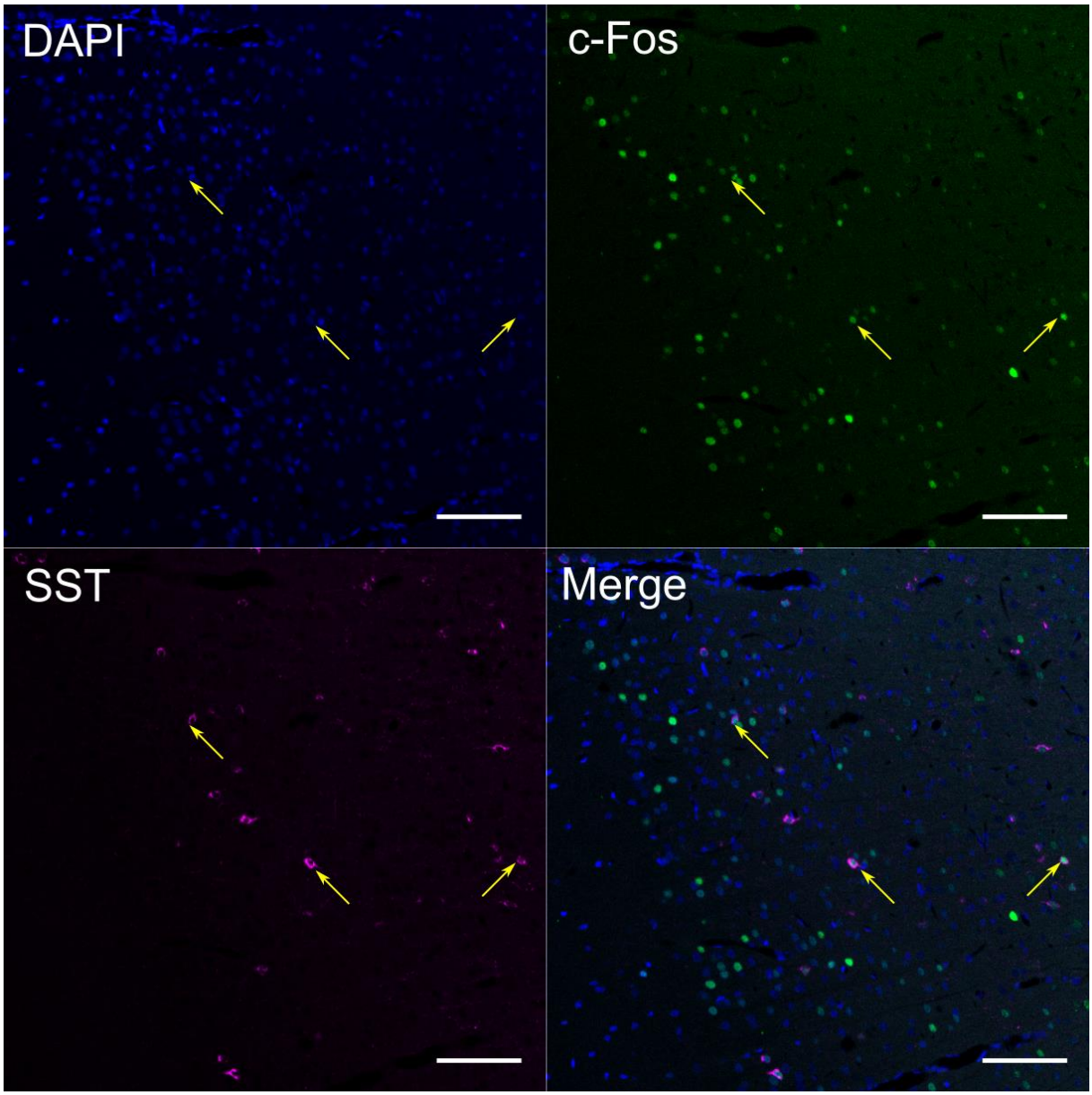

Figure 55. Representative image of double IF staining of c-Fos and SST in stimulated animals. *In single cells, c-Fos (green) is co-expressed with somatostatin (magenta), a marker of interneurons, e.g., Martinotti cells. DAPI counterstaining of nuclei (blue) was used to facilitate orientation in the section. Arrows indicate examples of c-Fos⁺/SST⁺ cells. Scale bar: 100 µm*

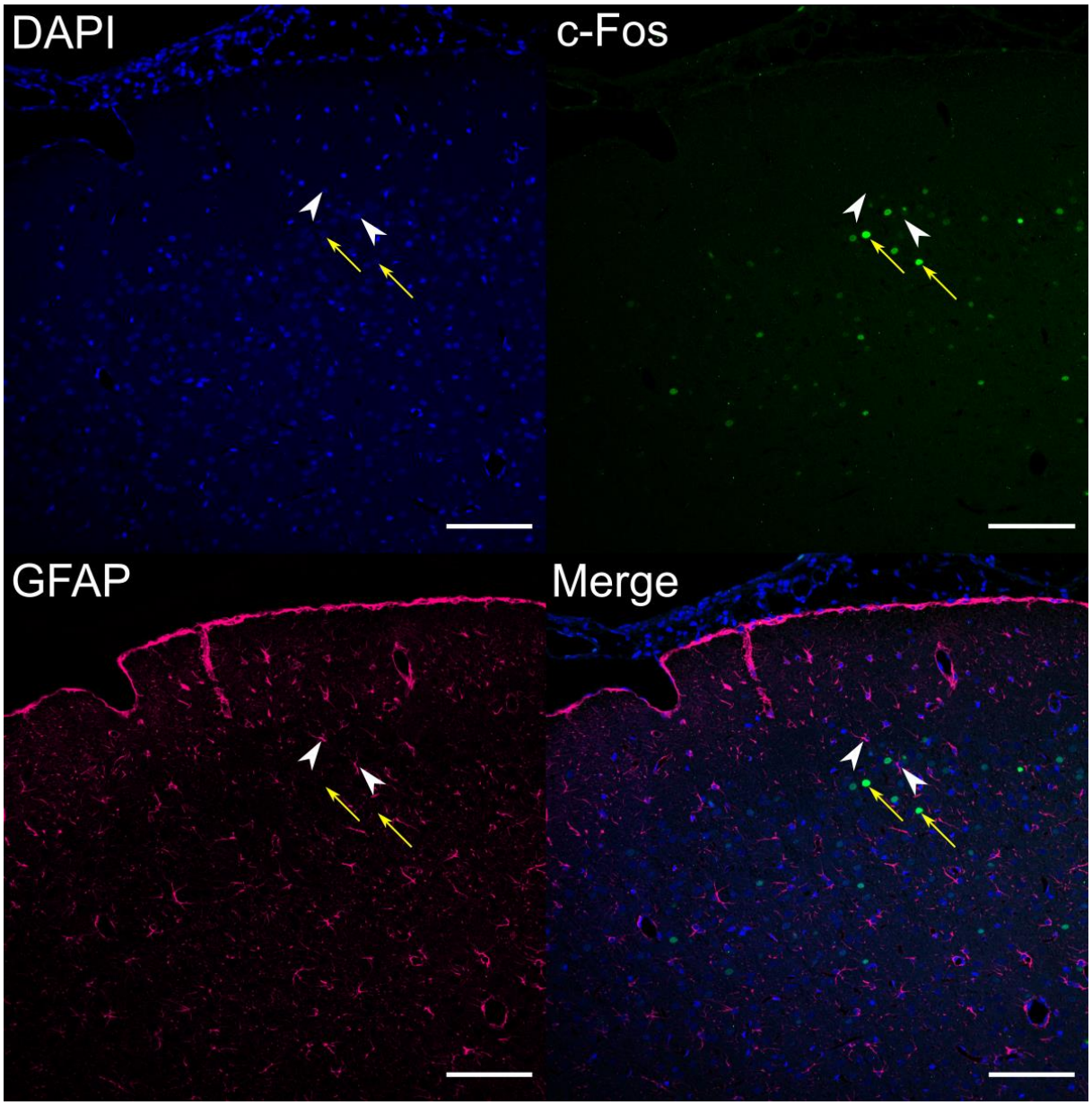

Figure 56. Representative image of double IF staining of c-Fos and GFAP in stimulated animals. *c-Fos (green) is not expressed in cells marked with GFAP (magenta), a common marker of astrocytes. DAPI counterstaining of nuclei (blue) was used to facilitate orientation in the section. Arrows indicate examples of c-Fos⁺ cells, magenta arrowheads point examples of CR⁺ cells, and white arrowheads – PV⁺ cells. Scale bar: 100 µm. Adapted and reproduced with permission from John Wiley and Sons: Advanced Healthcare Materials (221), under the terms of the Creative Commons CC BY license.*

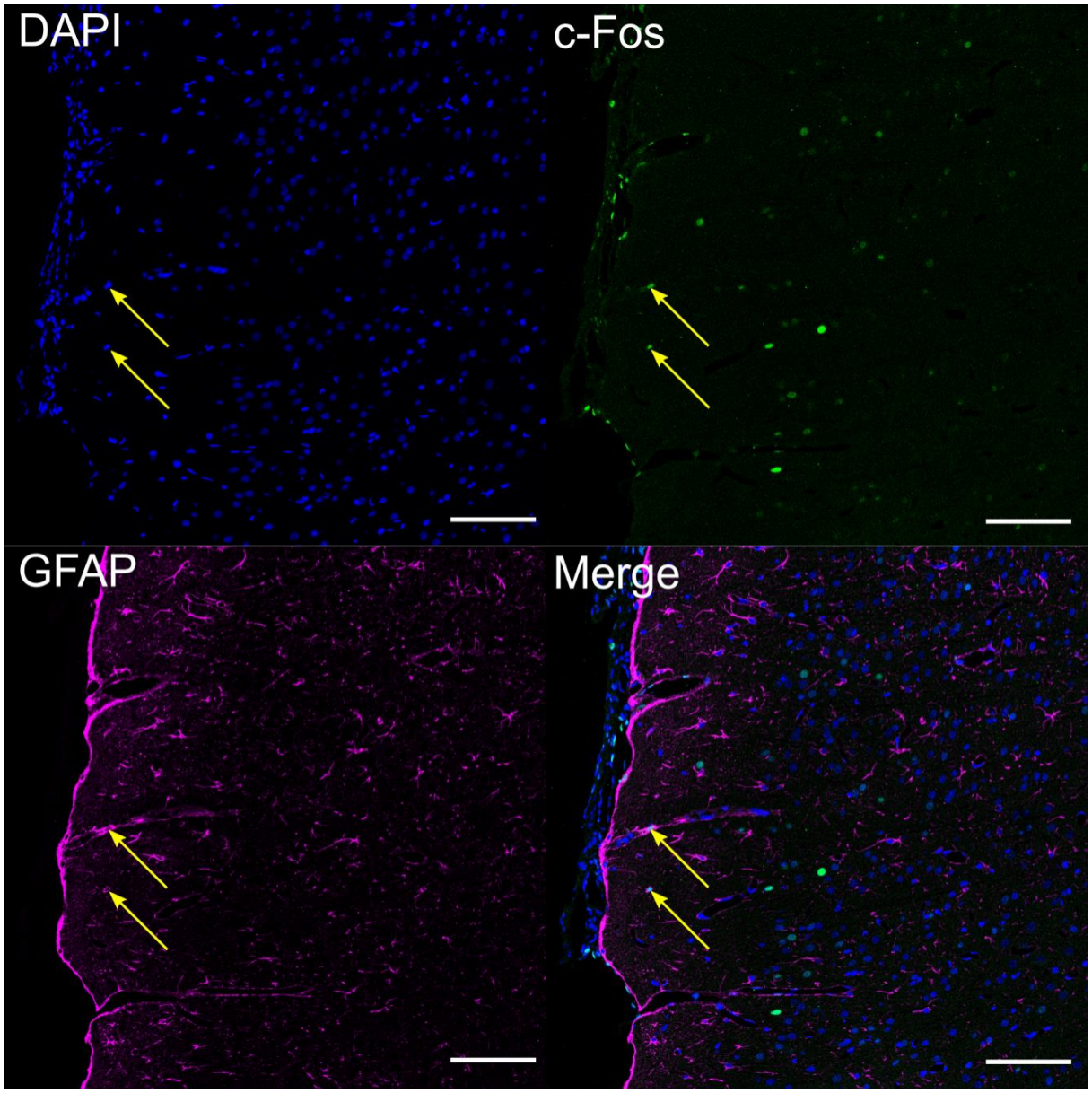

Figure 57. Double IF staining of c-Fos and GFAP in the animal with single c-Fos+/GFAP+ cells. *Arrows indicate double positive cells in the cortical layer I, close to the surgical site. Scale bar: 100 µm. Adapted and reproduced with permission from John Wiley and Sons: Advanced Healthcare Materials (221), under the terms of the Creative Commons CC BY license.*

9.3.4 Foreign body response

To investigate the reaction of brain tissue against implanted parylene OEPC, IHC staining for glial and immune cell markers was conducted in sections obtained from the animals sacrificed three weeks post-surgery. Among the analysed cell types, the main focus was on astrocytes (marked with GFAP), microglia (Iba1), macrophages and monocytes (CD68) as well as other leukocytes (CD45). Astrocytes and microglia are cell types native to the brain, exhibiting either a naïve or a reactive state, associated with neuroinflammation. Reactivity of those cells can be inferred from their morphology and proliferation rate. Leukocytes, including monocytes, are immune blood cells capable of migrating from blood vessels into the tissue in the course of the inflammatory process. The characterisation of the morphology, cell number and localisation of the mentioned cell types enables the description of the foreign body response, such as inflammation or glial scar formation. The evaluation of these factors shall contribute to a comprehensive assessment of the interaction between brain tissue and implanted parylene OEPC.

Upon visual inspection of the brain tissue, a more pronounced GFAP staining and an increased number of positive cells was observed in the ipsilateral parietal cortex compared to its contralateral counterpart (Figure 58). Particularly strong staining was present in the most superficial cortical layer near the surgical site. A detailed assessment of astrocytic morphology revealed a stronger GFAP staining within single cells as well as a rounder cell shape and cellular hypertrophy in the ipsilateral SOM (Figure 58, red arrows) than in the contralateral hemisphere (Figure 58, green arrows). This type of astrocytic morphology is associated with reactive gliosis. However, in the comparison between the sections from the OEPC-implanted and non-implanted animals, no discernible differences in cell number and morphology were noted. Hence, the astroglial reactivity should be attributed to the surgical procedure, not the implantation itself.

In a similar fashion, a visual examination of Iba1 staining uncovered a higher number of positive cells on the ipsilateral side close to the craniectomy compared to its contralateral counterpart (Figure 59). Numerous cells were present not only within the brain parenchyma, but also on its surface. Within the tissue, several $Iba1^+$ cells with round morphology were observed. Analysis of cellular morphology indicated a rounder shape, fewer processes, and less intricate ramification (fewer and shorter processes) in microglia within the brain parenchyma of SOM on the ipsilateral side (Figure 59, red arrows). On the contralateral side, cells were less abundant, less prevalent on the brain surface, and possessed more processes with intricate ramification (Figure 59, green arrows). Once

again, no distinguishable differences in cell number and morphology were observed between the implanted and non-implanted animals.

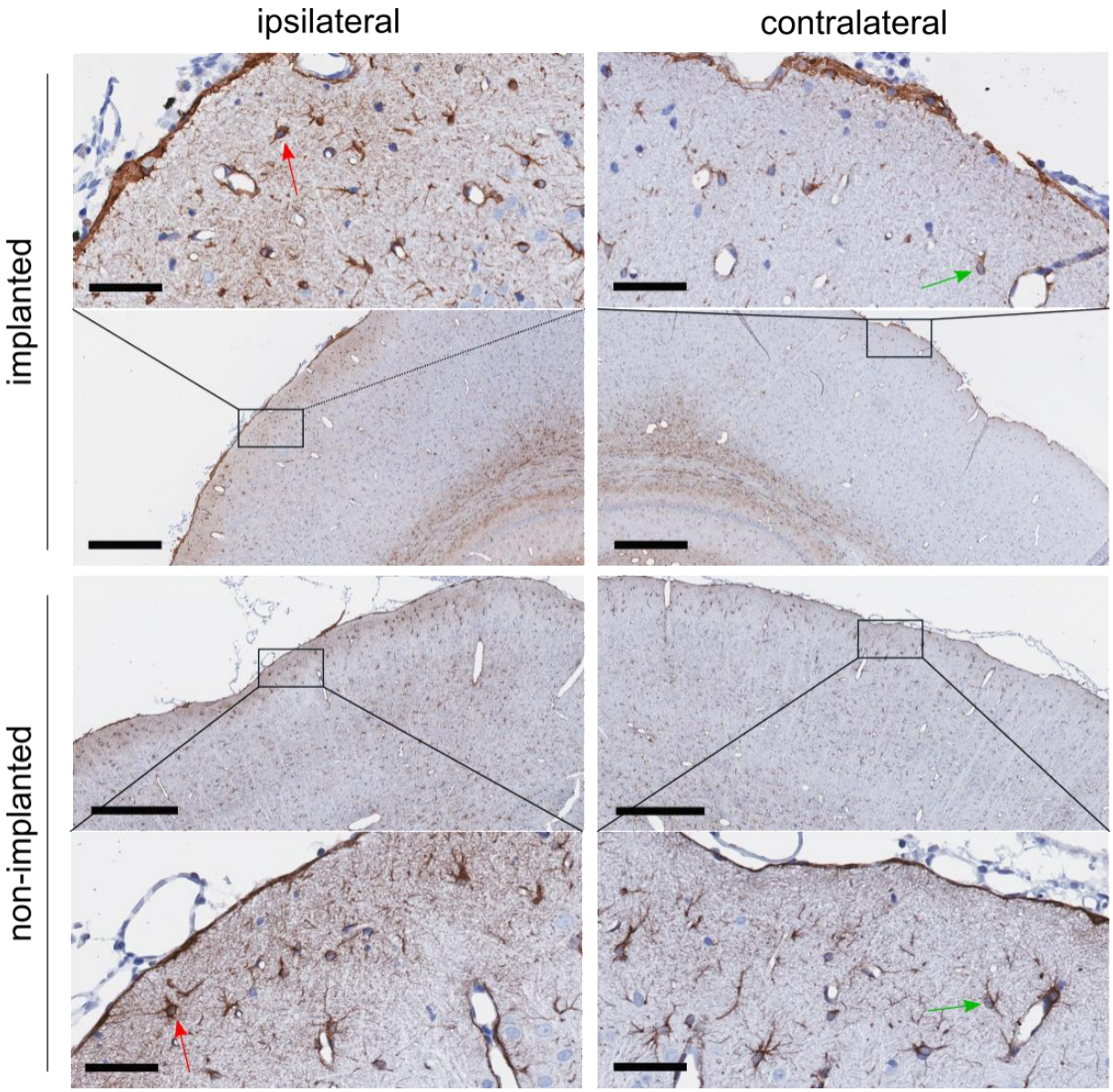

Figure 58. GFAP immunoreactivity in SOM following three weeks of OEPC implantation or sham surgery. *GFAP staining in OEPC-implanted (upper panel) and non-implanted animals (lower panel) was stronger in the ipsilateral hemisphere (left panel) than in its contralateral counterpart (right panel). Red arrows – GFAP⁺ cells displaying a reactive morphology; green arrows – GFAP⁺ cells not showing marks of reactivity. Image scale bar: 400 µm, insert scale bar: 50 µm. Adapted and reproduced with permission from John Wiley and Sons: Advanced Healthcare Materials (221), under the terms of the Creative Commons CC BY license.*

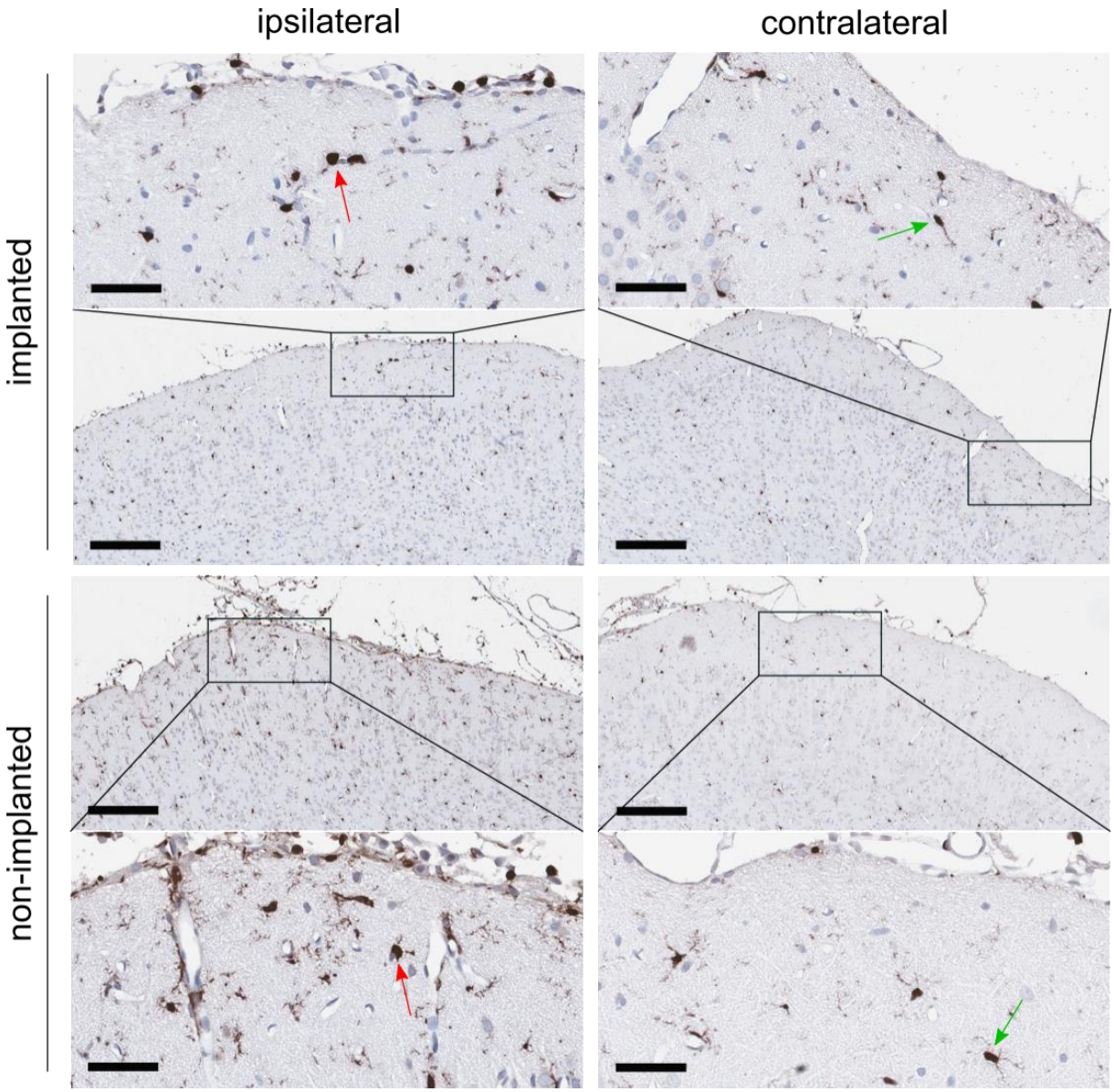

Figure 59. Iba1 immunoreactivity in SOM following three weeks of OEPC implantation or sham surgery. *Iba1 staining in OEPC-implanted (upper panel) and non-implanted animals (lower panel) was stronger in the ipsilateral hemisphere (left panel) than in its contralateral counterpart (right panel). Red arrows – Iba1⁺ cells showing a reactive morphology; green arrows – Iba1⁺ cells without marks of reactivity. Image scale bar: 200 µm, insert scale bar: 50 µm. Adapted and reproduced with permission from John Wiley and Sons: Advanced Healthcare Materials (221), under the terms of the Creative Commons CC BY license.*

Migration of immune cells into the brain parenchyma was evaluated through IHC staining of two common markers: CD45, a panleukocytic marker, and CD68, a marker specific to monocytes and macrophages. Weak CD45 signal was observed only in a few cells in the ipsilateral SOM near the surgical site, confined to the brain surface and the fibrous tissue covering the surface (Figure 60, red arrows). The brain parenchyma remained completely free of $CD45^+$ cells. The corresponding area in the contralateral hemisphere showed no presence of CD45-stained cells. Similarly, $CD68^+$ immune cells were identified exclusively on the ipsilateral side, close to the surgical opening (Figure 61, red arrows) and not in the contralateral parietal cortex. The stained cells were primarily located on the brain surface and within the fibrous tissue. Notably, a few $CD68^+$ cells were also observed within the walls of cerebral blood vessels (Figure 61, blue arrowheads). No cells were detected within the brain parenchyma.

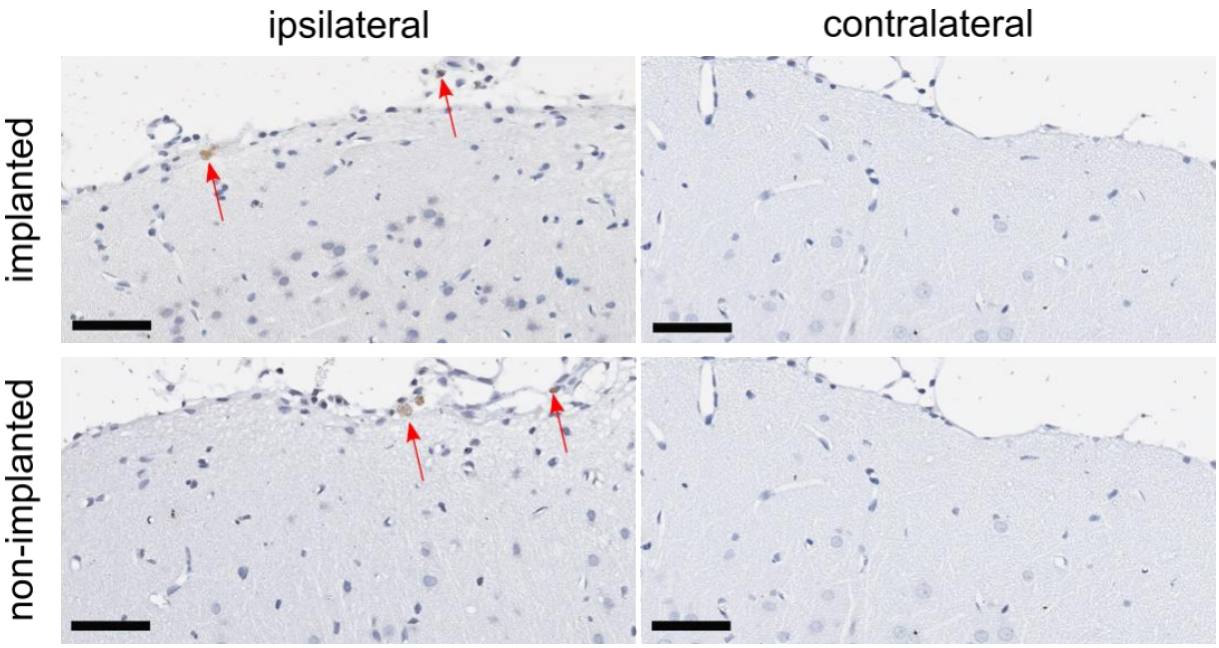

Figure 60. CD45 immunoreactivity in SOM following three weeks of OEPC implantation or sham surgery. *$CD45^+$ cells were observed in OEPC-implanted (upper panel) and non-implanted animals (lower panel) on the surface of the ipsilateral hemisphere (left panel). Contralateral SOM remained devoid of $CD45^+$ cells (right panel). Red arrows – $CD45^+$ cells. Scale bar: 50 µm. Adapted and reproduced with permission from John Wiley and Sons: Advanced Healthcare Materials (221), under the terms of the Creative Commons CC BY license.*

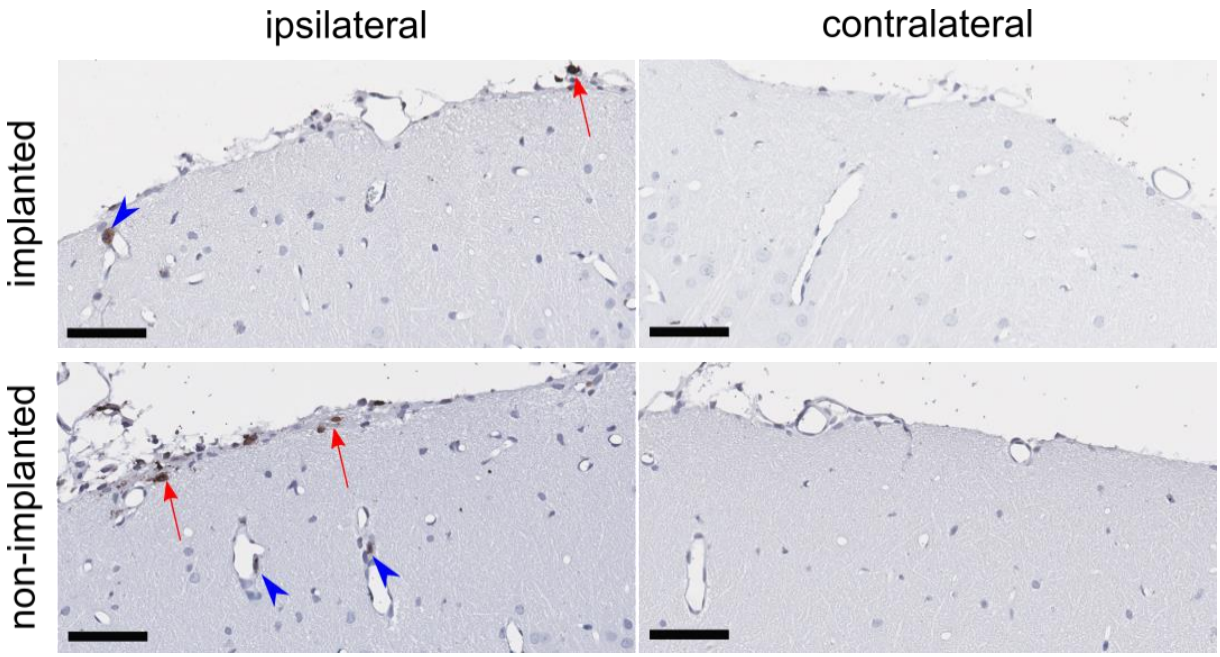

Figure 61. CD68 immunoreactivity in SOM following three weeks of OEPC implantation or sham surgery. *$CD68^+$ cells were observed in OEPC-implanted (upper panel) and non-implanted animals (lower panel) on the surface of the ipsilateral hemisphere and within blood vessels (left panel). Contralateral SOM remained devoid of $CD68^+$ cells (right panel). Red arrows – $CD68^+$ cells on the surface of the brain; blue arrowheads – $CD68^+$ cells inside the blood vessel walls. Scale bar: 50 µm. Adapted and reproduced with permission from John Wiley and Sons: Advanced Healthcare Materials (221), under the terms of the Creative Commons CC BY license.*

No extensive fibrotic tissue proliferation was observed. In some cases, fibrotic tissue was still present on the brain surface, but usually it was removed during the OEPC explantation.

9.3.5 Device durability during the implantation

Parylene OEPC implantation brought a lot of insight not only into the device biocompatibility, but also into the material stability and sustained functionality in the semi-chronic timescale. Material durability was examined at the microscopic level through SEM imaging (Figure 62). Both p-n layer and back electrode surfaces were compared between the explanted devices and controls freshly removed from the wafer. The surface of the p-n layer in control devices showed characteristic nanocrystal domains (Figure 62A), while it appeared smoother in the explanted OEPC (Figure 62B). Nevertheless, the granular appearance of the material was still discernible in the explanted devices. No signs of material deterioration, such as delamination, cracking, or pores were observed. The p-n surface remained unchanged also in the close vicinity of the attached tissue (Figure 63). No apparent differences in the back electrode surface were observed between the control and explanted OEPC (Figure 62C-D),

except for dot-like structures – probably debris – adhering to the latter. In summary, the observed changes in explanted devices indicate rather minor mechanical deterioration or adhesion of proteins and organic compounds.

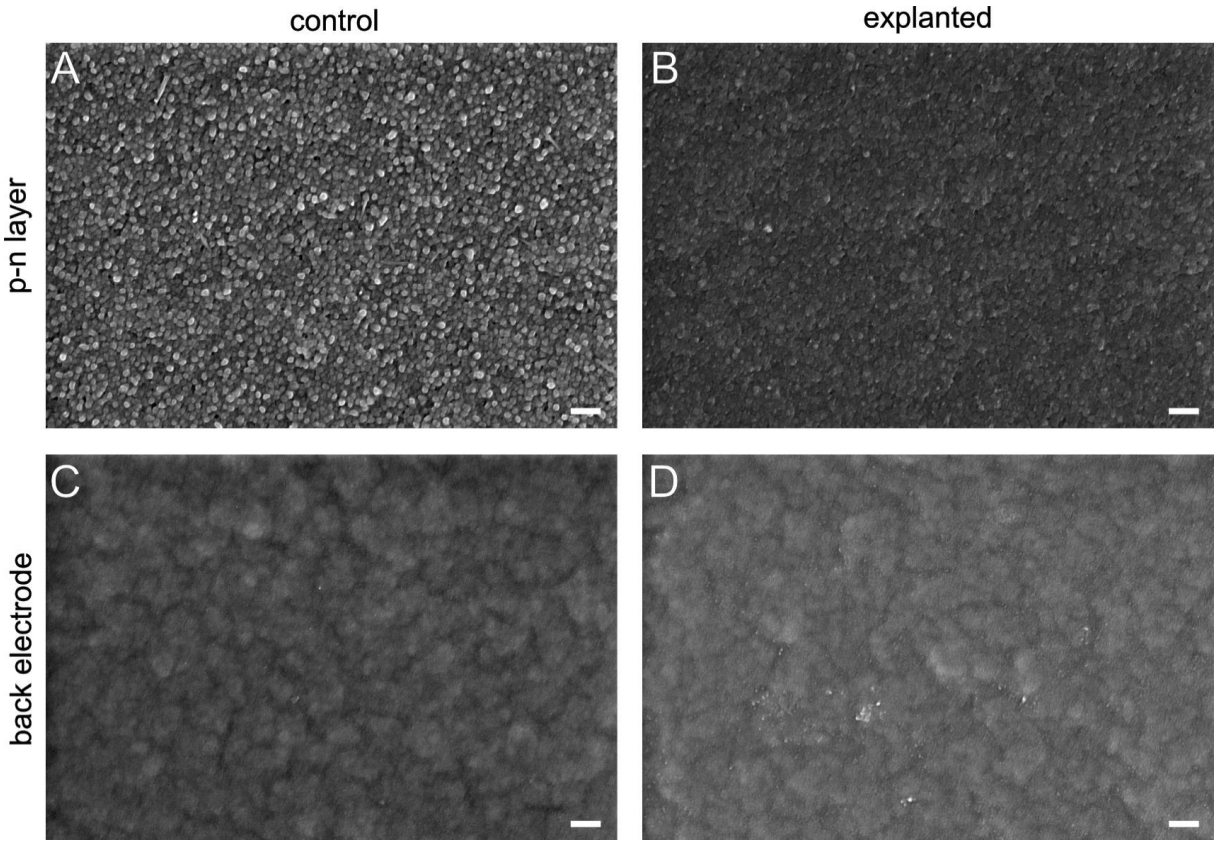

Figure 62. Representative SEM photomicrographs of parylene OEPC explanted three weeks post-surgery. *(A) Surface of the p-n layer of the control device removed directly from the wafer. (B) Surface of the p-n layer of the device explanted from the animal. (C) Surface of the back electrode of the control device. (D) Surface of the back electrode of the explanted device. Scale bar: 200 nm. Adapted and reproduced with permission from John Wiley and Sons: Advanced Healthcare Materials (221), under the terms of the Creative Commons CC BY license.*

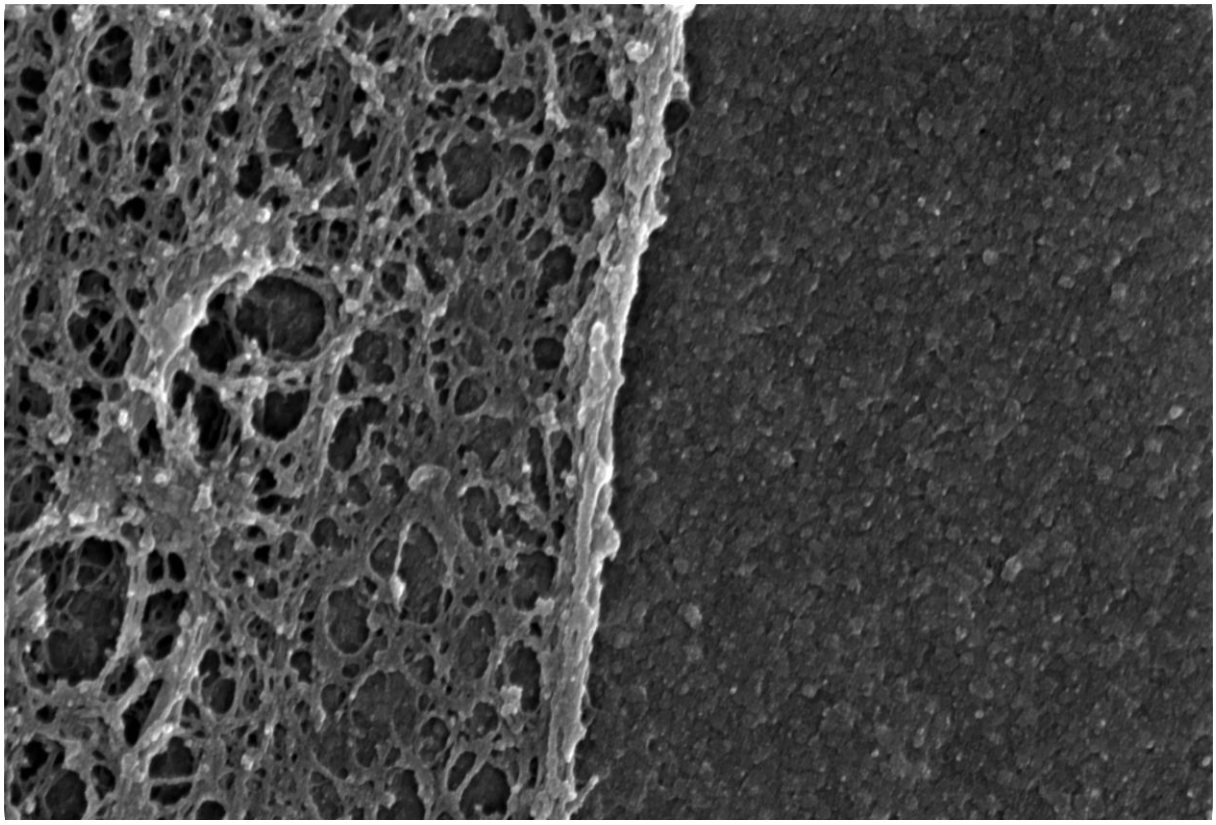

Figure 63. Representative SEM photomicrograph of the surface of the parylene OEPC with attached tissue. *Smoothening of the p-n layer was visible next to the tissue. No signs of delamination or other damage to the surface was observed. Adapted and reproduced with permission from John Wiley and Sons: Advanced Healthcare Materials (221), under the terms of the Creative Commons CC BY license.*

The functionality of the explanted parylene OEPC was carried out by measuring photovoltage time courses. The transient potentials evoked by red light pulses in the explanted devices showed only a minor decrease in the initial maximum voltage peak compared to the control OEPC freshly removed from the wafer (Figure 64). The shape of the waveform remained similar to that of the fresh control OEPC, displaying a distinct peak and steep discharging curve, which suggests an unaltered charging/discharging behaviour. The slight decrease in the voltage peak and less steep discharging curve in explanted OEPC can be attributed to the changes in the device surface, visible in SEM. Nevertheless, both structural and functional analysis indicated high stability of the parylene OEPC within the animal body.

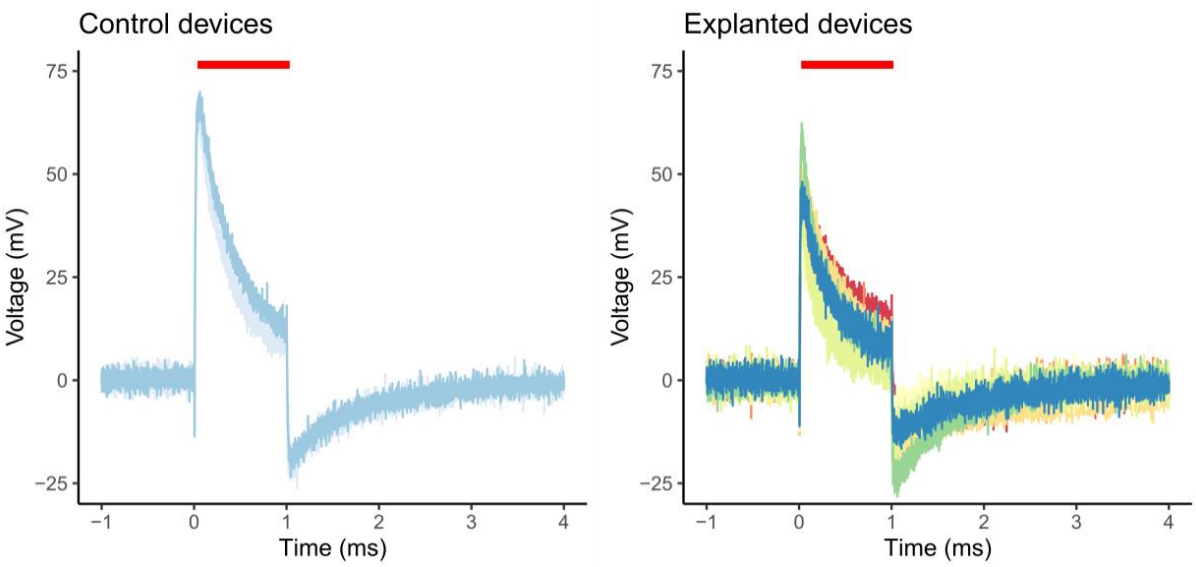

Figure 64. Measurement of transient photovoltage in explanted and control OEPC. *Visible charging behaviour during illumination (red bar) with consecutive discharging phase remained clearly discernible in both control (left) and explanted (right) devices. Control OEPC, n = 2; explanted OEPC, n = 9. Adapted and reproduced with permission from John Wiley and Sons: Advanced Healthcare Materials (221), under the terms of the Creative Commons CC BY license.*

10 DISCUSSION

OEPC offers an attractive alternative to standard neurostimulation, being a small, lightweight, and wirelessly controlled device. To fully elucidate its potential as an implant, an extensive characterisation of stimulation effects, biological responses, and device stability during a prolonged interaction between OEPC and biological systems is necessary. This study aims to provide a detailed description of these features in three models – specifically, in rat cultured cells, tissue culture, and living brain.

10.1 OEPC BIOCOMPATIBILITY AND NEUROSTIMULATION *IN VITRO*

10.1.1 Selection of the optimal coating strategy

Prior to assessment of the cytotoxicity of OEPC in cell culture, several coating strategies were tested. Despite excellent culture attachment and network formation on Geltrex – a coating material resembling ECM. It mostly consists of laminin, collagen, and various other proteins, building up a thick film reaching up to 20 µm (234). This could potentially negatively influence OEPC charging, which is why the second best coating material, PDL, was selected for subsequent experiments.

Interestingly, only few cells attached to PEI, a coating material frequently used in neuroscience, such as multi-electrode array chips (235, 236). They did not survive on the material, leaving a couple of dead cells attached throughout the experiment. This could be attributed to unknown interactions between the PTCDI and PEI, as the literature in this regard is lacking. PEI has been described to increase phototoxicity of sulfonated aluminum phthalocyanine (237). However, this could not explain the noxious effect of PEI in this case. First, PTCDI is the most superficial layer of the photoactive pixel and, unless destroyed, H_2Pc should not be in contact with the coating material. Moreover, H_2Pc used in the manufacturing of the OEPC was metal-free, which is not known to exhibit the same phototoxic effect. Lastly, in this preliminary test, the cells were not illuminated with red light, and unsubstituted H_2Pc is not known to be activated by low-intensity white light (238). Therefore, the exact nature of cytotoxic effects of PEI on OEPC requires additional studies.

10.1.2 OEPC cytotoxicity in primary cell culture

While in our previous studies (13, 15), neurons have already been successfully cultivated on OEPC surfaces with similar composition, this study aimed at detailed investigation of the course of cellular damage progression. Leveraging the nature of the LDH

assay, we repetitively collected media samples from the same primary cortical cell culture, reducing inter-specimen variance and cross-referencing results with microscopic images. Consistent with the study conducted by Schmidt et al. (15), we observed no discernible differences in cytotoxicity between neurons cultivated on OEPC and those on glass cover slips at selected time points: the initiation of the culture (DIV5), the midpoint (DIV10), and the end, shortly before OEPC stimulation (DIV14). This indicates good material biocompatibility for at least two weeks of culture.

However, noteworthy changes in cellular damage occurred over time in both control and OEPC groups. The substantial increase in the LDH release on DIV10, compared to DIV5, should be attributed to mitosis inhibition. Two compounds used in the study to inhibit cell proliferation, FdUrd and Ara-C, are well known cytostatics used in antitumour and antiviral therapies. Both present different mechanisms of action. In cell, FdUrd is converted to 5-fluoro-2'-deoxyuridine-5'-monophosphate, which inhibits thymidylate synthase, an enzyme responsible for production of 2'-deoxythymidine-5'-monophosphate (239). The lack of the nucleoside effectively blocks DNA synthesis. Ara-C, also known as cytarabine, is a pyrimidine nucleoside analogue. In cell, it is converted into the triphosphate form, which competes with cytidine during the S-phase of the cell cycle, inhibiting DNA synthesis (240).

During cell preparation from the brain, a heterogeneous cellular population is extracted, containing neurons, glial cells, neural precursor cells, vascular endothelial cells, meningeal fibroblasts etc. Among these, only differentiated neurons do not proliferate and are resistant to cytostatic drugs. To enrich the culture, the cells are allowed to proliferate during first four days to acquire more differentiated neurons from the precursor cells. After this time point, cytostatics are added for 24 hours to limit the proliferation of non-neuronal cells. As a result, the cells are not only unable to divide, but their DNA is also degraded, setting off apoptosis (241).

LDH is released upon any damage in the plasma membrane, being sensitive to necrosis, apoptosis, and other types of cellular damage (242). In case of our primary culture, LDH activity in supernatant peaked at DIV10, with the subsequent reduction in at DIV14. This supports the notion that cytostatic-induced apoptosis is the main contributor to the LDH release. Nevertheless, the sustained elevation of supernatant LDH activity at DIV14 compared to DIV5 suggests an increased cell death rate associated with the ageing of the culture. Neurobasal medium has been also described to cause excitotoxicity in hippocampal neurons after DIV12 (243), which could additionally contribute to cell damage and LDH increase at the latest timepoint.

The LDH assay conducted before and after light stimulation revealed a decrease in LDH levels post-treatment. This effect could not be attributed to the natural decay of LDH, as the enzyme's approximate 9-hour half-life in the culture medium (244) significantly exceeds the experimental time frame (90 minutes from the onset of OEPC stimulation to sample collection). Such a rapid reduction in LDH activity may stem from its inactivation by chemical compounds present in the medium. Hydrogen peroxide and ROS are known to be generated upon illumination of photoactive organic semiconductors (193, 196, 204, 245) and their inactivating effect on dehydrogenases, including LDH, has been previously documented (246, 247). Nevertheless, a thorough understanding of the generation of ROS in OEPC used in the study, as well as their exact effect on LDH activity, require further exploration.

Red light illumination might have caused photochemical reactions with light-sensitive compounds of the cellular media, leading to LDH depletion. Pre-treating DMEM with red or white light does not seem to cause significant changes in subsequent cell culture (248). However, the referenced study employed significantly lower light intensity (0.02 mW/mm^2) compared to the settings used in this study (3.2 to 8.21 mW/mm^2). Moreover, whether this holds true for Neurobasal A medium or the media supplements used for cell culture in this study remains unclear.

10.1.3 c-Fos expression after OEPC stimulation in primary cell culture

Light-controlled OEPC stimulation has been previously investigated in terms of voltage changes in cellular membrane (13, 14), action potential generation in primary hippocampal neurons (15), and activity synchronisation in chicken cardiac cells (249). However, most of these studies have focused on the visible effects of the stimulation at the single-cell level and have not addressed the possible neuronal integration of subthreshold depolarisation through spatial or temporal summation. This has left our understanding of neuronal activity in the whole network limited. To provide a more comprehensive characterisation of those effects, we decided to use c-Fos as a marker of recent neuronal activity.

Experiment 1

In Experiment 1, primary cortical neurons were subjected to two stimulation protocols: low-frequency light with a longer pulse, as previously described in the electrophysiological study (15), and high-frequency light with a shorter pulse, intended for use in the planned *in vivo* study. The c-Fos expression was characterised as positive cell percentage. $c\text{-}Fos^+$ cell percentage in the stimulated cell cultures was similar to that in cells treated with glutamate,

a major excitatory neurotransmitter. Cultured cortical neurons are the most responsive to glutamate at DIV14 (250), it is therefore reasonable to assume its addition at this time point elicits the most potent activation of the cells. The similar percentage of c-Fos$^+$, active cells indicates a high neurostimulatory potential of OEPC.

Low-frequency stimulation yielded a slightly higher increase in percentage of c-Fos$^+$ cells compared to other stimulation protocols. This may seem contrary to the current understanding of low-frequency electrical stimulation impact on cortical cells, being predominantly inhibitory and overall reducing neuronal excitability (251, 252, 253). In this case, photochemical stimulation cannot be ruled out, as OEPC are described to generate ROS (193), which can sensitise TRPV1 receptors, leading to their activation (194, 254). To avoid this effect and to constrain potential activation of inhibitory cells (255, 256, 257), a high-frequency protocol was employed in subsequent cell culture experiments. Nonetheless, the significance of the impact of low-frequency stimulation on cortical neurons should not be underestimated, as it presents a promising field for future exploration – particularly since 2 Hz stimulation of OTC resulted in significant c-Fos expression (Chapter 9.2 – Hippocampal OTC on PET OEPC).

Experiment 2

To exclude potential effect of light on the cultured neurons, Experiment 2 was devised. Red light illumination is known to influence mitochondrial metabolism (258), which could potentially facilitate neuronal excitability through changes in calcium balance (259). However, no such effects were observed in this study, as the intensity of fluorescent staining did not visibly differ between the light-treated cultures and negative control. Simultaneously, the addition of glutamate led to clear increase in the staining intensity. Therefore, c-Fos expression in OEPC-stimulated cells can be attributed to the devices themselves, and light treatment should not confound the results.

Experiments 3 and 4

Experiments 3 and 4 aimed to investigate the impact of the cell localisation on the OEPC on its activation during stimulation. In Experiment 3, stimulated cultures showed an increase in c-Fos$^+$ cell percentage compared to the controls, both on the p-n layer and on the back electrode. The OEPC photovoltage measured in the middle of the illuminated spot is higher than on the edges (13). To discern possible differences in cellular reaction to the varied voltage, c-Fos$^+$ cell percentage was compared between the inner and the outer parts of the p-

n layer. No significant differences were observed, indicating equal neuronal activity on the entire p-n pixel surface.

Although the cell culture was limited to the p-n layer, a margin of the culture extended to the metal surface of the back electrode, enabling a comparison of c-Fos expression in cells grown on this part of the OEPC. Since optical properties of the pigment p-n layer significantly differed from the gold surface, quenching some of the red and blue fluorescent signals, c-Fos IF staining could not be directly compared between those two surfaces. OEPC stimulation led to increase in c-Fos$^+$ cells on the back electrode. However, it was not clear, whether this effect stems from the direct stimulation of the back electrode, or from the propagation of the signal evoked in cells stimulated by the p-n layer within the neuronal network.

In Experiment 4, two physically separated cell clusters were seeded: one in the centre of the p-n layer, and the other on the edge of the back electrode. OEPC stimulation once again led to an increase in c-Fos$^+$ cell percentage in the cluster cultured on top of the p-n layer, consistent with the results observed in Experiment 3. However, c-Fos expression in cells grown on top of the back electrode did not differ between the stimulated and control groups. This indicates that the cellular activity on the back electrode in Experiment 3 probably stems from the signal propagation in the vast connections within the network. It is also plausible that the charge on the back electrode may not be sufficient to elicit action potentials in cells, as the back electrode surface area is bigger than the p-n layer, resulting in lower charge density that is insufficient for anodic stimulation (compare 5.3.3 – Photocapacitive stimulation). In order to achieve this, the size of the back electrode would have to be significantly reduced, although this would lead to an increase of p-n layer surface area and subsequently to a decrease in charge density there. Nevertheless, this could be a potential way to fine-tune the device's functionality.

In summary, it is reasonable to infer that the OEPC primarily functions through cathodic charging of the p-n layer, with any potential stimulation of the back electrode having a limited effect. However, neuronal activity was further propagated within the network. This finding suggests that OEPC application can lead not only to local activation of neurons, but also extend into other connected regions.

10.2 OEPC NEUROSTIMULATION *EX VIVO*

OTC slice culture offers an attractive platform that bridges cell culture and animal models. It is highly efficient, as multiple brain slices can be obtained from one animal, significantly reducing the number of animal experiments. Additionally, it provides insight into three-

dimensional cellular interactions in physiological state, which is not possible in standard dissociated cell culture. Therefore, OTC opens new avenues for experiments that cannot be conducted in primary cells or animals.

10.2.1 c-Fos expression after single OEPC stimulation

Single stimulation of OTC hippocampal slices results in discernible increase of c-Fos expression throughout the entire section. The vast majority of c-Fos$^+$ cells co-expressed NeuN, in accordance with its role as a marker of recent neuronal signalling (108). Unlike in the primary cell culture, no c-Fos staining in control slices was observed, indicating lack of spontaneous neuronal activity. Therefore, it is reasonable to assume that all of the active neurons in the stimulated slices responded to the electrical field generated by OEPC. c-Fos presence in cell layers located further away from the OEPC confirmed that it is possible to evoke activity not only in cells in the closest vicinity of the device surface, but also in a three-dimensional culture.

Single c-Fos$^+$ cells were observed on the free (not connected to the OEPC) surface of slices in both stimulated and control groups. However, as they did not express neuronal markers, they were presumably a part of non-neuronal slice population. c-Fos is known to be expressed in proliferating and differentiating rat astrocytes (260) and fibroblasts (261), and it is also plausible the observed cells were proliferating glia or fibroblasts forming a scar tissue on the surface of the slice.

10.2.2 Regenerative response after repetitive OEPC stimulation

Daily sessions of OEPC stimulation for seven consecutive days aimed to explore putative regenerative responses in cultured hippocampal slices. For this purpose, the expression of GAP-43 was analysed.

GAP-43 is a protein crucial for axonal growth and neuronal branching. Its synthesis occurs predominantly in the cell soma, although it is also described to be translated on ribosomes in axons (262). GAP-43 can be modified through palmitoylation or phosphorylation. The attachment of palmitic acid facilitates the protein's binding to membranes – in this manner, it can get easily transported along the axon within vesicles (263). Upon reaching the target location, it binds to the plasma membrane, where it remains even after its depalmitoylation (263). Phosphorylation of GAP-43 enables its functionality. The phosphorylated protein can either directly stabilise actin filaments or cluster phosphatidylinositol 4,5-bisphosphate, which promotes filament formation (264).

GAP-43 is abundantly present in axonal growth cones, especially in the developing nervous system (263). Its expression decreases drastically when mature synapses are already formed, and it is generally found at low levels in the adult brain. However, high basal protein levels can be found in brain regions associated with memory formation, such as the hippocampus, as it participates in long-term potentiation (264). Injury is known to increase GAP-43 expression in regenerating axons, reaching levels comparable to the ones expressed during development (265). An important modulator of GAP-43 functionality are neurotrophins, both increasing its expression (266, 267), and promoting its phosphorylation (264).

Our result indicate low basal expression of GAP-43, visible in control slices, not subjected to the treatment. Since tissue slicing can be viewed as an injury, it may indicate DIV12 is already past the period of GAP-43 upregulation, although in this experiment early expression of the protein was not assessed. OTC hippocampus stimulated daily for a week showed a visible increase in GAP-43 immunoreactivity. This may indicate that OEPC stimulation leads to intensified biosynthesis of the protein.

Alternatively, the stimulation can protect the tissue from a decrease in basal GAP-43 levels. Such a decrease can either occur naturally, as a return to baseline post-injury (tissue slicing). Furthermore, OTC is a degenerating system, with a significant neuronal death caused by axotomy (268). The observed lower expression of NeuN in control slices than in stimulated ones indicates a progressive loss of neurons in the culture, which seems to be stopped when OEPC stimulation is applied. This suggests an inhibitory effect of repeated electric stimulation on tissue death in the culture.

Nevertheless, the observed co-expression of GAP-43 with NeuN in some cells indicates an ongoing protein production in the cell body. Therefore, the increase in GAP-43 in the stimulated slices can be attributed to both preservation of expression through cell death protection, and *de novo* synthesis of the protein. The exact nature of the synthesis increase in the OTC slices remains unknown, as it could be attributed not only to neurotrophins, but also to cytokines (269), neurotransmitters (270, 271), and other growth factors (272) present in the tissue. Additionally, GAP-43 staining outside the somas could be axonal, indicating an outgrowth of the processes post-stimulation. However, to fully assess the scope of axonal regeneration, a three-dimensional staining would be beneficial.

10.3 OEPC BIOCOMPATIBILITY AND NEUROSTIMULATION *IN VITRO*

10.3.1 c-Fos expression after OEPC stimulation following semi-chronic implantation

In the brain, the impact of OEPC stimulation on c-Fos expression was investigated in SOM, EC, and HC. The stimulation conducted three weeks after implantation (following the completion of the post-surgical recovery phase) induced widespread activation of neurons in all regions of interest. Notably, no discernible differences were found between the ipsilateral and contralateral hemispheres.

The observed c-Fos expression in the contralateral SOM could be attributed to signal propagation over callosal connections. Rodent SOM establishes both homotopic (aimed at the same cortical layer) and heterotopic (extending to another layer) connections with its contralateral counterpart (273, 274). Most pyramidal neurons projecting through the corpus callosum are located in layers II/III (275), with their dendrites reaching towards layer I. Superficially located dendrites pose a perfect target for neurostimulation, as it is generally easier to evoke action potentials in processes than in neuronal soma (276). Less pronounced c-Fos staining in layers V and VI suggests that the photoinduced voltage does not reach deeper cortical layers and is mostly superficial. No differences in c-Fos expression in the thalamus (data not shown), a region to which layer V and VI neurons project, further underscore lack of deep cortical stimulation. However, a closer and more detailed analysis of c-Fos expression in the thalamic nuclei targeted by these neurons would be desirable for further understanding whether cortico-thalamic pathways could be affected by superficial OEPC stimulation.

Stimulation of one hemisphere reaching the contralateral cortex has multiple potential advantages in rehabilitation following trauma or stroke, as described in studies using standard electric stimulation and optogenetics (219, 220). In such cases, the implant could be positioned on the healthy hemisphere and the evoked signal could propagate to the affected region, without the need to invasively interact with the injured site. Moreover, the optogenetics study showed that targeting the lesion or perilesional area does not bring improvement, whereas contralateral stimulation does. It remains to be investigated, whether this kind of stimulation can be controlled and if so, to what extent.

Upregulated c-Fos expression was also observed in the hippocampal formation, specifically in HC and EC. The increase in the hippocampal and parahippocampal neuronal activity could be explained either through direct stimulation by the OEPC or through signal propagation from the stimulated SOM. The pattern of c-Fos staining indicates the influence of network activity

rather than penetration of electric field deep into the brain tissue. In SOM, c-Fos signal was visibly stronger in layers II/III than in layers V and VI, indicating a superficial effect of OEPC stimulation. In HC, by contrast, dorsal regions (CA1), located closer to the OEPC, showed fewer c-Fos$^+$ cells than portions located further away from the implant (such as DG and CA3).

Additionally, a model of OEPC-induced electric field generation in mouse cortex failed to predict voltage changes in brain regions below the cortex (16). Although the devices used in the mouse study differed in size and design from the ones used in the current study, it is reasonable to assume that the strongest electric signal is present in regions in closest proximity to the OEPC, and indications of high activity in other regions stem from network effects, rather than an unusually inhomogeneous electric field. Nevertheless, one cannot rule out that higher charge application, achieved through bigger OEPC size or higher light intensity, may be able to stimulate the hippocampus directly. Whether such stimulation is safe and free of any noxious effects on the cortex remains to be investigated in further studies.

The pattern of c-Fos expression in HC and EC further supports the idea of indirect stimulation through signal propagation in neuronal networks. In EC, the strongest c-Fos signal was observed in deeper layers, projecting directly to DG. Even though connections between EC and SOM are described as rather weak (210), there is still bilateral communication between the two regions and it is plausible that increased EC layer V c-Fos expression was influenced by signalling from SOM layers II/III. Additionally, EC also receives input from the thalamus, so the signal could also be propagated along somatosensory cortico-thalamic connections. In HC, the highest number of c-Fos$^+$ cells was observed in DG, with numbers decreasing in CA3 and CA1. This might indicate a robust signal reaching the initial segment of the trisynaptic circuit, gradually weakening with each synapse. The diminishing c-Fos expression in the CA regions could be a result of inhibitory signalling from interneurons or stem from an intrinsic hippocampal inhibitory mechanism, suggesting that the provided input is successfully processed and filtered within the limits of the neuronal circuitry (277, 278).

In DG, a higher number of c-Fos$^+$ cells was observed in the upper blade than in the lower blade. Despite growing experimental evidence pointing to functional differences between these two hippocampal subregions, the exact nature of these disparities remains largely unknown (279, 280). Preliminary studies on mice performing simple decision-making tasks indicated that the lower blade activity could be associated with subjective emotional responses, whereas the upper blade was involved in the actual responses (281). In epilepsy models, single stimuli could evoke burst discharges in the lower blade, but not in the upper blade,

indicative of their differential functions in the disease (282). The differential c-Fos expression between the upper and lower blade may indicate their distinct roles in somatosensory signal integration, however, exact data to support this claim is currently lacking.

While no noticeable differences were observed in the percentage of c-Fos$^+$ cells between the stimulated ipsilateral and contralateral SOM, a subtle increasing trend was identified in the contralateral EC and in the stimulated ipsilateral HC. Although the observed difference did not reach statistical significance, it could serve as a preliminary indication for further investigation into the extent of signal propagation following OEPC stimulation.

10.3.2 Characterisation of c-Fos$^+$ cell types

Multiple IF stainings shed light on the type of cells expressing c-Fos. As expected, c-Fos was present almost exclusively in neuronal cells, with the exception of one animal, where single c-Fos$^+$ astrocytes were detected. It is therefore reasonable to infer that the increase in c-Fos$^+$ cell number stems from neuronal activity following OEPC stimulation and is not significantly influenced by non-neuronal expression.

c-Fos biosynthesis in astrocytes is linked to several processes, including proliferation and differentiation (260), glutamatergic activation (283), or inflammatory signalling (284). Based on the spatial and temporal localisation of the c-Fos$^+$/GFAP$^+$ cells in the above-mentioned animal, these mechanisms may provide the most plausible explanation for the observed circumscribed astroglial c-Fos expression.

Among the interneuronal population, c-Fos was expressed only in a few SST$^+$ cells. SST is expressed in approximately 30% of interneurons, predominantly Martinotti cells, found mostly in layers II/III and V (285). Martinotti cells form inhibitory connections with distal portions of the apical dendrites of pyramidal neurons (286). Therefore, their activation may be a response to OEPC-stimulated activity of pyramidal neurons. However, direct stimulation of Martinotti cells cannot be excluded, as they extend their processes extend far into layer I, making them an appropriate target for superficial OEPC stimulation.

Triple c-Fos staining with PV and CR showed no co-expression of these markers. PV is predominantly expressed in two main interneuron subtypes: basket cells, located in cortical layer IV and targeting the soma and proximal dendrites of pyramidal neurons, and chandelier cells, forming mainly axo-axonic connections with pyramidal cells (287). Both classes of interneurons are characterised by short processes, limited to the nearest vicinity and not spanning through multiple cortical layers (288, 289, 290). CR marks mostly double bouquet

cells and bipolar interneurons, localised in the layers II/III, and interacting with distal dendrites of pyramidal cells (287). Although located relatively superficially, these cells do not project into layer I, which may explain the difference in c-Fos expression between CR^+ and SST^+ cells. Layer I is seemingly the main site of action during OEPC stimulation, where action potentials are generated in processes and propagated further towards the cell soma in layers II/III, and, through neuronal connections, to other brain regions.

Selective stimulation of neurons through cortical stimulation was also predicted by mathematical models (291, 292). However, whether targeted activation of selected neuronal population is possible in practice remains to be investigated.

10.3.3 Foreign body response following semi-chronic OEPC implantation

This study marks the first attempt to describe the impact of semi-chronic OEPC implantation on the cortex in rodents while simultaneously assessing its effect on the device. In the previous investigation with chronic OEPC implantation on the sciatic nerve, no detrimental histological changes were observed for over 100 days post-surgery (18). Illumination of the device resulted in leg kicks, confirming sustained device functionality (18). Nevertheless, until present, OEPC implantation in the brain has been performed only for the duration of the surgery (17, 293). The brain immune response, due to the presence of BBB, is unique and necessitates a thorough examination following foreign body implantation. For this reason, the tissue response to the device and OEPC functionality was assessed several weeks after the implantation.

IHC staining of common glia and immune cell markers showed discernible differences in the tissue response between the ipsilateral and contralateral cortices. Prominent staining of astrocyte and microglia markers on the brain surface and in cortical layer I, near the surgical site, stemmed from an increase in cell number and greater immunoreactivity of individual cells. Moreover, the cells showed morphological hallmarks of reactivity, such as cell body hypertrophy and disappearance of fine distal processes (294, 295). However, these changes were observed in both animals subjected to OEPC implantation and those after a sham surgery: craniectomy with dura removal, but no implant. It is therefore justifiable to assume that the surgical procedure itself caused glial reactivity and induced their proliferation, whereas the device placed on top of the brain surface did not additionally influence the glial cells.

Nevertheless, the astroglial reactivity was not sufficient to trigger glial scar formation, as only dispersed astrocytes were found in the vicinity of the surgical site. In the CNS, glial scar

is typically fully formed within 14 days post-injury (127). The lack of a significant glial scar formation is important, as its presence could substantially influence the electric field distribution in the brain tissue, possibly distorting the results of OEPC stimulation.

Similar expression pattern was observed in IHC staining of immune cell markers, CD45 – a pan-leukocytic marker, and CD68 – a marker of monocytes and macrophages. Namely, positive cells were observed exclusively in the superficial portion of the ipsilateral cortex. No discernible differences in the cell number and morphology were present between OEPC-implanted and non-implanted groups.

Positive cells were mostly observed on the brain surface, within the fibrous tissue. Single cells were present in the blood vessel walls or lumen, and no wandering cells were observed within the brain parenchyma. Absence of the immune cell infiltration indicates no underlying current inflammatory process (296). Importantly, no sample showed the presence of multinucleated foreign body giant cells, a hallmark of chronic foreign body reaction (126, 128).

The lack of extensively proliferating fibrotic tissue is also indicative of the good tolerability of the implant. Fibrotic encapsulation of electrodes is a common problem encountered in neural implants (126). The fibrous tissue acts as a barrier between the brain and the implant, which can severely hamper the stimulus delivery to the neurons. In this study, most of the fibrotic tissue was removed with the device during its explantation. However, in some animals it was possible to observe the fibrotic tissue, the thickness of which did not indicate the encapsulation process. As in the case of glial scar formation, the fibrous scar did not significantly influence the electric field distribution generated by the OEPC.

Altogether, it is justifiable to assume that the presence of parylene OEPC does not induce a significant immune reaction, affirming the device safety in extended implantation periods. Nonetheless, longer experimental implantations are needed for deeper understanding of long-term interactions between the device and the tissue, particularly considering time points where device damage, such as delamination, cracking, etc., could be anticipated. Such studies would be crucial not only with regard to FBR, but also for the exact determination of the implant durability.

10.3.4 Device durability and functionality following semi-chronic OEPC implantation

OEPC material durability and its functionality are crucial aspects for their development as putative implantable devices. Microstructural analysis provided insight into surface characteristics following implantation. Slight smoothening of the p-n layer could be explained

through a wear-off (caused by micromovements against the tissue), a peel-off during the explantation or by adhesion of organic chemicals.

Motion of the device itself was strongly limited by implantation of a resin window. Moreover, the hydrophobicity of the photoactive layer additionally warranted its close connection with the brain tissue. Although the brain itself is described to pulse in accordance with the blood flow (297), the amplitude of the movement is minute and it is rather improbable that it could cause visible changes on the material surface. The maintained uniformity of the surface suggested a lack of the peel-off effect – in this case it was expected to see patches of pigments instead of a homogenously smoothened surface.

Protein and other chemical material adsorption to the exposed foreign body surface occurs very early following the implantation (128). A uniform layer of proteins adsorbed to the metallic surfaces has been described in other studies of neural implants (298, 299, 300). Hence, it is most reasonable to assume that the smoothening of the p-n layer is the effect of natural protein adsorption associated with any foreign body implantation. Importantly, no significant degradation of the photoactive layer was observed, indicative of its high durability in a living organism.

Photovoltage measurements of the explanted devices indicated their sustained functionality, with their voltage output comparable to that of control devices. Slight decrease in the peak voltage might come from the smoothening of the highly porous p-n layer surface, effectively decreasing the electrochemical surface area and limiting electric field generation.

Thus, not only does the implantation not adversely affect the tissue, but it also does not negatively impact the OEPC itself. Nevertheless, it is clear that more studies involving longer implantation durations are necessary to gain a better understanding of the chronic effects on both the tissue and the devices.

10.4 c-Fos as a marker of neuronal activity in studies of external stimulation

c-Fos is a marker of recent neuronal activity widely used in *in vivo* studies employing electric stimulation (301, 302, 303). However, in our experience, its applicability was constrained to the post-recovery phase. The assessment of the effects of acute OEPC stimulation was impossible, as the entire operated hemisphere showed abundant c-Fos expression. This pattern is characteristic of cortical spreading depression (CSD) (304, 305) – a wave of depolarization followed by the suppression of neuronal activity, propagating

throughout the brain cortex and associated with numerous neurological disorders (306, 307). CSD can be triggered by multiple electrical, mechanical and chemical stimuli (308), such as desiccation or air contact (309), which may have occurred during surgery.

CSD has already been described as a consequence of durotomy in humans (310), supporting the observation that only craniectomy followed by dura removal seemed to induce a CSD-like response in the rat brain. Nevertheless, surgery-associated CSD alone could not account for the widespread c-Fos expression observed in many animals 24 and 48 hours following implantation. This might be linked to ongoing inflammation, as c-Fos plays a crucial role in proliferation and the inflammatory response in immune (311) and glial cells (312) as well as in nociception (116, 313). However, the daily application of an anti-inflammatory agent should have limited these processes in the tissue. Moreover, the observed co-expression of c-Fos and NeuN supports the neuronal origin of the abundant c-Fos expression. As CSD occurs in waves, and the length of resolution of a single wave varies from minutes to hours (314), it is possible that we observed various stages of recurrent CSD at different time points. Additionally, the parietal portion of SOM is particularly susceptible to CSD generation (315), so it may sustain CSD waves for longer periods.

The extensive neuronal activation observed in some animals, both in the early post-surgery groups and the chronically implanted groups, could be attributed to two mechanisms. Firstly, spontaneous activity associated with normal rat behaviour during their active phase (316) might have played a role. Throughout the experiment, the animals were kept in dimmed light as a precautionary measure to prevent excessive neuronal activity in the visual cortex. However, it could potentially provoke their activity, typically more pronounced at night, especially in Sprague Dawley rats (317). Additionally, any physical contact of the awake rat with the researcher or another rat could have triggered the activation of the respective regions of the somatosensory cortex, which was the primary focus area in the study.

Another limitation of the experimental design was the awakening of the animals following stimulation. The main objective of this procedure was to mimic normal animal behaviour to the best of our abilities, and to minimise the burden associated with prolonged anaesthesia. However, the induced awakening itself can provoke c-Fos expression in the cortex and hippocampus (318, 319), which could explain the large variance and the presence of the outliers in our experiments.

In light of the considerations outlined above, it is essential to incorporate factors related to the recovery phase, spontaneous neuronal activity in awake animals, and sleep-wake

cycles into the experimental design when investigating neurostimulation-induced c-Fos expression in the brain.

11 CONCLUSIONS

Increasing interest in wireless neurostimulation led to the employment of photoactive organic semiconductors in minimally invasive stimulating devices, OEPC. This study aimed to evaluate their utility in three rat models of increasing complexity: primary cortical cell culture, organotypic hippocampal slice culture, and implantation into experimental animals. The main goal of light-controlled OEPC stimulation was to elicit neuronal activation in all of those models. Indeed, post-stimulation increase in c-Fos expression in neuronal cells was observed in all: cultured cells, cultured tissue, and animal brain. Moreover, all models showed signs of signal propagation in vast neuronal networks, demonstrating that OEPC stimulation may be originally local in nature, but it can easily spread to other regions.

Cell culture experiments brought insights into the nature of the stimulation. Neuronal activity seems to be evoked mainly by the photoactive layer of the device, which is cathodic in nature during illumination. Therefore, it is crucial to target the stimulation focus with the light-sensitive portion of the OEPC, the p-n pixel, which can be formed in various shapes and sizes to further increase the spatial resolution of the treatment.

Stimulation of cultured hippocampal slices proved it possible to stimulate cells not only within the layer located in the closest vicinity of the OEPC, but also in layers situated further away. Moreover, the repeated stimulation regime results in a better condition of the culture, decreasing neuronal cell death and promoting regenerative processes.

Superficial cortical stimulation in adult rats results in signal propagation to the connected brain regions. It is possible to stimulate the contralateral cortex and deeper brain regions, such as parahippocampal formation, which can prove advantageous in putative therapy by OEPC. However, it is not clear if such stimulation could be directly controllable.

OEPC manufactured on different substrates, including medical-grade polymer, are biocompatible and remain stable and functional for several weeks. Cortical implantation is minimally invasive, and the presence of the device does not trigger foreign body reaction in the brain tissue.

OEPC is a novel tool, which has been validated as a useful platform for *in vitro, ex vivo* and *in vivo* studies of neurostimulation. The device offers a promising alternative stimulation method, which may find its use in the clinic. Before any trials with humans, more animal studies evaluating chronic safety and durability of OEPC are necessary – nevertheless, this study provides the first step on a long path to clinical application.

12 BIBLIOGRAPHY

1. Collaborators GBDN. Global, regional, and national burden of neurological disorders, 1990-2016: a systematic analysis for the Global Burden of Disease Study 2016. The Lancet Neurology. 2019;18(5):459-80.
2. Ding C, Wu Y, Chen X, Chen Y, Wu Z, Lin Z, et al. Global, regional, and national burden and attributable risk factors of neurological disorders: The Global Burden of Disease study 1990-2019. Front Public Health. 2022;10:952161.
3. Deuschl G, Beghi E, Fazekas F, Varga T, Christoforidi KA, Sipido E, et al. The burden of neurological diseases in Europe: an analysis for the Global Burden of Disease Study 2017. Lancet Public Health. 2020;5(10):e551-e67.
4. Sarica C, Conner CR, Yamamoto K, Yang A, Germann J, Lannon MM, et al. Trends and disparities in deep brain stimulation utilization in the United States: a Nationwide Inpatient Sample analysis from 1993 to 2017. Lancet Reg Health Am. 2023;26:100599.
5. Kogan M, McGuire M, Riley J. Deep Brain Stimulation for Parkinson Disease. Neurosurgery Clinics of North America. 2019;30(2):137-+.
6. Gonzalez HFJ, Yengo-Kahn A, Englot DJ. Vagus Nerve Stimulation for the Treatment of Epilepsy. Neurosurg Clin N Am. 2019;30(2):219-30.
7. Nowakowska M, Üçal M, Charalambous M, Bhatti SFM, Denison T, Meller S, et al. Neurostimulation as a Method of Treatment and a Preventive Measure in Canine Drug-Resistant Epilepsy: Current State and Future Prospects. Front Vet Sci. 2022;9:889561.
8. Bernstein JE, Kashyap S, Ray K, Ananda A. Infections in Deep Brain Stimulator Surgery. Cureus. 2019;11(8):e5440.
9. Grasmeder M, Verschuur C, Ferris R, Basodan S, Newman T, Sanderson A. Piloting the recording of electrode voltages (REVS) using surface electrodes as a test to identify cochlear implant electrode migration, extra-cochlear electrodes and basal electrodes causing discomfort. Cochlear Implants Int. 2021;22(3):157-69.
10. Choi H, Gaiha R, Moeschler SM, Bendel MA, McCormick ZL, Teramoto M, et al. Factors Associated With Implantable Pulse Generator Site Pain: A Multicenter Cross-Sectional Study. Neuromodulation. 2021;24(8):1351-6.
11. Zhao D, Huang R, Gan JM, Shen QD. Photoactive Nanomaterials for Wireless Neural Biomimetics, Stimulation, and Regeneration. ACS Nano. 2022;16(12):19892-912.
12. Medagoda DI, Ghezzi D. Organic semiconductors for light-mediated neuromodulation. Communications Materials. 2021;2(1):111.
13. Rand D, Jakesova M, Lubin G, Vebraite I, David-Pur M, Derek V, et al. Direct Electrical Neurostimulation with Organic Pigment Photocapacitors. Adv Mater. 2018;30(25):e1707292.
14. Jakesova M, Silvera Ejneby M, Derek V, Schmidt T, Gryszel M, Brask J, et al. Optoelectronic control of single cells using organic photocapacitors. Sci Adv. 2019;5(4):eaav5265.
15. Schmidt T, Jakesova M, Derek V, Kornmueller K, Tiapko O, Bischof H, et al. Light Stimulation of Neurons on Organic Photocapacitors Induces Action Potentials with Millisecond Precision. Adv Mater Technol. 2022;7(9):2101159.
16. Missey F, Botzanowski B, Migliaccio L, Acerbo E, Glowacki ED, Williamson A. Organic electrolytic photocapacitors for stimulation of the mouse somatosensory cortex. J Neural Eng. 2021;18(6).
17. Missey F, Donahue MJ, Weber P, Ngom I, Acerbo E, Botzanowski B, et al. Laser-Driven Wireless Deep Brain Stimulation using Temporal Interference and Organic Electrolytic Photocapacitors. Advanced Functional Materials. 2022;32(33):2200691.

18. Silvera Ejneby M, Jakesova M, Ferrero JJ, Migliaccio L, Sahalianov I, Zhao Z, et al. Chronic electrical stimulation of peripheral nerves via deep-red light transduced by an implanted organic photocapacitor. Nat Biomed Eng. 2022;6(6):741-53.
19. Eross L, Entz L, Fabo D. [Invasive neuromodulation in the treatment of drug-resistant epilepsies]. Orv Hetil. 2015;156(52):2103-9.
20. Dallapiazza R, McKisic MS, Shah B, Elias WJ. Neuromodulation for movement disorders. Neurosurg Clin N Am. 2014;25(1):47-58.
21. Witney AG. Neurostimulation Techniques for the Modulation of Pain. 2017:- Ch. 7.
22. Marquez-Franco R, Carrillo-Ruiz JD, Velasco AL, Velasco F. Deep Brain Stimulation Neuromodulation for the Treatment of Mood Disorders: Obsessive Compulsive Disorder and Treatment Resistant Depression. Front Psychiatry. 2021;12:764776.
23. Bao SC, Khan A, Song R, Kai-Yu Tong R. Rewiring the Lesioned Brain: Electrical Stimulation for Post-Stroke Motor Restoration. J Stroke. 2020;22(1):47-63.
24. Shin SS, Dixon CE, Okonkwo DO, Richardson RM. Neurostimulation for traumatic brain injury. J Neurosurg. 2014;121(5):1219-31.
25. Society IN. About Neuromodulation 2022 [Available from: https://www.neuromodulation.com/about-neuromodulation.
26. Krames ES, Rezai AR, Peckham PH. Introduction. In: Krames ES, Peckham PH, Rezai AR, editors. Neuromodulation (Second Edition): Academic Press; 2018. p. 1.
27. Güçlü B. Chapter 1 - Introduction to somatosensory neuroprostheses. In: Güçlü B, editor. Somatosensory Feedback for Neuroprosthetics: Academic Press; 2021. p. 3-40.
28. Francis J, Dingley J. Electroanaesthesia--from torpedo fish to TENS. Anaesthesia. 2015;70(1):93-103.
29. Finkelstein G. Mechanical neuroscience: Emil du Bois-Reymond's innovations in theory and practice. Frontiers in systems neuroscience. 2015;9:133.
30. Schuetze SM. The discovery of the action potential. Trends Neurosci. 1983;6:164-8.
31. Isitan C, Yan Q, Spencer DD, Alkawadri R. Brief history of electrical cortical stimulation: A journey in time from Volta to Penfield. Epilepsy Res. 2020;166:106363.
32. Fritsch G, Hitzig E. Electric excitability of the cerebrum (Über die elektrische Erregbarkeit des Grosshirns). Epilepsy Behav. 2009;15(2):123-30.
33. HORSLEY V, CLARKE RH. THE STRUCTURE AND FUNCTIONS OF THE CEREBELLUM EXAMINED BY A NEW METHOD. Brain. 1908;31(1):45-124.
34. Spiegel EA, Wycis HT, Marks M, Lee AJ. Stereotaxic Apparatus for Operations on the Human Brain. Science. 1947;106(2754):349-50.
35. Peterson JTB, Deer TR. A History of Neurostimulation. In: Deer TR, Leong MS, Buvanendran A, Gordin V, Kim PS, Panchal SJ, et al., editors. Comprehensive Treatment of Chronic Pain by Medical, Interventional, and Integrative Approaches: The AMERICAN ACADEMY OF PAIN MEDICINE Textbook on Patient Management. New York, NY: Springer New York; 2013. p. 583-6.
36. Gardner J. A history of deep brain stimulation: Technological innovation and the role of clinical assessment tools. Social Studies of Science. 2013;43(5):707-28.
37. Marín G, Castillo-Rangel C, Salomón-Lara L, Vega-Quesada LA, Zarate Calderon CJ, Borda-Low CD, et al. Deep brain stimulation in neurological diseases and other pathologies. Neurology perspectives.
38. Afra P, Adamolekun B, Aydemir S, Watson GDR. Evolution of the Vagus Nerve Stimulation (VNS) Therapy System Technology for Drug-Resistant Epilepsy. Front Med Technol. 2021;3:696543.
39. Services CfMM. Transcranial Magnetic Stimulation (TMS) in the Treatment of Adults with Major Depressive Disorder 2022 [Available from: https://www.cms.gov/medicare-coverage-database/view/lcd.aspx?lcdId=34522&ver=29.
40. Administration USFaD. Prodigy, Proclaim, and Proclaim XR Spinal Cord Stimulation (SCS) Systems – P010032/S189 2023 [Available from: https://www.fda.gov/medical-devices/recently-

approved-devices/prodigy-proclaim-and-proclaim-xr-spinal-cord-stimulation-scs-systems-p010032s189.
41. Administration USFaD. Prospera Spinal Cord Stimulation (SCS) System, Resilience Percutaneous Lead, HomeStream Remote Management – P210037 2023 [Available from: https://www.fda.gov/medical-devices/recently-approved-devices/prospera-spinal-cord-stimulation-scs-system-resilience-percutaneous-lead-homestream-remote.
42. Sobstyl M, Kupryjaniuk A, Prokopienko M, Rylski M. Subcallosal Cingulate Cortex Deep Brain Stimulation for Treatment-Resistant Depression: A Systematic Review. Front Neurol. 2022;13:780481.
43. Herrington TM, Cheng JJ, Eskandar EN. Mechanisms of deep brain stimulation. Journal of neurophysiology. 2016;115(1):19-38.
44. Su D, Chen H, Hu W, Liu Y, Wang Z, Wang X, et al. Frequency-dependent effects of subthalamic deep brain stimulation on motor symptoms in Parkinson's disease: a meta-analysis of controlled trials. Sci Rep. 2018;8(1):14456.
45. Hartshorn A, Jobst B. Responsive brain stimulation in epilepsy. Ther Adv Chronic Dis. 2018;9(7):135-42.
46. Chandrabhatla AS, Pomeraniec IJ, Horgan TM, Wat EK, Ksendzovsky A. Landscape and future directions of machine learning applications in closed-loop brain stimulation. npj Digital Medicine. 2023;6(1):79.
47. Smith JR, Fountas KN, Murro AM, Park YD, Jenkins PD, Morrell M, et al. Closed-loop stimulation in the control of focal epilepsy of insular origin. Stereotact Funct Neurosurg. 2010;88(5):281-7.
48. Krahl SE, Clark KB. Vagus nerve stimulation for epilepsy: A review of central mechanisms. Surg Neurol Int. 2012;3(Suppl 4):S255-9.
49. Peng Z, Zhou C, Xue S, Bai J, Yu S, Li X, et al. Mechanism of Repetitive Transcranial Magnetic Stimulation for Depression. Shanghai archives of psychiatry. 2018;30(2):84-92.
50. Klomjai W, Katz R, Lackmy-Vallée A. Basic principles of transcranial magnetic stimulation (TMS) and repetitive TMS (rTMS). Annals of Physical and Rehabilitation Medicine. 2015;58(4):208-13.
51. Woods AJ, Antal A, Bikson M, Boggio PS, Brunoni AR, Celnik P, et al. A technical guide to tDCS, and related non-invasive brain stimulation tools. Clinical neurophysiology : official journal of the International Federation of Clinical Neurophysiology. 2016;127(2):1031-48.
52. Antal A, Alekseichuk I, Paulus W. The New Modalities of Transcranial Electric Stimulation: tACS, tRNS, and Other Approaches. In: Brunoni A, Nitsche M, Loo C, editors. Transcranial Direct Current Stimulation in Neuropsychiatric Disorders: Clinical Principles and Management. Cham: Springer International Publishing; 2016. p. 21-8.
53. Chiken S, Nambu A. Mechanism of Deep Brain Stimulation: Inhibition, Excitation, or Disruption? The Neuroscientist : a review journal bringing neurobiology, neurology and psychiatry. 2016;22(3):313-22.
54. Vázquez-Vélez GE, Zoghbi HY. Parkinson's Disease Genetics and Pathophysiology. Annual Review of Neuroscience. 2021;44(1):87-108.
55. Rubchinsky LL, Park C, Worth RM. Intermittent neural synchronization in Parkinson's disease. Nonlinear Dyn. 2012;68(3):329-46.
56. Groiss SJ, Wojtecki L, Südmeyer M, Schnitzler A. Deep brain stimulation in Parkinson's disease. Ther Adv Neurol Disord. 2009;2(6):20-8.
57. Sillay K, Starr P. Chapter 42 - Deep Brain Stimulation in Parkinson's Disease. In: Krames ES, Peckham PH, Rezai AR, editors. Neuromodulation. San Diego: Academic Press; 2009. p. 539-48.
58. Montemurro N, Aliaga N, Graff P, Escribano A, Lizana J. New Targets and New Technologies in the Treatment of Parkinson's Disease: A Narrative Review. Int J Environ Res Public Health. 2022;19(14).

59. Fasano A, Hamani C, Honey CR, Kalia SK, Munhoz RP, Panisset M, et al. Deep Brain Stimulation Target Selection for Parkinson's Disease. Canadian Journal of Neurological Sciences / Journal Canadien des Sciences Neurologiques. 2017;44(1):3-8.
60. Louie KH, Petrucci MN, Grado LL, Lu C, Tuite PJ, Lamperski AG, et al. Semi-automated approaches to optimize deep brain stimulation parameters in Parkinson's disease. Journal of NeuroEngineering and Rehabilitation. 2021;18(1):83.
61. Boutet A, Madhavan R, Elias GJB, Joel SE, Gramer R, Ranjan M, et al. Predicting optimal deep brain stimulation parameters for Parkinson's disease using functional MRI and machine learning. Nature Communications. 2021;12(1):3043.
62. Roediger J, Dembek TA, Achtzehn J, Busch JL, Krämer A-P, Faust K, et al. Automated deep brain stimulation programming based on electrode location: a randomised, crossover trial using a data-driven algorithm. The Lancet Digital Health. 2023;5(2):e59-e70.
63. Chandra V, Hilliard JD, Foote KD. Deep brain stimulation for the treatment of tremor. Journal of the Neurological Sciences. 2022;435:120190.
64. Deuschl G, Paschen S, Witt K. Chapter 10 - Clinical outcome of deep brain stimulation for Parkinson's disease. In: Lozano AM, Hallett M, editors. Handbook of Clinical Neurology. 116: Elsevier; 2013. p. 107-28.
65. Fisher RS, Boas WvE, Blume W, Elger C, Genton P, Lee P, et al. Epileptic Seizures and Epilepsy: Definitions Proposed by the International League Against Epilepsy (ILAE) and the International Bureau for Epilepsy (IBE). Epilepsia. 2005;46(4):470-2.
66. Özkara Ç, Aronica E. Chapter 37 - Hippocampal sclerosis. In: Stefan H, Theodore WH, editors. Handbook of Clinical Neurology. 108: Elsevier; 2012. p. 621-39.
67. Fritschy JM, Kiener T, Bouilleret V, Loup F. GABAergic neurons and GABA(A)-receptors in temporal lobe epilepsy. Neurochem Int. 1999;34(5):435-45.
68. Wang S, Lévesque M, Fisher TAJ, Kennedy TE, Avoli M. CA3 principal cell activation triggers hypersynchronous-onset seizures in a mouse model of mesial temporal lobe epilepsy. Journal of neurophysiology. 2023;130(4):1041-52.
69. French JA. Refractory Epilepsy: Clinical Overview. Epilepsia. 2007;48(s1):3-7.
70. Engel J, Jr. Approaches to refractory epilepsy. Ann Indian Acad Neurol. 2014;17(Suppl 1):S12-7.
71. Apuzzo APAMLLCYLMLJ. Vagus Nerve Stimulation. Proceedings of the IEEE 2008;96(7):1142 - 51.
72. Asconapé JJ, Moore DD, Zipes DP, Hartman LM, Duffell WH, Jr. Bradycardia and asystole with the use of vagus nerve stimulation for the treatment of epilepsy: a rare complication of intraoperative device testing. Epilepsia. 1999;40(10):1452-4.
73. Administration USFaD. Premarket Approval (PMA) 2016 [Available from: https://www.accessdata.fda.gov/scripts/cdrh/cfdocs/cfpma/pma.cfm?id=P970003S207.
74. Morris GL, 3rd, Gloss D, Buchhalter J, Mack KJ, Nickels K, Harden C. Evidence-based guideline update: vagus nerve stimulation for the treatment of epilepsy: report of the Guideline Development Subcommittee of the American Academy of Neurology. Neurology. 2013;81(16):1453-9.
75. Fahoum F, Boffini M, Kann L, Faini S, Gordon C, Tzadok M, et al. VNS parameters for clinical response in Epilepsy. Brain Stimul. 2022;15(3):814-21.
76. Labar D. Vagus nerve stimulation for 1 year in 269 patients on unchanged antiepileptic drugs. Seizure. 2004;13(6):392-8.
77. Englot DJ, Rolston JD, Wright CW, Hassnain KH, Chang EF. Rates and Predictors of Seizure Freedom With Vagus Nerve Stimulation for Intractable Epilepsy. Neurosurgery. 2016;79(3):345-53.
78. Toffa DH, Touma L, El Meskine T, Bouthillier A, Nguyen DK. Learnings from 30 years of reported efficacy and safety of vagus nerve stimulation (VNS) for epilepsy treatment: A critical review. Seizure. 2020;83:104-23.

79. Mertens A, Gadeyne S, Lescrauwaet E, Carrette E, Meurs A, De Herdt V, et al. The potential of invasive and non-invasive vagus nerve stimulation to improve verbal memory performance in epilepsy patients. Scientific Reports. 2022;12(1):1984.
80. Oehrn CR, Molitor L, Krause K, Niehaus H, Schmidt L, Hakel L, et al. Non-invasive vagus nerve stimulation in epilepsy patients enhances cooperative behavior in the prisoner's dilemma task. Sci Rep. 2022;12(1):10255.
81. Salanova V, Witt T, Worth R, Henry TR, Gross RE, Nazzaro JM, et al. Long-term efficacy and safety of thalamic stimulation for drug-resistant partial epilepsy. Neurology. 2015;84(10):1017-25.
82. Winston GM, Guadix S, Lavieri MT, Uribe-Cardenas R, Kocharian G, Williams N, et al. Closed-loop vagal nerve stimulation for intractable epilepsy: A single-center experience. Seizure. 2021;88:95-101.
83. Parastarfeizabadi M, Kouzani AZ. Advances in closed-loop deep brain stimulation devices. Journal of NeuroEngineering and Rehabilitation. 2017;14(1):79.
84. Hofer AS, Schwab ME. Enhancing rehabilitation and functional recovery after brain and spinal cord trauma with electrical neuromodulation. Current opinion in neurology. 2019;32(6):828-35.
85. Silverstein J, Levy RM. Chapter 61 - Cortical Stimulation for the Treatment of Motor Deficits following Ischemic Stroke. In: Krames ES, Peckham PH, Rezai AR, editors. Neuromodulation. San Diego: Academic Press; 2009. p. 753-66.
86. Geremia NM, Gordon T, Brushart TM, Al-Majed AA, Verge VM. Electrical stimulation promotes sensory neuron regeneration and growth-associated gene expression. Exp Neurol. 2007;205(2):347-59.
87. Tiefenbach J, Chan HH, Machado AG, Baker KB. Neurostimulation for Functional Recovery After Traumatic Brain Injury: Current Evidence and Future Directions for Invasive Surgical Approaches. Neurosurgery. 2022:10.1227/neu.0000000000002134.
88. Ziesel D, Nowakowska M, Scheruebel S, Kornmueller K, Schafer U, Schindl R, et al. Electrical stimulation methods and protocols for the treatment of traumatic brain injury: a critical review of preclinical research. J Neuroeng Rehabil. 2023;20(1):51.
89. Guan B, Anderson DB, Chen L, Feng S, Zhou H. Global, regional and national burden of traumatic brain injury and spinal cord injury, 1990-2019: a systematic analysis for the Global Burden of Disease Study 2019. BMJ Open. 2023;13(10):e075049.
90. Mauritz W, Brazinova A, Majdan M, Leitgeb J. Epidemiology of traumatic brain injury in Austria. Wien Klin Wochenschr. 2014;126(1-2):42-52.
91. Wafa HA, Wolfe CDA, Emmett E, Roth GA, Johnson CO, Wang Y. Burden of Stroke in Europe: Thirty-Year Projections of Incidence, Prevalence, Deaths, and Disability-Adjusted Life Years. Stroke. 2020;51(8):2418-27.
92. Global, regional, and national burden of spinal cord injury, 1990-2019: a systematic analysis for the Global Burden of Disease Study 2019. The Lancet Neurology. 2023;22(11):1026-47.
93. Corrigan F, Wee IC, Collins-Praino LE. Chronic motor performance following different traumatic brain injury severity-A systematic review. Front Neurol. 2023;14:1180353.
94. Ingwersen T, Wolf S, Birke G, Schlemm E, Bartling C, Bender G, et al. Long-term recovery of upper limb motor function and self-reported health: results from a multicenter observational study 1 year after discharge from rehabilitation. Neurological Research and Practice. 2021;3(1):66.
95. Schiff ND, Giacino JT, Butson CR, Choi EY, Baker JL, O'Sullivan KP, et al. Thalamic deep brain stimulation in traumatic brain injury: a phase 1, randomized feasibility study. Nature Medicine. 2023;29(12):3162-74.
96. Tyler DJ, Polasek KH. Chapter 17 - Electrodes for the Neural Interface. In: Krames ES, Peckham PH, Rezai AR, editors. Neuromodulation. San Diego: Academic Press; 2009. p. 181-213.
97. Weiner RL. Peripheral nerve neurostimulation. Neurosurg Clin N Am. 2003;14(3):401-8.
98. Xu J, Sun Z, Wu J, Rana M, Garza J, Zhu AC, et al. Peripheral Nerve Stimulation in Pain Management: A Systematic Review. Pain Physician. 2021;24(2):E131-e52.

99. Stuart RM, Winfree CJ. Neurostimulation Techniques for Painful Peripheral Nerve Disorders. Neurosurgery Clinics of North America. 2009;20(1):111-20.
100. Steiner TJ, Stovner LJ. Global epidemiology of migraine and its implications for public health and health policy. Nature Reviews Neurology. 2023;19(2):109-17.
101. Lampl C, Buzath A, Baumhackl U, Klingler D. One-Year Prevalence of Migraine in Austria: A Nation-Wide Survey. Cephalalgia. 2003;23(4):280-6.
102. Weiner RL. Occipital neurostimulation for treatment of intractable headache syndromes. Acta Neurochir Suppl. 2007;97(Pt 1):129-33.
103. Tiwari V, Agrawal S. Migraine and Neuromodulation: A Literature Review. Cureus. 2022;14(11):e31223.
104. Mortimer JT, Bhadra N. Chapter 11 - Fundamentals of Electrical Stimulation. In: Krames ES, Peckham PH, Rezai AR, editors. Neuromodulation. San Diego: Academic Press; 2009. p. 109-21.
105. Borst JG, Sakmann B. Calcium current during a single action potential in a large presynaptic terminal of the rat brainstem. The Journal of physiology. 1998;506 (Pt 1)(Pt 1):143-57.
106. Grill WM. Chapter 14 - Principles of Electric Field Generation for Stimulation of the Central Nervous System. In: Krames ES, Peckham PH, Rezai AR, editors. Neuromodulation. San Diego: Academic Press; 2009. p. 145-55.
107. Berridge MJ. Neuronal Calcium Signaling. Neuron. 1998;21(1):13-26.
108. Chung L. A Brief Introduction to the Transduction of Neural Activity into Fos Signal. Development & reproduction. 2015;19(2):61-7.
109. Cullen PJ, Lockyer PJ. Integration of calcium and Ras signalling. Nat Rev Mol Cell Biol. 2002;3(5):339-48.
110. Barros VN, Mundim M, Galindo LT, Bittencourt S, Porcionatto M, Mello LE. The pattern of c-Fos expression and its refractory period in the brain of rats and monkeys. Front Cell Neurosci. 2015;9:72.
111. Lara Aparicio SY, Laureani Fierro ÁdJ, Aranda Abreu GE, Toledo Cárdenas R, García Hernández LI, Coria Ávila GA, et al. Current Opinion on the Use of c-Fos in Neuroscience. NeuroSci. 2022;3(4):687-702.
112. Lamprecht R, Dudai Y. Transient expression of c-Fos in rat amygdala during training is required for encoding conditioned taste aversion memory. Learn Mem. 1996;3(1):31-41.
113. Strekalova T, Zörner B, Zacher C, Sadovska G, Herdegen T, Gass P. Memory retrieval after contextual fear conditioning induces c-Fos and JunB expression in CA1 hippocampus. Genes, Brain and Behavior. 2003;2(1):3-10.
114. Tronel S, Sara SJ. Mapping of olfactory memory circuits: region-specific c-fos activation after odor-reward associative learning or after its retrieval. Learn Mem. 2002;9(3):105-11.
115. Katche C, Bekinschtein P, Slipczuk L, Goldin A, Izquierdo IA, Cammarota M, et al. Delayed wave of c-Fos expression in the dorsal hippocampus involved specifically in persistence of long-term memory storage. Proc Natl Acad Sci U S A. 2010;107(1):349-54.
116. Harris JA. Using c-fos as a Neural Marker of Pain. Brain Research Bulletin. 1998;45(1):1-8.
117. Munglani R, Fleming BG, Hunt SP. Remembrance of times past: the significance of c-fos in pain. Br J Anaesth. 1996;76(1):1-4.
118. Cunningham JT, Mifflin SW, Gould GG, Frazer A. Induction of c-Fos and ΔFosB Immunoreactivity in Rat Brain by Vagal Nerve Stimulation. Neuropsychopharmacology. 2008;33(8):1884-95.
119. Maeda Y, Ikeuchi M, Wacnik P, Sluka KA. Increased c-fos immunoreactivity in the spinal cord and brain following spinal cord stimulation is frequency-dependent. Brain Res. 2009;1259:40-50.
120. Mercante B, Enrico P, Floris G, Quartu M, Boi M, Serra MP, et al. Trigeminal nerve stimulation induces Fos immunoreactivity in selected brain regions, increases hippocampal cell proliferation and reduces seizure severity in rats. Neuroscience. 2017;361:69-80.

121. Qiu Z, Kala S, Guo J, Xian Q, Zhu J, Zhu T, et al. Targeted Neurostimulation in Mouse Brains with Non-invasive Ultrasound. Cell Reports. 2020;32(7):108033.
122. Alon G, Kantor G, Ho HS. Effects of electrode size on basic excitatory responses and on selected stimulus parameters. J Orthop Sports Phys Ther. 1994;20(1):29-35.
123. Koessler L, Colnat-Coulbois S, Cecchin T, Hofmanis J, Dmochowski JP, Norcia AM, et al. In-vivo measurements of human brain tissue conductivity using focal electrical current injection through intracerebral multicontact electrodes. Hum Brain Mapp. 2017;38(2):974-86.
124. Mandija S, Petrov PI, Vink JJT, Neggers SFW, van den Berg CAT. Brain Tissue Conductivity Measurements with MR-Electrical Properties Tomography: An In Vivo Study. Brain Topography. 2021;34(1):56-63.
125. Zhang D, Chen Q, Shi C, Chen M, Ma K, Wan J, et al. Dealing with the Foreign-Body Response to Implanted Biomaterials: Strategies and Applications of New Materials. Advanced Functional Materials. 2021;31(6):2007226.
126. Carnicer-Lombarte A, Chen S-T, Malliaras GG, Barone DG. Foreign Body Reaction to Implanted Biomaterials and Its Impact in Nerve Neuroprosthetics. Frontiers in Bioengineering and Biotechnology. 2021;9.
127. Yang T, Dai Y, Chen G, Cui S. Dissecting the Dual Role of the Glial Scar and Scar-Forming Astrocytes in Spinal Cord Injury. Front Cell Neurosci. 2020;14.
128. Anderson JM, Rodriguez A, Chang DT. Foreign body reaction to biomaterials. Semin Immunol. 2008;20(2):86-100.
129. Burton A, Won SM, Sohrabi AK, Stuart T, Amirhossein A, Kim JU, et al. Wireless, battery-free, and fully implantable electrical neurostimulation in freely moving rodents. Microsystems & Nanoengineering. 2021;7(1):62.
130. Jensen BN, Wang Y, Le Friec A, Nabavi S, Dong M, Seliktar D, et al. Wireless electromagnetic neural stimulation patch with anisotropic guidance. npj Flexible Electronics. 2023;7(1):34.
131. Su CL, Cheng CC, Yen PH, Huang JX, Ting YJ, Chiang PH. Wireless neuromodulation in vitro and in vivo by intrinsic TRPC-mediated magnetomechanical stimulation. Commun Biol. 2022;5(1):1166.
132. Jagdeo JR, Adams LE, Brody NI, Siegel DM. Transcranial Red and Near Infrared Light Transmission in a Cadaveric Model. PLOS ONE. 2012;7(10):e47460.
133. Salehpour FC, Paolo; Rouhi, Naser; Hamblin, Michael R.; De Taboada, Luis, Farajdokht, Fereshteh; Mahmoudi, Javad. Penetration Profiles of Visible and Near-Infrared Lasers and Light-Emitting Diode Light Through the Head Tissues in Animal and Human Species: A Review of Literature. Photobiomodulation, Photomedicine, and Laser Surgery. 2019;37(10):581-95.
134. Fenno L, Yizhar O, Deisseroth K. The development and application of optogenetics. Annu Rev Neurosci. 2011;34:389-412.
135. De Silva SR, Moore AT. Optogenetic approaches to therapy for inherited retinal degenerations. The Journal of physiology. 2022;600(21):4623-32.
136. Henriksen BS, Marc RE, Bernstein PS. Optogenetics for retinal disorders. J Ophthalmic Vis Res. 2014;9(3):374-82.
137. Lindner M, Gilhooley MJ, Hughes S, Hankins MW. Optogenetics for visual restoration: From proof of principle to translational challenges. Progress in Retinal and Eye Research. 2022;91:101089.
138. Sahel J-A, Boulanger-Scemama E, Pagot C, Arleo A, Galluppi F, Martel JN, et al. Partial recovery of visual function in a blind patient after optogenetic therapy. Nature Medicine. 2021;27(7):1223-9.
139. Luiz Alexandre Viana M, Helia T-F, Mélcar C, Matheus Felipe Guimarães A, Ana Paula Carneiro R, Rodrigo Souza da S, et al. Optogenetic Stimulation of the M2 Cortex Reverts Motor Dysfunction in a Mouse Model of Parkinson's Disease. The Journal of Neuroscience. 2019;39(17):3234.
140. Valverde S, Vandecasteele M, Piette C, Derousseaux W, Gangarossa G, Aristieta Arbelaiz A, et al. Deep brain stimulation-guided optogenetic rescue of parkinsonian symptoms. Nature Communications. 2020;11(1):2388.

141. Yoon HH, Min J, Hwang E, Lee CJ, Suh J-KF, Hwang O, et al. Optogenetic Inhibition of the Subthalamic Nucleus Reduces Levodopa-Induced Dyskinesias in a Rat Model of Parkinson's Disease. Stereotactic and Functional Neurosurgery. 2016;94(1):41-53.
142. Krook-Magnuson E, Armstrong C, Oijala M, Soltesz I. On-demand optogenetic control of spontaneous seizures in temporal lobe epilepsy. Nature Communications. 2013;4(1):1376.
143. Chen R, Gore F, Nguyen Q-A, Ramakrishnan C, Patel S, Kim SH, et al. Deep brain optogenetics without intracranial surgery. Nature Biotechnology. 2021;39(2):161-4.
144. Gilbert F, Harris AR, Kapsa RMI. Controlling Brain Cells With Light: Ethical Considerations for Optogenetic Clinical Trials. AJOB Neuroscience. 2014;5(3):3-11.
145. White M, Mackay M, Whittaker RG. Taking Optogenetics into the Human Brain: Opportunities and Challenges in Clinical Trial Design. Open Access Journal of Clinical Trials. 2020;12(null):33-41.
146. Cios A, Ciepielak M, Szymanski L, Lewicka A, Cierniak S, Stankiewicz W, et al. Effect of Different Wavelengths of Laser Irradiation on the Skin Cells. International Journal of Molecular Sciences. 2021;22:2437.
147. Hüll K, Morstein J, Trauner D. In Vivo Photopharmacology. Chemical Reviews. 2018;118(21):10710-47.
148. Stawski P, Sumser M, Trauner D. A Photochromic Agonist of AMPA Receptors. Angewandte Chemie International Edition. 2012;51(23):5748-51.
149. Sumser M, Stawski P. Photocontrol of AMPA Receptors with a Photochromic Ligand. In: Cambridge S, editor. Photoswitching Proteins: Methods and Protocols. New York, NY: Springer New York; 2014. p. 69-76.
150. Laprell L, Hüll K, Stawski P, Schön C, Michalakis S, Biel M, et al. Restoring Light Sensitivity in Blind Retinae Using a Photochromic AMPA Receptor Agonist. ACS Chemical Neuroscience. 2016;7(1):15-20.
151. Barber DM, Liu SA, Gottschling K, Sumser M, Hollmann M, Trauner D. Optical control of AMPA receptors using a photoswitchable quinoxaline-2,3-dione antagonist. Chem Sci. 2017;8(1):611-5.
152. Nikolaev MV, Strashkov DM, Ryazantsev MN, Tikhonov DB. Optical Control of N-Methyl-d-aspartate Receptors by Azobenzene Quaternary Ammonium Compounds. ACS Chemical Neuroscience. 2021;12(18):3347-57.
153. Nikolaev MV, Strashkov DM, Ryazantsev MN, Tikhonov DB. Development of a quaternary ammonium photoswitchable antagonist of NMDA receptors. European Journal of Pharmacology. 2023;938:175448.
154. Nikolaev M, Tikhonov D. Light-Sensitive Open Channel Block of Ionotropic Glutamate Receptors by Quaternary Ammonium Azobenzene Derivatives. International Journal of Molecular Sciences [Internet]. 2023; 24(18).
155. Izquierdo-Serra M, Bautista-Barrufet A, Trapero A, Garrido-Charles A, Díaz-Tahoces A, Camarero N, et al. Optical control of endogenous receptors and cellular excitability using targeted covalent photoswitches. Nature Communications. 2016;7(1):12221.
156. Lemoine D, Mondoloni S, Tange J, Lambolez B, Faure P, Taly A, et al. Probing the ionotropic activity of glutamate GluD2 receptor in HEK cells with genetically-engineered photopharmacology. eLife. 2020;9:e59026.
157. Banghart MR, Mourot A, Fortin DL, Yao JZ, Kramer RH, Trauner D. Photochromic blockers of voltage-gated potassium channels. Angew Chem Int Ed Engl. 2009;48(48):9097-101.
158. Quandt G, Höfner G, Pabel J, Dine J, Eder M, Wanner KT. First Photoswitchable Neurotransmitter Transporter Inhibitor: Light-Induced Control of γ-Aminobutyric Acid Transporter 1 (GAT1) Activity in Mouse Brain. Journal of Medicinal Chemistry. 2014;57(15):6809-21.
159. Cheng B, Shchepakin D, Kavanaugh MP, Trauner D. Photoswitchable Inhibitor of a Glutamate Transporter. ACS Chemical Neuroscience. 2017;8(8):1668-72.

160. Chabala LD, Lester HA. Activation of acetylcholine receptor channels by covalently bound agonists in cultured rat myoballs. The Journal of physiology. 1986;379(1):83-108.
161. Chabala LD, Gurney AM, Lester HA. Dose-response of acetylcholine receptor channels opened by a flash-activated agonist in voltage-clamped rat myoballs. The Journal of physiology. 1986;371(1):407-33.
162. Federico I, Manuel A. Optogenetics and photopharmacology in pain research and therapeutics. STEMedicine. 2020;1(3).
163. Schönberger M, Trauner D. A Photochromic Agonist for μ-Opioid Receptors. Angewandte Chemie International Edition. 2014;53(12):3264-7.
164. Westphal MV, Schafroth MA, Sarott RC, Imhof MA, Bold CP, Leippe P, et al. Synthesis of Photoswitchable Δ9-Tetrahydrocannabinol Derivatives Enables Optical Control of Cannabinoid Receptor 1 Signaling. Journal of the American Chemical Society. 2017;139(50):18206-12.
165. Levitz J, Broichhagen J, Leippe P, Konrad D, Trauner D, Isacoff EY. Dual optical control and mechanistic insights into photoswitchable group II and III metabotropic glutamate receptors. Proceedings of the National Academy of Sciences. 2017;114(17):E3546-E54.
166. Broichhagen J, Jurastow I, Iwan K, Kummer W, Trauner D. Optical Control of Acetylcholinesterase with a Tacrine Switch. Angewandte Chemie International Edition. 2014;53(29):7657-60.
167. Frank JA, Antonini M-J, Chiang P-H, Canales A, Konrad DB, Garwood IC, et al. In Vivo Photopharmacology Enabled by Multifunctional Fibers. ACS Chemical Neuroscience. 2020;11(22):3802-13.
168. Qazi R, Gomez AM, Castro DC, Zou Z, Sim JY, Xiong Y, et al. Wireless optofluidic brain probes for chronic neuropharmacology and photostimulation. Nature Biomedical Engineering. 2019;3(8):655-69.
169. Ma X, Johnson DA, He XJ, Layden AE, McClain SP, Yung JC, et al. In vivo photopharmacology with a caged mu opioid receptor agonist drives rapid changes in behavior. Nature Methods. 2023;20(5):682-5.
170. López-Cano M, Font J, Aso E, Sahlholm K, Cabré G, Giraldo J, et al. Remote local photoactivation of morphine produces analgesia without opioid-related adverse effects. British Journal of Pharmacology. 2023;180(7):958-74.
171. Berry MH, Holt A, Levitz J, Broichhagen J, Gaub BM, Visel M, et al. Restoration of patterned vision with an engineered photoactivatable G protein-coupled receptor. Nature Communications. 2017;8(1):1862.
172. Nicolai L. Über drahtlose elektrische Gewebereizung, besonders des Gehirnes, mittels dezimeterwellen-impulsgesteuerter selbständiger, transistorierter Reizstromgeneratoren. Pflüger's Archiv für die gesamte Physiologie des Menschen und der Tiere. 1962;275(3):327-46.
173. Zeier H, Tschannen G, Seitz H, Fideler A. A device for wireless electric brain stimulation in operant conditioning situations. Physiology & Behavior. 1968;3(4):587-90.
174. Wise KD. Silicon microsystems for neuroscience and neural prostheses. IEEE Engineering in Medicine and Biology Magazine. 2005;24(5):22-9.
175. Chien C-N, Jaw F-S. Miniature telemetry system for the recording of action and field potentials. Journal of Neuroscience Methods. 2005;147(1):68-73.
176. Song WG, Wang YL, Chai J, Li Q, Yuan K, Han TZ. A wireless miniature device for neural stimulating and recording in small animals. In: Jiao L, Wang L, Gao X, Liu J, Wu F, editors. Advances in Natural Computation, Pt 2. Lecture Notes in Computer Science. 42222006. p. 884-93.
177. Szurman P, Warga M, Roters S, Grisanti S, Heimann U, Aisenbrey S, et al. Experimental implantation and long-term testing of an intraocular vision aid in rabbits. Archives of Ophthalmology. 2005;123(7):964-9.

178. Wyatt JL, Rizzo JF, Theogarajan L, Shire DB, Kelly SK, Gingerich MD, et al. Engineering development of a prototype wireless subretinal prosthesis. Investigative Ophthalmology & Visual Science. 2005;46.
179. Walter P, Kisvarday ZF, Gortz M, Alteheld N, Rossler G, Stieglitz T, et al. Cortical activation via an implanted wireless retinal prosthesis. Investigative Ophthalmology & Visual Science. 2005;46(5):1780-5.
180. Schwarz M, Ewe L, Hauschild R, Hosticka BJ, Huppertz J, Kolnsberg S, et al. Single chip CMOS imagers and flexible microelectronic stimulators for a retina implant system. Sensors and Actuators a-Physical. 2000;83(1-3):40-6.
181. Doorish JF. A wireless photovoltaic Mini epi-Retinal Prosthesis (MeRP) 1: concept and design. Journal of Modern Optics. 2006;53(9):1267-85.
182. Laube T, Brockmann C, Buß R, Lau C, Höck K, Stawski N, et al. Optical energy transfer for intraocular microsystems studied in rabbits. Graefe's Archive for Clinical and Experimental Ophthalmology. 2004;242(8):661-7.
183. Mathieson K, Loudin J, Goetz G, Huie P, Wang L, Kamins TI, et al. Photovoltaic retinal prosthesis with high pixel density. Nature Photonics. 2012;6(6):391-7.
184. Ghezzi D, Antognazza MR, Maccarone R, Bellani S, Lanzarini E, Martino N, et al. A polymer optoelectronic interface restores light sensitivity in blind rat retinas. Nature Photonics. 2013;7(5):400-6.
185. Mandel Y, Goetz G, Lavinsky D, Huie P, Mathieson K, Wang L, et al. Cortical responses elicited by photovoltaic subretinal prostheses exhibit similarities to visually evoked potentials. Nature Communications. 2013;4(1):1980.
186. Đerek V, Rand D, Migliaccio L, Hanein Y, Głowacki ED. Untangling Photofaradaic and Photocapacitive Effects in Organic Optoelectronic Stimulation Devices. Frontiers in Bioengineering and Biotechnology. 2020;8.
187. Đerek V, Rand D, Migliaccio L, Hanein Y, Glowacki ED. Untangling Photofaradaic and Photocapacitive Effects in Organic Optoelectronic Stimulation Devices. Front Bioeng Biotechnol. 2020;8:284.
188. Cesare P, Moriondo A, Vellani V, McNaughton PA. Ion channels gated by heat. Proc Natl Acad Sci U S A. 1999;96(14):7658-63.
189. Meza RC, Ancatén-González C, Chiu CQ, Chávez AE. Transient Receptor Potential Vanilloid 1 Function at Central Synapses in Health and Disease. Front Cell Neurosci. 2022;16.
190. Wu X, Jiang Y, Rommelfanger N, Yang F, Zhou Q, Yin R, et al. Tether-free photothermal deep-brain stimulation in freely behaving mice via wide-field illumination in the near-infrared-II window. Nature Biomedical Engineering. 2022;6:1-17.
191. Shapiro MG, Homma K, Villarreal S, Richter C-P, Bezanilla F. Infrared light excites cells by changing their electrical capacitance. Nature Communications. 2012;3(1):736.
192. Tan CL, Knight ZA. Regulation of Body Temperature by the Nervous System. Neuron. 2018;98(1):31-48.
193. Jakešová M, Apaydin DH, Sytnyk M, Oppelt K, Heiss W, Sariciftci NS, et al. Hydrogen-Bonded Organic Semiconductors as Stable Photoelectrocatalysts for Efficient Hydrogen Peroxide Photosynthesis. Advanced Functional Materials. 2016;26(29):5248-54.
194. DelloStritto DJ, Connell PJ, Dick GM, Fancher IS, Klarich B, Fahmy JN, et al. Differential regulation of TRPV1 channels by H2O2: implications for diabetic microvascular dysfunction. Basic Res Cardiol. 2016;111(2):21.
195. Morad H, Luqman S, Tan C-H, Swann V, McNaughton PA. TRPM2 ion channels steer neutrophils towards a source of hydrogen peroxide. Scientific Reports. 2021;11(1):9339.
196. Savva A, Hama A, Herrera-Lopez G, Schmidt T, Migliaccio L, Steiner N, et al. Photo-Chemical Stimulation of Neurons with Organic Semiconductors. Adv Sci (Weinh). 2023;10(31):e2300473.

197. Merrill DR, Bikson M, Jefferys JG. Electrical stimulation of excitable tissue: design of efficacious and safe protocols. J Neurosci Methods. 2005;141(2):171-98.
198. Halliwell B. Reactive oxygen species and the central nervous system. J Neurochem. 1992;59(5):1609-23.
199. Rostami-Tapeh-Esmail E, Golshan M, Salami-Kalajahi M, Roghani-Mamaqani H. Perylene-3,4,9,10-tetracarboxylic diimide and its derivatives: Synthesis, properties and bioapplications. Dyes and Pigments. 2020;180:108488.
200. Anghelone M, Jembrih-Simbürger D, Pintus V, Schreiner M. Photostability and influence of phthalocyanine pigments on the photodegradation of acrylic paints under accelerated solar radiation. Polymer Degradation and Stability. 2017;146:13-23.
201. Zhang Y, Lovell JF. Recent applications of phthalocyanines and naphthalocyanines for imaging and therapy. Wiley Interdiscip Rev Nanomed Nanobiotechnol. 2017;9(1).
202. Rennie CC, Edkins RM. Targeted cancer phototherapy using phthalocyanine–anticancer drug conjugates. Dalton Transactions. 2022;51(35):13157-75.
203. Li X, Peng X-H, Zheng B-D, Tang J, Zhao Y, Zheng B-Y, et al. New application of phthalocyanine molecules: from photodynamic therapy to photothermal therapy by means of structural regulation rather than formation of aggregates. Chemical Science. 2018;9(8):2098-104.
204. Gryszel M, Sytnyk M, Jakešová M, Romanazzi G, Gabrielsson R, Heiss W, et al. General Observation of Photocatalytic Oxygen Reduction to Hydrogen Peroxide by Organic Semiconductor Thin Films and Colloidal Crystals. ACS Applied Materials & Interfaces. 2018;10(16):13253-7.
205. Fischl B, Dale AM. Measuring the thickness of the human cerebral cortex from magnetic resonance images. Proc Natl Acad Sci U S A. 2000;97(20):11050-5.
206. Palomero-Gallagher N, Zilles K. CHAPTER 23 - Isocortex. In: Paxinos G, editor. The Rat Nervous System (Third Edition). Burlington: Academic Press; 2004. p. 729-57.
207. Vetreno RP, Yaxley R, Paniagua B, Johnson GA, Crews FT. Adult rat cortical thickness changes across age and following adolescent intermittent ethanol treatment. Addict Biol. 2017;22(3):712-23.
208. Tracey D. CHAPTER 25 - Somatosensory System. In: Paxinos G, editor. The Rat Nervous System (Third Edition). Burlington: Academic Press; 2004. p. 797-815.
209. Nelson RJ, Liu Y. Somatosensory Cortex: Functional Architecture. In: Squire LR, editor. Encyclopedia of Neuroscience. Oxford: Academic Press; 2009. p. 79-84.
210. Witter MP, Amaral DG. CHAPTER 21 - Hippocampal Formation. In: Paxinos G, editor. The Rat Nervous System (Third Edition). Burlington: Academic Press; 2004. p. 635-704.
211. Hiremath SV, Tyler-Kabara EC, Wheeler JJ, Moran DW, Gaunt RA, Collinger JL, et al. Human perception of electrical stimulation on the surface of somatosensory cortex. PLOS ONE. 2017;12(5):e0176020.
212. Flesher SN, Collinger JL, Foldes ST, Weiss JM, Downey JE, Tyler-Kabara EC, et al. Intracortical microstimulation of human somatosensory cortex. Science Translational Medicine. 2016;8(361):361ra141-361ra141.
213. Johnson LA, Wander JD, Sarma D, Su DK, Fetz EE, Ojemann JG. Direct electrical stimulation of the somatosensory cortex in humans using electrocorticography electrodes: a qualitative and quantitative report. J Neural Eng. 2013;10(3):036021.
214. Grundmann L, Rolke R, Nitsche MA, Pavlakovic G, Happe S, Treede R-D, et al. Effects of transcranial direct current stimulation of the primary sensory cortex on somatosensory perception. Brain Stimul. 2011;4(4):253-60.
215. De Ridder D, De Mulder G, Verstraeten E, Sunaert S, Moller A. Somatosensory cortex stimulation for deafferentation pain. In: Sakas DE, Simpson BA, editors. Operative Neuromodulation: Volume 2: Neural Networks Surgery. Vienna: Springer Vienna; 2007. p. 67-74.
216. Sasaki R, Watanabe H, Onishi H. Therapeutic benefits of noninvasive somatosensory cortex stimulation on cortical plasticity and somatosensory function: A systematic review. The European journal of neuroscience. 2022;56(5):4669-98.

217. Bellistri E, Aguilar J, Brotons-Mas JR, Foffani G, de la Prida LM. Basic properties of somatosensory-evoked responses in the dorsal hippocampus of the rat. The Journal of physiology. 2013;591(10):2667-86.
218. Pidoux M, Mahon S, Deniau J-M, Charpier S. Integration and propagation of somatosensory responses in the corticostriatal pathway: an intracellular study in vivo. The Journal of physiology. 2011;589(2):263-81.
219. Cheng MY, Wang EH, Woodson WJ, Wang S, Sun G, Lee AG, et al. Optogenetic neuronal stimulation promotes functional recovery after stroke. Proc Natl Acad Sci U S A. 2014;111(35):12913-8.
220. Jason BC, Hiroki K, John HM. Electrical Stimulation of Motor Cortex in the Uninjured Hemisphere after Chronic Unilateral Injury Promotes Recovery of Skilled Locomotion through Ipsilateral Control. The Journal of Neuroscience. 2014;34(2):462.
221. Nowakowska M. JM, Schmidt T., Opančar A., Polz M., Reimer R., Fuchs J., Patz S., Ziesel D., Scheruebel S., Kornmueller K., Rienmüller T., Đerek V., Głowacki E.D., Schindl R., Üçal M. Light-Controlled Electric Stimulation with Organic Electrolytic Photocapacitors Achieves Complex Neuronal Network Activation: Semi-chronic Study in Cortical Cell Culture and Rat Model. Advanced Healthcare Materials 2024.
222. Lobner D. Comparison of the LDH and MTT assays for quantifying cell death: validity for neuronal apoptosis? J Neurosci Methods. 2000;96(2):147-52.
223. Schindelin J, Arganda-Carreras I, Frise E, Kaynig V, Longair M, Pietzsch T, et al. Fiji: an open-source platform for biological-image analysis. Nature Methods. 2012;9(7):676-82.
224. Linkert M, Rueden CT, Allan C, Burel JM, Moore W, Patterson A, et al. Metadata matters: access to image data in the real world. J Cell Biol. 2010;189(5):777-82.
225. Gähwiler BH, Capogna M, Debanne D, McKinney RA, Thompson SM. Organotypic slice cultures: a technique has come of age. Trends Neurosci. 1997;20(10):471-7.
226. Schwabe K, Boldt L, Bleich A, van Dijk RM, Helgers SOA, Hager C, et al. Nest-building performance in rats: impact of vendor, experience, and sex. Lab Anim. 2020;54(1):17-25.
227. Team RC. R: A Language and Environment for Statistical Computing. Vienna, Austria2022.
228. Wickham H. dplyr: A Grammar of Data Manipulation. 2023.
229. Wickham H. Welcome to the Tidyverse. Journal of Open Source Software. 2019;4(43):1686.
230. Weisberg JFaS. An {R} Companion to Applied Regression. Third ed: Sage; 2019.
231. Wickham H. ggplot2: Springer Cham; 2016.
232. Slowikowski K. ggrepel: Automatically Position Non-Overlapping Text Labels with 'ggplot2'. 2023.
233. Kassambara A. ggpubr: 'ggplot2' Based Publication Ready Plots. 2023.
234. Reed J, Walczak WJ, Petzold ON, Gimzewski JK. In situ mechanical interferometry of matrigel films. Langmuir. 2009;25(1):36-9.
235. Xu X, Radulescu CI, Utami KH, Pouladi MA. Obtaining Multi-electrode Array Recordings from Human Induced Pluripotent Stem Cell-Derived Neurons. Bio Protoc. 2017;7(22):e2609.
236. Amin H, Maccione A, Marinaro F, Zordan S, Nieus T, Berdondini L. Electrical Responses and Spontaneous Activity of Human iPS-Derived Neuronal Networks Characterized for 3-month Culture with 4096-Electrode Arrays. Front Neurosci. 2016;10:121.
237. Baek S, Na K. A nano complex of hydrophilic phthalocyanine and polyethylenimine for improved cellular internalization efficiency and phototoxicity. Colloids Surf B Biointerfaces. 2013;101:493-500.
238. George L, Müller A, Röder B, Santala V, Efimov A. Photodynamic self–disinfecting surface using pyridinium phthalocyanine. Dyes and Pigments. 2017;147:334-42.
239. Roobol C, De Dobbeleer GB, Bernheim JL. 5-fluorouracil and 5-fluoro-2'-deoxyuridine follow different metabolic pathways in the induction of cell lethality in L1210 leukaemia. Br J Cancer. 1984;49(6):739-44.

240. El-Subbagh HI, Al-Badr AA. Chapter 2 - Cytarabine. In: Brittain HG, editor. Profiles of Drug Substances, Excipients and Related Methodology. 34: Academic Press; 2009. p. 37-113.
241. Smets LA. Programmed cell death (apoptosis) and response to anti-cancer drugs. Anti-Cancer Drugs. 1994;5(1).
242. Kumar P, Nagarajan A, Uchil PD. Analysis of Cell Viability by the Lactate Dehydrogenase Assay. Cold Spring Harb Protoc. 2018;2018(6).
243. Hogins J, Crawford DC, Zorumski CF, Mennerick S. Excitotoxicity triggered by Neurobasal culture medium. PLoS One. 2011;6(9):e25633.
244. Riss T, Niles A, Moravec R, Karassina N, Vidugiriene J. Cytotoxicity Assays: In Vitro Methods to Measure Dead Cells. In: Markossian S, Grossman A, Brimacombe K, Arkin M, Auld D, Austin C, et al., editors. Assay Guidance Manual. Bethesda (MD)2004.
245. Yu X, Hu Y, Shao C, Huang W, Li Y. Polymer semiconductors: A unique platform for photocatalytic hydrogen peroxide production. Materials Today. 2023;71:152-73.
246. Kendig DM, Tarloff JB. Inactivation of lactate dehydrogenase by several chemicals: implications for in vitro toxicology studies. Toxicol In Vitro. 2007;21(1):125-32.
247. Tabatabaie T, Potts JD, Floyd RA. Reactive Oxygen Species-Mediated Inactivation of Pyruvate Dehydrogenase. Archives of Biochemistry and Biophysics. 1996;336(2):290-6.
248. Dani S, Schütz K, Dikici E, Bernhardt A, Lode A. The effect of continuous long-term illumination with visible light in different spectral ranges on mammalian cells. Sci Rep. 2024;14(1):9444.
249. Polz M, Ziesel D, Shrestha N, Pelzmann B, Lang P, Scherübel S, et al. Photovoltaic Stimulation Induces Overdrive Suppression in Embryonic Chicken Cardiomyocytes. Current Directions in Biomedical Engineering. 2023;9(2):12-5.
250. King AE, Chung RS, Vickers JC, Dickson TC. Localization of glutamate receptors in developing cortical neurons in culture and relationship to susceptibility to excitotoxicity. Journal of Comparative Neurology. 2006;498(2):277-94.
251. Manzouri F, Meisel C, Kunz L, Dümpelmann M, Stieglitz T, Schulze-Bonhage A. Low-frequency electrical stimulation reduces cortical excitability in the human brain. Neuroimage Clin. 2021;31:102778.
252. Yamamoto J, Ikeda A, Kinoshita M, Matsumoto R, Satow T, Takeshita K, et al. Low-frequency electric cortical stimulation decreases interictal and ictal activity in human epilepsy. Seizure. 2006;15(7):520-7.
253. Alagapan S, Schmidt SL, Lefebvre J, Hadar E, Shin HW, Fröhlich F. Modulation of Cortical Oscillations by Low-Frequency Direct Cortical Stimulation Is State-Dependent. PLOS Biology. 2016;14(3):e1002424.
254. Ma F, Zhang L, Westlund KN. Reactive Oxygen Species Mediate TNFR1 Increase after TRPV1 Activation in Mouse DRG Neurons. Molecular Pain. 2009;5:1744-8069-5-31.
255. Ghafouri S, Fathollahi Y, Semnanian S, Shojaei A, Mirnajafi-Zadeh J. Effects of Low Frequency Stimulation on Spontaneous Inhibitory and Excitatory Post-Synaptic Currents in Hippocampal CA1 Pyramidal Cells of Kindled Rats. Cell J. 2017;18(4):547-55.
256. Ghasemi Z, Naderi N, Shojaei A, Raoufy MR, Ahmadirad N, Barkley V, et al. The inhibitory effect of different patterns of low frequency stimulation on neuronal firing following epileptiform activity in rat hippocampal slices. Brain Res. 2019;1706:184-95.
257. Manzouri F, Meisel C, Kunz L, Dümpelmann M, Stieglitz T, Schulze-Bonhage A. Low-frequency electrical stimulation reduces cortical excitability in the human brain. NeuroImage: Clinical. 2021;31:102778.
258. Tafur J, Mills PJ. Low-intensity light therapy: exploring the role of redox mechanisms. Photomed Laser Surg. 2008;26(4):323-8.
259. Groten CJ, MacVicar BA. Mitochondrial Ca2+ uptake by the MCU facilitates pyramidal neuron excitability and metabolism during action potential firing. Communications Biology. 2022;5(1):900.

260. Hisanaga K, Sagar SM, Hicks KJ, Swanson RA, Sharp FR. c-fos proto-oncogene expression in astrocytes associated with differentiation or proliferation but not depolarization. Brain Res Mol Brain Res. 1990;8(1):69-75.
261. Gauthier-Rouvière C, Fernandez A, Lamb NJ. ras-induced c-fos expression and proliferation in living rat fibroblasts involves C-kinase activation and the serum response element pathway. Embo j. 1990;9(1):171-80.
262. Smith CL, Afroz R, Bassell GJ, Furneaux HM, Perrone-Bizzozero NI, Burry RW. GAP-43 mRNA in growth cones is associated with HuD and ribosomes. J Neurobiol. 2004;61(2):222-35.
263. Denny JB. Molecular mechanisms, biological actions, and neuropharmacology of the growth-associated protein GAP-43. Curr Neuropharmacol. 2006;4(4):293-304.
264. Chung D, Shum A, Caraveo G. GAP-43 and BASP1 in Axon Regeneration: Implications for the Treatment of Neurodegenerative Diseases. Frontiers in Cell and Developmental Biology. 2020;8.
265. Hoffman PN. Expression of GAP-43, a rapidly transported growth-associated protein, and class II beta tubulin, a slowly transported cytoskeletal protein, are coordinated in regenerating neurons. J Neurosci. 1989;9(3):893-7.
266. Koponen E, Lakso M, Castrén E. Overexpression of the full-length neurotrophin receptor trkB regulates the expression of plasticity-related genes in mouse brain. Molecular Brain Research. 2004;130(1):81-94.
267. Nao RK, Da-Peng F, Klaus MG, Annie MB, Stanley JW, Wolfram T. BDNF and NT-4/5 Prevent Atrophy of Rat Rubrospinal Neurons after Cervical Axotomy, Stimulate GAP-43 and Tα1-Tubulin mRNA Expression, and Promote Axonal Regeneration. The Journal of Neuroscience. 1997;17(24):9583.
268. Humpel C. Organotypic brain slice cultures: A review. Neuroscience. 2015;305:86-98.
269. Hakkoum D, Stoppini L, Muller D. Interleukin-6 promotes sprouting and functional recovery in lesioned organotypic hippocampal slice cultures. Journal of Neurochemistry. 2007;100(3):747-57.
270. Console-Bram LM, Baird DH, Fitzpatrick-McElligott SG, McElligott JG. Modulation of GAP-43 mRNA by GABA and glutamate in cultured cerebellar granule cells. Brain Res. 1998;783(2):316-25.
271. Kesterson KL, Lane RD, Rhoades RW. Effects of elevated serotonin levels on patterns of GAP-43 expression during barrel development in rat somatosensory cortex. Developmental Brain Research. 2002;139(2):167-74.
272. Soto I, Marie B, Baro DJ, Blanco RE. FGF-2 modulates expression and distribution of GAP-43 in frog retinal ganglion cells after optic nerve injury. J Neurosci Res. 2003;73(4):507-17.
273. Hayama T, Ogawa H. Regional Differences of Callosal Connections in the Granular Zones of the Primary Somatosensory Cortex in Rats. Brain Research Bulletin. 1997;43(3):341-7.
274. Fenlon LR, Suárez R, Richards LJ. The anatomy, organisation and development of contralateral callosal projections of the mouse somatosensory cortex. Brain Neurosci Adv. 2017;1:2398212817694888.
275. Greig LC, Woodworth MB, Galazo MJ, Padmanabhan H, Macklis JD. Molecular logic of neocortical projection neuron specification, development and diversity. Nat Rev Neurosci. 2013;14(11):755-69.
276. Rattay F. The basic mechanism for the electrical stimulation of the nervous system. Neuroscience. 1999;89(2):335-46.
277. Acsády L, Kamondi A, Sík A, Freund T, Buzsáki G. GABAergic cells are the major postsynaptic targets of mossy fibers in the rat hippocampus. J Neurosci. 1998;18(9):3386-403.
278. Lehtonen SM, Waselius T, Penttonen M, Nokia MS. Hippocampal responses to electrical stimulation of the major input pathways are modulated by dentate spikes. Hippocampus. 2022;32(11-12):808-17.
279. Schmidt B, Marrone DF, Markus EJ. Disambiguating the similar: the dentate gyrus and pattern separation. Behav Brain Res. 2012;226(1):56-65.

280. Borzello M, Ramirez S, Treves A, Lee I, Scharfman H, Stark C, et al. Assessments of dentate gyrus function: discoveries and debates. Nat Rev Neurosci. 2023;24(8):502-17.
281. Fredes F, Masaracchia L, Capogna M, Vidaurre D. Differential activity patterns in the upper and lower blade of the dentate gyrus2023.
282. Scharfman HE, Sollas AL, Smith KL, Jackson MB, Goodman JH. Structural and functional asymmetry in the normal and epileptic rat dentate gyrus. Journal of Comparative Neurology. 2002;454(4):424-39.
283. Edling Y, Ingelman-Sundberg M, Simi A. Glutamate activates c-fos in glial cells via a novel mechanism involving the glutamate receptor subtype mGlu5 and the transcriptional repressor DREAM. Glia. 2007;55(3):328-40.
284. Rubio N. Interferon-gamma induces the expression of immediate early genes c-fos and c-jun in astrocytes. Immunology. 1997;91(4):560-4.
285. Jiang X, Lachance M, Rossignol E. Chapter 4 - Involvement of cortical fast-spiking parvalbumin-positive basket cells in epilepsy. In: Rossignol E, Carmant L, Lacaille J-C, editors. Progress in Brain Research. 226: Elsevier; 2016. p. 81-126.
286. Donato C, Balduino Victorino D, Cabezas C, Aguirre A, Lourenço J, Potier MC, et al. Pharmacological Signature and Target Specificity of Inhibitory Circuits Formed by Martinotti Cells in the Mouse Barrel Cortex. J Neurosci. 2023;43(1):14-27.
287. Corbin JG, Butt SJ. Developmental mechanisms for the generation of telencephalic interneurons. Dev Neurobiol. 2011;71(8):710-32.
288. Niquille M, Limoni G, Markopoulos F, Cadilhac C, Prados J, Holtmaat A, et al. Neurogliaform cortical interneurons derive from cells in the preoptic area. eLife. 2018;7.
289. Kirkcaldie MTK. Chapter 4 - Neocortex. In: Watson C, Paxinos G, Puelles L, editors. The Mouse Nervous System. San Diego: Academic Press; 2012. p. 52-111.
290. Feldmeyer D, Qi G, Emmenegger V, Staiger J. Inhibitory Interneurons and their Circuit Motifs in the Many Layers of the Barrel Cortex. Neuroscience. 2017;368.
291. Komarov M, Malerba P, Golden R, Nunez P, Halgren E, Bazhenov M. Selective recruitment of cortical neurons by electrical stimulation. PLOS Computational Biology. 2019;15(8):e1007277.
292. Halgren AS, Siegel Z, Golden R, Bazhenov M. Multielectrode Cortical Stimulation Selectively Induces Unidirectional Wave Propagation of Excitatory Neuronal Activity in Biophysical Neural Model. J Neurosci. 2023;43(14):2482-96.
293. Missey F, Botzanowski B, Migliaccio L, Acerbo E, Głowacki ED, Williamson A. Organic electrolytic photocapacitors for stimulation of the mouse somatosensory cortex. J Neural Eng. 2021;18(6).
294. Escartin C, Galea E, Lakatos A, O'Callaghan JP, Petzold GC, Serrano-Pozo A, et al. Reactive astrocyte nomenclature, definitions, and future directions. Nature Neuroscience. 2021;24(3):312-25.
295. Bennett ML, Viaene AN. What are activated and reactive glia and what is their role in neurodegeneration? Neurobiology of disease. 2021;148:105172.
296. Shi C, Pamer EG. Monocyte recruitment during infection and inflammation. Nat Rev Immunol. 2011;11(11):762-74.
297. Terem I, Ni WW, Goubran M, Rahimi MS, Zaharchuk G, Yeom KW, et al. Revealing sub-voxel motions of brain tissue using phase-based amplified MRI (aMRI). Magn Reson Med. 2018;80(6):2549-59.
298. Williams RL, Williams DF. The spatial resolution of protein adsorption on surfaces of heterogeneous metallic biomaterials. Journal of Biomedical Materials Research. 1989;23(3):339-50.
299. Horbett TA, Latour RA. 2.1.2 - Adsorbed Proteins on Biomaterials. In: Wagner WR, Sakiyama-Elbert SE, Zhang G, Yaszemski MJ, editors. Biomaterials Science (Fourth Edition): Academic Press; 2020. p. 645-60.
300. Kim J. Systematic approach to characterize the dynamics of protein adsorption on the surface of biomaterials using proteomics. Colloids and Surfaces B: Biointerfaces. 2020;188:110756.

301. Sgambato V, Abo V, Rogard M, Besson MJ, Deniau JM. Effect of electrical stimulation of the cerebral cortex on the expression of the fos protein in the basal ganglia. Neuroscience. 1997;81(1):93-112.
302. Shehab S, D'souza C, Ljubisavljevic M, Redgrave P. High-frequency electrical stimulation of the subthalamic nucleus excites target structures in a model using c-fos immunohistochemistry. Neuroscience. 2014;270:212-25.
303. Krukoff TL, Morton TL, Harris KH, Jhamandas JH. Expression of c-fos protein in rat brain elicited by electrical stimulation of the pontine parabrachial nucleus. The Journal of Neuroscience. 1992;12(9):3582.
304. Iqbal Chowdhury GM, Liu Y, Tanaka M, Fujioka T, Ishikawa A, Nakamura S. Cortical spreading depression affects Fos expression in the hypothalamic paraventricular nucleus and the cerebral cortex of both hemispheres. Neuroscience Research. 2003;45(2):149-55.
305. Ingvardsen BK, Laursen H, Olsen UB, Hansen AJ. Possible mechanism of c-fos expression in trigeminal nucleus caudalis following cortical spreading depression. Pain. 1997;72(3):407-15.
306. Charles AC, Baca SM. Cortical spreading depression and migraine. Nature Reviews Neurology. 2013;9(11):637-44.
307. Dreier JP. The role of spreading depression, spreading depolarization and spreading ischemia in neurological disease. Nature Medicine. 2011;17(4):439-47.
308. Bradley DP, Huang CLH, James MF, Smith JM. Physiological studies of cortical spreading depression. Biological Reviews. 2006;81(4):457-81.
309. BureŠ J, BureŠOvÁ O. Chapter 12 - Inducing Cortical Spreading Depression. In: Myers RD, editor. Methods in Psychobiology: Academic Press; 1972. p. 319-43.
310. Carlson AP, William Shuttleworth C, Mead B, Burlbaw B, Krasberg M, Yonas H. Cortical spreading depression occurs during elective neurosurgical procedures. Journal of Neurosurgery JNS. 2017;126(1):266-73.
311. Hop HT, Arayan LT, Huy TXN, Reyes AWB, Vu SH, Min W, et al. The Key Role of c-Fos for Immune Regulation and Bacterial Dissemination in Brucella Infected Macrophage. Frontiers in Cellular and Infection Microbiology. 2018;8.
312. Cruz-Mendoza F, Jauregui-Huerta F, Aguilar-Delgadillo A, García-Estrada J, Luquin S. Immediate Early Gene c-fos in the Brain: Focus on Glial Cells. Brain sciences [Internet]. 2022; 12(6).
313. Carneiro-Nascimento S, Levy D. Cortical spreading depression and meningeal nociception. Neurobiology of Pain. 2022;11:100091.
314. Torrente D, Cabezas R, Avila MF, García-Segura LM, Barreto GE, Guedes RCA. Cortical spreading depression in traumatic brain injuries: Is there a role for astrocytes? Neuroscience Letters. 2014;565:2-6.
315. Bogdanov VB, Middleton NA, Theriot JJ, Parker PD, Abdullah OM, Ju YS, et al. Susceptibility of Primary Sensory Cortex to Spreading Depolarizations. The Journal of Neuroscience. 2016;36(17):4733.
316. Grassi-Zucconi G, Menegazzi M, De Prati AC, Bassetti A, Montagnese P, Mandile P, et al. C-fos mRNA is Spontaneously Induced in the Rat Brain During the Activity Period of the Circadian Cycle. European Journal of Neuroscience. 1993;5(8):1071-8.
317. Stryjek R, Modlinska K, Turlejski K, Pisula W. Circadian Rhythm of Outside-Nest Activity in Wild (WWCPS), Albino and Pigmented Laboratory Rats. PloS one. 2013;8:e66055.
318. Radhika B, Jonathan ES, Clifford BS, James IM, Robert WM, Priyattam JS. Effects of Sleep on Wake-Induced c-fos Expression. The Journal of Neuroscience. 1997;17(24):9746.
319. Cirelli C, Tononi G. On the Functional Significance of c-fos Induction During the Sleep-waking Cycle. Sleep. 2000;23(4):9-25.

13 APPENDIX

13.1 LIST OF MATERIALS

Cell culture and cytotoxicity	
Fisherbrand Sterile Cell Strainers	Fisher Scientific, Cat. No. 22-363-548
Accutase solution	Sigma Aldrich, Cat. No. A6964
Gibco TrypLE Express	Thermo Fisher Scientific, Cat. No. 12605010
Gibco Poly-D-lysine	Thermo Fisher Scientific, Cat. No. A3890401
Gibco Dulbeccos's Minimal Essential Media	Thermo Fisher Scientific, Cat. No. 42430025
Gibco Fetal Bovine Serum, heat inactivated	Thermo Fisher Scientific, Cat. No. 10100147
Gibco MEM Non-Essential Amino Acids Solution	Thermo Fisher Scientific, Cat. No. 11140050
Gibco Penicillin-Streptomycin (10 000 U/mL)	Thermo Fisher Scientific, Cat. No. 15140122
Gibco Neurobasal A	Thermo Fisher Scientific, Cat. No. 10888022
Gibco B-27	Thermo Fisher Scientific, Cat. No. 17504044
Gibco GlutaMAX	Thermo Fisher Scientific, Cat. No. 35050061
Normocin	InvivoGen, Cat. No. ant-nr-1
bFGF	PeproTech, Cat. No. 100-18B-50UG
EGF	PeproTech, Cat. No. AF-100-15-100UG
D-(+)-glucose	Sigma Aldrich, Cat. No. G8270-100G
CyQUANT LDH Cytotoxicity Assay	Thermo Fisher Scientific, Cat. No. C20301
Surgery	
Fentanyl (Fentanyl-hameln, 50 µg/ml)	Hameln Pharma
Midazolam (Midazolam-hameln, 5 mg/ml)	Hameln Pharma
Medetomidine (Domitor, 1 mg/ml)	Orion Pharma
Flumazenil (Flumazenil Kabi, 0,1 mg/ml)	Fresenius Kabi
Atipamezole (Antisedan, 5 mg/ml)	Orion Pharma
Enrofloxacin (Baytril, 50 mg/ml)	Bayer
Carprofen (Rimadyl, 50 mg/ml)	Pfizer
Natrium chloride 0.9%	Fresenius Kabi
BioMed Clear Resin	Formlabs
iCEM Self Adhesive composite	Heraeus Kulzer
Vicryl Plus, FS-2, 5/0	Ethicon, Cat. No. VCP391H
Trephine drill bits, 10mm length, RA L, 229	Meisinger, Cat. No. 3300229205040
Histology and immunohistochemistry	
Formaldehyde 37%	Roth, Cat. No. 7398.4
ROTI PreMix PBS	Roth, Cat. No. 0890.2
Triton X-100	Millipore, Cat. No. 1.08603.1000
Sodium citrate tribasic dihydrate	Sigma Aldrich. Cat. No. C7254-1KG
Ethanol absolute 99.9% vol.	AustrAlco
Xylene	Roth, Cat. No. 4436.2
Methanol	VWR internation, Cat. No. NC1179385
Hydrogen peroxide solution 30% (w/w)	Sigma Aldrich, Cat. No. 31642-500ML-M
Normal goat serum	Abcam, Cat. No. ab7481
Gibco Horse serum, heat inactivated	Thermo Fisher Scientific, Cat. No. 26050-088
VECTASTAIN ABC HRP Kit	Vector, Cat. No. PK-4000
ImmPACT DAB Substrate Kit	Vector, Cat. No. SK-4105
Hämalaunlösung n. Mayer	Gatt-Koller, Cat. No. 401296170

Tissue-Tek Glas Mounting Medium	Sakura Finetek, Cat. No. 6419
Fluoroshield with DAPI	Sigma Aldrich, Cat. No. F6057-20ML
SEM preparation and imaging	
Sodium cacodylate trihydrate	Merck
OsO_4 stock solution(4% in water)	EMS
L(+)-Ascorbic acid	Roth
Ethanol	Lactan
Hexamethyldisilazane	VWR Chemicals
Liquid conductive silver	EMS

13.2 LIST OF DEVICES

Cell culture and cytotoxicity	
Tissue chopper	McIlwain Tissue Chopper (RRID:SCR_015798)
CASY Cell Counter and Analyser System Model TT	OMNI Life Science (RRID:SCR_002080)
SPECTROstar Omega Microplate Reader	BMG Labtech
Surgery	
Stereotactic frame	Kopf Instruments
Dental Wireless LED Curing Light	Heraeus Kulzer
Light stimulation	
High-Power 1-Channel LED Driver with Pulse Modulation	ThorLabs, Cat. No. DC 2200
Histology and immunohistochemistry	
Tissue-Tek VIP 5 Tissue Processor	Sakura
TES Valida Modular Paraffin Embedding Center	MEDITE Medical GmbH
Microm HM 560 Cryostat	Thermo Fisher Scientific
Rotary microtome HM355 S	Thermo Fisher Scientific
Decloaking Chamber NxGen	BioCare Medical, Cat. No. DC 2012
Aperio ScanScope AT	Leica
Nikon A1R Confocal Laser Microscope	Nikon (RRID:SCR_020317)
SEM preparation and imaging	
Sputter coater Bal-Tec SCD500	Bal-Tec
Scanning Electron Microscope Sigma 500	Zeiss

13.3 LIST OF SOFTWARE

Histology and immunohistochemistry	
Fiji	U. S. National Institutes of Health; Bethesda, Maryland, USA (RRID: SCR_002285)
QuPath (v0.4.3)	RRID:SCR_018257
SEM preparation and imaging	
ImageSP	SysProg
Statistics and data visualisation	
RStudio	Posit, PBC

13.4 ICC PROTOCOL

Day 1	
1	4% (v/v) FA for 15 min at RT
2	3 × 5 min PBST wash
3	Blocking solution (NGS 5% v/v in PBST) for 60 min at RT
4	Remove the blocking solution and add primary antibody diluted in NGS 5% (v/v) in PBST; incubate overnight at 4 °C
Tag 2	
1	3 × 5 min PBST wash
From now on work in darkness	
2	Add secondary antibody diluted in NGS 5% (v/v) in PBST; incubate for 60 min at RT
3	3 × 5 min PBST wash
4	Cover slip using anti-fading aqueous mounting media with DAPI
5	Apply nail polish at the corners of cover slip

13.5 IHC WITH DAB PROTOCOL

Day 1	
1	2 × 10 min xylene
2	1 × 10 min xylene:EtOH 1:1
3	1 × 5 min 100% EtOH
4	1 × 30 min in H_2O_2 0,3% (v/v) in methanol
5	1 × 5 min 90% EtOH, 70% EtOH, 50% EtOH
6	2 × 5 min diH_2O wash
7	Na-citrate 10 mmol pH 6 in Decloaking chamber (95 °C, 20 min); 20 min cool down on ice
8	3 × 5 min PBST wash
9	Circle sections with PAP pen and put them into humidity chamber filled with distilled water
10	Blocking solution (NGS 5% v/v in PBST) for 60 min at RT
11	Remove the blocking solution and add primary antibody diluted in NGS 5% (v/v) in PBST; incubate overnight at 4 °C
Tag 2	
1	3 × 5 min PBST wash
2	Add secondary antibody diluted in NGS 5% (v/v) in PBST; incubate for 60 min at RT
3	3 × 5 min PBST wash
4	Add ABC kit for 30 min at RT
5	3 × 5 min PBST wash
6	Add DAB solution and develop the colour with visual control under the microscope
7	2 × 5 min diH_2O wash
8	Shortly (1-2 s) soak in haematoxylin solution
9	Bluing under running distilled H_2O for 5 min
10	5 min × 50% EtOH, 70% EtOH, 90% EtOH, 100% EtOH, xylene:EtOH 1:1, xylene
11	Cover slip using xylene-based mounting media

13.6 IF MULTIPLE STAINING PROTOCOL

Day 1	
1	2 × 10 min xylene
2	1 × 10 min xylene:EtOH 1:1
3	1 × 5 min 100% EtOH, 90% EtOH, 70% EtOH, 50% EtOH
4	2 × 5 min diH_2O wash
5	Na-citrate 10 mmol pH 6 in Decloaking chamber (95 °C, 20 min); 20 min cool down on ice
6	3 × 5 min PBST wash
7	Circle sections with PAP pen and put them into humidity chamber filled with distilled water
8	Blocking solution (NGS 5% v/v in PBST) for 60 min at RT
9	Remove the blocking solution and add primary antibody diluted in NGS 5% (v/v) in PBST; incubate overnight at 4 °C
Tag 2	
1	3 × 5 min PBST wash
From now on work in darkness	
2	Add secondary antibody diluted in NGS 5% (v/v) in PBST; incubate for 60 min at RT
3	3 × 5 min PBST wash
4	Cover slip using anti-fading aqueous mounting media with DAPI
5	Apply nail polish at the corners of cover slip